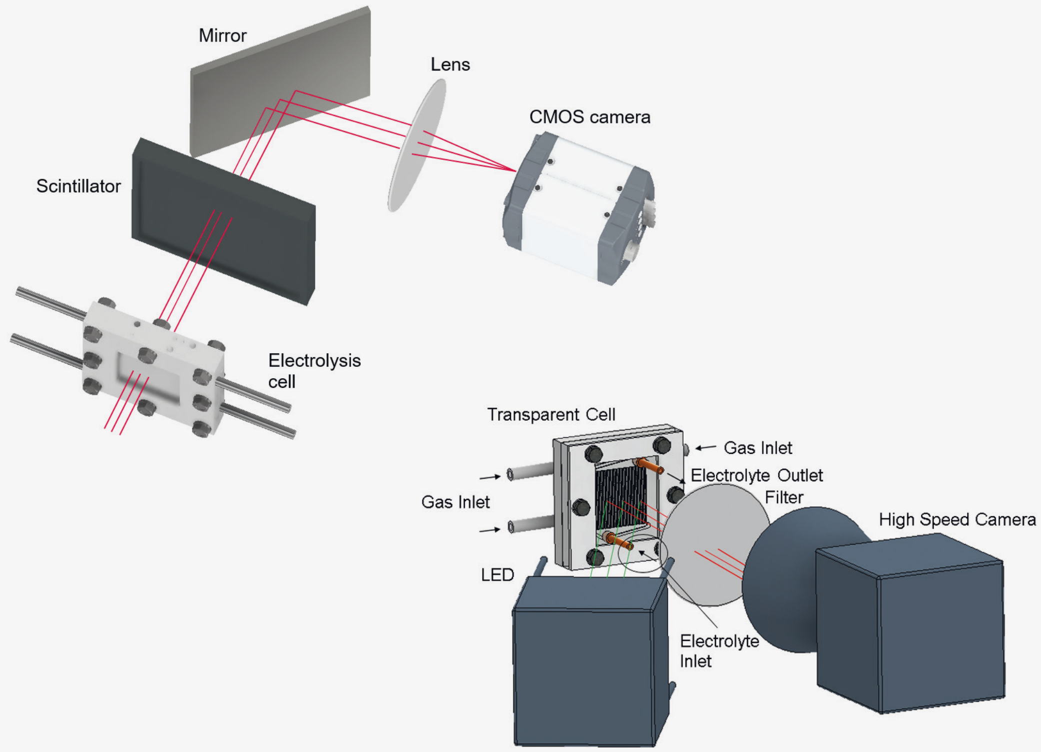

Methodological Approach Enabling the Two-phase Flow Investigation in Alkaline Electrolysis under Demanding Conditions

Stefanie Renz

Energie & Umwelt / Energy & Environment
Band / Volume 661
ISBN 978-3-95806-821-6

Mitglied der Helmholtz-Gemeinschaft

JÜLICH
Forschungszentrum

Schriften des Forschungszentrums Jülich
Reihe Energie & Umwelt / Energy & Environment Band / Volume 661

Forschungszentrum Jülich GmbH
Institute of Energy Technologies (IET)
Elektronische Verfahrenstechnik (IET-4)

Methodological Approach Enabling the Two-phase Flow Investigation in Alkaline Electrolysis under Demanding Conditions

Stefanie Renz

Schriften des Forschungszentrums Jülich
Reihe Energie & Umwelt / Energy & Environment Band / Volume 661

ISSN 1866-1793 ISBN 978-3-95806-821-6

Bibliografische Information der Deutschen Nationalbibliothek.
Die Deutsche Nationalbibliothek verzeichnet diese Publikation in der
Deutschen Nationalbibliografie; detaillierte Bibliografische Daten
sind im Internet über http://dnb.d-nb.de abrufbar.

Herausgeber und Vertrieb: Forschungszentrum Jülich GmbH
Zentralbibliothek, Verlag
52425 Jülich
Tel.: +49 2461 61-5368
Fax: +49 2461 61-6103
zb-publikation@fz-juelich.de
www.fz-juelich.de/zb

Umschlaggestaltung: Grafische Medien, Forschungszentrum Jülich GmbH

Druck: Grafische Medien, Forschungszentrum Jülich GmbH

Schriften des Forschungszentrums Jülich
Reihe Energie & Umwelt / Energy & Environment, Band / Volume 661

D 82 (Diss. RWTH Aachen University, 2024)

ISSN 1866-1793
ISBN 978-3-95806-821-6

Acknowledgement

This dissertation was established at the Institute for Energy Technologies - Electrochemical Process Engineering (IET-4) at the Forschungszentrum Jülich GmbH. Throughout my PhD time, I was supported by a lot of people who helped me realize my ideas and shape them into this dissertation. First and foremost, I would like to express my gratitude to Univ. Prof. Dr. i. R. rer. nat. Werner Lehnert for his support and encouragement, and I wish him all the best in his well-deserved retirement. I would also like to thank Univ. Prof. Dr.-Ing. Andreas Jupke for his supervision and Univ. Dipl.-Ing. Dr.techn. Viktor Hacker for his co-supervision.

I deeply appreciate the support and guidance that I got working at the institute in Jülich; I would especially like to thank Dr. Felix Lohmann-Richters for the countless, fruitful discussions and the constant encouragement and trust in my work. My gratitude also goes to Dr. Martin Müller, Michael Hehemann, Werner Zwaygardt, Dr. Eugen Hoppe, Dr. Edward Rauls, Richard Wegener, Norbert Commerscheidt, Birgit Schuhmacher, Thomas Pütz and to my former fellow PhD students, especially Sharon Pape and Lukas Ritz. I would also like to thank Dennis Widuch and Tala Ghaddar for trusting me with their supervision and for their invaluable support throughout my work.

I was repeatedly surprised by the willingness of colleagues from other institutes to go the extra mile in discussing and supporting my ideas, which ultimately contributed to this work. In particular, I would like to extend my heartfelt thanks to Dr. Yannik Beßler, Dr. Eberhard Rosenthal, Felix Zinn, Dr. Alexander Belt, and Dr. Karsten Bittkau.

I would like to express my deepest gratitude to Dr. Tobias Arlt, Dr. Nikolay Kardjilov from Helmholtz Zentrum Berlin and Dr. Alessandro Tengattini, Dr. Lukas Helfen and Dr. Cyrille Courture from Institute Laue-Langevin, who helped me realise my neutron radiography measurements. Additionally, I would like to thank Senior Professor Gerry Swiegers and Dr. Aaron Hodges for our fruitful collaboration on the properties of potassium hydroxide.

I would also like to thank Antonia Illich and the Equal Opportunities Bureau within the Forschungszentrum Jülich GmbH for all their support in founding and establishing the women's network Female Voice. I would also like to thank Dr. Freia Harzendorf, Cristina Manzano, Anna Lührs, and Dr. Ramona Kloß. I greatly valued and enjoyed the work we did together toward promoting equal rights and opportunities for all people, regardless of gender, and raising awareness of the disparities that still exist.

Lastly, I would like to express my sincere gratitude to my family and friends for all their support.

Abstract

In this examination, a methodological approach is developed for the investigation of the two-phase flow behavior of an alkaline electrolysis cell using multiphase particle image velocimetry. Typically, imaging techniques or transparent cells are used to investigate the gas bubble behavior inside electrochemical cells. Certain drawbacks of these methods urge the necessity for a universally applicable two-phase flow investigation method for alkaline electrolysis cells. Therefore, a method is developed which is able to investigate both phases (liquid and gaseous) using a transparent half-cell. The half cell is capable of simulating the alkaline electrolysis two-phase flow behavior on anode or cathode side separately. By exchanging the electrolyte solution for a model electrolyte solution with the same density and viscosity as potassium hydroxide, the two-phase flow investigation can be done at lower temperatures than the usual alkaline electrolysis operation temperature. This is especially advantageous at temperatures above boiling point where pressurized operation is necessary because, with the proposed measurement method, the necessity of operating the electrolysis cell under pressure is avoided. Additionally, the exchange of potassium hydroxide to a less corrosive model electrolyte solution prevents the used transparent cell from getting dull from highly concentrated lye. The simulated cell is operated with equivalent volumes of nitrogen gas instead of hydrogen and oxygen for safety reasons. For method validation, the NeXT (Neutron and X-Ray Tomograph) device at Institute Laue-Langevin (ILL) in Grenoble is used to observe the gas bubbles forming and moving inside the flow channel of an alkaline electrolysis cell. For the first time, a temporal resolution of 0.02 seconds could be achieved for an active cell area of several cm^2. Measurement methods like neutron radiography are a powerful tool to analyze the gas bubble behavior inside alkaline electrolysis flow cells, but has limited accessibility. For both measurement methods, neutron radiography measurements and multiphase particle image measurements, cells of the same flowfield geometry are used. For the comparison of both investigation methods, an alkaline water electrolysis single cell is operated at different operation conditions. In this work, the results of both measurement methods are shown and compared. The applicability of an experimentally "simulated" electrolysis cell, measured with multiphase particle image velocimetry measurements, is shown, as well as the assumptions, prerequisites, and limitations of the simulation of the two-phase flow of an alkaline electrolysis cell. Using the simulated electrolysis half-cell is advantageous compared to neutron radiography measurements because smaller gas bubbles can be identified. Especially for difficult operation conditions like in alkaline electrolysis at intermediate temperatures, where measurements like neutron radiography are extremely difficult to realize, a flow behavior analysis method, which is easy to apply, is helpful. Additionally, the flow behavior of electrochemical flow cells can be optimized for improved electrolysis cell designs and higher efficiencies. This examination is the first step towards a simpler investigation of the two-phase flow behavior of electrochemical cells with the application example of a low temperature alkaline electrolysis zero-gap cell, with the potential to extend the method to intermediate temperature alkaline electrolysis or any other electrochemical device that forms gas bubbles.

Zusammenfassung

In dieser Dissertation wird ein methodischer Ansatz vorgestellt um das Zwei-Phasen Strömungsverhalten von alkalischen Elektrolysezellen zu untersuchen mittels Mehrphasen Particle Image Velocimetry. Üblicherweise wird das Gasblasenverhalten von elektrochemischen Zellen durch bildgebende Verfahren visualisiert, oder durch Nutzung transparenter Zellen. Diese Methoden bergen einige Nachteile, weshalb ein Bedarf besteht nach einer universell anwendbaren Methode um die Zwei-Phasen Strömung von alkalischen Elektrolysezellen zu untersuchen. Die hier entwickelte Methode ermöglicht es sowohl die flüssige als auch die gasförmige Phase der Zweiphasenströmung zu untersuchen. Genutzt wird dazu eine transparente Halbzelle, die in der Lage ist das Zwei-Phasen Strömungsverhalten einer alkalischen Elektrolysehalbzelle zu simulieren ohne eine gasbildende elektrochemische Reaktion. Durch das Ersetzen des Standardelektrolyten, meist Kaliumhydroxidlösung, mit einem Modellelektrolyten mit derselben Dichte und Viskosität kann die Zwei-Phasen Strömung bei niedrigeren Temperaturen untersucht werden als nötig bei einem tatsächlichen Elektrolysebetrieb. Vorteilhaft ist das insbesondere bei Betriebstemperaturen oberhalb der Siedetemperatur, bei denen ein Druckbetrieb nötig wäre, die hier entwickelte Methode kann den Druckbetrieb vermeiden. Zusätzlich sorgt der Austausch der Kaliumhydroxidlösung für weniger korrosive Bedingungen. Die simulierte Zelle wird bei gleichen Gasvolumina aus Sicherheitsgründen mit Stickstoff betrieben, anstatt Wasserstoff und Sauerstoff. Für die Validierung der Methode werden die Gasblasen einer Elektrolysezelle im Zellinneren visualisiert durch den Neutronen- und Röntgenstrahlentomograph NeXT vom Institut Laue Langevin (ILL) in Grenoble. Zum ersten Mal wurde eine zeitliche Auflösung erreicht von 0.02 Sekunden bei einer aktiven Zellfläche von einigen cm2. Bei Neutronenradiographie handelt es sich um eine äußerst leistungsstarke Messmethode, die allerdings schwer zugänglich ist. Beide Messmethoden nutzen Zellen mit derselben Zellgeometrie. Für den Vergleich beider Methoden wurde eine alkalische Wasserelektrolysezelle betrieben bei zahlreichen Betriebsbedingungen. In dieser Arbeit werden die Ergebnisse beider Messmethoden verglichen. Die Anwendbarkeit einer experimentell simulierten Elektrolysezelle, gemessen mit Mehrphasen Particle Image Velocimetry Messungen, wird gezeigt, sowie die Annahmen, Voraussetzungen und Einschränkungen der Simulation der Zwei-Phasen Strömung einer alkalischen Elektrolysezelle. Das Benutzen der simulierten Halbzelle ist, neben der Zugänglichkeit, vorteilhaft gegenüber Neutronenradiographie, da kleinere Gasblasen detektiert werden können. Insbesondere für Betriebsbedingungen die Druck erfordern, wie sie beispielsweise bei der alkalischen Elektrolyse im Mitteltemperaturbereich vorherrschen ist Neutronenradiographie äußerst schwer anzuwenden. Hier insbesondere ist eine Methode hilfreich, mit der man einfacher die Zwei-Phasen Strömung untersuchen kann. Zusätzlich kann mit der Methode das Strömungsverhalten optimiert werden, um eine verbesserte Elektrolysezelle zu entwerfen und höhere Effizienzen zu erzielen. Diese Dissertation ist der erste Schritt in Richtung einer einfachen Untersuchungsmethode der Zwei-Phasen Strömung von Elektrochemischen Zellen mit dem Anwendungsbeispiel einer niedertemperatur alkalischen Elektrolysezelle, welche potentiell auch für andere elektrochemische Strömungszellen angewendet werden kann.

Contents

1 Introduction

Hydrogen is a key player in the reduction of greenhouse gases and has the potential to help realize the energy transition from fossil fuels to the usage of renewable energies to supply the global power demand. At the moment, hydrogen is predominately produced from non-renewable sources. The origin of hydrogen is classified by colors to label the production method. Blue and gray hydrogen is produced by steam reforming of natural gas or another non-renewable source. Hydrogen is classified as blue hydrogen when the emitted CO_2 is captured, if not, then it is called gray hydrogen. Brown hydrogen is produced from lignite coal or methane gasification, black hydrogen is produced from black coal gasification. Green hydrogen is the name for hydrogen produced by electrolysis if the used electricity is produced by renewable energy sources. Only 4% of the present world hydrogen production comes from electrolysis and is labelled green hydrogen. [1] The extension of green hydrogen production is essential to fulfil the climate targets in order to reduce CO_2 emissions. To do so, the electrolysis capacity needs to be extended, and therefore, there is a demand for highly efficient electrolyzer.

Using renewable energy sources for electricity production has two main problems; What is done with the electricity produced at times when the demand is lower than the production? Secondly, how do we meet the demand for electricity at times when the electricity production is too low to meet the demand, e.g. because of the weather conditions? One solution is to store the produced excess energy and use it during times of higher demand. Storing electricity as electrical energy needs a lot of space for the storage capacity (e.g. Li-Ion-Batteries) and potentially a lot of resources for the production of these storages.

Using water electrolysis, the electrical energy is converted into chemical energy by splitting water into hydrogen and oxygen, which can be stored in pressurized gas tanks. For the conversion, fuel cells are used to convert oxygen and hydrogen back into electricity. The produced hydrogen can also be used to be fed to the natural gas supply system (up to 2 Vol-%) or as a resource for methane or diesel fuel production. [2]

Alkaline Water Electrolysis (AWE) is a well-known technology and has been investigated and industrially operated for decades [3]. Over the years, the Polymer Electrolyte Membrane (PEM) Electrolyzer became more popular in research. PEM electrolyzers have the advantage that instead of an alkaline electrolyte, water is used, and the ion conduction is realized by a proton conducting membrane. The efficiency of a PEM electrolyzer is higher compared to the efficiency of a conventional alkaline electrolyzer. Nonetheless, the drawback of PEM electrolysis is the need for scarce metals like platinum or iridium as catalysts. Alkaline electrolysis uses the ignoble metal nickel or nickel alloys as catalysts. The usage of non-scarce metals is a huge advantage over PEM electrolysis.

At the moment, there are a few strategies in research to increase the efficiency of alkaline electrolysis. One strategy is to use anion exchange membranes (AEM), which have the advantage that the concentration of the electrolyte solution can be significantly decreased to low values or even using water, as it is done in PEM electrolysis because an anion conducting membrane is used instead of a diaphragm. The disadvantage of AEM electrolysis is, again, the need for scarce metal catalysts. Another research field is the increase of the operation temperature of alkaline electrolysis cells. The main difficulty is finding a suitable diaphragm material, stable cell materials, especially at the anode, and suitable gasket materials. [3] The third field of research is about changing the design of alkaline electrolysis cells with the goal of improving the gas discharge from the cell [4].

The idea of developing zero-gap alkaline electrolysis cells was to improve the efficiency by reducing the total ohmic loss to a single contribution, which results from the diaphragm resistance. Gas bubbles that might block active areas on the electrodes should be only on the interface of flow channel and electrode, where they are directly transported out of the cell with the electrolyte solution. For some years, it has been known that the ohmic resistance of zero-gap alkaline electrolysis cells is also influenced by gas bubbles forming inside the cell. There are speculations about the reasons, but so far, no one has found the one specific reason for an increasing ohmic resistance with the current density. [5–7] The influence of gas bubbles on the ohmic resistance of alkaline electrolysis cells shows the importance of understanding and improving the two-phase flow behavior inside alkaline electrolysis flow cells. Typically, gas bubble behavior is investigated either by imaging techniques using a neutron or x-ray beam or with transparent flow cells. Imaging techniques are a good method for the operando investigation of the gas bubbles behavior of electrolysis flow cells with a sufficient temporal and spatial resolution. The drawback of these methods is their accessibility. Due to the limited amount of research facilities with the expensive, needed measurement devices, conducting the measurements is time-consuming. The time for the application process, the decision process, the preparation of the measurements, and the transport of the measurement equipment to the actual measurements can take from months up to a year. The limited available beam time has to be well prepared. Additionally, the measurement equipment needs to be transportable and needs to decay after the measurements, if it was in direct proximity to the beam. Two-phase flow investigation of alkaline electrolysis cells using transparent cells has the advantage, over imaging techniques, that only standard measurement devices like a high-speed camera are needed to record the gas bubbles inside the cell. The disadvantage of transparent cells is that, depending on the concentration and the temperature, the transparent cell material is unsuitable for the alkaline conditions of the electrolyte solution, and the cell turns turbid or is not mechanically stable enough. Both imaging techniques and transparent cells are hardly suitable for pressurized operation of alkaline electrolysis cells. For imaging techniques, the problem is that test rigs for pressurized operation are not easily transportable and adaptable to the facility to access the neutron or x-ray beam. For transparent cell materials, there is a risk of leakage at pressurized operation. Additionally, in case of elevated temperatures in the transparent cell, the problem of the cell material becoming turbid is getting more severe.

These difficulties, the open research questions, and the influence of the gas bubbles on the ohmic resistance show the need for a reliable and overall usable measurement method for the investigation of the gas bubble behavior inside an alkaline electrolysis cell. Therefore, in this examination, a methodology is developed that allows the investigation of the gas bubble behavior inside an alkaline electrolysis cell, as well as the investigation of the liquid phase. For the investigation of the two-phase flow behavior inside an alkaline electrolysis cell, a transparent model half cell of a zero-gap alkaline electrolysis is used. Inside the half-cell, the electrolysis process or, to be more precise, the two-phase flow behavior during the electrolysis cell is simulated. Simulating the alkaline electrolysis two-phase flow means in detail that model electrolyte solutions are used to replace potassium hydroxide. The model electrolyte solutions are chosen with the criteria to have the same density and viscosity as potassium hydroxide at an alkaline electrolysis operation condition, where the two-phase flow is of interest while being less corrosive and, most importantly, having a lower temperature. The latter allows the investigation of the two-phase flow behavior of an alkaline electrolysis cell, potentially also at elevated temperature operation (where pressurized operation is necessary in order to keep the electrolyte solution in a liquid phase) without actually operating under pressure because the model electrolyte solution has the same density and viscosity as potassium hydroxide at temperatures below the evaporation boundary. In this examination, the comparability of the simulated two-phase flow behavior with a model electrolyte solution and the actual two-phase flow inside an alkaline electrolysis operated with potassium hydroxide is investigated, as well as the limitations and assumptions are presented. Neutron radiography is used to investigate the actual two-phase flow behavior inside an alkaline electrolysis cell. For the simulated two-phase flow behavior with a model electrolyte solutions in a transparent half-cell multiphase particle image velocimetry is used.

The dissertation has the following structure:

- Section 2 describes the fundamentals relevant for this evaluation.
  - Section 2.1 is about the fundamentals of alkaline water electrolysis, the thermodynamics of alkaline electrolysis with a description of the influence of temperature and pressure on the performance, and about the options and difficulties alkaline electrolysis is facing by increasing the operation temperature.
  - Section 2.2 explains the fundamentals of gas-liquid flows in general and in an alkaline electrolysis cell furthermore, the principle of gas bubble formation is explained, the relevant dimensionless numbers are described, and the relevant properties of liquids are addressed.
  - Section 2.3 describes the fundamentals of neutron radiography and lists the relevant publications where imaging techniques became of use to investigate electrochemical cells.
  - Section 2.4 is about particle image velocimetry, about the working principle and the idea behind the evaluation method, as well as about the usage of particle image velocimetry for two-phase flows.
- Section 3 introduces the methods and measurement techniques used to obtain the results of this examination.
  - Section 3.1 describes the neutron radiography measurement procedure, the settings on-site, the cell assembly, as well as the image processing, and the evaluation methods for gas bubble velocity and gas layer thicknesses.

  - Section 3.2 describes the particle image velocimetry measurements to identify the electrolyte velocity and the measurement of the gas bubbles inside the transparent cell. The method for choosing the electrolyte, the gas, and the particles is described, as well as the image processing and determination of the gas bubble and electrolyte velocity and the gas amount distribution inside the channel.

  - Section 3.3 contains the liquid analysis methods used in this examination, which are UV/Vis measurements, density measurements, viscosity measurements, and the determination of the contact angle. For the replacement of potassium hydroxide with an alternative electrolyte solution, the important properties of potassium hydroxide need to be known. Therefore, in this section, a literature review on measurement data of these properties is done, and the method for developing empirical equations from the measurement data for potassium hydroxide solution is explained.

- Section 4 presents the measurement results.

  - Section 4.1 describes the results of the property analysis of potassium hydroxide and shows the resulting empirical equations. Additionally, an error analysis is done between calculated values and the measurement data.

  - Section 4.2 shows the characterization of different electrolyte solutions that can potentially replace potassium hydroxide in the particle image velocimetry measurements. Two electrolyte solutions are chosen using empirical equations, and the validation of the properties of the model electrolyte solutions through measurements is shown. The operation conditions necessary to replace potassium hydroxide at various operation conditions are determined.

  - Section 4.3 contains the results of the electrochemical measurements, as well as the visualization of the gas bubbles inside an alkaline electrolysis cell using neutron radiography. Polarization curves and results from electrochemical impedance spectroscopy (EIS) measurements are shown. For the gas bubble visualization, the results of the mean gas layer thickness for different operation conditions, the results of the gas bubble velocity and the resulting contact angles are shown.

  - Section 4.4 shows the results of the multiphase particle image velocimetry measurements, in particular, the electrolyte velocity and the gas bubble velocity, and the contact angle. The gas amount in each channel is determined and compared to the results of the neutron radiography measurements. A general comparison of the two-phase flow behavior determined through neutron radiography and particle image velocimetry measurements is made. The applicability of particle image velocimetry measurements in order to determine the two-phase flow behavior of alkaline electrolysis cells is analyzed, and limitations are discussed.

- Section 5 contains a general summary of the used methodical approach. The assumptions, limitations, and opportunities that the usage of simulated alkaline electrolysis cells offers for the investigation of the two-phase flow behavior are discussed.

- Section 6 discusses the next steps towards reliable two-phase flow investigation through multiphase flow particle image velocimetry measurements with simulated alkaline electrolysis cells, especially towards the usage at intermediate temperatures and potentially the applicability for other electrochemical flow cells.

2 Scientific Fundamentals and State of the Art

In this section, the fundamentals important for the methodical approach for enabling the investigation of the two-phase flow behavior inside an alkaline electrolysis cell are explained. The fundamentals are directed toward using the two-phase flow investigation approach for the investigation of intermediate temperature alkaline electrolysis in the future. Therefore, the fundamentals of alkaline electrolysis are revisited, and the temperature and pressure influence on the operation is discussed. Briefly, the difficulties that arise by increasing the operation temperature in alkaline electrolysis are described. Furthermore, the fundamentals of two-phase flow in electrochemical flow cells, gas bubble formation, and two-phase flow relevant dimensionless numbers are presented. The fundamentals of physical properties related to two-phase flows are given, as well as the fundamentals of neutron radiography and particle image velocimetry.
The here described fundamentals have, in part, been published in the Journal of the Electrochemical Society as a review publication under the title "Review—Challenges and Opportunities for Increased Current Density in Alkaline Electrolysis by Increasing the Operating Temperature".

2.1 Alkaline Water Electrolysis

Alkaline water electrolysis has existed for more than 130 years and was the first industrially used electrolysis process [8]. The standard alkaline electrolysis process consists of electrodes out of nickel because of the good activity. Ni-alloys are often coated on the electrodes as catalysts [9]. For metal components up to 80°C operation temperature, carbon steel can be used at temperatures above nickel alloys, or pure nickel needs to

be chosen [10]. Anode and cathode are separated by an ion-permeable conductor for which mostly Zirfon is applied. Zirfon is made from polysulfone and zirconium oxide and is supplied by Agfa Gevaert NV[1]. The ion conductivity is ensured by using alkaline electrolytes, mostly potassium hydroxide or sodium hydroxide, whereas potassium hydroxide is mostly preferred due to higher ionic conductivity. [3, 8]
The electrochemical reactions occurring at the anode and cathode, as well as the overall reaction, are the following:

$$\begin{array}{llcll} \text{Total:} & H_2O & \longrightarrow & H_2 + 0.5\,O_2 & (\mathrm{E}^0 = \text{-1.23 V vs. SHE}) \\ \text{Cathode:} & 2\,H_2O + 2\,e^- & \longrightarrow & H_2 + 2\,OH^- & (\mathrm{E}^0 = \text{-0.83 V vs. SHE}) \\ \text{Anode:} & 2\,OH^- & \longrightarrow & 0.5\,O_2 + H_2O + 2\,e^- & (\mathrm{E}^0 = \text{0.4 V vs. SHE}) \end{array}$$

The reaction on anode and cathode are shown in Figure 2.1 for an alkaline zero-gap electrolysis cell with the gas evolution of hydrogen at the cathode side and oxygen on the anode side.

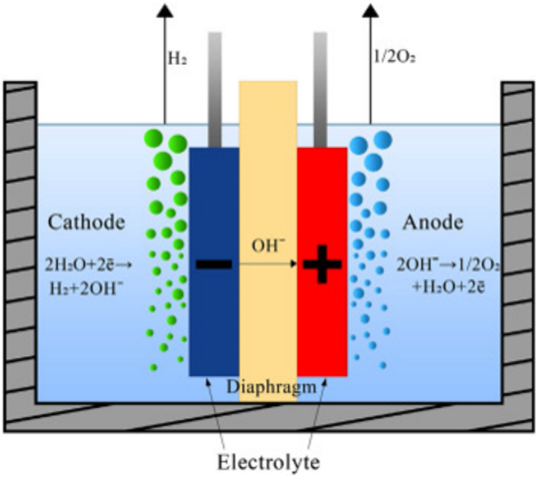

Figure 2.1: Principle of Zero-gap Alkaline Water Electrolysis Cell [11].

The typical low temperature alkaline water electrolysis is operated at 80°C and ambient pressure. The concentration of potassium hydroxide at this operation condition mostly lays at approximately 30 wt.-%. With the mentioned operation conditions Kim et al. [12] reached a cell voltage of 1.8 V at 0.5 A/cm^2. For operation conditions of 200°C, 20 bar and 45 wt.-% Chatzichristodoulou et al. [13] reached a cell voltage of 1.75 V at 3.75 A/cm^2.

---

[1] https://www.agfa.com/

2.1.1 Temperature and Pressure Influence on AWE Efficiency

To understand the influence of temperature and pressure on the electrolysis operation, it is necessary to have a look at the thermodynamics of the cell. Therefore, in the following sub-section, the first and second laws of thermodynamics and the species balance equations are described. An illustration of the system boundaries is given in Figure 2.2. The indices A and C stand for anode (A) and cathode (C), out and in mark the incoming and outgoing streams, and g and l stand for gaseous (g) and liquid (l) phase of the regarding stream. The cell is exchanging energy and mass beyond the system boundary and is, therefore, considered an open system. The exchanged energy and mass flows are considered constant. Due to that, the balance equations are formulated in a stationary integral formulation. The electrolysis operation is considered reversible, which means that the following assumptions are made:

- no entropy production
- no driving forces for the electrochemical reaction or transport of species to and from the electrode
- no permeation of gases through the diaphragm
- the gases are saturated with water vapour
- the operation is considered isotherm
- the pressure at the cathode and anode sides are constant

The electrolyte is considered to be at liquid state except for the fraction of water vapour which saturates the gas phase of the product gas streams.
The in and outgoing molar flow rates can be seen in the species balance equations 2.1 to 2.3 for water ($\dot{n}_{H_2O}$), hydrogen ($\dot{n}_{H_2}$) and oxygen ($\dot{n}_{O_2}$) molar flow rates:

$$\frac{dn_{H_2O}}{dt} = 0 = \dot{n}_{H_2O}^{C,in,l} - \dot{n}_{H_2O}^{C,out,l} - \dot{n}_{H_2O}^{C,out,g} + \dot{n}_{H_2O}^{A,in,l} - \dot{n}_{H_2O}^{A,out,l} - \dot{n}_{H_2O}^{A,out,g} - \frac{I}{2F} \tag{2.1}$$

$$\frac{dn_{H_2}}{dt} = 0 = -\dot{n}_{H_2}^{C,out} + \frac{I}{2F} \tag{2.2}$$

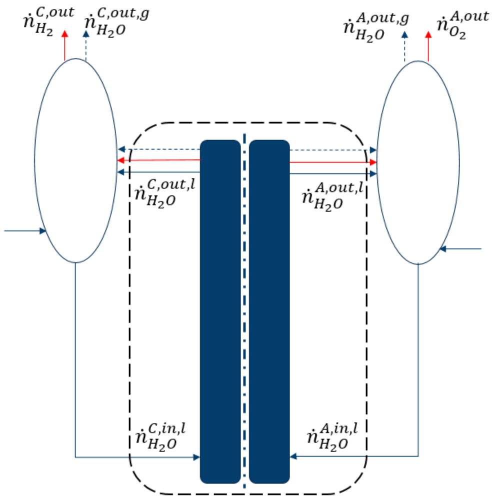

Figure 2.2: Illustration of an Electrolysis Cell with System Boundary (Black Dashed Line) for Thermodynamic Balancing

$$\frac{dn_{O_2}}{dt} \quad = \quad 0 \quad = \quad -\dot{n}_{O_2}^{A,out} + \frac{I}{4F} \tag{2.3}$$

The species balance equations 2.1 to 2.3 consist of the in and outgoing streams, as well as a term for the reaction rate for the electrochemical conversion of water splitting through electricity into hydrogen and oxygen. The term for the reaction rate considers the current (I), the valency (z), and the Faraday constant (F). From the energy balance and entropy balance, it is possible to determine the reversible heat (q_{rev}) and reversible work ($w_{t,rev}$). The reversible work describes the needed electrical, respectively mechanical work for the reaction, and the reversible heat is the needed or released heat of the system. Their equations are derived from the first and second laws of thermodynamics and are shown in Equation 2.4 and 2.6. The energy balance (Equation 2.4) consists of the Gibbs-Free-Energy ($g = h - Ts$) for the different species and the electrical energy supplied to the cell.

$$\begin{aligned}\frac{dE}{dt} = 0 = \quad & -(h_{H_2O}^{in,l}(T,p) - Ts_{H_2O}^{in,l}(T,p))(\dot{n}_{H_2O}^{A,in,l} + \dot{n}_{H_2O}^{C,in,l}) \\ & -(h_{O_2+H_2O}^{A,out,g}(T,p,x_{H_2O}^{A,out,g}) - Ts_{O_2+H_2O}^{A,out,g}(T,p,x_{H_2O}^{A,out,g}))(\dot{n}_{O_2+H_2O}^{A,out,g}) \\ & -(h_{H_2+H_2O}^{C,out,g}(T,p,x_{H_2O}^{C,out,g}) - Ts_{H_2+H_2O}^{C,out,g}(T,p,x_{H_2O}^{C,out,g}))(\dot{n}_{H_2+H_2O}^{C,out,g}) \\ & -P_{el}^{rev}\end{aligned} \tag{2.4}$$

From the energy balance, the specific reversible work can be calculated (cf. Equation 2.5). The specific reversible work is the minimum work necessary to produce one mole of hydrogen, depending on the operation condition. The equation consists of terms for the Gibbs-Free-Energy of water (at operation condition), hydrogen, and oxygen (both at standard pressure ($p^0 = 1bar$)) as well as a term for pressure correction considering the partial pressure of oxygen and hydrogen at operation pressure. The first three terms equal the specific free reaction enthalpy of water ($\Delta_r g(T, p^0)$) at standard pressure.

$$\begin{aligned} w_t^{rev} &= \tfrac{P_{el}^{rev}}{\dot{n}_{H_2}^{C,out}} \\ &= -g_{H_2O}^{in,l}(T,p) + \tfrac{1}{2} g_{O_2}^{A,out}(T,p^0) + g_{H_2}^{C,out}(T,p^0) \\ &\quad +RT\ln\left[\left(\tfrac{p_{O_2}^A}{p^0}\right)^{\frac{1}{2}}\left(\tfrac{p_{H_2}^C}{p^0}\right)\right] \end{aligned} \tag{2.5}$$

The entropy balance takes the entropy of the different species at the operation conditions into account and the additional source or sink (depending on the temperature) term for the reversible heat consumed or produced by the cell.

$$\begin{aligned} \tfrac{dS}{dt} = 0 = \quad & -Ts_{H_2O}^{in,l}(T,p)(\dot{n}_{H_2O}^{A,in,l} + \dot{n}_{H_2O}^{C,in,l}) \\ & Ts_{O_2+H_2O}^{A,out,g}(T,p,x_{H_2O}^{A,out,g})\dot{n}_{O_2+H_2O}^{A,out,g} \\ & Ts_{H_2+H_2O}^{C,out,g}(T,p,x_{H_2O}^{C,out,g})\dot{n}_{H_2+H_2O}^{C,out,g} \\ & -Q^{rev} \end{aligned} \tag{2.6}$$

From the entropy balance, the specific reversible heat can be calculated by Equation 2.7. The specific reversible heat is the heat which is released ($q_{rev} > 0$) or consumed ($q_{rev} < 0$) per produced mole of hydrogen.

$$\begin{aligned} q^{rev} &= \tfrac{Q^{rev}}{\dot{n}_{H_2}^{C,out}} \\ &= T(-s_{H_2O}^{in,l}(T,p^0) + \tfrac{1}{2} s_{O_2}^{A,out,g}(T,p^0) + s_{H_2}^{C,out}(T,p^0)) \\ &\quad -RT\ln\left[\left(\tfrac{p_{O_2}^A}{p^0}\right)^{\frac{1}{2}}\left(\tfrac{p_{H_2}^C}{p^0}\right)\right] \\ &\quad +\left(\tfrac{1}{2}\tfrac{x_{H_2O}^{A,out,g}}{1-x_{H_2O}^{A,out,g}} + \tfrac{x_{H_2O}^{C,out,g}}{1-x_{H_2O}^{C,out,g}}\right)(h_{H_2O}^{out,g}(T,p) - h_{H_2O}^{out,l}(T,p)) \end{aligned} \tag{2.7}$$

The first three terms of Equation 2.7 combined are the reaction entropy of the water splitting reaction ($T \cdot \Delta_r s(T, p^0)$). The fourth term considers the operation pressure, and the remaining terms consider the specific energy needed for the evaporation of water. The minimum necessary voltage needed to split water into hydrogen and oxygen is the reversible cell voltage, which is dependent on the Gibbs free energy (ΔG), the number of transferred electrons (z), and the Faraday constant (F) (see Equation 2.8).

$$E_{rev}(T) = -\frac{\Delta G}{zF} \tag{2.8}$$

At standard conditions of 298K and 1 bar, the standard formation Gibbs free energy of water splitting reaction for water at liquid state (cf. Section 2) $\Delta G_0 = -237.1\frac{kJ}{mol}$ leads to the reversible cell voltage of $E_{rev} = 1.23V$. Since the naming of different cell voltages is not consistent in literature here, the naming after LeRoy [14] is used. The enthalpic voltage takes the entropic contribution into account, which is supplied, for example, in the form of heat (see Equation 2.9).

$$E_{\Delta H}(T,p) = -\frac{\Delta H_f}{zF} = -\frac{\Delta G - T\Delta S}{zF} \tag{2.9}$$

At standard conditions of 298K and 1 bar, the standard formation enthalpy of water splitting reaction for water at liquid state $\Delta H_{f,0} = -285.8\frac{kJ}{mol}$ leads to the enthalpic voltage of $E_{\Delta H} = 1.48V$. The cell voltage considering temperature and pressure is given by the Nernst equation (ref. Equation 2.10), which consists of the reversible cell voltage (E_{rev}) and an additional term considering the pressure influence. The equation equals the reversible work calculated into a voltage and results, therefore, from the first law of thermodynamics.

$$E_{Nernst}(T,p) = E_{rev}(T) + \frac{RT}{zF}\ln\left[\left(\frac{p^A_{O_2}}{p^0}\right)^{\frac{1}{2}}\left(\frac{p^C_{H_2}}{p^0}\right)\right] = \frac{w^{rev}_t}{zF} \tag{2.10}$$

The total cell voltage of electrolysis cells is typically given as a sum of the Nernst voltage, the ohmic resistance of the cell (IR_{cell}), and terms considering the overvoltage of anode (η_A) and cathode (η_C) as a measure of the activation energy at the electrodes, as well as losses caused by mass transport limitations (η_{mt}). In Figure 2.3, the different described contributions to the total cell voltage can be seen. The mass transport limitation losses are not included in Figure 2.3. Mass transport limitations occur at high current densities when evolving gas bubbles cannot be transported out of the cell efficiently because the gas amount/ electrolyte solution ratio is too high. In the direct vicinity of the cathode, the electrolyte solution is oversaturated, which results in an additional contribution to the losses because the ionic conductivity decreases once the optimal concentration is exceeded. These losses are also not included in Figure 2.3.

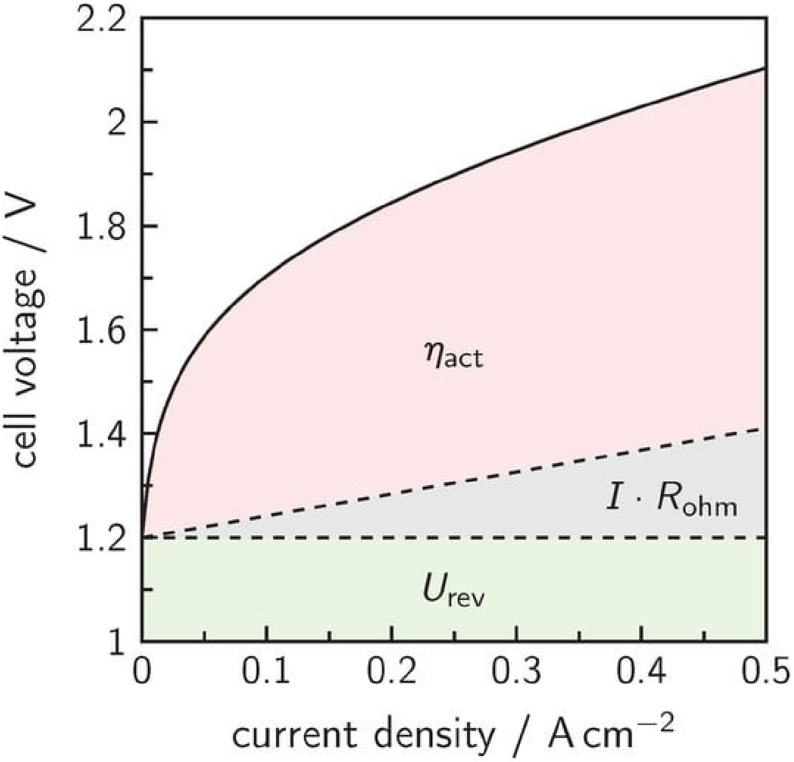

Figure 2.3: Total Cell Voltage with the Different Contributing Losses [15].

The total cell voltage can be seen in Equation 2.11:

$$E_{cell}(T,p) = E_{Nernst}(T,p) + IR_{cell} + \eta_C + \eta_A + \eta_{mt} \tag{2.11}$$

From Figure 2.4 (a), it can be seen that the reversible cell voltage decreases with increasing temperature and increases with pressure. In Figure 2.4 (b), it is shown that the reversible cell voltage is slightly increasing with increasing concentration of the electrolyte. The electrolyte concentration influences the reversible cell voltage through the partial pressure of hydrogen and oxygen. The reason is that higher electrolyte concentrations result in lower water vapor pressure while the system pressure is constant.

The increase of the reversible cell voltage with increasing pressure is especially to consider when shifting the operation temperature towards higher temperatures, where

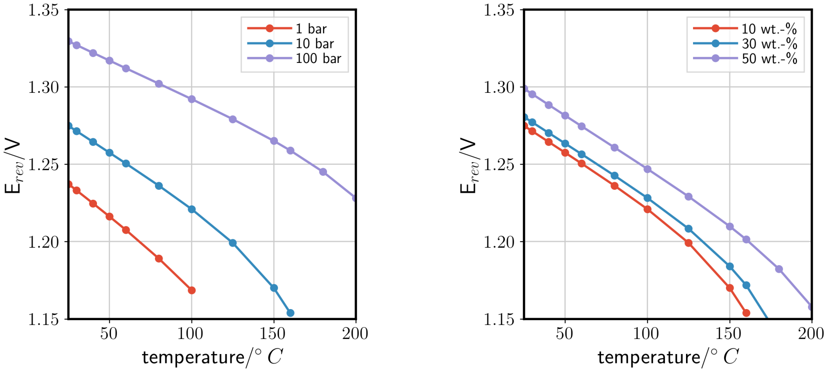

(a) (b)

Figure 2.4: Dependency of the Reversible Cell Voltage on Temperature at Different Pressures (a) at 10 wt.-% and Concentrations (b), at 10 bar.

pressurized operation becomes necessary in order to avoid evaporation of the electrolyte solution. The efficiency-decreasing effect of the increasing pressure at higher temperatures is exceeded by highly improving kinetics and increasing ionic conductivity. [3]
Additionally to the considered amount of energy for electrolysis operation in the cell voltage E_{cell}, the energy needed for heating up the cell material and electrolyte solution has to be taken into account, as well as energy for evaporation of water and radiation and convection losses. For a detailed discussion of the losses contributing to the cell voltage other than the losses caused by gas bubbles, it is referred elsewhere [14].
From the thermodynamic relations, it can be seen that there are ways to improve the efficiency of alkaline electrolysis. The development of thinner diaphragms and better catalysts increases the efficiency at all temperatures. The same applies to the improvement of gas bubble movement out of the cell and reducing the ohmic resistance that way. Operating alkaline electrolysis cells and stacks at intermediate temperatures has huge potential of creating the path for highly efficient alkaline electrolysis operation, but still, a lot of research needs to be done in that field, as explained in more detail in the following section. The main focus of this examination is to improve the two-phase flow behavior with a focus on the reduction of the ohmic resistance. Potentially, in this dissertation, the developed method can be applied to intermediate temperatures and increase the efficiency even further. From the thermodynamic fundamentals, it is possible to get an impression of the potential efficiency rise.

2.1.2 Ohmic Resistance in AWE Cells

The traditional alkaline electrolysis cell consisted of two metal plates, a gap filled with electrolyte solution on both sides, separated by an ionic conductive membrane or an electrolyte solution-filled diaphragm. 1967 the first zero-gap cell was introduced by Costa et al. [16] with mesh electrodes pressed directly on the diaphragm. The improvement of the zero-gap design is the decrease in ohmic resistance. The cell resistance of a traditional alkaline electrolysis cell consists of the following terms:

$$R_{cell} = R_{circuit} + R_{electrolyte} + R_{bubbles} + R_{diaphragm} \tag{2.12}$$

The resistance of the cell (R_{cell}) consists of the resistance of the electric circuit ($R_{circuit}$), the electrolyte resistance, the resistance of the diaphragm, and the resistance caused by forming gas bubbles. By looking at the two-phase flow of electrolysis cells, the two cell resistances that are influenced by the two-phase flow behavior are the electrolyte cell resistance and the resistance caused by gas bubbles.

The electrolyte of a traditional alkaline electrolysis cell causes two different resistance terms, one for aqueous electrolyte solution and one for immobilized electrolyte solution inside the pores of the diaphragm (equals $R_{diaphragm}$). The aqueous electrolyte resistance describes the resistance of the electrolyte solution, which is located between the electrodes outside of the pores of the porous separator. Allebrod et al. [17] showed that the conductivity of aqueous and immobilized electrolyte differs. Therefore, the resistance is divided into two terms ($R_{electrolyte}$ (aqueous electrolyte) and $R_{diaphragm}$ (immobilized electrolyte)).

The bubble resistance can be caused by two different kinds of effects. The first is the bubble forming on the electrodes. The active area of the electrode is being reduced by gas bubbles, which block the electrode area partly. The second effect occurs in conventional alkaline electrolysis cells and is caused by gas bubbles that are flowing towards the outlet of the electrolyte-gas mixture and hinder the ionic conductivity. Especially at higher current densities, when a large amount of gas is flowing toward the outlet, this effect is getting more severe. The more electrolyte volume is displaced by gas bubbles, the more the ionic conductivity drops because less electrolyte solution is present. The phase of gas is called void fraction. [18]

In zero-gap cells, the gap where this can happen does not exist (in theory) because the electrodes are directly pressed onto the diaphragm, and the gas bubbles have to leave through the backside of the electrodes [19]. In addition to that, theoretically, the resistance caused by aqueous electrolyte does not play a role in a zero-gap cell since there is no aqueous electrolyte between the electrodes and the diaphragm, only the immobilized in the pores of the porous separator.

2.1.3 Material Stability at Intermediate Temperature AWE

Especially under elevated temperatures and caustic environment, only a limited amount of materials withstand the challenging conditions occurring inside an alkaline electrolysis cell. The presence of oxygen on the anode side and hydrogen on the cathode side, as well as the applied voltage to the cell, reduce the number of potential materials even further. Metal components in contact with the electrolyte, the diaphragm, anode and cathode catalyst material, and gaskets, respectively, insulation material need to be found with a suitable lifetime under the prevailing conditions.

For metal materials, studies in literature investigated two types of corrosion; general corrosion (GC) and stress corrosion cracking (SCC) at elevated temperatures. [20–22] GC describes the reduction of material in thickness when exposed to a certain environment. SCC, on the other hand, is being investigated by not only exposing the metal to the medium but also applying tensile stress. The system pressure does not seem to influence the corrosion rate (GC), but the partial pressure is influencing SCC [23]. Both types of corrosion are found to be more severe under oxygen environment compared to hydrogen [20].

Stainless steel and nickel alloys are known for their stability in caustic environment. In the literature, a handful of suitable nickel or nickel alloys are found to have acceptable corrosion rates at intermediate temperatures in alkaline environment. Some materials show a break-away uniform corrosion behavior, which describes a uniform corrosion rate that increases at a certain point in time significantly. The investigation of GC for some alloys can be seen in Figure 2.5.

An interesting finding has been made by constantly renewing the lye during long-term corrosion testing. As a result, the corrosion rate increased. From this observation, an investigation showed that the corrosion rate decreased when iron and silicate ions are present in the solution because they form a passivation layer [20, 22]. Pruett [24] introduced a categorical rating for metallic materials in category A with a corrosion rate of < 50 μm a^{-1} and category B with a corrosion rate of < 500 μm a^{-1}. Kreysa [25] divided the different alloys in the categories resistant (<100 μm a^{-1}) and fairly resistant (< 500 μm a^{-1}). From these categories, a few alloys are promising to withstand the operation at up to 180°C; Alloy 400 and Alloy 690 appear to be suitable for alkaline

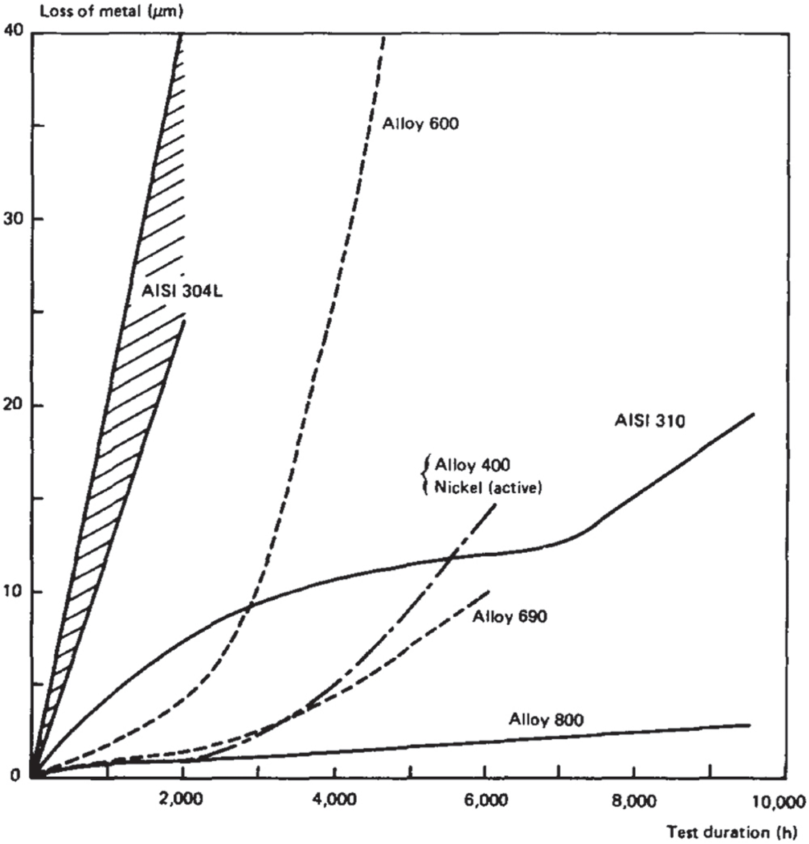

Figure 2.5: Corrosion Rates of Different Alloys at 150 °C and 38 wt.-% Potassium Hydroxide under Oxygen Atmosphere [20].

media in an oxygen environment. Alloy 800 has a suitable low enough corrosion rate but is susceptible regarding SCC. Nonetheless, none of the here mentioned alloys was tested under conditions where voltage was applied. [3, 20, 22]

In low temperature alkaline electrolysis, the state-of-the-art diaphragm was made from asbestos, which was exchanged for materials less harmful to health later on. Nowadays, Zirfon is used as a standard diaphragm, which is supplied by Agfa Gevaert NV[1] [26]. The here used Zirfon (Zirfon Perl UTP 500) is a 500 μm thick diaphragm out of polysulphone and ZrO_2. The material causes the temperature limitation for Zirfon at 110 °C/120 °C. Regardless of the health risk, asbestos is also only usable until 100 °C.

---

[1] https://www.agfa.com/

For higher temperatures, mostly ceramic diaphragms are investigated in literature. In the 80s, porous oxide diaphragms were tested regarding their lifetime in a caustic environment. The problem of using metal-containing oxides, which are more noble than hydrogen, is that they are being reduced at a certain temperature during electrolysis and therefore becoming conductive. [27–31]

Another option for porous oxide diaphragms are titanates of metals that are less noble than hydrogen, like $CaTiO_3$ [31–33] or $SrTiO_3$ [34, 35]. These materials need a supportive layer for the mechanical stability of the diaphragms, such as metal foam [34–36]. The pore sizes of these diaphragms are mostly in the micrometre range [3]. Chatzichristodoulou et al. [13] developed a diaphragm manufactured by tape-casting out of yttria-stabilized zirconia. This diaphragm has a smaller pore size than 1 μm in contrast to the diaphragm of, for example, Wendt et al. [33], who are using a diaphragm made of titanate with several micrometre pore size. According to Schalenbach et al. [37], the optimal pore size is smaller than 100 nm for an optimal gas purity.

A commonly used material for gaskets or as an insulator material in low temperature alkaline electrolysis cells is polytetrafluoroethylene (PTFE). Fluorinated polymers are known for their good chemical stability under a caustic environment. That applies also to elevated temperatures in alkaline electrolysis cells due to the temperature stability of PTFE. A second fluorinated polymer that has been tested for good chemical stability at higher temperatures is perfluoroalkoxy alkane (PFA). In addition to the two fluorinated polymers, polyphenylene sulfide (PPS) is also suitable for the prevailing conditions. All three polymers are temperature stable in concentrated lye up to 200 °C or even higher temperatures. [38]

Alkaline electrolysis at intermediate temperatures is from a thermodynamic point of view a good possibility to realize hydrogen production without scarce metal use. The long-term production of hydrogen this way, nonetheless, is strongly dependent on the finding of suitable materials, more detailed research and development needs to be done.

2.2 Two-Phase Flow in Electrochemical Flow Cells

In the previous sub-section, the general fundamentals of alkaline electrolysis are given. As briefly described, the two-phase flow behavior has an essential influence on the performance of an electrolysis cell. The important fundamentals, dimensionless numbers to characterize the flow, and the needed physical properties are described in detail below for an alkaline electrolysis cell.

2.2.1 Fundamentals

The species balance equation of hydroxide ions inside an alkaline electrolysis cell is given by Equation 2.13.

$$\frac{\partial c_{OH^-}}{\partial t} = -\nabla \cdot \vec{N}_{OH^-} + R_{OH^-} \tag{2.13}$$

The partial derivative of the hydroxide ion concentration (c_{OH^-}) is a sum of the gradient of the flux density of the hydroxide ions ($\vec{N}_{OH^-}$) and the local production rate (R_{OH^-}). The flux density consists of a convective term for the movement of the OH^- ions that move with the electrolyte solution, a diffusive term driven through the concentration gradient, and the migrating ions caused by the electrical field. [39]

The formation of gas bubbles inside the flow cell has an effect on the flow of electrolyte solution and its conductivity [40–42]. For a better understanding of the interaction of gas bubbles with the electrolysis process, the gas formation is described briefly.

If gas bubbles are formed, or gas is dissolved in the electrolyte solution depends on the local state of saturation of the electrolyte solution. Especially in the direct vicinity of the electrodes, the electrolyte solution is supersaturated. Therefore, the bubbles are formed at small defects or cracks on the electrode surface. [43, 44]

The detachment of the gas bubbles depends on the electrolyte volume flow, the contact angle between the bubble and surface, and the surface roughness [45]. Manthey et al. [46] describe in detail the relevant forces on a gas bubble inside a flow channel before departing. They conclude from their model that if the departure diameter, resulting from forces along the channel direction, is bigger compared to the departure diameter resulting from forces perpendicular to the channel direction, the gas bubbles are beginning to slide before departure in the flow direction. The gas bubble slides until the detachment diameter is reached. After detachment of the gas bubbles, the bubbles grow further inside the flow channel and coalesce with other gas bubbles. The degree of coalescence is influenced by the properties of the electrolyte and the bubbles, as well as the operation condition [47, 48]. The process of coalescence starts with the colliding of the bubbles, while there is still a liquid film in between the gas bubbles. The liquid film is forced to drain until the two bubbles are fully merged. There are three mechanisms to collide for gas bubbles, either due to (local) turbulences, buoyancy, or

laminar shear [49]. The mass transfer is affected by coalescence [50].
Depending on the ratio of gas bubbles and electrolyte solution, as well as coalescence behavior, the two-phase flow can be divided into different flow regimes. For flow channels, the categories below are named in the literature. The naming of the different existing flow regimes is not entirely coherent here the naming convention of Ito et al. [51] is used:

- Dispersed bubbly flow: round, single bubbles of the size smaller than the channel cross-section
- Plug flow: bubbles bigger than channel square size with an elongated shape
- Slug flow: the bubble length is multiple times longer than the width
- Churn flow: longer bubbles are followed by smaller bubbles and vice versa
- Annular flow: the gas phase is predominant in the channel, sometimes interrupted by a small amount of liquid

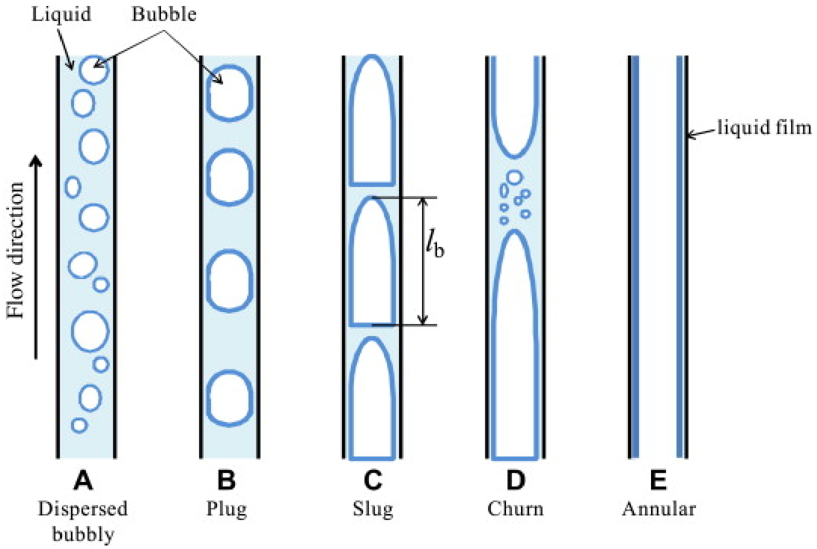

Figure 2.6: Classification of Flow Regime for Two-phase Flow in Flow Channel [51].

The two-phase flow behavior can be categorized by the flow regime (see Figure 2.6) and, therefore, the gas-liquid ratio inside the flow channel or tubes. The Mishima-Ishii model correlates the drift flux model with the rise velocity of the gas bubbles [52]. With the help of flow regime maps for different pipe geometries, it is possible to identify the different flow regimes from the gas velocity and the liquid velocity. [53]

2.2.2 Nucleation of Gas Bubbles

Gas bubbles nucleate when the liquid is brought into a metastable state of the vapor phase. The metastable state is either produced through a temperature rise, through a pressure drop or if the gas amount exceeds the saturation limit. The classical nucleation theory (CNT) describes the vapour bubble formation of single species systems, as well as the formation of gas bubbles from supersaturated binary mixtures. [54] Here, only the latter is discussed.

The nucleation of gas bubbles in electrolysis cells is induced by the electrogeneration of dissolved gas. The electrolyte solution is assumed to be saturated with gas, which means the gas bubbles form through supersaturation inside the liquid phase. Here there are two relevant types of gas bubble formation from supersaturated liquids. The first one is the homogeneous nucleation. The gas bubbles form in the liquid bulk phase at a high level of supersaturation. The second type is heterogeneous nucleation, which occurs at a lower level of supersaturation, and the gas bubbles start to form at small cracks or other surface imperfections, like porous electrodes. If gas bubbles already exist, the nucleation energy is negligible, and the existing gas bubbles rather grow through diffusion of gas into the gas bubbles than nucleation of new gas bubbles. [55]

The free energy of formation of a nucleus of a gas bubble is the energy necessary to create a new phase boundary and the energy that is used to change the state of dissolved gas into gas volume inside a gas bubble. The free energy is dependent on the gas bubble radius and has a unique maximum value dependent on the pressure, temperature, and concentrations associated with the critical radius. The critical radius is the limit, where the gas bubbles begin to grow because it is energetically favored, if the radius is smaller, the gas bubbles will shrink. [56]

Selamet et al. [57] saw in their investigation of the flow channel of an electrolysis cell using soft x-ray that the gas bubbles mostly form under the ribs and concluded that the reason for that is most likely because it is the shortest path for the electrons. From the location of formation, the gas bubbles are moving towards the channel to exit the cell.

2.2.3 Importance of the Two-phase Flow in an AWE Flow Cell

The theoretical idea to apply the zero-gap design in alkaline electrolysis cells, was to have only the circuit and the diaphragm resistance left as contributions to the ohmic resistance. Recently, few authors proved this theory wrong, because the ohmic resistance is increasing with increasing current density, and it is believed to be caused also by the influence of bubble coverage [5, 7, 19].

Haverkort et al. [5] investigated the ohmic losses in a 10 cm^2 cell using a zero-gap design with Zirfon diaphragm and expanded metal electrodes with eye-shaped holes. They suggested that an ohmic drop comes from an inactive electrode front. This theory was tested by applying an epoxy layer on the front of the electrode, which led to similar results as without an epoxy layer. As possible reasons for the inactivity of the electrode front, they stated gas bubbles blocked separator pores, the compression of the electrodes [29] and local supersaturation of product gas near the separator, which reduces the reactivity [5]. Furthermore, Haverkort et al. [5] investigated the ohmic loss coming from local hydroxide depletion. They additionally investigated the introduction of a small gap between electrodes and diaphragm. Earlier publications suggested that an "almost-zero gap" can improve the performance compared to a zero-gap cell design [58], which is according to the results of Haverkort et al. [5]. The possible reasons why the small gap increases the performance, Haverkort et al. [5] assumes the reason to be an improved transport of dissolved gas. de Groot et al. [7] reviewed the existing measurements of low temperature alkaline electrolysis cells using Zirfon and calculated the area-specific resistances of each publication normalized to 30 wt.-% KOH and 80 °C and compared the resulting resistances with the resistance of Zirfon of 0.13 Ωcm^2. The analysis resulted in widely varying area resistances. Simulations helped to find possible explanations; An uneven current density, the influence of gas bubbles, a small gap that occurs due to manufacturing tolerances and assembling and nanobubbles in the porous diaphragm or electrodes (pore size Zirfon diaphragm: 0.15 μm) [7].

In order to simply avoid the ohmic resistance of formed gas bubbles (concentration overpotential), Hodges et al. [4] developed a capillary-fed electrolysis cell with a reservoir tank of electrolyte below the electrode-diaphragm sandwich structure. The electrolyte solution is moving through the separator by capillary forces and distributing the cell with water for the reaction. The gases are produced at the electrode with little to no interference with the electrolyte flow.

Swiegers et al. [59] discussed the different contributions of formed gas bubbles inside conventional alkaline electrolysis cells and the reduction potential of the single contributions. The contributing effects are nucleation, growth, and detachment of gas bubbles, concentration overpotentials caused by the supersaturation of electrolyte solution with gas in the vicinity of the electrodes. Amongst others, they name the decrease of active cell area due to bubble blocking, as well as the decrease in conductivity, because of gas bubble void reducing the conductivity of the electrolyte solution and non-uniform current density distribution.

Several studies investigated the gas formation during the electrolysis process. Maier et al. [60] summarized two different concepts of flow regime influence on the performance of the two-phase flow inside the flow channel of PEM electrolysis cells. The first assumes the water supply of the electrodes to be interrupted by elongated gas bubbles [51], the second concept is about gas bubbles causing turbulences inside the flow channel and tend to even more so with increasing bubble size, which leads to earlier detachment of forming gas bubbles [61]. The first concept would lead to an increased concentration overpotential, and the second one to a decreased concentration overpotential. Chandran et al. [62] shows the relation between the gas bubble diameter and the operation condition [62]. Panchenko et al. [63] investigated mass flow phenomena in different layers of a PEM electrolysis cell and investigated the influence of different porous transport layers. The investigations were done conducting performance measurements like recording polarization curves, as well as using imaging methods, such as neutron radiography and synchrotron radiography. [63–65] Hoeh et al. [66] tested different porous transport layers and characterized them electrochemically regarding their mass transport properties. Using imaging methods such as neutron radiography and synchrotron radiography, the flow behavior inside a PEM electrolysis cell was investigated. Both characterization methods resulted in a pore network model simulation. [66–68] Maier et al. [60] concluded from their review on mass transport in PEM water electrolysis that so far the available literature has published rather contradictory findings on PEM electrolysis performance in relation to the flow regimes.

For alkaline water electrolysis, a lot fewer publications on the two-phase flow behavior, especially the gas bubble velocity respectively the electrolyte velocity, are available. The investigations on the flow regime and with that, on gas bubble velocity/ electrolyte velocity, which are made for PEM electrolysis, could also give insight into AWE two-phase flow behavior. Flow regime maps, as an example is shown in Figure 2.7, need to be done for the exact system with the exact flow channel geometry, surface tension, liquid and gas properties, and system operation condition.

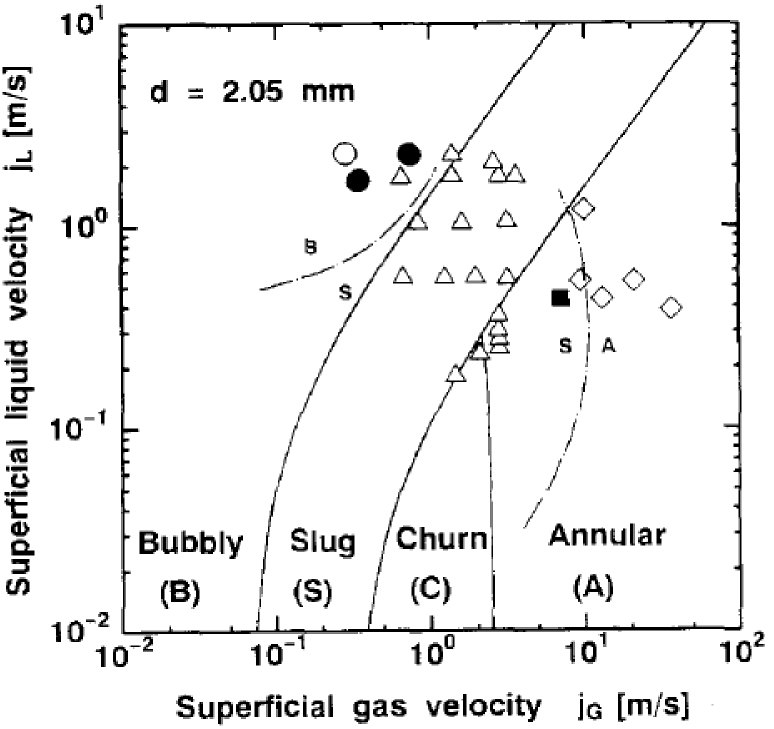

Figure 2.7: Example of a Flow Regime Map of a Tube with an Inner Diameter of 2.05 mm for an Air-Water Flow [52].

This sub-section shows how many factors influence the two-phase flow behavior, how the two-phase flow behavior influences the efficiency of the electrolysis performance, and how little is known about the two-phase flow behavior so far. All this shows the necessity for a standardized, simple-to-apply method for the investigation of the two-phase flow behavior in alkaline electrolysis cells.

2.2.4 Dimensionless Numbers relevant for Convective Flow in Electrolysis Cells

To characterize two-phase flow behaviors, dimensionless numbers can be used. One of the relevant numbers is the Reynolds number, which is used to differentiate laminar and turbulent flow and describes the relation of inertial forces to viscous forces. When viscous forces dominate, the flow is kept in line and, therefore, laminar. When the inertial forces dominate, the flow is turbulent. The definition of the Reynolds number can be seen in Equation 2.14, which consists of the relation of the electrolyte density (ρ_{KOH}), the mean fluid velocity (u) and the characteristic length (L), which is in flow channel of an electrolysis cell the diameter (round channel) or hydraulic diameter (rectangular channel) of the channel, divided by the viscosity of the electrolyte solution (η_{KOH}).

$$Re = \frac{\text{inertia force}}{\text{viscous force}} = \frac{\rho_{KOH} u L}{\eta_{KOH}} \tag{2.14}$$

Another relevant dimensionless number for describing the two-phase flow is the capillary number (see Equation 2.15) which is the relation of viscous forces and surface tension forces on the interface between liquid and gaseous phase, where η_{KOH}, u and σ_{KOH} are the viscosity of the electrolyte, the mean electrolyte velocity and the surface tension of the electrolyte in air.

$$Ca = \frac{\text{viscous force}}{\text{surface tension force}} = \frac{\eta_{KOH} u}{\sigma_{KOH}} \tag{2.15}$$

The Bond number (see Equation 2.16) is used to characterize the shape of gas bubbles in the surrounding liquid medium and is described through the acceleration of gravity (g), the density difference of electrolyte solution and gas bubble ($\rho_{KOH} - \rho_{H_2/O_2}$), the characteristic length (L) and the surface tension of the electrolyte solution in air (σ_{KOH}).

$$Bo = \frac{\text{gravitational force}}{\text{surface tension force}} = \frac{g(\rho_{KOH} - \rho_{H_2/O_2})L^2}{\sigma_{KOH}} \tag{2.16}$$

The Weber number (see Equation 2.17) is used to describe the interface between different phases, like gas bubbles in liquid flow. The number is the relation of inertial force and surface tension force. ρ_{KOH}, u, L and σ_{KOH} refer to the density of the electrolyte solution, the electrolyte solution velocity, the characteristic length, and the electrolyte surface tension in air.

$$We = \frac{\text{inertia force}}{\text{surface tension force}} = \frac{\rho_{KOH} u^2 L}{\sigma_{KOH}} \tag{2.17}$$

The theory of similarity is used to decrease the measurement effort. For example, with model measurement set-ups in a smaller size or measurements with other fluids, the theory of similarity is used to solve the real systems problems through calculation with dimensionless numbers. [69, p.120 ff.]

2.2.5 Physical Properties relevant for Two-Phase Flow Behavior

The dimensionless numbers (see Equation 2.14 to 2.17) are calculated with the physical properties density, viscosity and surface tension. In the following sub-sections, these properties are described in detail with respect to electrolyte solutions. Although all the physical properties mentioned below are dependent on the pressure in reality, here, the assumption is applied that the pressure does not play a relevant role in the here used operation conditions. This assumption is made since the increase in pressure results in only a non-relevant increase in volume. [70, p.7]

Mass Density

The mass density is an intensive quantity and is the quotient of the mass and the volume of a material. For the exact thermodynamical description of the mass density of an electrolyte solution, the distribution of anion and cation in an aqueous solution needs to be known. This is difficult because the ions are not randomly distributed but interact. In addition, the hydrogen-bonded water molecules will hydrate the anions and cations in various ways. The model which is mostly used to describe the interaction of anions and cations is the Debye-Hückel Theory, for the details of this theory, refer to [71, p.23ff.]. The Debye-Hückel Theory, however, describes the behavior of electrolyte solutions with the assumption of infinite dilution [72]. Therefore, for concentrated electrolyte solutions, the Debye-Hückel Theory needs to be extended, or other models need to be used, but mostly empirical relations are developed from measurement data. The mass density is dependent on temperature, concentration, and pressure. As Harms [73, p.5ff.] describes, the pressure influence is much less severe compared to the influence of the temperature, which is why most publications about density of electrolyte solutions do not consider the pressure influence [74–78]. The density of electrolyte solutions as a function of temperature has a density maximum (same as pure water) [79] at low temperatures. After the temperature of maximum density, the density decreases with increasing temperature. With increasing concentration of the electrolyte solution, the density increases [74].

Viscosity

The dynamic viscosity defines a fluid's resistance to flow and can be described by Equation 2.19. Equation 2.19 results from the general transport equation (see Equation 2.18), which relates a flux ($\mathbf{J}$) that flows through a defined area in a defined time with the transport quantity density Γ over a constant of proportionality a.

$$\mathbf{J} = -a \cdot \nabla\Gamma \tag{2.18}$$

$$F = -\eta \cdot A \cdot \frac{\partial v}{\partial x} \tag{2.19}$$

In the case of Equation 2.19, the flux over time can be rewritten as a force (F) (or the derivative of the momentum) divided by area (A), the constant of proportionality (a) (cf. Equation 2.18) equals the dynamic viscosity (η), and the transport quantity, in this case, is the velocity (v).

The theoretical basis of Equation 2.19 comes from the model of a still-standing plate and a moving plate with area (A) at a certain distance with a layer of liquid in between. The velocity of the liquid layer changes from zero to the velocity of the moving plate with increasing coordinates from a still-standing plate to a moving one. F is the force that is needed for the movement of the moving plate. The viscosity for Newtonian fluids is independent of the velocity gradient, which means the viscosity is constant. This does not apply to non-Newtonian fluids. [80, p.117 ff.]

Here, only Newtonian fluids will be considered, for non-Newtonian fluid behavior, it is referred to [81].

The dynamic viscosity is an electrolyte solution-specific value and is temperature- and concentration-dependent as well as pressure-dependent. The density of the liquid changes with the pressure, as well as the binding energy of the liquid molecules, and with that, the viscosity of the liquid is changing. [82, 83]

Nevertheless, the temperature and concentration dependence is much more severe than the pressure effect [83], which is why the pressure dependence of the dynamic viscosity is mostly neglected in literature [76, 77, 84, 85].

For pure (Newtonian) liquids, the relation between temperature and viscosity is that the logarithmic viscosity is proportional to the reciprocal temperature. For electrolyte solutions, the relation is a little more complicated because of the ionic interaction. Nonetheless, the general relation of temperature dependence can also be applied to electrolyte solutions; The viscosity decreases with increasing temperature. The viscosity increases exponentially with the concentration. [75]

Ionic Conductivity

The ionic conductivity of a liquid depends on how many ions are in a defined volume of solution and their drift velocity. Therefore, it is a liquid-specific measure, because the drift velocity depends, amongst other measures, on the electrical field and the ion mass. The ionic conductivity describes the charge transfer through a material in the form of ions. Electrolyte solutions are good conductors because they contain water as a polar solvent and salts. The salts are hydrated when solved in water due to the polarity, which means that the positive hydrogen side of the water attaches to the anion and the negative oxygen side to the cation. The mole flow of a species can be described by Faraday's Law (see Equation 2.20), which describes the flow of electric charge through the liquid in the form of ions.

$$\dot{n} = \frac{I}{zF} \tag{2.20}$$

Faraday's Law for electrolysis describes the mole flow ($\dot{n}$) of a species, which results from the current (I) that is applied to the solution divided by the valence of the species (z) and the Faraday constant (F). [86, p.524ff.]

The ionic conductivity is dependent on the temperature, the salt concentration, and the system pressure. The pressure dependence of electrolyte solutions is mostly neglected and is becoming only essential when operating close or above the thermodynamic critical point [87]. The electrolyte solutions that play a role in this examination are assumed to be fully dissociated. If electrolyte solutions are not fully dissociated, the pressure has an influence [88].

With increasing temperature, the ionic conductivity is increasing and has a maximum ionic conductivity depending on the electrolyte concentration. For increasing temperatures, the maximum ionic conductivity is shifted towards higher concentrations. [74]

Surface Properties

The surface free energy is the work that is needed in order to increase the surface area of a solid phase. The surface tension is the work resulting from molecular forces of a liquid, which intends to keep the surface as small as possible. The relation between the liquid surface tension (γ_{lg}), the solid surface energy (γ_{sg}) and the liquid-solid interfacial tension (γ_{sl}) can be seen in Equation 2.21. The contact angle (θ) is defined as the tangential angle of the liquid-solid-air interface and is shown in Figure 2.8.

$$\gamma_{sg} = \gamma_{lg} \cdot \cos\theta + \gamma_{sl} \tag{2.21}$$

When no interactions between the solid and the liquid face exist, the contact angle would be 180°, but in reality, interactions always occur. [89, p.7ff.] Liquids with a contact angle greater than 90° are called hydrophobic, and liquids with a contact angle smaller than 90° are called hydrophilic. [89, p.123ff.]

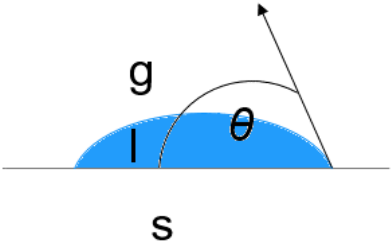

Figure 2.8: Illustration of the Contact Angle of a Droplet on a Surface.

The surface energy is divided into a polar and a dispersed fraction. The assumption is that polar interactions of the two interacting phases only interact with each other, and the dispersed interactions only interact with each other. Polar interactions are induced by an asymmetry of electron density in molecules and are mostly stronger than dispersed interactions. Disperse Interactions are caused by statistical fluctuations of the electron density distribution in a molecule. [89, p.136ff.] The higher the surface energy, the stickier the surface. [89, p.123ff.] Adding salt to an electrolyte solution increases the surface tension because of the repulsion of the ions from the surface caused by the electrostatic image force [90]. Increasing the temperature of the system decreases the surface tension of an electrolyte solution [90, 91].

2.3 Fundamentals of Neutron Radiography

In this work, neutron radiography measurements are conducted. Therefore, the fundamentals of neutron radiography are described, especially the interaction of neutrons with matter. Through neutron radiography, it is possible to investigate several technical or scientific applications. The needed neutrons for neutron radiography need to be emitted by induced nuclear fission in nuclear research reactors. Neutrons have a high penetration thickness for metals and, therefore, result in detailed images with high contrast for atoms with a higher attenuation coefficient (e.g. hydrogen). From Figure 2.9 it can be seen that in contrast to x-rays, a beam of thermal neutrons has an irregularly distributed mass attenuation coefficient.

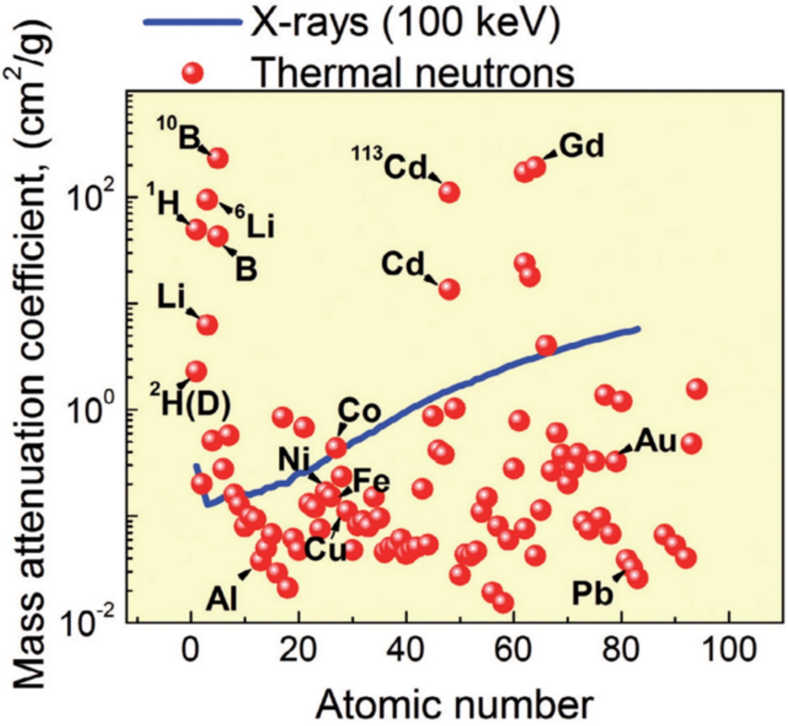

Figure 2.9: Comparison of Mass Attenuation Coefficients of Thermal Neutrons and X-rays [92].

Molecules like hydrogen, lithium, and cadmium have a high mass attenuation coefficient compared to metal molecules like Nickel, Cobalt, and Iron. Because of the high difference of attenuation between hydrogen and most other molecules, it is possible

to visualize matter with a high hydrogen content even when the hydrogen-containing matter is hidden behind non-transparent matter. [93]
The interaction of neutrons with matter is with the nucleus of an atom or with the magnetic field. The neutron is not charged and, therefore, does not interact with electrons or protons. The neutron does have a mass and a spin, which can cause a destabilization of the nucleus. As a result of neutron absorption, the atom can emit secondary neutrons, protons, α-particles, photons, γ-rays, and fission products. [94, p.120ff]
The incident beam is either absorbed, scattered, or transmitted through the matter. The transmitted neutron beam strikes a detector. The ratio of incident beam I_0 and detected beam I is described through Beer-Lambert's law (see Equation 2.22). [95, p.227]

$$I = I_0 \, exp(-\Sigma \, z) \tag{2.22}$$

Beer-Lambert's law describes the exponential decline of a beam passing through the matter of thickness (z) by an attenuation coefficient (Σ), which is assumed to be constant throughout the material [95, p.112]. In literature, a few investigations of two-phase flow behavior of electrochemical cells with neutron radiography are published. An overview on these publications is given in Table 2.1.

Table 2.1: Two-phase Flow Investigations of Electrolysis Cells by Neutron Radiography.

Authors		**type of electrolysis cell**	**min. temporal resolution** [s]	**spatial resolution** [μm]	**measurement method**
Selamet et al.	[96]	PEM	10	75	In-plane
Hoeh et al.	[66]	PEM	1	10	Through-plane
Seweryn et al.	[97]	PEM	10	75	In-plane
Panchenko et al.	[64]	PEM	5	6.3	In-plane
de Beer et al.	[98]	PEM	10	10	In-plane
Gebhard et al.	[99]	Chlor-Alkali	2.5	6.5	Through-Plane
Minaar et al.	[100]	PEM	2	11	Through-plane

In-plane neutron radiography measurements are typically conducted to see detailed effects or layer-specific effects of the two-phase flow within a flow cell. Beer et al. [98] have investigated a PEM flow cell regarding the water drag through the membrane from anode to cathode side. Panchenko et al. [64] tested different porous transport layer (PTL) materials and their different water-gas distributions. Seweryn et al. [97] looked at the water content of the anodic PTL and concentrated on the mass transport limitations within PEM electrolysis cells. Selamet et al. [96] found out that two different flow phenomena exist in their PEM electrolysis cell, which used a mesh flow field. They saw small gas bubbles growing and being removed and large gas bubbles which blocked the flowfield.

Through-plane measurements are mostly conducted in order to investigate the overall two-phase flow behavior inside the flow cell. Gebhard et al. [99] conducted measurements on a chlor-alkali electrolysis cell in order to see the distribution and the entering of electrolyte solution inside the electrodes. Hoeh et al. [66] and Minnaar et al. [100] conducted through-plane neutron radiography measurements in order to measure the average gas amount inside their cell.

2.4 Particle Image Velocimetry

Particle image velocimetry (PIV) is a measurement method that results in the velocity distribution inside a flow channel or any other flow geometry. The method was introduced in the late 1970's first for 2D applications [101, 102] and has been extended to 3D applications in 1991 [103] using holography. The measurement method can be used for both laminar and turbulent flow behavior [104].

2.4.1 Fundamentals

For the measurements, the fluid is seeded with tracer particles. With a laser or a LED, the region of interest is illuminated, and the light is scattered by the particles. The light is pulsed with a pulse frequency, which depends on the flow velocity and the desired magnification. PIV measurements are typically divided by particle density into laser speckle velocimetry (the particle dense is too high to identify individual particles with the evaluation algorithm) and particle tracking velocimetry (individual particles are being identified by the evaluation algorithm) [105]. The typical scheme of a PIV measurement set-up can be seen in Figure 2.10. The scattered light of the particles is recorded by a high-speed lens.

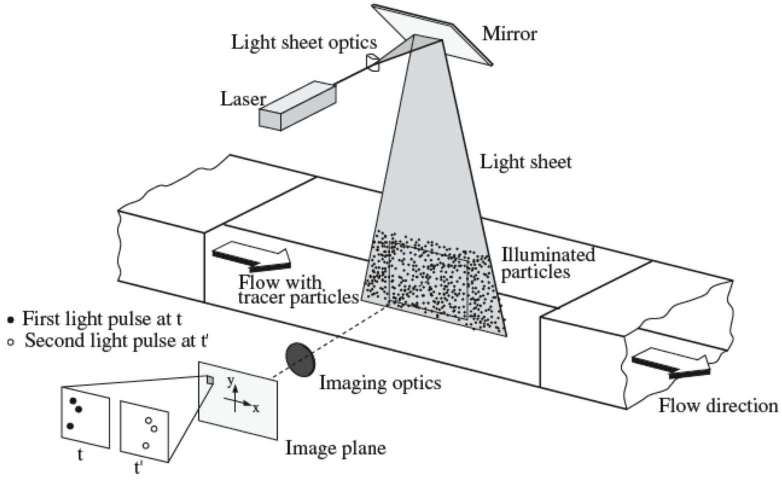

Figure 2.10: Example of a Particle Image Velocimetry Set-up [106, p.4].

The tracer particles should have the same density as the fluid they are seeded in order to avoid the gravitational sinking of the particles. Smaller particles follow the liquid movement better. The measurement of the flow velocity is therefore measured indirectly through the particle movement. [106] For the evaluation of the velocity, the images are analyzed in pairs. Each image is divided into so-called interrogation windows. Due to the particle density, the movements of single particles are hard to follow, which is why during the evaluation of PIV images, the mean particle movement of a group of particles is determined. The high particle density is needed to obtain a sufficient image resolution. If the PIV measurements are done with one camera, the resulting images show particle movement of a plane, and the third dimension is not shown.

The image processing can be done by three different methods; Young's fringe, auto-correlation, or cross-correlation [107]. Here we are focusing solely on cross-correlation. For the other methods, it is referred to elsewhere [108]. In order to track the gas bubble movement, an interrogation window of a certain size of the image of time step t is taken and compared to the particle pattern in the image at the following time step t'. To find the particle pattern in the image at time step t' the interrogation window is moved iteratively over the image with a certain overlap to the interrogation window scanned before (see Figure 2.11).

For each iteration step the cross-correlation function R is calculated, which can be seen

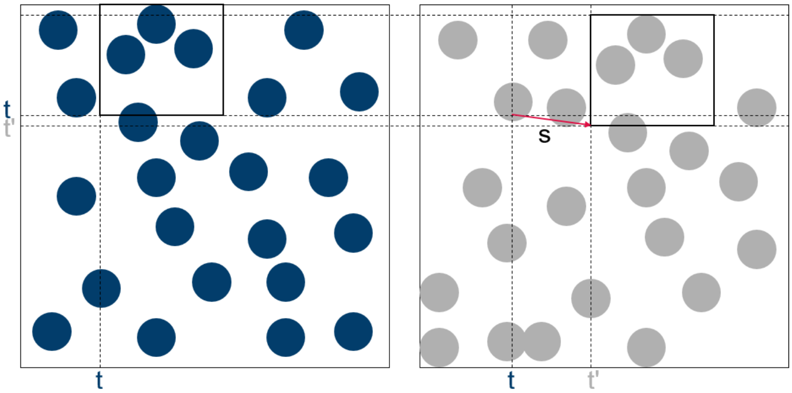

Figure 2.11: Interrogation Window Displaying Particle Movement from Time Step t to t'.

in Equation 2.23.

$$R(\mathbf{s}) = \int I_1(\mathbf{X}) I_2(\mathbf{X} + \mathbf{s}) d\mathbf{X} \tag{2.23}$$

The cross-correlation function consists of the two-dimensional spatial convolution of the scattered light at the particles at location $\mathbf{X}$ at time step t and the scattered light at the particles at the location displaced by the displacement vector $\mathbf{X} + \mathbf{s}$ at the following time step t'. An example of how the cross-correlation function looks is given in Figure 2.12. The function consists of smaller noise peaks and a high peak where the particle distribution of the two images correspond. [109] For the evaluation of the PIV images, it is assumed that the particles in direct vicinity move in the same direction [106, p.5].

Cross-correlation is always done with two consecutive images. From the displacement vector and the frame rate, the velocity can be determined.

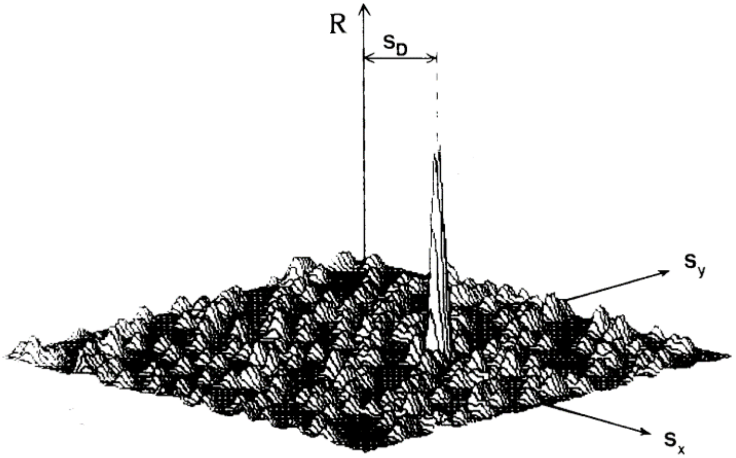

Figure 2.12: Cross-correlation Function [109, p.196].

2.4.2 Particle Image Velocimetry Measurements in Multiphase Flows

Mostly, particle image velocimetry measurements are conducted to find the velocity of a liquid or gaseous media. Sometimes, particle image velocimetry measurements are combined with other image-processing techniques in order to analyze liquids containing gas bubbles. In this examination, the term multiphase flows means liquids containing gas bubbles. Measuring multiphase flow behavior is difficult and poorly understood so far [110]. According to Chen et al. [111] particle image velocimetry is the most promising measurement technique for measuring multiphase flow.

There are three main difficulties when using PIV for multiphase flows. When the gas bubble concentration is too high, the tracer particles cannot or poorly be detected from the images [112]. Brücker [110] recommends a gas bubble void fraction limit of 5% [110]. On the other hand, it is difficult to detect gas bubbles when they are too small and cannot be distinguished from the particles. Deen et al. [112], therefore, recommend a gas bubble void fraction of 1-4% [112]. A third difficulty during multiphase PIV measurements is when shadows of e.g. gas bubbles darken the scattered light of the particles [112].

The scattered light of the particles and the gas bubbles is not always explicitly differentiable. To identify the different phases, phase discrimination techniques can be used, such as amplitude discrimination, using fluorescent particles, or particle pattern recognition. When the gas bubbles and the tracer particles have different scattering characteristics, amplitude discrimination can be used [113, 114]. The use of two different cameras with different filters in combination with a beam-splitting prism allows the use of fluorescent particles [115, 116]. If the particles and gas bubbles can be divided by size or shape, particle pattern recognition can be used [117, 118].

Using cross-correlation in the evaluation of multiphase flow images results in two peaks for the cross-correlation function and, therefore, in two different displacement vectors [112]. One strategy to distinguish the gas bubble movement from the particle movement is to adjust the signal-to-noise ratio and, therefore, filter the signal of the particles from the pictures to analyze the gas bubble movement and use it as a mask for analyzing the particle movement [119]. Another possibility is using a median filter for the separation of the gas bubbles and the particles. The median filter does not filter the gas bubbles. The filtered image with only gas bubbles can then be subtracted from the original image, resulting in an image with only particles [120, 121]. Deen et al. [122] used fluorescent particles and two cameras with different filters and beam-splitting prism.

In all the mentioned approaches above, the two analyzed pictures during cross-correlation are further divided into four images in total, one pair for the particle movement analysis and one pair of images for the gas bubble movement analysis.

3 Methods and Measurement Techniques

In the following section, the detailed measurement methods are explained that are used to investigate the two-phase flow of an alkaline electrolysis zero-gap cell. All measurement methods use the same flowfield geometry in order to ensure the highest grade of comparability. In the first two sub-sections, Section 3.1 and Section 3.2, the flow visualization methods, neutron radiography measurements, and particle image velocimetry are described. The measurement set-ups are explained, and the evaluation and image processing methods are stated. In the third sub-section, Section 3.3, liquid characterization methods are described, which are needed to prepare the neutron radiography and particle image velocimetry measurements.

3.1 Neutron Radiography

The Neutron and X-ray Tomograph (NeXT-Grenoble) is an instrument that was launched in 2016 and is located at Institut Laue Langevin (ILL) in Grenoble, France. NeXT-Grenoble was developed together with the Universite Grenoble Alpes. The neutron beam comes from a heavy-water-cooled and moderated swimming pool-type reactor, which has a thermal power of 58 MW. The nuclear research reactor has a neutron flux of 1.5 x 10^{15} n/cm^2/s in the moderator region and a flux of 3 x 10^8 n/cm^2/s for an L/D (L: pinhole/sample distance, D: pinhole size) of 333 at the sample position for a used pinhole of 30 mm, which makes the neutron source the source with the to date highest neutron flux in the world. As highlighted by Tengattini et al. [123], the neutron beam is not entirely homogeneous. Using a larger pinhole, like in this case 30 mm, results in a more homogeneous wavelength distribution at the detector, especially in the central 100 mm. The wavelength of the neutron beam is between 1.4 nm and

0.1 nm, with a peak at 0.28 nm. [123]

3.1.1 Measurement Set-up and Cell Design

The neutron beam entering the imaging zone penetrates the cell, which is mounted to a rotatable sample table. In this case, the sample table remains in a fixed position, and the beam is directed at the cell at a 90-degree angle, the measurements are conducted as through-plane measurements. The transmitted beam interacts with the scintillator and is transformed into visible light. The visible light is redirected by a mirror at a 45-degree angle and focused by a lens into the CMOS camera. The redirection by a mirror is done to protect the camera from the beam and most of the scattered radiation [124]. Some mathematical corrections have to be applied because of the conversion of the neutron beam to visible light through the scintillator. The corrections are needed due to the ratio of neutron flux to light flux, as well as in terms of changing spatial resolution. For more details regarding the mathematical image correction, it is referred to Rayleigh [125]. The arrangement of measurement equipment can be seen in Figure 3.1.

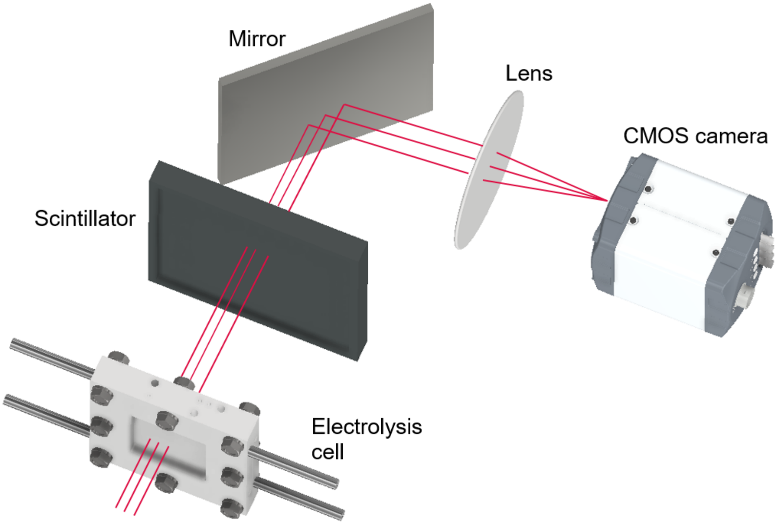

Figure 3.1: Scheme of the Neutron Radiography Set-up at ILL in Grenoble.

To quantify the change of attenuation through the different layers of material and fluids of the neutron beam, a few preparatory measurements have to be conducted before starting the main measurements with an operating alkaline zero-gap electrolysis cell. The regarding images can be seen in Figure 3.2.

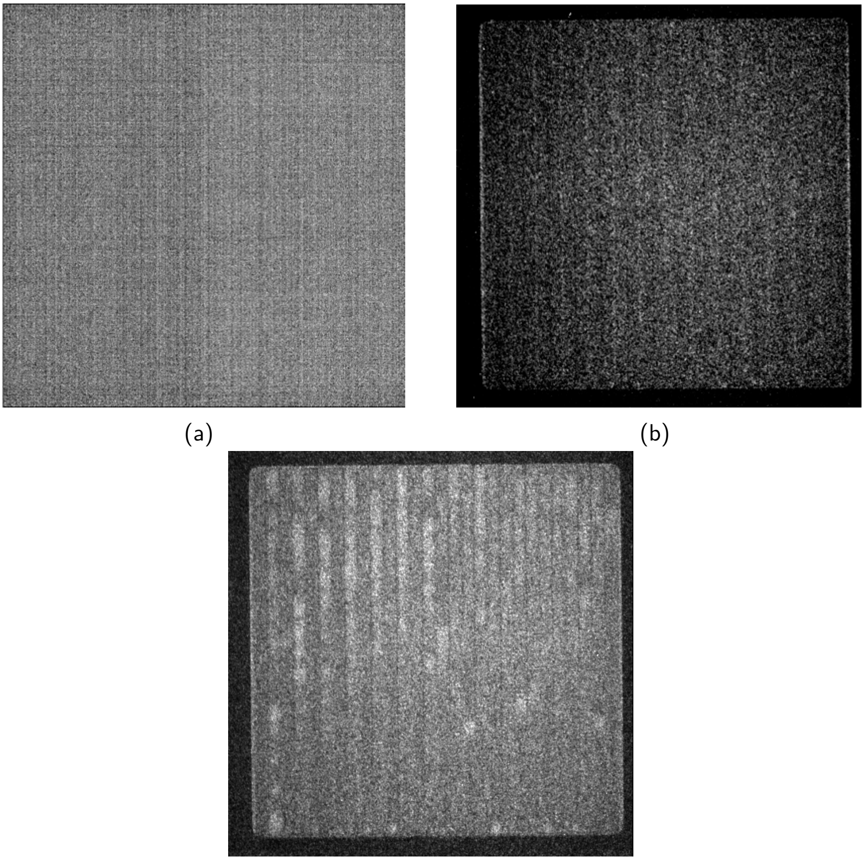

(a) (b)

(c)

Figure 3.2: Preparatory Images for the Evaluation of the Operando Cell Measurements; Camera Noise without Cell and without Neutron Beam (a), Cell with Electrolyte Solution Flooded Cell in the Beam (b) Example Image of Flowfield with Gas Bubbles during Cell Operation (c).

To quantify the noise of the camera, the cell is removed from the beam area, and the beam is turned off. The resulting gray values of the camera noise (see Figure 3.2 (a)) are to be subtracted from each recorded image. One more setting has to be recorded for the evaluation, the cell penetrated by the neutron beam with the flooded flow channels. From the two settings, the attenuation coefficient can be determined (see Equation 3.2) by Beer-Lambert's law (see Equation 3.1) with the thickness of the electrolyte layer of 1.5 mm channel depth (d_{KOH}). Using Equation 3.2 and calculating the attenuation coefficient (Σ) for different images with different transmissions per pixel (T_{image}) results in a constant value, which is the attenuation coefficient (Σ). All gray values of the images with gas bubbles and the images of the flooded cell are subtracted by the gray value of the camera noise T_{noise}. Once the attenuation coefficient is determined, the gas layer thickness, for example, can be calculated with it, which is explained in more detail later.

$$\frac{T_{image} - T_{noise}}{T_{wet} - T_{noise}} = \exp\left(-\Sigma \cdot d_{KOH}\right) \tag{3.1}$$

$$\Sigma = -\frac{1}{d_{KOH}} \cdot \ln\left(\frac{T_{image} - T_{noise}}{T_{wet} - T_{noise}}\right) \tag{3.2}$$

The cell that was used for the neutron radiography measurements is an alkaline electrolysis cell in a zero-gap configuration. A scheme of the electrolysis cell assembly can be seen as an exploded view in Figure 3.3 The cell consists of two monopolar plates with a flowfield made from Nickel Alloy 201, the flowfield can be seen in Figure 3.4.

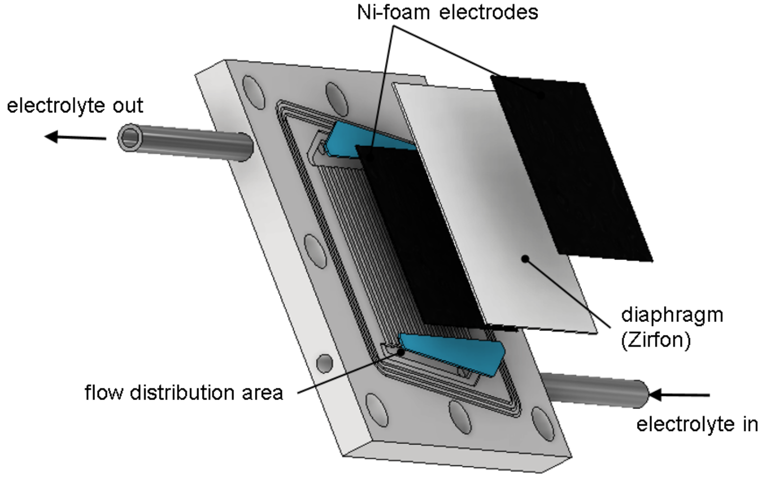

Figure 3.3: Scheme of the Cell Assembly of the Alkaline Zero-gap Electrolysis Cell used for Neutron Radiography Measurements.

The flowfield has parallel flow channels, and the electrolyte flow enters the cell from the lower pipe (right side of Figure 3.3). After passing the inlet pipe, the cell has a flow distribution area to distribute the flow equally over all parallel channels. The flow distribution area is covered with a metal plate due to cell stability and sealing

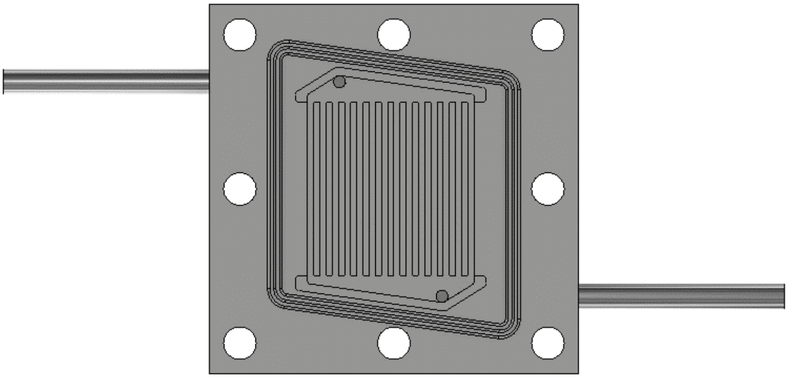

Figure 3.4: Flowfield Plate of the Alkaline Zero-gap Electrolysis Cell used for Neutron Radiography Measurements.

reasons. The electrolyte solution passes through the flow channel, distributing the cell with water for the reaction, realizing the ionic conductivity through the provision of hydroxide ions, and removing the forming gas bubbles on the way out of the cell. In this case, potassium hydroxide is used as an electrolyte solution with a concentration of 32.7 wt.-%. The flow channels have a length of 42 mm and a cross-sectional area of 1.5 mm x 1.5 mm. As electrode material, Nickel foam with a thickness of 0.3 mm and a specific surface of 5400 m^2/m^3 supplied by Recemat BV[2] is used. The diaphragm material is the state-of-the-art material *Zirfon UTP 500* supplied by Agfa Gevaert NV[1] with a thickness of 500 μm. The active cell area of the used cell is 17.64 cm^2. The current connection is made by cable lugs connected to the top of each monopolar plate. The cell is heated by heating rods with 4 mm in diameter and one preheater cell on anode and cathode side each. The temperature is measured on the lower left side of the monopolar plate with a Nickel-Chromium/Nickel thermocouple and controlled with a temperature control unit supplied by Elotech Industrieelektronik GmbH[3]. The electrolyte solution is pumped by a membrane pump of type *Simbdos 10* supplied by KNF DAC GmbH[4]

---

[2] https://www.recemat.nl/

[1] https://www.agfa.com/

[3] https://www.elotech.de/

[4] https://www.knf.com/

3.1.2 Measurement Settings

During the neutron radiography measurements, the cell is operated at different operation conditions, changing electrolyte volume flow, current density, and temperature. The measurement procedure is started by heating up the cell to 80 °C and afterwards, a breaking-in period of five hours is done. After the breaking-in period, the main measurements start. Four different temperatures are measured; 80 °C, 70 °C, 60 °C and 50 °C. For each temperature, four different electrolyte volume flows are applied; 100 ml/min, 50 ml/min, 25 ml/min, and 10 ml/min, and then the operation is moved on to the next temperature. The volume flows are chosen in a random order, the temperatures are set in a descending order.

Polarisation Curves

At each temperature/volume flow combination, a polarization curve is measured. The power supply of the cell is done by a potentiostat *Gen 20-76* supplied by TDK Lambda Germany GmbH[5]. The cell is operated in galvanostatic mode. The polarization curve is measured at the following current densities; 0.01 A/cm^2, 0.05 A/cm^2, 0.1 A/cm^2, 0.2 A/cm^2, 0.4 A/cm^2, 0.6 A/cm^2, 0.8 A/cm^2 and 1 A/cm^2. Each current density is applied for 5 minutes, starting with the lowest current density ascending. For the graphic display, the last minute of each measured current density is used to calculate the mean value and plotted as a polarization curve of the regarding operation point.

Electrochemical Impedance Spectroscopy

The electrochemical impedance is measured using a *IM6* potentiostat supplied by Zahner Elektrik GmbH & Co.KG[6]. The impedance is measured before and after every polarization curve. During the measurements, the main focus is laid on the high frequency resistance in order to get an indication of the ohmic resistance of the electrolysis cell and how the resistance is influenced by gas bubbles inside the cell. Before and after the polarization curves, the impedance is measured at a current density of 1 mA/cm^2 with an amplitude of 20 mV. During the breaking in of the cell, the impedance is also

---

[5] https://www.emea.lambda.tdk.com/

[6] https://www.zahner.de/

measured at the following time steps after starting the breaking in; 10 min, 30 min, 1 hour, 3 hours, 5 hours. In addition to the impedance measurements at the mentioned time steps, the impedance is measured for 80 °C for each volume flow, also at current densities of 0.01 A/cm^2, 0.05 A/cm^2 and 0.1 A/cm^2, every time with an amplitude of 20 mV

3.1.3 Evaluation of Neutron Radiography Images with *Trackmate*

Trackmate is a tracking software that was developed and optimized by Ershov et al. [126] in order to track objects from fluorescence microscopy images. The software was developed to identify and track moving objects from images and can be used as a plugin to *ImageJ* [127], which makes it suitable also for gas bubble detection and tracking.

The images are reduced from 32-bit to 16-bit images for calculation time reasons before starting the evaluation with *Trackmate*. The chosen detector in *Trackmate* is the Laplacian of Gaussian (LoG) detector. The Laplacian of an image makes use of the second derivative of an image and is, therefore, able to identify edges on images. Unlike operators using the first derivative, the Laplacian does not determine changes in intensity but the derivative of changes in intensity. Since an image is a structure of discrete pixel values, the second derivative has to be approximated using a convolution operator. Noise has an influence on the result of the Laplacian and can result in noise-produced edges, which is why the image, in this case, is smoothed by a Gaussian filter first. [128]

As a tracker for the gas bubbles, the LAP tracker is chosen in *Trackmate*. LAP stands for linear assignment problem and was developed by Jaqaman et al. [129]. The tracking is done by creating track segments and linking the identified objects from frame to frame. This is done by minimizing a cost matrix of a specific shape. For detailed information about the LAP tracker, it is referred to [129].

3.1.4 Evaluation of Gas Amount in Neutron Radiography Images

The evaluation of the gas amount inside the flow channels is done in two ways. The first one is to determine the gas layer thickness from the neutron radiography measurements. Since the gas layer thickness is not be able to determine from the proposed method for visualizing the two-phase flow of an alkaline electrolysis cell, as a second step, the percentage of the gas amount in each channel is determined as a measure of comparison between the neutron radiography measurements and the multiphase particle image velocimetry measurements.

Determination of the Gas Layer Thickness

To evaluate the gas amount from the images resulting from the neutron radiography measurements, the images need to be processed in a first step. The image processing is done by Helmholtz-Zentrum Berlin GmbH (HZB) at the Institute of Applied Materials[7] using custom developed image processing algorithms.

The resulting images are gray-scale images (values between 0 and 255). The gas bubbles have gray pixel values (values between 0 and 255). The gray values depend on the grade of transmission of the neutron beam, respectively, the thickness of the gas layer the neutron beam is attenuated. Using Beer-Lambert's Law (cf. Equation 3.3), the gas layer thickness of each image pixel can be determined with the attenuation coefficient (Σ) (determined using Equation 3.2), the gray value of the pixel of the image with flooded channels (T_{wet}) and the gray values of the pixel of the image that is investigated (T_{image}) and the contribution to the transmission by the camera noise (T_{noise}). The resulting gas layer thickness at each channel location (d_{gas}) is averaged for the different operation points to analyze the average gas distribution inside the flow channel.

$$d_{gas} = -\frac{1}{\Sigma} \cdot \ln\left(\frac{T_{image} - T_{noise}}{T_{wet} - T_{noise}}\right) \tag{3.3}$$

The gas amount measured through neutron radiography measurements is compared to the theoretical averaged value for the gas thickness ($d_{gas,theo.}$) calculated through

---

[7] https://www.helmholtz-berlin.de/forschung/oe/ce/materialforschung/index_en.html

Faraday's Law by Equation 3.4.

$$\begin{aligned} d_{gas,theo.}(x) &= \tfrac{V_{gas}(x)}{A(x)} \\ &= \tfrac{\dot{V}_{gas}(x)}{\dot{V}_{gas}(x)+\dot{V}_{KOH}} \cdot \tfrac{V_{tot}(x)}{A(x)} \\ &= \tfrac{\dot{V}_{O_2}(x)+\dot{V}_{H_2}(x)}{\dot{V}_{O_2}(x)+\dot{V}_{H_2}(x)+\dot{V}_{KOH}} \cdot \tfrac{V_{tot}(x)}{A(x)} \end{aligned} \tag{3.4}$$

The theoretical gas thickness ($d_{gas,theo.}$) is calculated through the gas ratio of the total Volume (V_{tot}) divided by the active cell area (A). To calculate the gas volume flow ($\dot{V}_{gas}$), the Faraday efficiency is considered, which considers the ratio of the effectively produced amount of gas to the theoretical, possibly produced amount of gas. For electrolysis cells, this efficiency can be assumed to be 100 %. For an electrolysis stack, the Faraday efficiency can be determined by the empirical equation published by Mónica Sánchez et al. [130], which can be seen in Equation 3.5. The Faraday efficiency in stacks is reduced by parasitic currents.

$$\eta_F = \left(\frac{i^2}{478645.74 - 2953.15 \cdot \vartheta + i^2} \right) \cdot (1.03960 - 0.00104\vartheta) \tag{3.5}$$

The current density (i) in this empirical equation is inserted in A/m^2, and the temperature (ϑ) needs to be inserted in ° C.

Determination of the Percentage of the Gas Content in the Flow Channel

Additionally, the gas amount is determined by a second method for comparison of neutron radiography measurements and particle image velocimetry measurements. A measure of the comparability between the modeled transparent quartz glass electrolysis half cell used for particle image velocimetry measurements and the alkaline electrolysis cell used for neutron radiography measurements is the gas amount in the different flow channels. Since the images taken during particle image velocimetry measurements can be evaluated only in 2D and not with a gas layer thickness as done for the neutron radiography images, the gas amount is additionally evaluated using the visible cross-sectional area of the gas bubbles to determine the percentage of gas inside the cell. Since these values are used not to quantify the gas amount but to compare the gas distribution inside the flow channel of the two different measurement set-ups, this is a valid method here.

The gas amount is evaluated by image processing in Python using *numpy* [131] (version

1.23.3) for image array processing and *opencv* [132] (version 4.6.0) for image processing and filtering. At first, the images are binarized, which means setting the different pixel values from a grayscale to the value of 255 (white pixel value) and everything except the gas bubbles to 0 (black pixel value). An example image of the processed images can be seen in Figure 3.5.

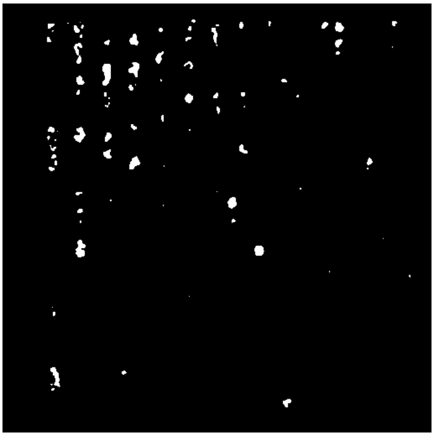

Figure 3.5: Binarized Image for Determination of the Gas Amount in the Channel of the AWE cell.

From the amount of white pixel values, the percentage gas amount inside the channel calculated with the total gas amount in the picture can be determined. For the analysis, 5000 images are analyzed for every operation point, and the gas amount per channel is averaged.

3.2 Particle Image Velocimetry

The multiphase particle image velocimetry measurements are conducted in order to track flow velocities. Here, the electrolyte velocity inside a transparent cell is tracked, and additionally, the gas bubble velocity and gas amount are measured. Through particle image velocimetry measurements, it is possible to visualize the liquid phase in an electrolysis cell by seeding the liquid with particles. With this measurement method, the liquid phase, which cannot be made visible during operando neutron radiography measurements, can be characterized.

3.2.1 Cell Assembly and Measurement Set-up

The cell that is used for particle image velocimetry measurements simulates a half cell of an alkaline electrolysis zero-gap flow cell without having any electrochemical functionality itself. The cell design can be seen in Figure 3.6 and Figure 3.7. It consists of a quartz glass plate (cf. Figure 3.6 (a)) and a stainless steel plate (cf. Figure 3.6 (b)).

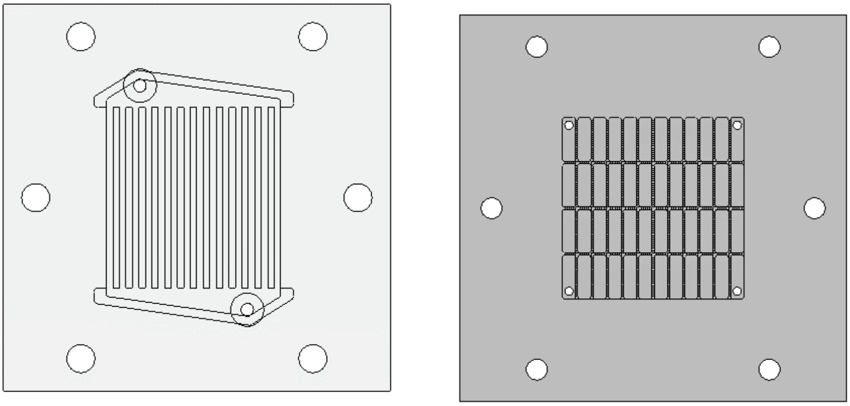
(a) (b)

Figure 3.6: Quartz Glass Plate (a) with Parallel Flow Channel and Gas Distribution Plate (b) for the Particle Image Velocimetry Measurements.

The cell size is 90 mm x 90 mm for the glass plate, and the active cell area is 17.64 cm^2 and has the same design as the cell used for neutron radiography. The cell consists of a quartz glass plate with an electrolyte flowfield, which is mounted against a metal plate with a gas distribution flowfield. The quartz glass plate has 14 parallel flow channels with a length of 42 mm and a cross-sectional area of 1.5 mm x 1.5 mm for each channel. The gas distribution plate is made from stainless steel and has 48 small pockets distributed over the area of 42 mm x 42 mm with small areas of land in between for mechanical stability. The gas is introduced at all four corners of the gas distribution area.

The simulation of an electrochemical cell is done by introducing gas to the cell on the backside of the steel plate through the gas distribution flowfield. Which is then fed to the parallel flow channel of the glass plate through layers of different materials. The first layer from the gas distribution flowfield side is a sintered metal plate followed by a porous PTFE sheet and a top layer of nickel foam. The porous PTFE is used to ensure the gas transport into the cell and ensures through the hydrophobic properties

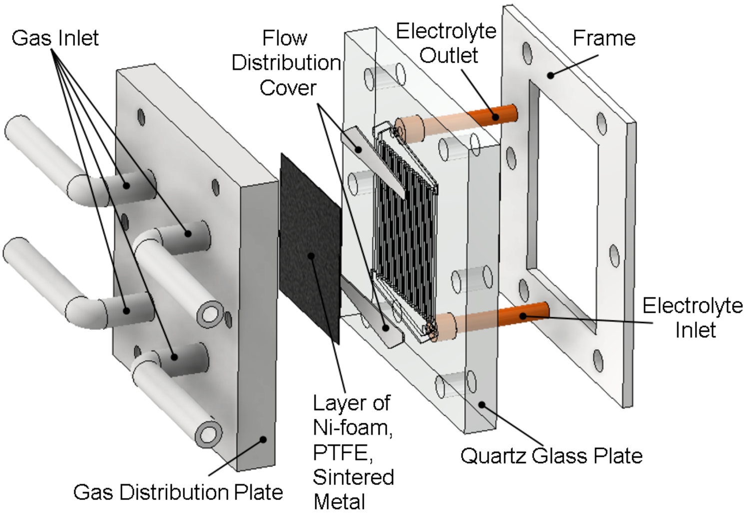

Figure 3.7: Explosion Drawing of the Cell used for Particle Image Velocimetry Measurements.

of the PTFE that no liquid can penetrate the sintered metal and the gas flowfield to avoid uneven gas distribution. The purpose of the sintered metal is to distribute the gas equally over the flowfield. The nickel foam ensures the right gas bubble diameter because nickel foam is the same material as the electrodes used in the alkaline electrolysis cell. The used nickel foam, which is 300 µm in thickness and manufactured by Recemat BV[2] is an in research commonly used electrode material of the here simulated alkaline zero-gap flow cell. The gas bubbles are transported out of the cell by an electrolyte flow after entering the flow channel. The flow channels are milled in the glass plate. The cell assembly makes it possible to study the electrolyte flow behavior through particle image velocimetry measurements and simultaneously record the gas bubble movement in the flowfield. In Figure 3.8, a scheme of the particle image velocimetry set-up can be seen.

For the particle image velocimetry measurements, an air-cooled LED from ILA 5150 GmbH[8] is used with a wavelength range in the green spectrum of visible light. The LED illuminates the parallel flow channel of the transparent cell. The electrolyte solution fed to the cell is seeded with fluorescent particles, which are excited by light of the wavelength of 530 nm (green light) and emit light in the wavelength of 590 nm (red

---

[2] https://www.recemat.nl/

[8] https://www.ila5150.de/

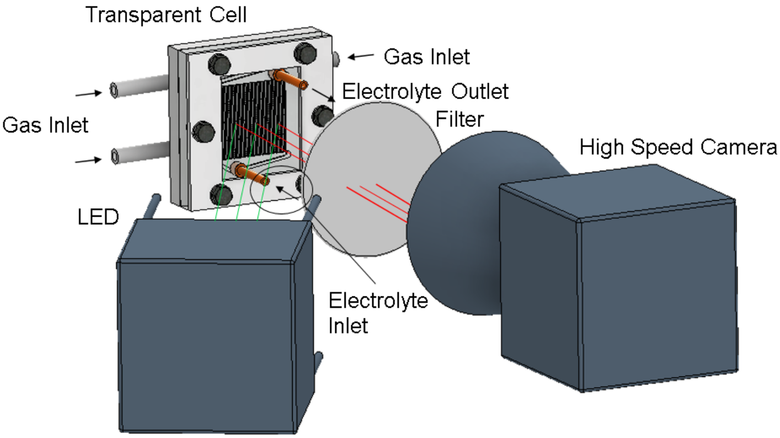

Figure 3.8: Scheme of the Used Particle Image Velocimetry Set-up.

light). The particles are fluorescent polymer microspheres made from Polyamide with a Rhodamine b coating and are supplied by Applied Microspheres B.V.[9]. Since the nickel foam, the gas bubbles, and other components used for the cell assembly can reflect the green light coming from the LED, a filter is used, which is permeable only to the emitted red light by the particles. The filtered light is recorded by a high-speed camera with a frame rate of 2000 frames per second. The used camera is a *FASTCAM Mini AX100* from Photron Inc.[10]. Not shown in Figure 2.10 are the following components: A synchronization unit *SigMa Synchonizer* from ILA 5150 GmbH[8] which is used to synchronize the exposure time of the high-speed camera with the LED. The used electrolyte solution is pumped by a membrane pump to get the same flow conditions as in the alkaline electrolysis cell used for neutron radiography measurements. The gas is introduced by a mass flow controller from Brooks Instrument GmbH[11] (*5850E series*) which are controlled by a Brooks Instrument GmbH[11] control unit (*Read Out & Control Electronics 0154*). The measurement equipment is connected to a computer, which stores and processes the recorded data.

During the particle image velocimetry measurements, instead of the electrolyte solution of a typical alkaline electrolysis cell, a model electrolyte solution is used.

The idea is to be able to simulate the flow behavior of different operation points of

---

[9] https://www.applied-microspheres.com/

[10] https://photron.com/

[8] https://www.ila5150.de/

[11] https://www.brooksinstrument.com/

an alkaline electrolysis cell by adapting the electrolyte solution, its temperature, and its concentration. Assuming an alkaline electrolysis cell is operated for each operation point at the optimum ionic conductivity, which results in a specific concentration and, with that, in a specific density and viscosity for each operation point.

A cell out of transparent material like quartz glass is potentially becoming turbid over time, depending on the concentration and temperature, if run with potassium hydroxide solution. With the intention of being able to simulate not only low temperature but also intermediate temperature alkaline water electrolysis flow behavior, which means operating under pressure, it is difficult to realize a cell design with a transparent material mechanically stable enough for pressurized operation. Because of these difficulties, the cell is operated with electrolyte solutions that have the same density and viscosity at a lower temperature without pressure to simulate potassium hydroxide. In addition, for safety reasons, the gases are changed from hydrogen and oxygen to nitrogen. The assumption is made that the gas volume of the two-phase flow behaves similarly when the gas amount introduced to the cell is calculated according to the ideal gas law (see Equation 3.6 and 3.7) for the changed operation condition with the model electrolyte solutions.

$$pV = nRT \tag{3.6}$$

Through the operation condition in an alkaline electrolysis cell (V_{real}, p_{real}, T_{real}) the needed gas volume $V_{sim.}$ in the simulated cell at different temperature and pressure can be determined according to the following equation:

$$\frac{p_{real}V_{real}}{T_{real}} = \frac{p_{sim.}V_{sim.}}{T_{sim.}}. \tag{3.7}$$

Important for the particle image velocimetry measurements is that the particle image velocimetry particle to pixel ratio is chosen carefully. If the particle image velocimetry particles take up too few pixels, the used evaluation algorithm *openpiv*, which is further described in Section 3.2.5, cannot reliably track the particle. The particles should take up at least four pixels [133]. In order to guarantee this condition, the measurement of the gas bubble movement and the electrolyte movement is measured separately.

The gas bubbles are big enough to measure the flowfield as a whole, for the particle movement with the electrolyte solution, the flowfield is measured in segments. The segments of the cell can be seen in Figure 3.9. The flowfield channels are divided into three parts for the recording of the velocity of the electrolyte solution with approximately 14 mm channel length per segment.

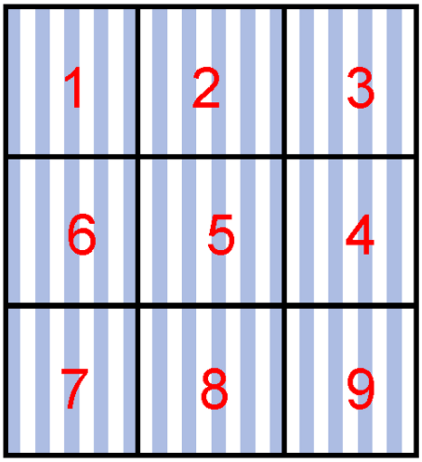

Figure 3.9: Measurement Pattern for the Particle Image Velocimetry Measurements.

The whole flowfield of the transparent cell is measured in 9 segments. Each flow channel is divided into thirds, the segments 1, 6, and 7 contain 4 flow channels, the remaining segments contain five thirds of a flow channel each.
For the image recording of the gas bubble movement, the whole flowfield is recorded at once, as already explained. After recording the images with gas bubbles, the gas flow is stopped, and a background image without gas bubbles is taken for image processing purposes.

3.2.2 Selection of Electrolyte Solution

The usage of the quartz glass cell and multiphase particle image velocimetry measurements offers the possibility to investigate the two-phase flow of an alkaline electrolysis cell at lower operation temperatures. This is done by simulating a half cell of an alkaline electrolysis cell, as explained before. Simulation means that the two-phase flow is not induced by an electrochemical reaction, but instead, the gas is introduced through the backside of the nickel foam, as also explained before. The model electrolyte solution in the particle image velocimetry quartz glass cell has the same liquid flow properties regarding viscosity and density at a temperature ($\vartheta_{PIV,j}$) as potassium hydroxide at a temperature $\vartheta_{KOH,j}$, with $\vartheta_{KOH,j} > \vartheta_{PIV,j}$ and $\vartheta_{PIV,j}$ being always lower than the evaporation boundary ($\vartheta_{PIV,j} < \vartheta_{PIV,evap.}$). With these two conditions, it is possible to potentially investigate the two-phase flow of alkaline electrolysis cells over a wide temperature range without the need for pressurized operation.

In order to find suitable model electrolyte solutions, a mathematical optimization is done to find potential candidates that have the same viscosity and density at $\vartheta_{PIV,j}$, then potassium hydroxide at $\vartheta_{KOH,j}$. Afterwards, the potential model electrolyte solutions are validated in their density and viscosity values experimentally.

The selection of model electrolyte solutions is done by using Equation 3.8 and Equation 3.9.

$$\ln \eta = \ln \eta_w + (d_{0,i} + d_{1,i}\vartheta + d_{2,i}\vartheta^2)c_i \tag{3.8}$$

The calculation of the density (ρ) and the viscosity (η) of electrolyte solutions can be done using the Ezrokhi method as suggested by Zaytsev et al. [76]. Both equations are semi-empirical equations with the same structure, the logarithmic viscosity respectively the density, results from the logarithmic value of pure water (ρ_w, η_w) added by a polynomial which consists of empirical coefficients specific for the electrolytes (i) ($d_{0,i}$, $d_{1,i}$, $d_{2,i}$, $b_{0,i}$, $b_{1,i}$ and $b_{2,i}$) and the temperature (ϑ) multiplied by the concentration of the electrolyte solution (c_i) [76, p.1724, 1728].

$$\ln \rho = \ln \rho_w + (b_{0,i} + b_{1,i}\vartheta + b_{2,i}\vartheta^2)c_i \tag{3.9}$$

For the water density (ρ_w) the suggested, empirical equation by Zaytsev et al. [76] is used (see Equation 3.10) [76].

$$\rho_w = 1000 - 0.062\vartheta - 0.00355\vartheta^2 \tag{3.10}$$

For the water viscosity, the pressure dependence was evaluated, and therefore the Equation 3.11 was used, which was published by Likhachev [134].

$$\eta_w = \eta_0 \cdot \exp ap + \frac{E - bp}{R \cdot (T - \theta - dp)} \tag{3.11}$$

The semi-empirical equation consists of the constants η_0, E, θ, a, b and d, p is the pressure and R is the universal gas constant. The values of the constants can be seen in Table 3.1.

The influence of the pressure (p) is neglected for the viscosity of water (see Equa-

Table 3.1: Values of Constants for Equation 3.11.

Property	Value	Unit
η_0	$2.04055 \cdot 10^{-5}$	Pas
E	4.753	kJ/mol
θ	139.7	K
a	$4.42 \cdot 10^{-4}$	bar^{-1}
b	$9.565 \cdot 10^{-4}$	kJ/(mol bar)
d	$1.24 \cdot 10^{-2}$	K/bar

tion 3.11) and set to ambient pressure, since up to a pressure of 20 bar (realistic pressure for intermediate temperature alkaline electrolysis) the difference to ambient pressure in a temperature range between 0 °C and 200 °C is 0.3 % maximal deviation. Zaytsev et al. [76] published a list with coefficients for 128 possible electrolytes [76, p.125ff., p.129ff.]. Using this list, a custom-made Python algorithm is used in order to find suitable electrolyte solutions for each operation point to replace potassium hydroxide. The operation points and the density and viscosity, which are needed, can be seen in Table 3.2.

In the first step of the algorithm, density and viscosity values for a temperature range of 15 °C $\geq \vartheta \geq$ 60 °C and a concentration range of 2 wt.-% $\geq$ c $\geq$ 40 wt.-% for all 128 possible electrolytes are calculated. Afterwards, the values of the calculated list are checked if they are in the density range of 1273 kg/m^3 $\geq \rho \geq$ 1307 kg/m^3 and viscosity range of 0.49 mPas $\geq \eta \geq$ 1.65 mPas. If so, an optimization is carried out for each of the operation points shown in Table 3.2, in order to find the temperature and concentration of the model electrolyte to match the density and viscosity of potassium hydroxide at each operation point. For the optimization, the Python package *scipy.optimize* (version 1.9.3) is used [135] with the *least-squares* problem formulation. The optimization problem formulation can be seen in Equation 3.12. The optimization problem consists of the reformulated Equations 3.9 and 3.8 with Equation 3.11 and 3.10 to define the water viscosity ($\eta_{w,j}$) and water density ($\rho_{w,j}$) for each of the possible 128 electrolytes (i) for every relevant temperature (j) which are the

Table 3.2: Simulated Operation Points for Particle Image Velocimetry Measurements.

Temperature Electrolysis [° C]	**KOH Concentration** [wt.-%]	**Density** [kg/m^3]	**Viscosity** [mPas]	**Pressure** [bar]
50	32.5	1306.61	1.64	1
50	30.4	1282.59	1.518	1
60	32.5	1300.33	1.37	1
60	31.3	1286.83	1.315	1
70	32.5	1293.24	1.17	1
70	32.1	1288.74	1.151	1
80	32.5	1285.39	1.01	1
80	32.7	1288.6	1.017	1
90	34.8	1286.68	0.907	1
100	36.0	1283.21	0.815	20
110	37.2	1300.16	0.784	20
120	38.3	1299.61	0.724	20
130	39.3	1298	0.673	20
140	40.3	1295.33	0.628	20
150	41.2	1291.6	0.589	20
160	42.0	1286.83	0.554	20
170	42.8	1281.04	0.528	20
180	43.4	1274.26	0.495	20

temperatures shown in Table 3.2.

$$
\begin{aligned}
\min_{\vartheta_i, c_i} \quad & \mathbf{f}(\rho_{KOH,j}, \eta_{KOH,j}) \\
\textbf{s.t.} \quad & \mathbf{f}(\rho_{KOH,j}, \eta_{KOH,j}) = \begin{bmatrix} 10^{\log_{10}(\rho_{w,j})+(b_{0,i}-b_{1,i}\cdot\vartheta_i+b_{2,i}\cdot\vartheta_i^2)\cdot c_i} - \rho_{KOH,j} \\ 10^{\log_{10}(\eta_{w,j})+(d_{0,i}+d_{1,i}\cdot\vartheta_i+d_{2,i}\cdot\vartheta_i^2)\cdot c_i} - \eta_{KOH,j} \end{bmatrix} = \mathbf{0} \\
& \rho_{KOH,j} \text{ see Equation 4.5 with } c_{opt} \text{ from Equation 4.4} \\
& \eta_{KOH,j} \text{ see Equation 4.6 with } c_{opt} \text{ from Equation 4.4} \\
& \rho_{w,i} = 1000 - 0.062 \cdot \vartheta_i - 0.0355 \cdot \vartheta_i^2 \\
& \eta_{w,i} = \eta_0 \cdot \exp a + \tfrac{E-b}{R\cdot(T_i-\theta-d)} \\
& i \in [\mathrm{Al(NO_3)_3}, \mathrm{Al_2(SO_4)_3}, ..., \mathrm{Zn(NO_3)_2}, \mathrm{ZnSO_4}] \\
& j \in \vartheta_{KOH} = [50, 50, 60, 60, ..., 170, 180]
\end{aligned}
\tag{3.12}
$$

As an optimization algorithm, the default option, the Levenberg-Marquardt method, is used. The Levenberg-Marquardt is an optimization algorithm for unconstrained optimization and uses the Newton method with a trust-region framework. Trust region search algorithm defines a trusted search area around the iterate and, at the same time, chooses a step length and direction for the iteration. [136]

For the least squares algorithm, the default values implemented for the Python package are used except for the tolerance for determination by the change of the cost function, which is changed to ftol $= 1 \cdot 10^{-15}$, as well as the tolerance for determination by the change of the independent variables, which is also set to xtol $= 1 \cdot 10^{-15}$ [137]. The values set the tolerance as delta to the optimal value within the algorithm to accept a result as optimal or not. The default values were not small enough to solve the optimization problem in this specific case.

3.2.3 Selection of Gas for Particle Image Velocimetry Measurements

The produced gases in a water electrolysis cell are oxygen and hydrogen. Because of safety concerns here, the gases are exchanged, and nitrogen is used due to simplicity, availability, and economical reasons.

The amount of gas inside the cell is regulated through the inflowing gas volume flow. The needed gas volume flow for the regarding operation points can be seen in Table 3.3. The amount of gas is calculated by Equation 3.13. Equation 3.13 uses Equation 3.7 multiplied by the Faraday efficiency [138].

$$\dot{V}_{N_2,\vartheta_{PIV,j}} = \eta_F(i) \cdot \frac{i \cdot A \cdot V_m}{zF} \tag{3.13}$$

The gas volume flow of nitrogen $(\dot{V}_{N_2,\vartheta_{sim,k}})$ at the temperature k that simulates the electrolysis process at a certain operation point (j) results from the assumption that the gas volume of hydrogen respectively oxygen $(V_{H_2/O_2,\vartheta_j})$ needs to be equal to result in a similar two-phase flow behavior in the simulated electrolysis cell compared to the actual electrolysis cell two-phase flow behavior.

Using nitrogen instead of oxygen and hydrogen in a simulated half-cell changes certain things of the flow behavior and properties within the cell. What kind of changes need to be considered is discussed in this sub-section.

The properties that need to be discussed because they have an influence on the two-phase flow behavior are the following: solubility, size of molecules, crossover, and diffusion.

The electrolyte solution in an electrolysis cell is assumed to be saturated with gas at

Table 3.3: Gas Amount of Nitrogen as a Replacement of Oxygen and Hydrogen for Particle Image Velocimetry Measurements.

Current Density [A/cm^2]	**N_2 as O_2 replacement** [ml/min]	**N_2 as H_2 replacement** [ml/min]
0.01	0.61	1.23
0.05	3.07	6.15
0.1	6.15	12.29
0.2	12.29	24.59
0.4	24.59	49.17
0.6	36.88	73.76
0.8	49.17	98.35
1.0	61.47	122.94

steady-state operation. Hanafizadeh et al. [139] concluded from their investigations that changes in the gas density have only little influence on the detachment of gas bubbles. They found out that the detachment frequency of gas bubbles is mainly dependent on the surface tension. According to Pallas et al. [140], for pure water, the interfacial tension in the presence of nitrogen, air, and helium was indistinguishable. This leads to the assumption that the interfacial tension for the three used gases here (Nitrogen, Hydrogen, and Oxygen) is also similar in aqueous solutions.

In the investigation published by Hanafizadeh et al. [139] gas formation, detachment, and growth are investigated with different gases injected by a needle. The authors concluded that gases with lower densities result in larger bubbles (volume-wise). In addition, the gas density and surface tension were investigated separately while all other conditions were kept constant. A higher gas density results in a faster detachment and larger gas bubble volume due to buoyancy forces. With increasing surface tension, the gas bubble volume increases. [139]

In order to establish a two-phase flow behavior similar to an alkaline electrolysis half-cell with the same flowfield geometry, the gas is not directly injected. The nitrogen gas is introduced to the cell through a gas flowfield, which is a pocket of the size of the active cell area but with ribs for mechanical stability to support a sintered metal plate. On top of the sintered metal plate is a layer of porous PTFE foil to have a hydrophobic layer, which prevents the electrolyte solution from streaming into the gas flowfield. The sintered metal plate and the porous PTFE sheet are used as porous media for the uniform distribution of nitrogen gas into the half-cell. In order to control the volume and size of the gas bubbles, an additional layer on top of the porous PTFE is placed in the half-cell. The layer is a sheet of nickel foam of the same material that is used as electrodes in the alkaline electrolysis cell that is simulated here. The idea is that the gas bubbles are injected through the sintered metal plate and porous PTFE layer and coalesce on their way through the nickel foam as they do in the electrolysis cell. The gas bubbles can create a similar size distribution in the simulated electrolysis cell because of the nickel foam, and the effects described by Hanafizadeh et al. [139] are assumed to be disabled in this case as long as the introduced gas volume is the same as the hydrogen and oxygen amount at the particular operation point.

3.2.4 Selection of Particle Image Velocimetry Particles

Since particle image velocimetry measurements are a passive method of flow velocity measurement methods, the particles that are used to determine the flow velocity are a vital part of successful measurements. Samimy et al. [141] state that for liquids, the following condition for the Stokes number has to be applied; $Sto = t_P/t_F < 0.1$ [141]. The Stokes number describes the relation of particle residence time t_P and fluid residence time t_F. In Equation 3.14 to 3.16, the maximum Stokes number for the planned measurements is calculated. The relevant, necessary values can be seen in Table 3.4. The most critical operation is at 50 °C and a potassium hydroxide solution of 32.5 wt.-%, because the resulting Stokes number is highest at these conditions.

$$t_P = d_P^2 \frac{\rho_P}{18\eta} = 2.2039 \cdot 10^{-5}\ [s] \tag{3.14}$$

The residence time of the particles (t_P) results from the equilibrium of velocity of particles with the fluid velocity and consists of the particle density (ρ_P), the fluid viscosity η and the particle diameter (d_P).

$$t_F = \frac{L}{u_F} = 2.03 \cdot 10^{-3}\ [s] \tag{3.15}$$

The residence time (t_F) results from the flow velocity u_F and the characteristic length of a rectangular channel (L).

$$Sto = \frac{t_P}{t_F} = \frac{2.2039 \cdot 10^{-5}\ [s]}{2.03 \cdot 10^{-3}\ [s]} = 0.012 < 0.1 \tag{3.16}$$

The ratio results in a Stokes number, which fulfils the condition of Samimy et al. [141]. The particles with a size of 20 μm made from polyamide with a RhodaminB coating

Table 3.4: Values for Particle Choice for Particle Image Velocimetry Measurements.

Property	**Description**	**Value**	**Unit**
ϑ	System Temperature	50	°C
c_{KOH}	KOH Concentration	32.5	wt.-%
ρ_P	Density Particle	1000	kg/m^3
η_{min}	Minimum Viscosity Liquid	0.9436	mPas
d_P	Diameter Particle	$20 \cdot 10^{-6}$	m
L	Characteristic Length Rectangular Channel	0.003	m
x	Channel Edge Length	1.5	mm
V_{max}	Maximum Volume Flow	100	ml/min
u_F	Liquid Velocity	0.741	m/s

manufactured by Applied Microspheres B.V.[9] have shown good applicability in pre-tests regarding flow behavior, visibility and plausibility at evaluation (which is described in detail in the following sub-section (see Section 3.2.5)). The used particles have an excitation wavelength of 530 nm (visible green light) and an emission wavelength of 590 nm (visible red light).

3.2.5 Evaluation of Particle Image Velocimetry Measurements

The evaluation of the images of the modeled alkaline electrolysis cell using multiphase particle image velocimetry is done separately for the liquid and the gas phase, as explained below. For each phase, all 2000 images (equivalent to 1 second) are used.

Liquid Phase Evaluation

For the evaluation of the images to determine the liquid phase velocity, the open source package *openpiv* is used [142] which is available for Matlab, C++, and Python, in this case it is implemented in Python (version 0.23.8).

The *openpiv* community provides example code for the evaluation of particle image velocimetry images. Here, the code is adapted to the here needed functions. The

---

[9] https://www.applied-microspheres.com/

sub-packages *preprocess*, *tools*, *validation*, *pyprocess*, *filters* and *scaling* are used. An example of what the packages are used for can be seen in Table 3.5.

Table 3.5: Examples of the Functionality of the Relevant *Openpiv* Sub-packages.

sub-package	**functionality**
preprocess	- Array normalization to [0,1] - subtracting image background - intensity capping
tools	- transforming coordinates to physical based coordinates - reading image file as array
validation	- checks velocity vectors for spatial consistency - deletes inconsistent vectors
pyprocess	- cross-correlation algorithm (see Section 2.4)
filters	- filters outlier - replaces outliers with iterative inpainting algorithm - smooths the vector data
scaling	- applies uniform scaling to coordinates and velocity vectors

Evaluation of the Gas Amount inside the Cell

The determination of the gas amount inside the transparent simulated electrolysis half cell is done by evaluating binarized images where the gas bubbles have black pixel values (0 value) and the surrounding has white pixel values (255 value). Before binarization, image processing is done. As first step, the background of the images is subtracted. A picture of the background of the glass cell is taken without gas bubbles inside the channel. Afterwards, the images are filtered, as described in more detail below. With the binarized images, the cross-section of the gas bubbles can be calculated, and the gas distribution in percentage per channel is compared to the gas distribution in the alkaline electrolysis cell images.

The image processing of the particle image velocimetry images of the 14 channels of the transparent quartz glass cell is done using python packages *numpy* [131] (version 1.23.3), for the processing of the image data in form of arrays, and *opencv* [132] (version 4.6.0) for the image processing and visualization. The images are read using *opencv* as grayscale picture and normalized to pixel values between 0 and 255. The background image is read in the same way as the images. All images are rotated, if necessary (in case the cell is not 100% vertical), to align the channel vertically in the images. Then, the background image is subtracted from all images using *opencv*. Afterwards, the resulting image is binarized, all grayscale values greater than zero (black pixel) are set to 255 (white pixel). In preparation for noise reduction, the image is masked in order to exclude all pixels that do not belong to the flow channel. To reduce the noise *opencv* filter *medianBlur* is used. The *medianBlur* filter is a median filter that is used to reduce noise. The reduction is done using a square of a size of k x k pixel with k being an odd integer. For the k x k frame, the median is calculated, and the central pixel is replaced by the median value. The median blur is processed over all pixels of the image. An example of a masked and filtered image can be seen in Figure 3.10.

Figure 3.10: Result of the Python Image Processing for Evaluating the Gas Amount of the Gas Bubble Particle Image Velocimetry Images.

After image processing, the gas amount can be evaluated by evaluating the total amount of black pixels. This is done for the total gas amount in every image and for every channel in every image. Then, the gas amount is averaged over 2000 images per operation point, and a total gas amount per channel is determined.

Gas Bubble Velocity

The gas bubble velocity of the gas bubbles measured by particle image velocimetry is determined by the *ImageJ* plug-in *Trackmate* [126] (version 7.9.2). The used detector is a thresholding detector, which considers pixel values larger than a chosen threshold, and the tracker is the LAP tracker, which is already described in Section 3.1.3. Gas bubbles detected with the thresholding detector can be seen in Figure 3.11.

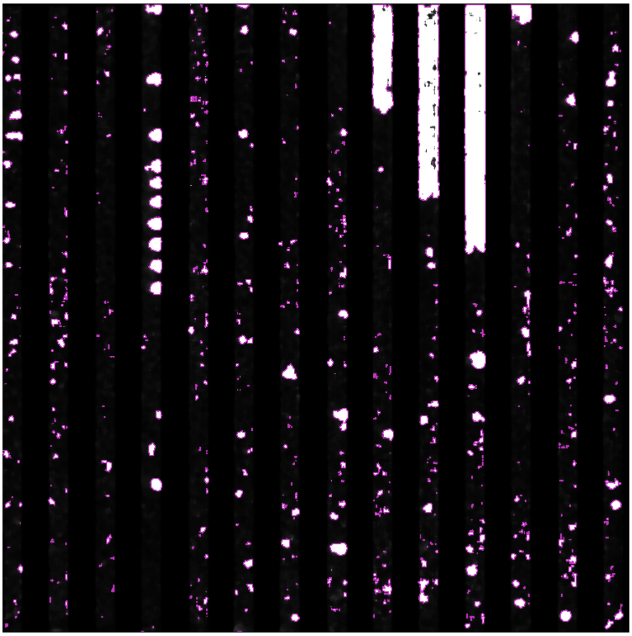

Figure 3.11: Bubble Tracking of the Particle Image Velocimetry Images using *Trackmate*, Detection using the Thresholding Detector (Detected Gas Bubbles Circled in Pink).

In order to use *Trackmate*, the images need to be preprocessed and binarized. The algorithm to do so is the same procedure as described above when describing the evaluation of the gas amount inside the cell during particle image velocimetry.

3.3 Liquid Characterization Methods

For comparison of liquid flow behavior of electrolytes, a few physical properties are important depending on what the focus of comparison lies on. The comparison of liquid flows can be made, for example, by the theory of similarity using dimensionless numbers. In this examination, a similar approach to the theory of similarity is used. Here, the focus lies on simulating an alkaline electrolysis cell flow behavior by exchanging the nickel cell with a transparent cell material and additionally the gas and liquid electrolyte are exchanged for liquids that can be handled safer and operated at lower temperatures. The consequences of exchanging material and fluids for the flow behavior are that the fluid-solid material interaction is changing, as well as the liquid-solid interaction. Interaction means that the contact angle between gas, liquid, and solid phases is changing because the surface energy is dependent on the material, and also, the contact angle of the liquid-solid phase interface is material dependent. Two other physical properties that play an important role in the behavior of fluids are density and viscosity. Important for flow visualization in a transparent cell through particle image velocimetry measurements is the transmissivity for the light of the used wavelength of the used LED and the emitted wavelength of the particles.

3.3.1 UV/Vis Measurement

UV/Vis measurements are either done to investigate solids or liquids. Here, the focus lies on the investigation of liquids for their transmission properties. The liquid is measured with a defined wavelength spectra. The electromagnetic radiation can be described by Equation 3.17.

$$c = \nu \cdot \lambda \tag{3.17}$$

The speed of light (c), in this case, equals the product of frequency (ν) and wavelength (λ). When the light is directed at the liquid, the radiation, depending on the frequency, interacts with an electron of a molecule of the liquid. The electron is rising to an orbital with higher energy, and through emitting radiation, the molecule is able to reach the ground state again.

The incoming intensity of light is partially adsorbed, partially reflected, and partially transmitted. The transmitted light is detected by a detector. Lambert's Law is valid for monochromatic light in diluted solutions (see Equation 3.18).

$$log\frac{I_T}{I_0} = \epsilon_{mol} \cdot c \cdot d \tag{3.18}$$

Equation 3.18 describes that the logarithmic fraction of outgoing (I_T) and incoming intensity (I_0) of light equals the product of molar absorption coefficient ((ϵ_{mol}), concentration of solution (c) and thickness of liquid layer (d). [143]

The used device for the UV/VIS measurements is a *Lambda 950* spectrophotometer

manufactured by Perkin Elmer Inc.[12]. The used wavelength spectrum is between 300 nm and 800 nm for which the device is using a photomultiplier for detection, starting at 800 nm, stepwise descending towards 300 nm. [144]
During the measurements, the liquids were measured inside cuvettes, and reference measurements without cuvette and with a pure water containing cuvette are made as reference measurements. Through these measurements, the transmission of the liquids at specific wavelengths can be obtained.

3.3.2 Density Measurement

The conducted density measurements are done with the *DMA35* density meter manufactured by Anton Paar GmbH[13]. The density meter uses the oscillating U-tube method. For this measurement method, the sample liquid is introduced into a borosilicate glass pipe. The pipe is vibrating at the characteristic frequency, which depends on the sample density. The sample temperature is measured additionally with a temperature sensor inside the measurement device since the density is temperature dependent, as explained in Section 2.2.5. [145–147]

3.3.3 Viscosity Measurement

For the viscosity measurements a viscosimeter manufactured by Anton Paar GmbH[13] is used that works with the rotational principle. The viscosity value that is measured is the dynamic viscosity. Two different measurement principles exist for rotational viscosimeters; The Searle principle uses a so-called measuring bob, which is rotated inside a measurement cup filled with a liquid. The second measurement principle is the Couette principle. For this principle, the cup is rotated, and the measurement bob is standing still. In this case, the *MCR302* device is used, which is working with the Searle principle. The measurements are conducted using a measurement bob, which is driven by a servo motor and a high-resolution digital encoder. The encoder records the rotational speed, which induces a motor torque through the resistance force of the liquid against the rotation. With the motor torque, the dynamic viscosity is determined. The measurement bob is available in different shapes. In this case, a cone-plate measuring

---

[12] https://www.perkinelmer.com/de/

[13] https://www.anton-paar.com/

system *CP50* is used supplied by Anton Paar GmbH[13]. The cone plate has a defined angle of 1 ° which is standardized in ISO 3219 [148]. The diameter of the used cone plate is 50 mm. The advantage of measuring with a cone plate is that the angle results in a constant shear rate over the entire gap. Since the dynamic viscosity for Newtonian fluids is constant over the shear rate, the dynamic viscosity can be determined directly. [147, 149, p.242ff.] The temperature during the viscosity measurements is controlled by the peltier system *H-PTD 200* supplied by Anton Paar GmbH[13], to ensure a homogeneous temperature throughout the measurement.

Validation of Viscosimeter Precision with Calibration Oil

To identify potential measurement errors of the viscosimeter, the viscosity of a calibration oil, which has a similar viscosity range to potassium hydroxide, is measured first. The calibration oil is the *1BW* by ZMK & ANALYTIK GmbH[14]. The dynamic viscosity of the calibration oil at different temperatures is known and compared to the measured values. The values of the dynamic viscosity of the calibration oil given by the supplier can be seen in Table 3.6.

Table 3.6: Dynamic Viscosity of Calibration Oil *1BW* according to ZMK & ANALYTIK.

Temperature [° C]	**Dynamic Viscosity** [mPas]	**Measurement Uncertainty** [μPas]
20	0.97	± 1.843
23	0.92	± 1.748
25	0.90	± 1.710
30	0.84	± 1.596
40	0.73	± 1.387

The manufacturer states a measurement uncertainty of 0.19% for the oil [150]. In the right column, the measurement uncertainty of the dynamic viscosity is listed (0.19% of the dynamic viscosity value).

To measure as accurately as possible, the measurements for the calibration oil and the electrolyte solutions are done with ten repeats each. The measurement error is calculated using Equation 3.19 to determine the maximum relative measurement error ($\Delta_{max,j}$) and Equation 3.20 to determine the minimum relative measurement error ($\Delta_{min,j}$). The indices i and j refer to the number of measurements and the regarding

---

[14] https://www.zmk-wolfen.de/

temperature at which the measurement is carried out. The index m in Equation 3.19 and Equation 3.20 stands for "measurement" and is used for all measured values.

$$\Delta_{max,j} = \begin{cases} \frac{\max(\eta_{m,ij})-\eta_{m,mean,j}}{\eta_{m,mean,j}} \cdot 100\%, & \max(\eta_{m,ij}) > \eta_{ref.,j} \cdot 1.0019 \\ \\ \frac{\eta_{ref.,j}\cdot 1.0019-\eta_{m,mean,j}}{\eta_{m,mean,j}} \cdot 100\%, & \text{else} \end{cases} \tag{3.19}$$

The maximum relative measurement error ($\Delta_{max,j}$) is either calculated by the difference of maximum viscosity value of the ten repeating measurements for the regarding temperature ($\max(\eta_{m,ij})$) and the mean viscosity for the regarding temperature ($\eta_{m,mean,j}$) divided by the mean viscosity ($\eta_{m,mean,j}$). Or in case the uncertainty range of the reference viscosity value $1.0019 \cdot \eta_{ref,j}$ is greater than the maximum measurement error $\max(\eta_{m,ij})$, the difference in the numerator is changed to the difference of reference viscosity value added by supplier uncertainty value $1.0019 \cdot \eta_{ref,j}$ subtracted by the mean viscosity at the regarding temperature ($\eta_{m,mean,j}$). In the reversed way, the minimum relative error is calculated ($\Delta_{min,j}$) (see Equation 3.20).

$$\Delta_{min,j} = \begin{cases} \frac{\eta_{m,mean,j}-\min(\eta_{m,ij})}{\eta_{m,mean,j}} \cdot 100\%, & \min(\eta_{m,ij}) < \eta_{ref.,j} \cdot 0.9981 \\ \\ \frac{\eta_{m,mean,j}-\eta_{ref.,j}\cdot 0.9981}{\eta_{m,mean,j}} \cdot 100\%, & \text{else} \end{cases} \tag{3.20}$$

Ewoldt et al. [151] discuss potential measurement errors during viscosity measurements with a rotational viscosimeter. Measuring the viscosity of Newtonian fluids does not result in a constant viscosity over the shear rate as it is supposed to be because of measurement errors. Especially at low shear rates, the so-called low-torque limit effect results in a non-constant viscosity. The low-torque limit effect describes the effect that the measurement results for dynamic viscosity might not be reliable at low shear rate values for liquids with a low viscosity. This means that at lower shear rates, it might occur that the needed torque for measuring low viscosities is below the minimum torque of the device. At higher shear rates, secondary flow effects result in measurement errors. The secondary flow is caused by high velocities and is a second flow that is superposed on the primary shear flow induced by sample inertia, which means the torque is increased and, therefore, the resulting viscosity is increasing as well. [151]

Amongst others, these two measurement effects are the reason why the shear rate range has to be chosen carefully for viscosity measurements with a rotational viscosimeter.

In order to identify the shear rate range where the dynamic viscosity is constant over the shear rate, measurements with the calibration oil are conducted over wide shear rate ranges at 20 °C and 40 °C with ten repeating measurements each.

Validation of Calculated Dynamic Viscosity of Model Electrolyte Solutions

For the model electrolyte solution, the density and viscosity values, which are calculated by empirical equations taken from Zaytsev et al. [76, p.1724ff.], validating measurements are conducted for the calculated values. For the viscosity measurements, the viscosimeter described in this sub-section is used. For the density measurements, the density meter described in Section 3.3.2 is used. For each operation point, ten repeating measurements are done. The acceptance boundary for the ten measurement values is ± 5 %. If this limitation is exceeded, the concentration and/ or the temperature is changed in order to meet the density and viscosity of potassium hydroxide at the regarding operation point.
The relative error is calculated by Equation 3.21 for the maximum relative error and by Equation 3.22 for the minimum relative error

$$\Delta_{max,j} = \frac{\max\left(\eta/\rho_{m,i}\right) - \eta/\rho_{calc,j}}{\eta/\rho_{calc,j}} \cdot 100\% \tag{3.21}$$

$$\Delta_{min,j} = \frac{\eta/\rho_{calc,j} - \min\left(\eta/\rho_{m,i}\right)}{\eta/\rho_{calc,j}} \cdot 100\% \tag{3.22}$$

For the maximum relative error of every temperature/ concentration combination (j) the difference of the maximum value (i) of the ten density (or viscosity) $(\max\left(\eta/\rho_{m,i}\right))$ measurements and the calculated density (or viscosity) $(\eta/\rho_{calc,j})$ is divided by the calculated density (or viscosity) and multiplied by 100, for the relative error to be in percentage. For the minimum relative error $(\min\left(\eta/\rho_{m,i}\right))$, the same is done except the difference of the calculated density (or viscosity) and the minimum value (i) of the ten measurements is taken for the calculation. The mean density/ viscosity is the mean value of the ten measurements for the regarding operation property.

3.3.4 Contact Angle Measurements

The contact angle is an important measure of the interaction of fluids with a solid surface under a particular gaseous atmosphere. In this case, the three phases are hydrogen or oxygen with liquid potassium hydroxide in a flow channel out of Nickel (Alloy 201) during the electrolysis operation investigated by neutron radiography. The contact angle resulting from the electrolysis operation is compared to the contact angle of the three-phase boundary of nitrogen, alternative electrolyte solution, and quartz glass channel measured during particle image velocimetry measurements. The viscosity and density values of potassium hydroxide are used as criteria for the comparability of the liquid properties. In order to be able to evaluate the properties of the two-phase flow in interaction with the solid material of the flow channel, the contact angle is the property that is able to provide a qualitative comparison between the two-phase flow inside the alkaline electrolysis cell and the two-phase flow inside the glass cell, that simulates the electrolysis operation.

The method for the contact angle determination is explained in [152]. Yu et al. [152] used the sub-pixel polynomial fitting (SPPF) method to determine the contact angle of liquid water droplets breaking through a gas diffusion layer of a PEM fuel cell. The SPPF method originates from Chini et al. [153] and is a method that can determine the contact angle of symmetric and asymmetric droplets. In this case, the method is adapted to gas bubbles, but since the SPPF method is an image processing method that uses binarized images, it can be easily adapted to gas bubbles.

The images of the gas bubbles inside an alkaline electrolysis cell flow channel measured by neutron radiography are binarized by the image processing algorithms at Helmholtz Zentrum Berlin[7]. For the contact angle analysis 500 images (equals 10 seconds) per operation point measured by neutron radiography are evaluated.

For the images of the two-phase flow inside the glass cell measured by particle image velocimetry measurements, the images are also pre-processed. First, images with a higher light intensity are excluded. Afterwards, the background is subtracted, and the noise is reduced. The noise reduction is done by setting all pixels to black (0 value in the range of 0-255), which are next to another black pixel. In a second step, for all remaining white pixels (255 value in the range of 0-255), it is checked if the neighboring pixel was white before, if so, the pixel color is reversed again to white, if not, the pixel stays black. The procedure can be repeated to effectively reduce noise, in this case, the removal is done twice.

---

[7] https://www.helmholtz-berlin.de/forschung/oe/ce/materialforschung/index_en.html

Subsequently, the *scipy* [135] (version 1.9.3) Gaussian filter [154] was used with a standard deviation for the Gaussian kernel of 2.4. The Gaussian filter transforms an input by convolution with a Gaussian function. The image is binarized afterwards. For the contact angle analysis, 100 images (equal to 0.05 seconds) per operation point, measured during particle image velocimetry measurements, are evaluated.

For the binarized images of both measurement methods, the upper outline is calculated. The calculation of the outline structure of the gas bubble is the first step in the determination of the contact angle. The SPPF method uses three steps in total for the determination of the contact angle. At first, boundary points of the gas bubble are defined as 2D cross-section, which is done by determination of the outline structure of the gas bubble. The second step is to find the three-phase point where the gas bubble surrounded by electrolyte solution touches the surface of the flow channel. A first-order polynomial curve fitting is done from the contact point of the gas bubble with the wall. Lastly, a second-order polynomial is fitted to the curvature of the gas bubble through the contact point, and the contact angle is determined.[152]

3.3.5 Analysis of Published Measurement Data of Physical Properties of Potassium Hydroxide

Potassium hydroxide is the electrolyte solution commonly used in alkaline electrolysis and other applications. Several measurement results for properties like density, viscosity, and ionic conductivity are published, and a few empirical equations for these properties are developed in literature. Le Bideau et al. [75] wrote a review publication of published measurement data and the existing empirical equations of thermophysical properties essential for modeling alkaline water electrolysis cells of potassium hydroxide and sodium hydroxide.

For this examination, the analysis of Le Bideau et al. [75] is extended for the three properties density, dynamic viscosity, and ionic conductivity towards higher operation temperatures, and the empirical equations are updated.

Ionic Conductivity

In Table 3.7, the publications about ionic conductivity of potassium hydroxide containing measurement data and/ or empirical equations are listed. They are ordered by publication year, starting with the oldest.

The ionic conductivity is an important physical property for alkaline electrolysis since the ion conductivity is facilitated by the electrolyte solution. This type of electrolysis does not have an ion conducting membrane but a porous diaphragm without ion conducting properties. The ion conduction is done by the electrolyte solution in and outside of the pores. As in Section 2.2.5 described, the ionic conductivity of electrolyte solutions depends on the system temperature and the electrolyte concentration. In all publications listed in Table 3.7, the pressure influence on the ionic conductivity is neglected. Allebrod et al., Vogel, Klochko et al., Yushkevich et al., Lown et al. [17, 84, 85, 155, 156] all measured the ionic conductivity above the evaporation boundary, which is why they all conducted their measurements in an autoclave under pressurized conditions to remain in a liquid state of the electrolyte solution. All authors conducted their measurements with different and often custom-made electrode set-ups, as specified in Table 3.7. Darken et al. [157] developed an empirical equation only valid at 25 °C. See et al. [158] published an empirical equation, which was later extended by Gilliam et al. [74], because they updated the coefficients after evaluating more measurement data sets.

Allebrod et al. [17] investigated the influence of the ionic conductivity on electrolyte solution being immobilized in pores compared to aqueous electrolyte solution.

Table 3.7: Published Measurement Data and Empirical Equations for Ionic Conductivity of KOH.

Source	**Temperature** [°C]	**Concentration** [wt.-%]	**Measurement Method**	**Published Data**	**Empirical Equation**
[157]	25	0 - 42	flask cell with platinum electrode	✓	$\kappa_{KOH} =$ $272 - 121.64c^{1/2} + 141c(1 - 0.2274c^{1/2})$ c: molarity/mol/l
[85]	25 - 200	2 - 81	a.c. method	✓	
[84]	50 - 260	40 - 90	four electrode method	graphical data	
[155]	25 - 260	5 - 50	custom made apparatus with electrode	✓	
[156]	25 - 200	5 - 50	custom made cell with electrodes separated by diaphragm	✓	

Table 3.7: Published Measurement Data and Empirical Equations for Ionic Conductivity of KOH (continued).

Source	Temperature [°C]	Concentration [wt.-%]	Measurement Method	Published Data	Empirical Equation	
[158]	-15 - 100	15 - 45	YSI Model 35 Conductance Meter	✓	$\kappa_{KOH} =$	$0.279844803wt\% - 0.00924129482T$
						$-0.000149660371T^2$
						$-0.000905209551Twt\%$
						$+0.000114933252T^2wt\%^{0.1765}$
						$+0.0696648518\frac{T}{wt\%} - 28.9815658\frac{wt\%}{T}$
					T:	temperature/K,
					$wt\%$:	concentration/wt.-%
[74]	0 - 100	0 - 47	modified Jones conductivity cell	x	$\kappa_{KOH} =$	$-2.041c - 0.0028c^2 + 0.005332c\vartheta$
						$+207.2\frac{c}{\vartheta} + 0.001043c^3 - 0.0000003c^2\vartheta^2$
					ϑ:	temperature/°C,
					c:	molarity/mol/l

Table 3.7: Published Measurement Data and Empirical Equations for Ionic Conductivity of KOH (continued).

Source	**Temperature** [°C]	**Concentration** [wt.-%]	**Measurement Method**	**Published Data**	**Empirical Equation**
[17]	25 - 200	35 - 50	Van der Pauw technique	graphical data	$\kappa(35wt\%) = -2.15 \cdot 10^{-7}\vartheta^3 + 6.44 \cdot 10^{-5}\vartheta^2 + 0.007675\vartheta + 0.3299$ $\kappa(45wt\%) = -1.78 \cdot 10^{-7}\vartheta^3 + 7.04 \cdot 10^{-5}\vartheta^2 + 0.005973\vartheta + 0.2706$ $\kappa(55wt\%) = -3.3 \cdot 10^{-7}\vartheta^3 + 1.06 \cdot 10^{-4}\vartheta^2 + 0.005205\vartheta + 0.0283$ ϑ: temperature/°C, $wt\%$ concentration in wt.-%
[159]	18 - 80	0 - 42	not stated	✓	

Mass Density

The density of potassium hydroxide is probably the best investigated physical property of potassium hydroxide solution. As described is Section 2.2.5, the density of electrolyte solutions is dependent mainly on temperature and electrolyte concentration. The pressure dependence is mostly neglected, as it is also done in the published measurements on potassium hydroxide density listed in Table 3.8.

The method used in most measurements is measuring with a pycnometer. In most measurements, at temperatures higher than boiling temperature, alternative measurement methods are used. The empirical equations developed in literature are mostly of non-linear polynomial type, except the equation published by Gilliam et al. [74], which is of exponential type for the potassium hydroxide density multiplied with a temperature-dependent coefficient. Le Bideau et al. [75] developed the latest empirical equation for potassium hydroxide and uses a polynomial function. Gilliam et al. [74] did not conduct measurements on their own but used the measurement data obtained by Zaytsev et al., Akerlof et al. [76, 160] and Klochko et al. [85]. The measurement data sets used by Le Bideau et al. [75] to update the coefficients are not stated.

Table 3.8: Published Measurement Data and Empirical Equations for Density of Potassium Hydroxide.

Source	**Temperature** [°C]	**Concentration** [wt.-%]	**Measurement Method**	**Published Data**	**Empirical Equation**
[78]	20 - 40	5 - 29	Pycnometer	✓	
[160]	0 - 70	0 - 50	Pycnometer	✓	
[157]	25	0 - 42	no measurements	x	$\rho_{KOH} = 0.997 + 0.05120c - 0.00365c^{3/2}$ c: molarity/mol/l
[85]	0 - 125	10 - 60	Pycnometer	✓	
[161]	0 - 400	0 - 99.5	custom measurement method	✓	
[162]	60 - 161	6 - 77	hydrostatic weighing method of Kohlrausch	✓	
[84]	140 - 185	40 - 75	buoyancy method	graphical data	
[163]	-60 - 60	18 - 46	not stated	✓	$\rho_{KOH} = \rho_w + k(\vartheta)wt\% + 2.91 \cdot 10^{-5}wt\%^2$ ρ_w: water density/g/cm^3, ϑ: temperature/°C, $wt\%$: concentration/wt.-%

Table 3.8: Published Measurement Data and Empirical Equations for Density of Potassium Hydroxide (continued).

Source	**Temperature** [°C]	**Concentration** [wt.-%]	**Measurement Method**	**Published Data**	**Empirical Equation**
[77]	20 - 180	0 - 60	archimedic principle	graphical data	
[164]	0 - 100	5 - 60	not stated	✓	$\rho_{KOH} = \rho_w + 54.59wt\% - 0.1156wt\%\vartheta$ $+1.009 \cdot 10^{-3}wt\%\vartheta^2 - 4.383wt\%^{3/2}$ $+2.34 \cdot 10^{-2}wt\%^{3/2}\vartheta - 1.86 \cdot 10^{-4}$ $\cdot wt\%^{3/2}\vartheta^2$ ρ_w: water density/kg/m^3, ϑ: temperature/°C, $wt\%$: concentration/mol/m^3
[76]	0 - 90 (200*)	2 - 50	Pycnometer	✓	$\rho_{KOH} = 10^{(\log_{10}\rho_w + 3664.2 \cdot 10^{-4} - 548.8 \cdot 10^{-6} \cdot \vartheta)} \cdot wt\%$ $\rho_w = 1000 - 0.062\vartheta - 0.00355\vartheta^2$ ϑ: temperature/°C, $wt\%$: concentration/wt.-%, ρ_w: water viscosity/Pas

---

*The values from 90 °C to 200 °C are extrapolated

Table 3.8: Published Measurement Data and Empirical Equations for Density of Potassium Hydroxide (continued).

Source	Temperature [°C]	Concentration [wt.-%]	Measurement Method	Published Data	Empirical Equation
[74]	0 - 200	not specified	no measurements	✓	$\rho_{KOH} = A(\vartheta) \cdot \exp(0.086wt\%)$ $\rho_{KOH} = k_1(\vartheta)c^2 + k_2(\vartheta)c + k_3(\vartheta)$ ϑ: temperature/°C c: molarity/mol/l $wt\%$: concentration/wt.-% A, k_i: coefficients (complete list see [74])
[165]	15 - 60	2 - 15	not stated	✓	$\rho_{KOH} = (1.0198 - 4 \cdot 10^{-4}\vartheta + 0.0435c) \cdot 10^3$ ϑ: temperature/°C, c: molarity/mol/l
[75]	0 - 100	0 - 50	no measurements	✓	$\rho_{KOH} = 3.899 \cdot 10^{-1} + 1.914 \cdot 10^{-1}wt$ $+9.993 \cdot 10^{-3}\vartheta + 2.208 \cdot 10^{-1}\vartheta wt$ ϑ temperature/°C wt: concentration/wt-fraction
[166]	20 - 70	10 - 40	Aerometer and precision Pt-100	✓	
[159]	-7 - 82	0 - 50	not stated	✓	

Dynamic Viscosity

The viscosity of potassium hydroxide is mostly measured at temperatures below the boiling temperature for a wide concentration range up to mostly at least 50 wt.-%. The viscosity measurements and empirical equations in literature can be seen in Table 3.9. Mostly, capillary methods like an Ostwald or Ubbleohde viscosimeter are used as measurement devices. At higher temperatures above 100 °C of the electrolyte solution only Ripoche et al. [77],Vogel [84] and Klochko et al. [85] conducted measurements for the dynamic viscosity. Klochko et al. [85] obtained the results in a pressurized atmosphere. Vogel [84] and Ripoche et al. [77] obtained their results for each concentration along the specific evaporation boundary line. The developed empirical equation published by Zaytsev et al. [76] is valid between 0 °C and 100 °C and uses the Ezrokhi method. This method describes the logarithmic electrolyte dynamic viscosity as a sum of the logarithmic water dynamic viscosity and a polynomial that considers the influence of the electrolyte concentration on the dynamic viscosity. The empirical equation that is stated to calculate the dynamic viscosity of water limits the empirical equation to the mentioned temperature range. Guo et al. [165] describes the dynamic viscosity dependent on temperature and concentration of potassium hydroxide through an exponential function with a multivariate polynomial as exponent, which considers temperature and concentration as variables. The equation is valid in the temperature range between 15 °C and 60 °C. Kuznetsov et al. [166] uses a multivariate polynomial with a grade of 7 and temperature and concentration as variables to describe the dynamic viscosity, which is valid for a temperature range of 20 °C to 70 °C.

Table 3.9: Published Measurement Data and Empirical Equations for Dynamic Viscosity of Potassium Hydroxide.

Source	**Temperature** [°C]	**Concentration** [wt.-%]	**Measurement Method**	**Published Data**	**Empirical Equation**
[167]	20	1.43 - 28.38	adapted Ostwald viscosimeter	✓	
[78]	20 - 40	5 - 29	Ostwald-Fenske viscosimeter	✓	
[85]	0 - 125	10 - 60	Ostwald viscosimeter	✓	
[84]	10 - 240	0 - 70	rolling ball viscosimeter	graphical data	
[163]	-60 - 60	18 - 46	not stated	✓	
[77]	20 - 150	0 - 52	oscillating sphere method	graphical data	
[76]	0 - 90 (200*)	2 - 50	method of capillary flow/ Hepler viscosimeter	✓	$\eta_{KOH} = 10^{(\log_{10}\eta_w + 112.7\cdot 10^{-2} + 20.6\cdot 10^{-4}\cdot\vartheta)} \cdot wt\%$ $\eta_w =$ $0.59849 \cdot (43.252 + \vartheta)^{-1.5423}$ ϑ: temperature/°C, $wt\%$: concentration/wt.-%, η_w: water viscosity/Pas

---

*The values from 90 °C to 200 °C are extrapolated

Table 3.9: Published Measurement Data and Empirical Equations for Dynamic Viscosity of Potassium Hydroxide (continued).

Source	Temperature [°C]	Concentration [wt.-%]	Measurement Method	Published Data	Empirical Equation
[165]	15 - 60	2 - 15	Ubbleode capillary viscosimeter	✓	$\eta_{KOH} = \exp\left(0.43 - 0.0251\vartheta + 10^{-4}\vartheta^2 + 0.1307c\right)$ ϑ: temperature/°C, c: molarity/mol/l
[166]	20 - 70	10 - 40	SV-10 viscosimeter	✓	$\eta_{KOH} = 32.8074\vartheta - 292.147\vartheta^2 + 941.402\vartheta^3$ $+(-2.12909\vartheta + 72.4232\vartheta^2$ $-646948\vartheta^3)wt\% + (0.797615\vartheta$ $+0.715697\vartheta^2 - 62.1809\vartheta^3)wt\%^2$ $+(-0.0088673\vartheta - 0.00483085\vartheta^2$ $+2.408\vartheta^3)wt\%^3 + (0.000209089\vartheta$ $-0.00355252\vartheta^2 + 0.00897189\vartheta^3)wt\%^4$ ϑ: temperature/°C, $wt\%$: concentration/wt.-%
[159]	4 - 71	0 - 50	not stated	graphical data	

Mathematical Function Development

For all three physical properties, the literature measurement data was evaluated, and as base functions, already developed empirical equations from literature are used. The equation with the smallest error compared to all available data points is taken as the base function to optimize coefficients to calculate the mentioned physical property.
The published empirical equations used as base functions are optimized in their coefficients with measurement data points as input data. The coefficients are obtained through nonlinear unconstrained optimization using the Levenberg-Marquardt method and python *scipy* package [135] (version 1.9.3) and least squares algorithm from subpackage *optimize* [168]. The general form of the optimization problem can be seen in Equation 3.23.

$$\begin{aligned} \min_{x_i} \quad & \mathbf{f}(\vartheta, c) \\ \mathbf{s.t.} \quad & i \in \mathbb{N}_0 \end{aligned} \tag{3.23}$$

The optimization problem (Equation 3.23) is a function that is dependent on temperature and concentration of potassium hydroxide and has a number of i coefficients that are optimized to fit the input measurement data points best.
Since the ionic conductivity has a convex shape and has, therefore, not only an optimal plane as a function dependent on the concentration and temperature but in addition has a one-dimensional function for the optimal concentration for each specific temperature. To determine the function that runs along the maximum path, again, the python package *scipy* [135] (version 1.9.3) was used with the subpackage *optimize* [137]. Within the *optimize* package, a minimization algorithm, in this case using the Nelder-Mead method [169] that applies a simplex search algorithm and is a direct search method for the function minimum, is used. The fundamental optimization problem to find the optimum ionic conductivity dependent on temperature is formulated as shown in Equation 3.24.

$$\begin{aligned} \min_{c_j} \quad & \mathbf{f}(\vartheta_j, x) \\ \mathbf{s.t.} \quad & g(\vartheta) = c_{opt} \\ & j \in \mathbb{R}_0 \end{aligned} \tag{3.24}$$

The empirical function for the optimum ionic conductivity is minimized with temperature data points and the resulting optimized coefficients from Equation 3.23 as input. The optimization results in discrete concentration values for every input temperature value. From the discrete values, a polynomial regression is fitted to the data points, which results in function g. The function g gets temperature as an input and results in the optimal ionic conductivity for a given temperature.

4 Results

In this section, the results of the in Section 3 described measurements are shown, discussed, and, where it is reasonable, compared. In the first section (Section 4.1), the results of the analysis of the properties ionic conductivity, density, and viscosity of potassium hydroxide are shown. The deviation between the different measurement data sets against each other and the deviation of the data to the resulting empirical equations is evaluated. Section 4.2 deals with the results of finding model electrolyte solutions for potassium hydroxide in order to use during particle image velocimetry measurements. The possible electrolytes are listed, and suitable electrolyte solutions are chosen, considering operation temperature for the replacement of potassium hydroxide, availability, price, manageability, and safety concerns. The chosen electrolyte solutions are tested beforehand to ensure their suitability for the measurements.

In Section 4.3, the results of the electrochemical measurements and the gas bubble behavior inside the cell are shown, as well as the relation between electrochemical effects on gas bubble behavior is discussed. In the following section (Section 4.4), the investigation of the gas bubble behavior in the transparent cell, used during particle image velocimetry measurements, is shown, and the grade of comparability with the alkaline electrolysis cell with the same geometry of the flowfield, used for neutron radiography measurements, is discussed. Furthermore, the results of the liquid phase of the two-phase flow are evaluated.

4.1 Characterization of Potassium Hydroxide Properties

In the following sub-section, the literature review and analysis of the, for this examination relevant, properties of potassium hydroxide are shown and discussed. An empirical equation is developed for each of the properties, ionic conductivity, density, and dynamic viscosity. In order to do so, coefficients of suitable, already existing empirical equations are optimized. The optimization is done as described in Section 3.3.5. The, for the optimization used, measurement values are discussed regarding deviations amongst each other, amongst different authors, and the deviation to the resulting empirical equations. The error analysis is done through the calculation of the relative error using Equation 4.1.

$$\Delta = \frac{x_{data} - x_{correlation}}{x_{data}} \cdot 100\% \tag{4.1}$$

The relative error is determined through the deviation of the published measurement data (x_{data}) to the value calculated by the empirical equation ($x_{correlation}$) divided by the measurement value.

The results presented in this chapter for the mass density, the dynamic viscosity and the ionic conductivity have been published in the *Journal of Chemical & Engineering Data* under the title "Critical Analysis of Published Physical Property Data for Aqueous Potassium Hydroxide. Collation into Detailed Models for Alkaline Electrolysis" [170].

4.1.1 Ionic Conductivity

The ionic conductivity increases with temperature and has an optimal path depending on the potassium hydroxide concentration. In order to describe this behavior, the empirical equation for the ionic conductivity developed by Gilliam et al. [74] is used. The equation is a nonlinear polynomial and is shown by Equation 4.2.

$$\kappa = a_0 c + a_1 c^2 + a_2 cT + a_3 \frac{c}{T} + a_4 c^3 + a_5 c^2 T^2 \tag{4.2}$$

This equation is used for temperatures between 0 °C and 80 °C with the coefficients that Gilliam et al. [74] published because they fit best for this temperature range. The empirical equation in this temperature range is valid for a concentration range between 0 wt.-% and 45 wt.-%. The concentration in this range is inserted in molarity (m) and the temperature (T) in Kelvin. The unit of the resulting ionic conductivity is S/cm. The conversion of concentration from molarity to wt.-% is done by Equation 4.3.

$$wt.-\% = \frac{m \cdot 100\, M}{\rho} \tag{4.3}$$

Here, the molarity (m) is multiplied by the molar mass (M), divided by the density (ρ), and multiplied by 100 to convert the weight fraction to weight percent. For temperatures above 80 °C up to 200°C the coefficients of Equation 4.2 are optimized with the published measurement data sets (cf. Table 3.7). For both temperature ranges, the coefficients can be seen in Table 4.1.

Table 4.1: Optimized Coefficients for the Calculation of the Ionic Conductivity through Equation 4.2.

	$0\ ^{\circ}\mathrm{C} \leq \vartheta \leq 80\ ^{\circ}\mathrm{C}$ 0 wt.-%≤ c ≤ 45 wt.-% c: m	$80\ ^{\circ}\mathrm{C} < \vartheta \leq 200\ ^{\circ}\mathrm{C}$ 0 wt.-%≤ c ≤ 60 wt.-% c: wt.-%
a_0	-2.041	$2.2204 \cdot 10^{-3}$
a_1	-0.0028	$-1.3077 \cdot 10^{-3}$
a_2	0.005332	$3.3647 \cdot 10^{-4}$
a_3	207.2	-10.7021
a_4	0.001043	$7.0101 \cdot 10^{-6}$
a_5	$-3 \cdot 10^{-7}$	$-3.2033 \cdot 10^{-9}$

All data sets are used for the optimization as input data except the data points published by Darken et al. [157] because they do not seem to match all other measurement points. The deviation of measurement points amongst each other will be discussed later in this sub-section in more detail.

The course of the functions for the two different temperature and concentration ranges can be seen in Figure 4.1. The lower temperature range up to 80°C can be seen in blue, and the second temperature range is depicted in gray.

Since the courses of the empirical equations of the ionic conductivity are convex, an optimal concentration for the highest ionic conductivity is determined depending on the temperature. The maximal path of both validity ranges is marked by a dashed black line in Figure 4.1. The regarding empirical function is shown in Equation 4.4.

$$wt. - \%(\kappa_{opt.}) = b_0 T^2 + b_1 T + b_2 \tag{4.4}$$

The concentration in wt.-% at the optimal ionic conductivity (κ_{opt}) of potassium hydroxide is approximated by a second order polynomial with different coefficients for the different validity ranges of the empirical equation (Equation 4.2) of the ionic conductivity. The two sets of coefficients with their validity ranges can be seen in Table 4.2.

The temperature (T) in Equation 4.4 is inserted in Kelvin. The optimal concentration with the highest ionic conductivity increases with increasing temperatures and lies approximately between 30 wt.-% at 50 °C and 45 wt.-% at 200 °C.

In order to evaluate the deviation among the measurement data points, as well as the

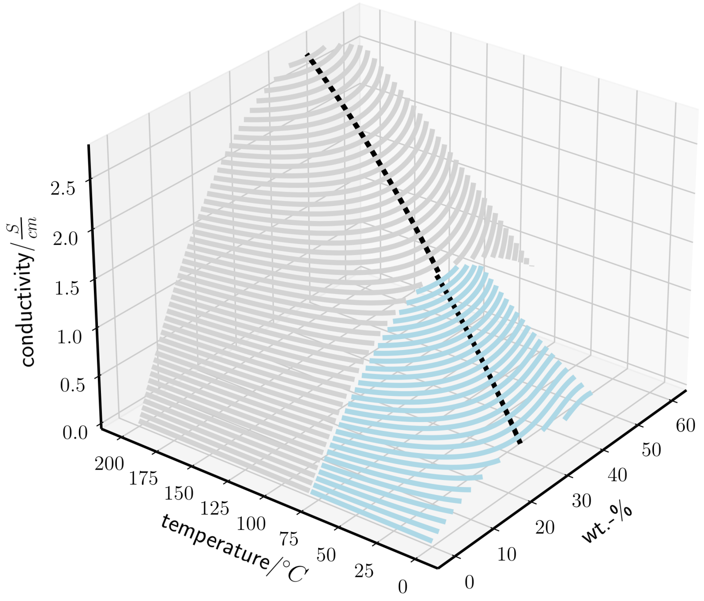

Figure 4.1: Contour Plot of the Ionic Conductivity Dependent on Temperature and Concentration.

measured data points, to the calculated values by the empirical equation, a graph as shown in Figure 4.2 is chosen. On the x-axis, the values resulting from the empirical equation are plotted against the data points taken from literature measurements on the y-axis. On the diagonal, the black line marks the location where the data points would lie if the empirical equation and the data sets would result in the exact same values.

The data points in Figure 4.2 with a '+' as a marker in the scatter plot are considered in the coefficient optimization of the empirical equation (Equation 4.2), the data points with a 'x' are excluded. Here, all data sets are used except the data measured by Darken et al. [157]. The data set is far off compared to all other data sets and is therefore not considered. In general, the data points are in good accordance with each other and the empirical equations. All data points measured by Lown et al. [156] with a concentration of 37.5 wt.-% deviate from the other data, which leads to the assumption that there might be a systematic error at this concentration in their measurements.

Table 4.2: Coefficients for the Calculation of the Optimal Concentration of Potassium Hydroxide with the Highest Ionic Conductivity Depending on the Temperature for Equation 4.2.

	$0\ °C \leq \vartheta \leq 80\ °C$ 0 wt.-%$\leq$ c ≤ 45 wt.-% c: wt.-%	$80\ °C < \vartheta \leq 200\ °C$ 0 wt.-%$\leq$ c ≤ 60 wt.-% c: wt.-%
b_0	-8.3408$\cdot 10^{-4}$	-3.5397$\cdot 10^{-4}$
b_1	0.6436974	0.38497315
b_2	-90.55717049	-58.32579755

The measured data points of Vogel [84] have a higher deviation for ionic conductivities of 0.9 S/cm to 1.3 S/cm. For the two data sets measured by Yushkevich et al. [155] and Klochko et al. [85], the higher deviating values from the empirical equation are at greater ionic conductivity values and correspond to elevated temperatures and high concentrations. The deviations to the empirical equation are likely to be explained by only two available data sets measured at elevated temperatures as well as the deviation amongst these data sets.

In the validity ranges which the empirical equations are developed for, the relative error is determined for every data point using Equation 4.1. The distribution of relative error in percentage plotted against the number of data points with the related relative error is shown in Figure 4.3.

The relative error of the data set of Darken et al. [157] as well as the data points at a concentration of 37.5 wt.-% published by Lown et al. [156] are excluded from the error evaluation due to reasons explained above. The relative error of the empirical equation for calculating the ionic conductivity is almost normal distributed around a relative error of 0 %. The deviation lies at -25 % and +15 %, with most data points laying in a range of ± 10 % relative error.

What can neither be seen from Figure 4.2 nor from Figure 4.3 is the relative error distribution and the data point distribution in relation to the temperature or the concentration. Therefore, this information is presented in Figure 4.4 (a) over the temperature range and in Figure 4.4 (b) over the potassium hydroxide concentration. The error bars are, to a certain extent, transparent, which means the darker the red color of the bars, the more bars are at the specific temperature or concentration.

The highest occurring errors are at low temperatures and high concentrations. For high concentrations, the data point density is rather thin, which might explain the high error, for low temperatures, there is no obvious explanation for the deviation. As already mentioned, but here graphically illustrated, the data point density is low at

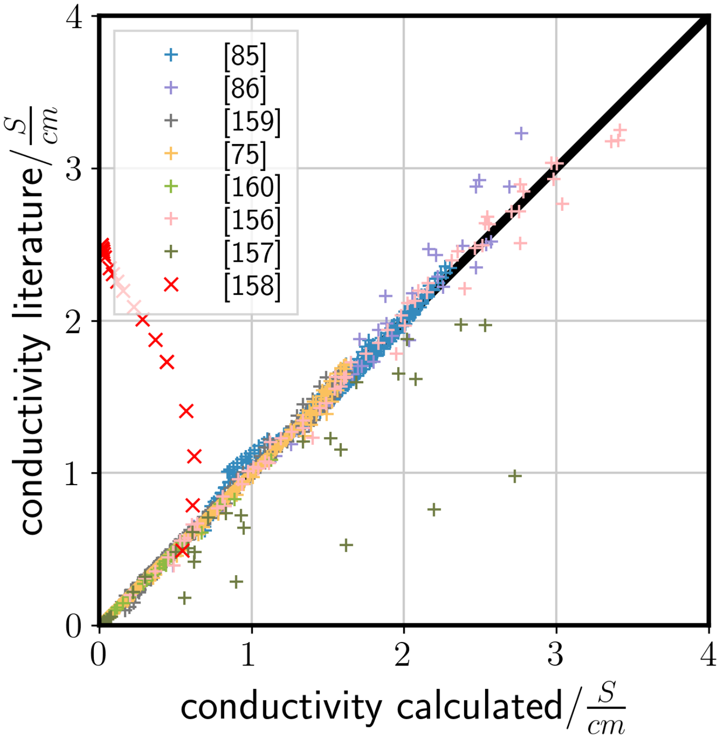

Figure 4.2: Scatter Plot of the Calculated Ionic Conductivity Plotted Against the Measured Values (+: Data Points are used for the Development of the Empirical Equation,
x: Data Points are not Used.)

higher temperatures above 100 °C. For the concentration, the data point density is, apart from a few exceptions, almost equally distributed up to 45 wt.-%.

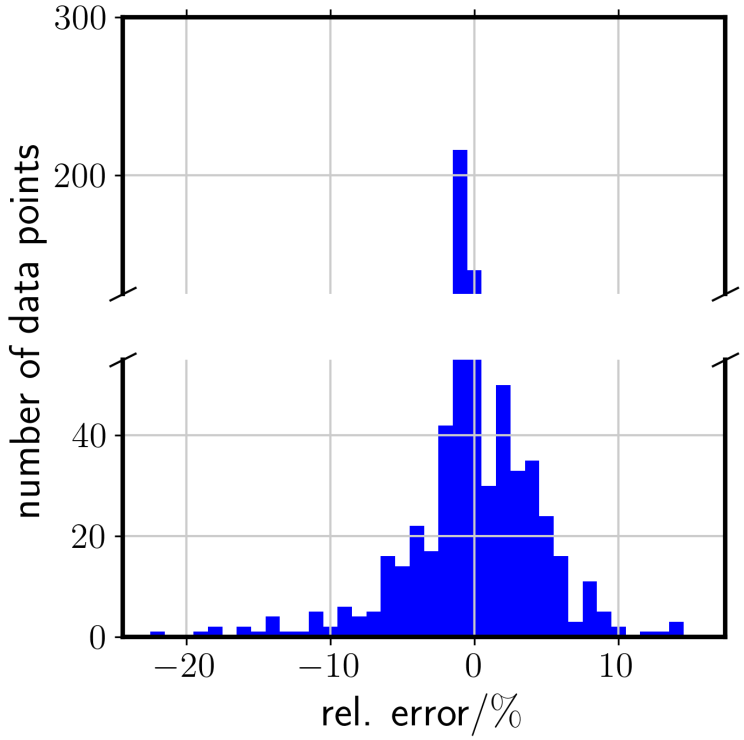

Figure 4.3: Relative Error of the Results of the Empirical Equation for Ionic Conductivity to the Published Measurement Data Points Plotted Against the Number of Data Points.

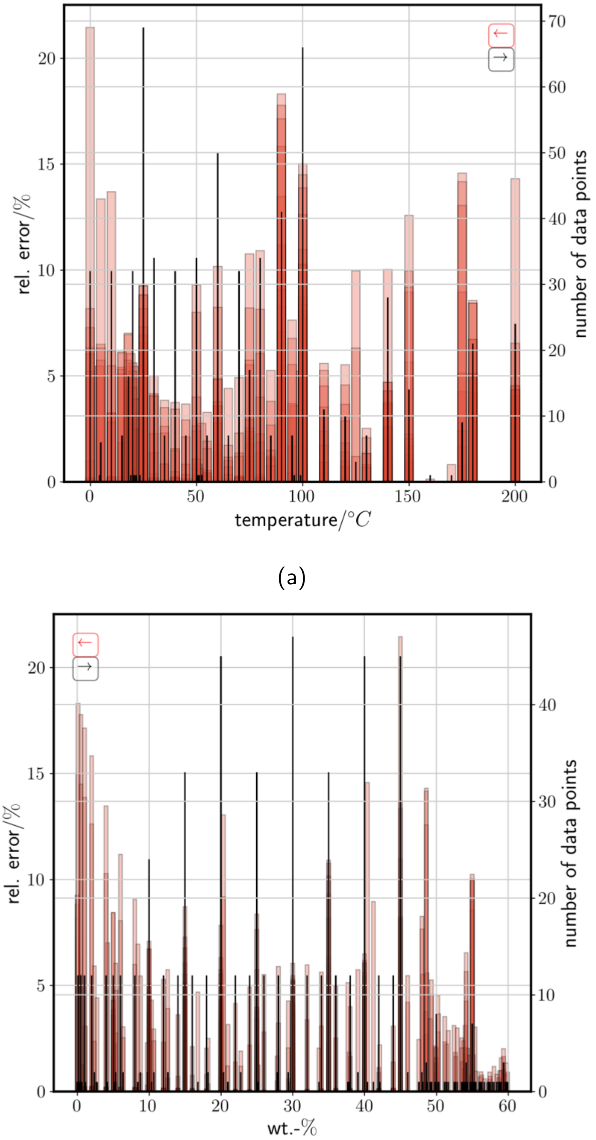

(a)

(b)

Figure 4.4: Relative Error of the Ionic Conductivity in Relation to Temperature (a) and Concentration (b).

4.1.2 Mass Density

The density of potassium hydroxide is a function of temperature and electrolyte concentration, which increases with decreasing temperature. The concentration has a greater influence on the density than the temperature. The density increases with increasing electrolyte concentration. Gilliam et al. [74] have published an empirical equation, which is based on data sets of Klochko et al. [85], Zaytsev et al. [76] and Akerlof et al. [160]. The here used empirical equation for the density of potassium hydroxide can be seen in Equation 4.5.

$$\rho_{KOH}(\vartheta, c) = (a_0\vartheta^3 + a_1\vartheta^2 + a_2\vartheta + a_3) \cdot \exp(a_4 c) \tag{4.5}$$

The difference between Equation 4.5 and the empirical equation published by Gilliam et al. [74] is that Gilliam et al. [74] are using a look-up table with discrete values, instead the third order polynomial shown here. Here, the look-up table from Gilliam et al. [74] for the discrete coefficients is approximated through a continuous function. Using all data points listed in Table 3.8 and using them for the optimization of coefficients of Equation 4.5 did not result in a more accurate empirical equation by comparing the relative errors compared to the empirical equation developed by Gilliam et al. [74]. This is why the equation is used with the coefficients published by Gilliam et al. [74] and the through regression approximated coefficients for the polynomial. All coefficients are listed in Table 4.3.

Table 4.3: Optimized Coefficients for the Calculation of the Density of Potassium Hydroxide using Equation 4.5.

	$0\ °C \leq \vartheta \leq 200\ °C$
a_0	$5.1998 \cdot 10^{-6}$
a_1	$-39.771334 \cdot 10^{-4}$
a_2	$-848.089182 \cdot 10^{-4}$
a_3	1001.5409980109
a_4	0.0086

The values of Equation 4.5 are inserted in °C for the temperature and in wt.-% for the concentration, and the resulting unit of the density is in kg/m^3. The validity range is between 0 °C and 200 °C and concentration-wise valid up until the saturation boundary of the solution, which is not considered by the empirical equation and though needs to be considered separately. In Figure 4.5, the course of the empirical equation in relation to temperature and concentration is shown.

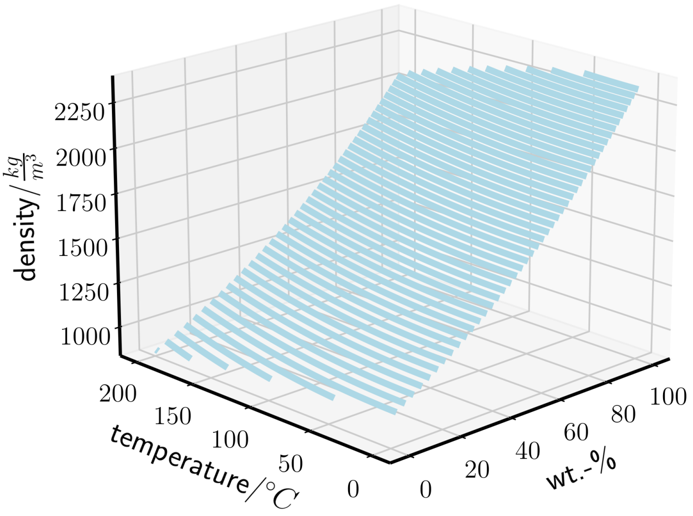

Figure 4.5: Contour Plot of the Density of Potassium Hydroxide Dependent on Temperature and Concentration (Saturation Boundary of Potassium Hydroxide not Considered).

The evaluation of the quality of the empirical equation for the density of potassium hydroxide is done using the same method used for the ionic conductivity. In Figure 4.6, a scatter plot is shown depicting all published measurement data plotted above the calculated data points. As previously explained, since the empirical equation of Gilliam et al. [74] is used, which is based on Zaytsev et al. [76], Klochko et al. [85] and Akerlof et al. [160], only the three authors are marked as used data sets. In addition, Gilliam et al. [74] is also marked, although they did not publish measurement data, they published the look-up table, which is used in this evaluation for the approximation of coefficients for the third order polynomial of Equation 4.5.

From the unused measurement data points, it can be seen that all measurements are in good accordance with the empirical equation except the measurement data from Mashovets et al. [161] and single data points from Hitchcock et al. [78]. All other publications seem to be in good accordance with the empirical equation and to each other.

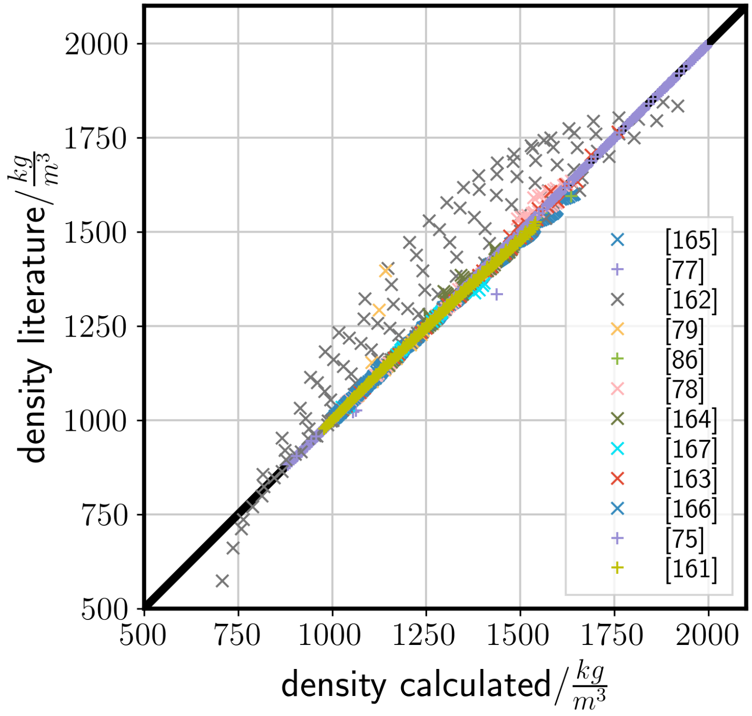

Figure 4.6: Scatter Plot of the Calculated Density Plotted against the Measured Values (+: Data Points are used for the Development of the Empirical Equation, x: Data Points are not Used).

From Figure 4.7, the relative error between all published measurement data points and the empirical equation can be seen. The highest deviations are -7.64 % and +18.3 %. The three measurement points with the highest deviation (see Figure 4.7) are two values published by Hitchcock et al. [78] and one value of the measurement data set of Mashovets et al. [161]. Except for these three values, all data points have a smaller relative error than ±5 %.

The evaluation of literature data regarding data amount in relation to temperature and concentration can be done using Figure 4.8. The measurement data amount for the density of potassium hydroxide is apart from a few exceptions at a high level for the temperature range up to 100 °C and a concentration up to 45 wt.-%. For the temperature range above 100 °C and greater than 45 wt.-%, the data amount drops. Not considering the three data points with higher deviation between the empirical equation and measurement value, the relative error seems to be increasing with increasing concentration. For the temperature, the relative error increases up to 50 °C and then decreases again up to 100 °C. From 100 °C the relative error is again increasing.

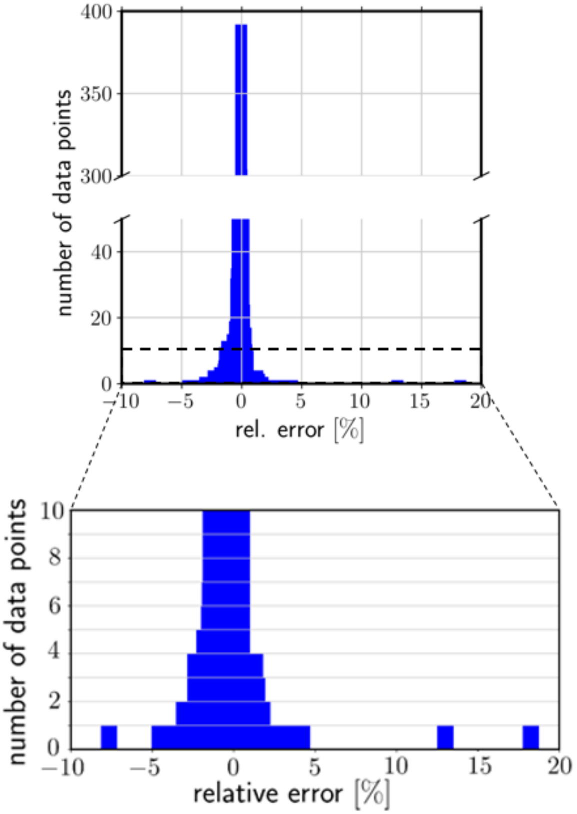

Figure 4.7: Relative Error of the Results of the Empirical Equation for the Density to the Published Measurement Data Points Plotted Against the Number of Data Points.

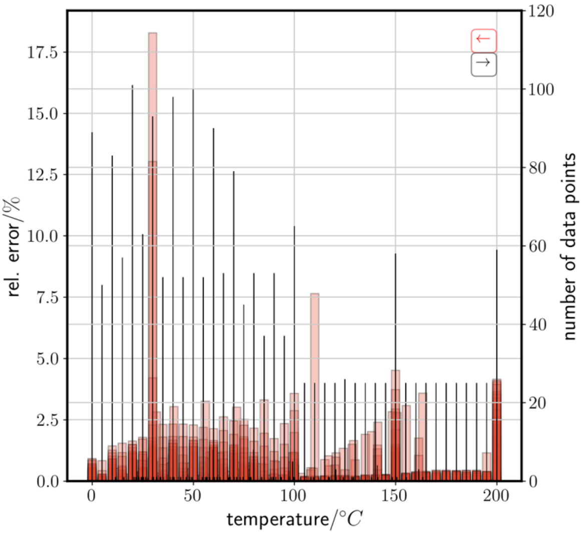

(a)

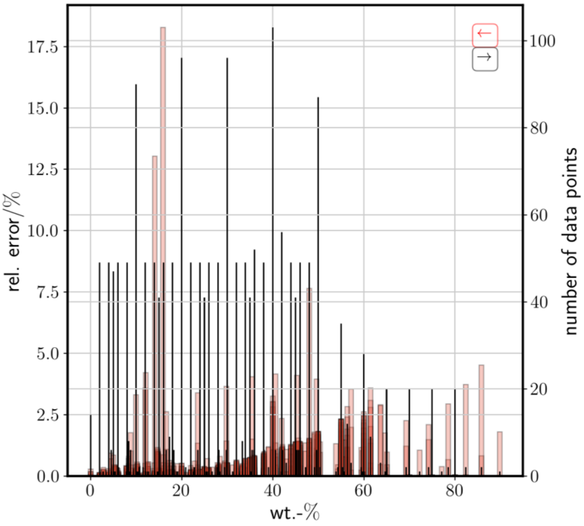

(b)

Figure 4.8: Relative Error of the Density in Relation to Temperature (a) and Concentration (b).

4.1.3 Dynamic Viscosity

For the dynamic viscosity of potassium hydroxide, which is also dependent on temperature and concentration, an empirical equation is developed which uses a base function published by Zaytsev et al. [76]. The function is using the Ezrokhi method. This method describes the physical properties of electrolyte solutions by dividing them into one term describing the properties of pure water and an additional term adding the contribution of the salt (in this case, potassium hydroxide) to the property. The equation can be seen in Equation 4.6.

$$\eta_{KOH}(\vartheta, c) = 10^{\log(\eta_w) + (a_0 + a_1\vartheta + a_2\vartheta^2)c} \tag{4.6}$$

The dynamic viscosity is described by ten to the power of the sum of the decadic logarithm of the dynamic viscosity of water (η_w) and a second order polynomial multiplied by the concentration (c), which is, in this case, the weight fraction of potassium hydroxide. For the approximation of the dynamic viscosity of water, the semi-empirical equation of Likhachev [134] is used (cf. Equation 4.7). The original equation considers the influence of pressure on the dynamic viscosity. The pressure influence is neglected (set to p = 1 bar) in this evaluation because the influence of pressure is considerably small at pressures below 250 bar [134].

$$\eta_w(T) = 2.4055 \cdot 10^{-5} \cdot \exp\left(4.42 \cdot 10^{-4} + \frac{4.753 - 9.565 \cdot 10^{-4}}{0.008314 \cdot (T - 139.7 - 1.24 \cdot 10^{-2})}\right) \tag{4.7}$$

The resulting unit of the dynamic viscosities of Equation 4.6 and Equation 4.7 is Pas. In Table 4.4, the coefficients for Equation 4.6 are listed. The validity range for the empirical equation to calculate the dynamic viscosity of potassium hydroxide is a lot smaller compared to the validity ranges of the empirical equations for ionic conductivity and density. The empirical equation is valid for temperatures between 50 °C and 200 °C and for concentrations between 30 wt.-% and 45 wt.-%. The reasons for the rather small validity range are discussed later in this sub-section.

The general course of the dynamic viscosity in relation to temperature and concentration can be seen in Figure 4.9. The viscosity decreases with increasing temperature and increases with increasing concentration.

By looking at Figure 4.10 it can be seen that the deviation of measurement data points for dynamic viscosity is much bigger compared to the other two measurement data sets

Table 4.4: Optimized Coefficients to Calculate the Dynamic Viscosity using Equation 4.6.

	$50\ ^{\circ}\mathrm{C} \leq \vartheta \leq 200\ ^{\circ}\mathrm{C}$ 30 wt.-%$\leq$ c ≤ 45 wt.-%
a_0	1.5842220626
a_1	-0.00232635280
a_2	$2.30282775753 \cdot 10^{-6}$

for ionic conductivity and density. In Figure 4.10, all measurement data points for every temperature and every concentration are displayed, as well as the points outside of the validity ranges of the empirical equation. The highly deviating data points published by Vogel [84], for example, are mostly data points with concentrations above 45 wt.-%. Comparing the measurement data sets with each other, it can be seen that the scattering of data points is quite broad. A possible reason for that is that the viscosity measurements are sensitive to measurement errors, and the measurement methods might also have an influence on the preciseness of the results.

By excluding the data points outside the validity range, the deviation of data to the empirical equation still results in comparably high relative errors, as can be seen in Figure 4.11. The relative error values are between - 21 % and + 40 %. By excluding the few higher deviating values that can be seen in Figure 4.11, the relative error is still at ± 13 %. From the number of measurement data points, it can be seen that the amount of data is a lot less compared to the other two physical properties discussed in the two subsections before, which also might have an influence on the deviation of measurement data to the empirical equation.

By looking at the temperatures and concentrations where the data points were obtained, it can be seen that the measurement data points are almost equally distributed over the whole validity range (cf. Figure 4.12). On the other hand, that also means that only a handful of measurement values are available for every temperature/ concentration combination. The relative error of the dynamic viscosity starts at 50 °C at a high value and decreases to approximately 90 °C, fluctuates then slightly, and from 130 °C on the relative error is continuously increasing again. Over the concentration, no trend is visible for the course of the relative error.

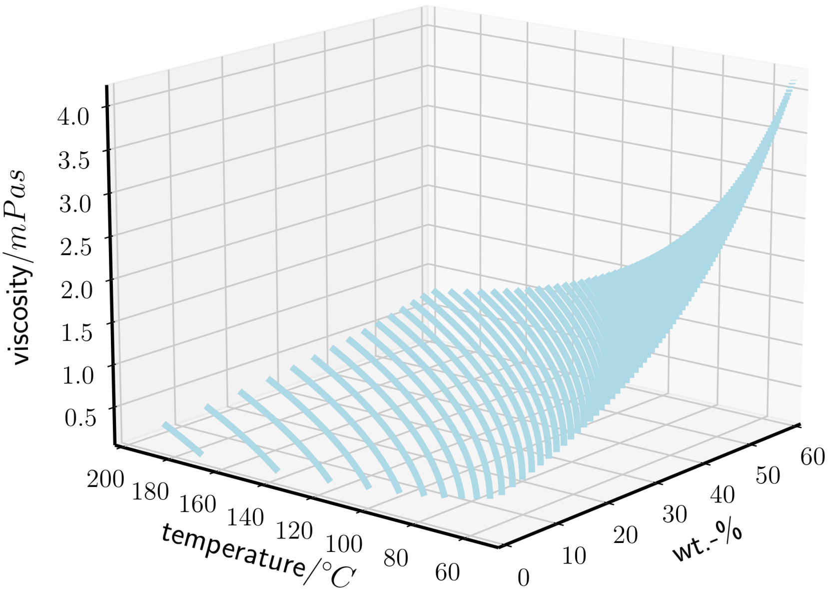

Figure 4.9: Contour Plot of the Dynamic Viscosity of Potassium Hydroxide Dependent on Temperature and Concentration.

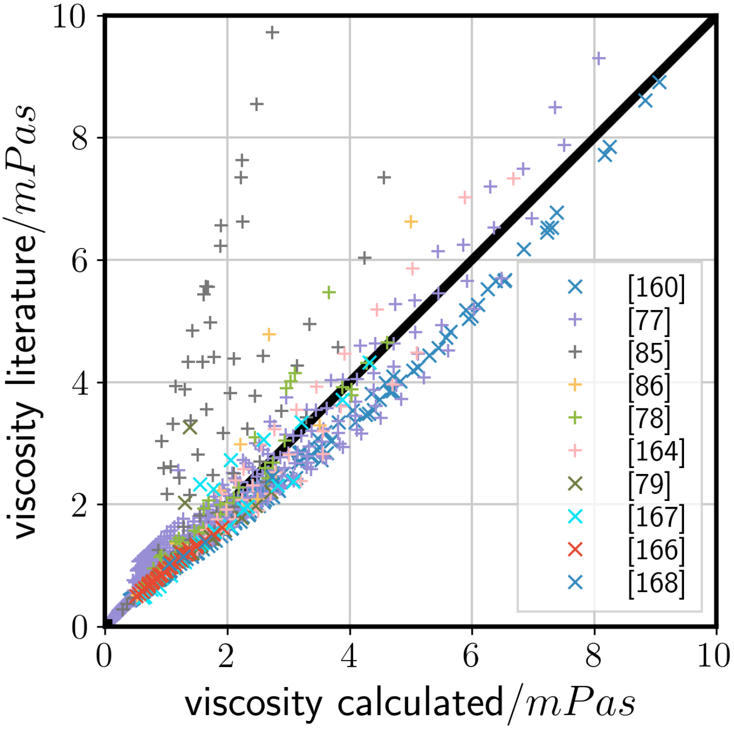

Figure 4.10: Scatter Plot of the Calculated Dynamic Viscosity Plotted against the Measured Values
(+: Data Points are used for the Development of the Empirical Equation, x: Data Points are not Used).

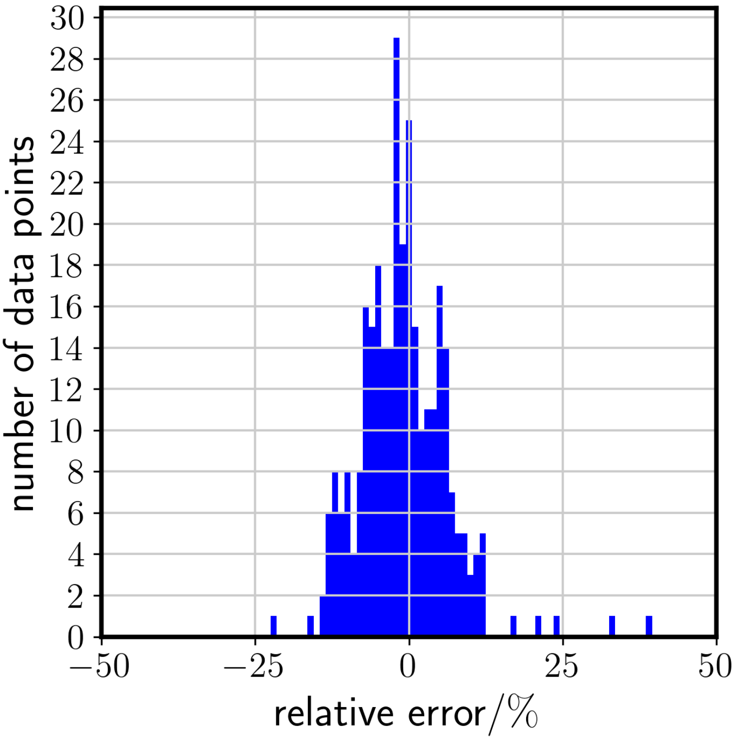

Figure 4.11: Relative Error of the Results of the Empirical Equation for the Dynamic Viscosity to the Published Measurement Data Points Plotted against the Number of Data Points.

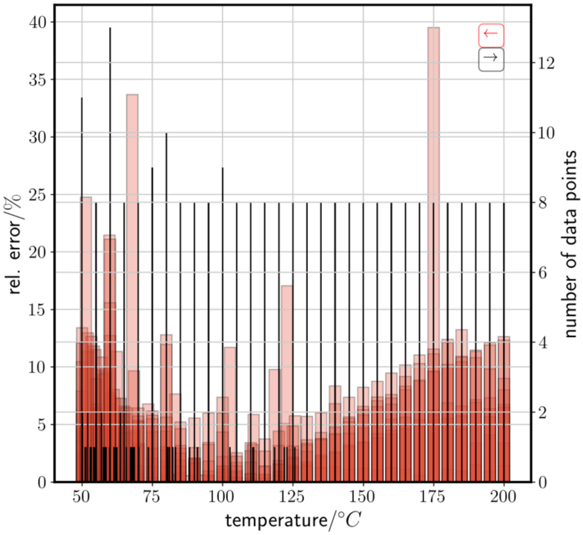

(a)

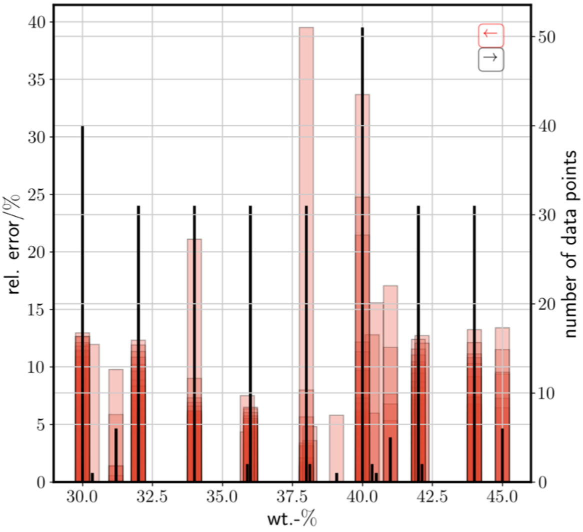

(b)

Figure 4.12: Relative Error of the Dynamic Viscosity in Relation to Temperature (a) and Concentration (b).

4.1.4 Summary

To simulate the two-phase flow of an alkaline electrolysis cell, an important part is to understand the physical properties of the electrolyte, potassium hydroxide. In this sub-section, (semi-) empirical equations were developed for the physical properties; mass density, dynamic viscosity and ionic conductivity. For each of the properties a thorough literature review has been done for measurement data as well as for already existing equations. As base equation, the most fitting equation was chosen, and the coefficients were optimized using all existing data sets in the relevant temperature and concentration range of potassium hydroxide. The deviation of the empirical equations and the measurement data was evaluated as a relative error, but also by evaluating the deviation depending on the temperature, respectively concentration, and the available number of data points at this specific state.

4.2 Characterization of the Model Electrolyte Solutions

In this section, potential model electrolyte solutions are shown, discussed, and chosen if suitable to simulate potassium hydroxide. A suitable electrolyte solution is a solution that has, for the various temperatures and concentration combinations, the same density and viscosity as potassium hydroxide but at lower temperatures. The goal is to find an electrolyte solution that is less corrosive and can be operated at lower temperatures to avoid pressurized operation with the simulated cell, while still being physically as close as possible to potassium hydroxide. The model electrolyte solutions are to replace potassium hydroxide during the particle image velocimetry measurements in the transparent cell shown in Section 3.2. A mathematical optimization is used, as described in Section 3.2.2, by testing 128 electrolyte solutions on their suitability to replace potassium hydroxide. The coefficients for the empirical equations to find electrolyte solutions at the desired density and dynamic viscosity are taken from Zaytsev et al. [76, p.1725ff., p.1729ff.]. In Table 4.5, all possible electrolyte solutions resulting from the optimization are listed.

All electrolyte solutions are able to simulate different temperature/ concentration combinations of potassium hydroxide by adjusting their temperature and concentration. The temperature ranges that the listed electrolyte solution can simulate of potassium

Table 4.5: Resulting Possible Electrolyte Solutions Found by Optimization Using Equation 3.9 and 3.8 taking the Coefficients from Zaytsev et al.[76, p.1725ff., p.1729ff.] for Simulating Potassium Hydroxide.

Electrolyte	**Temperature Range KOH** [°C]	**Temperature Range Electrolyte** [°C]
$Ba(OH)_2$	50-160	9-93
$BaBr_2$	50-180	10-76
BaI_2	50-180	9-73
$Ca(OH)_2$	50-180	14-81
CdI_2	50-180	15-72
CsBr	70-180	6-50
CsCl	60-180	6-61
CsI	70-180	7-54
$K_2Cr_2O_7$	50-180	10-71
K_2CrO_4	50-170	15-90
KBr	70-180	7-65
KCl	70-180	10-95
KI	70-180	9-59
KNO_3	70-180	10-83
Li_2SO_4	50-180	9-59
NH_4I	70-180	6-54
$RbNO_3$	60-180	10-66

hydroxide are also listed in Table 4.5. The criteria for the temperature of the electrolyte solutions is that the temperature is above 5 °C, so that the temperature is above the freezing point (with some buffer) and below 95 °C in order to be below the boiling point. The concentration has to be in the solubility limit of the solution. From the list, the electrolyte solutions were filtered by price, hazard, and, most importantly, their transparency. With these criteria, a handful of electrolyte solutions seem to be suitable. After the first tests, the choice was made that BaI_2 is suitable for lower temperatures between 50 °C and 90 °C and KI for temperatures from 100 °C up to 180 °C. The optimization in order to find the right temperature and concentration of BaI_2 and KI was done as described in Section 3.2.2. The results from the optimization can be seen graphically in Figure 4.13, where the density is plotted against the viscosity. In red dots, the values of potassium hydroxide are shown at the optimal ionic conductivity for each temperature, and the annotation in red states the temperature and concentration combination of potassium hydroxide at this point. The gray dots present the values of potassium hydroxide with a concentration of 32.5 wt.-%, the red annotations of these points state the operation temperature. The gray dots represent the measurement conditions of the alkaline electrolysis cell operated in Grenoble, France, that was used during neutron radiography measurements. The black '+'- marker shows which operation points of potassium hydroxide are simulated by BaI_2, and the black square marks the operation points simulated by KI. The annotations in black font stand for the temperature and concentration of either BaI_2 or KI. The black solid lines are a fragment of the function of the model electrolyte function of the dynamic viscosity dependent on the density at the regarding temperature (is kept constant) resulting from the optimization over different concentrations (is varied).

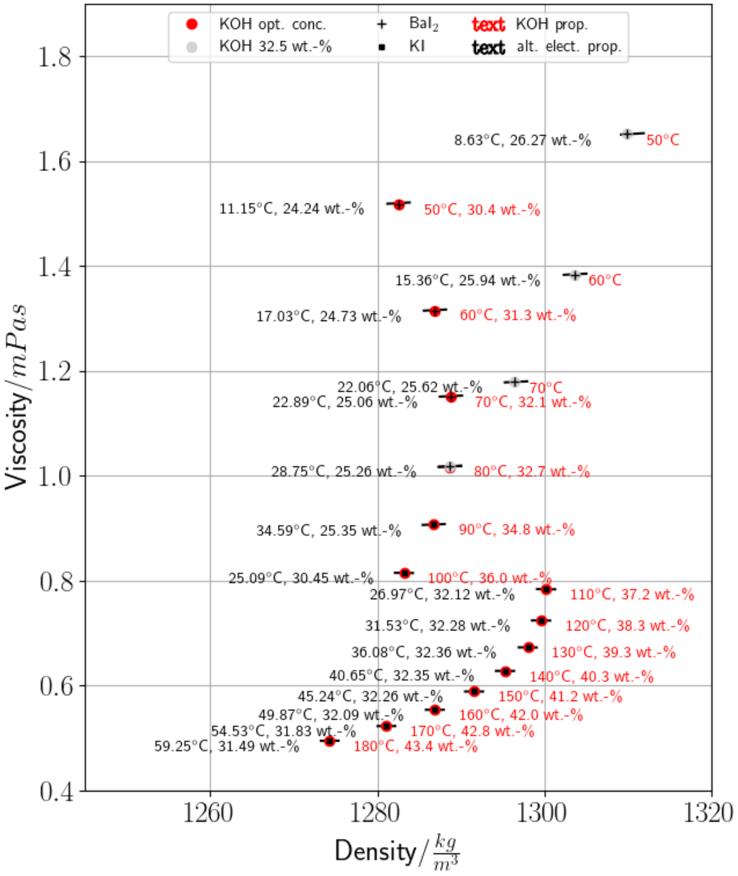

Figure 4.13: Density Plotted against Viscosity of Alternative Electrolyte Concentration and Temperature Combinations for the Simulation of Potassium Hydroxide at Various Operation Points.

In addition, the values are summarized in Table 4.6 with the Density and Viscosity that the electrolyte solutions have at each operation point for potassium hydroxide.

Table 4.6: Listed Values of Model Electrolyte Concentration and Temperature for the Simulation of Potassium Hydroxide.

Electrolyte	**Density** [kg/m^3]	**Viscosity** [mPas]	**Temperature KOH** [°C]	**Concentration KOH** [wt.-%]	**Temperature alt. Electr.** [°C]	**Concentration alt. Electr.** [wt.-%]
BaI_2	1306.61	1.64	50	32.5	8.63	26.27
BaI_2	1300.33	1.37	60	32.5	15.36	25.94
BaI_2	1293.24	1.17	70	32.5	22.06	25.62
BaI_2	1285.39	1.01	80	32.5	28.73	25.26
BaI_2	1282.59	1.518	50	30.4	11.15	24.24
BaI_2	1286.83	1.315	60	31.3	17.03	24.73
BaI_2	1288.74	1.151	70	32.1	22.89	25.06
BaI_2	1288.6	1.017	80	32.7	28.75	25.26
BaI_2	1286.68	0.907	90	34.1	34.59	25.35
KI	1283.21	0.815	100	36	25.09	30.45
KI	1300.16	0.784	110	37.2	26.97	32.12
KI	1299.61	0.724	120	38.3	31.53	32.28
KI	1298	0.673	130	39.3	36.08	32.36
KI	1295.33	0.628	140	40.3	40.65	32.35
KI	1291.6	0.589	150	41.2	45.24	32.26
KI	1286.83	0.554	160	42	49.87	32.09
KI	1281.04	0.523	170	42.8	54.53	31.83
KI	1274.26	0.495	180	43.4	59.25	31.49

Since the values for the temperature and concentration of BaI_2 and KI at each operation point are optimized with empirical equations, the values need to be validated by viscosity and density measurements. In order to do that, the measurements are conducted as described in Section 3.3.

4.2.1 Validating Measurements of the Viscosimeter Conducted with Calibration Oil

Before the measurements with the two electrolyte solutions are verified, viscosity measurements with the calibration oil *1BW* are done, as described in Section 3.3. With the calibration oil, the necessary shear rate range can be identified, as well as the measurement error of the viscosimeter.

With the calibration oil *1BW*, viscosity measurements over a broad shear rate range were conducted. The viscosity of a Newtonian fluid is supposed to be constant over the course of the shear rate. The effects that cause the viscosity not to be constant over the course of the shear rate are discussed in Section 3.3.3 in detail. The here chosen shear rate range between 300 s^{-1} and 800 s^{-1}, where the viscosity is constant (within some measurement fluctuation boundaries), is shown in Figure 4.14, in this case for 40 °C.

The result for 20 °C can be found in Appendix A.1.1.

With the chosen shear rate range, the viscosity of the calibration oil is measured. From the supplier, five different viscosity reference values for different temperatures are given with a certain measurement uncertainty (cf. Table 3.6). The viscosity for these five temperatures is measured in order to verify the accuracy of the viscosimeter. For each temperature, ten repeating measurements are done with the identified shear rate between 300 s^{-1} and 800 s^{-1}. In Figure 4.15, the viscosity reference value from the supplier (blue 'x' marker, $\eta_{ref.,j}$) is shown as well as the mean of the measured viscosity (red '$+$' marker, $\eta_{m,mean,j}$) over the temperature.

The error bars show the range of viscosity fluctuations during the ten measurements ($\eta_{m,ij}$) with the measured value as a base value. Additionally, the reference values provided by the supplier are shown in the figure (blue cross marker). The red ($\Delta_{min,j}$, negative deviation) and black ($\Delta_{max,j}$, positive deviation) bars show the relative error of the measured viscosity calculated by Equation 3.19 and Equation 3.20. From the resulting relative error values, it can be seen that they have values below 2 % and

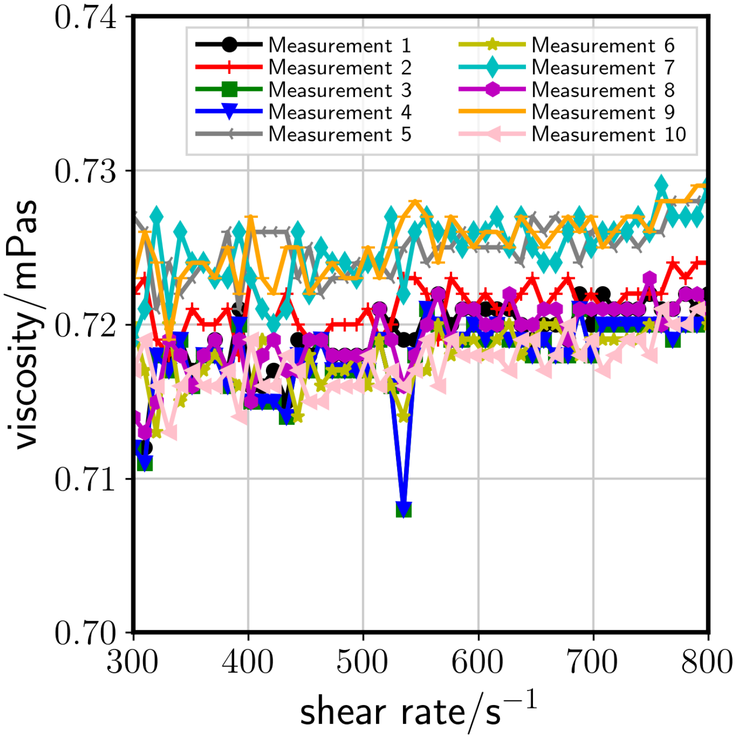

Figure 4.14: Ten Viscosity Measurements with the Calibration Oil *1BW* at 40 °C in Order to Identify the Shear Rate Range For The Viscosity Range of Potassium Hydroxide (0 °C $\leq \vartheta \leq$ 180 °C).

do not seem to have a systematic tendency of the error values over the temperature. Therefore, the most deviating relative error is assumed to be the overall measurement error. In Table 4.7, the resulting relative error values are listed, and the two maximal deviations are marked with a red box. The measurement error of the viscosimeter is considered to be - 1.88 % and + 1.76 %. Except for two values, the measurement error is in the measurement uncertainty range given by the supplier. All measurement values for the viscosity measurements of the calibration oil *1BW* can be found in Appendix A.1.1. The measurement uncertainty of the densitymeter is given by the supplier of ± 1 kg/m^3.

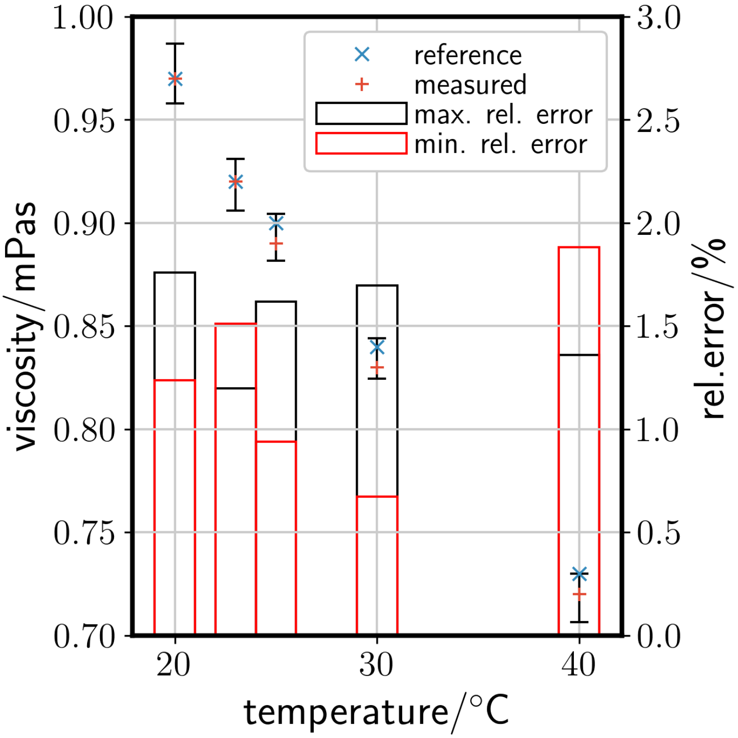

Figure 4.15: Viscosity Measurements with the Calibration Oil 1BW to Identify the Measurement Uncertainty of the Viscosimeter MCR302 Calculated by Equation 3.19 and Equation 3.20.

Table 4.7: Minimum and Maximum Relative Error of Viscosimeter *MCR302* Determined by Equation 3.19 and 3.20.

Temperature [°C]	**Min. Rel. Error $\Delta_{\mathrm{min,j}}$** [%]	**Max. Rel. Error $\Delta_{\mathrm{max,j}}$** [%]
20	-1.24	1.76
23	-1.51	1.20
25	-0.94	1.62
30	-0.67	1.70
40	-1.88	1.36

4.2.2 Validating Measurements for the Dynamic Viscosity and the Mass Density of the Model Electrolyte Solutions

For BaI_2 and KI, the dynamic viscosity and the density are measured by conducting ten repeating measurements for each temperature/ concentration combination ($\rho_{m,ij}$, $\eta_{m,ij}$). The measurement results for all conducted measurements can be found in Appendix A.1.1 and Appendix A.1.2. In Table 4.8 and Table 4.9 an overview of the mean values calculated from the measured density (column "Mean Density") and viscosity (column "Mean Viscosity") is given, as well as the calculated values from the optimization for density and viscosity of the two electrolyte solutions (column "Calc. Density" and "Calc. Viscosity"). The relative error of the mean measurement value for density respectively, viscosity, and the calculated value of the properties is calculated for each operation temperature j ($\Delta_{rho,j}$, $\Delta_{eta,j}$). In addition the relative error calculated by Equation 3.21 ($\Delta_{max,j}$) and Equation 3.22 ($\Delta_{min,j}$) are determined as described in Section 3.3.3. The latter relative error is determined to check the results of the used empirical equation for density and viscosity.

Table 4.8: Density and Viscosity Measurements with $\mathrm{BaI_2}$ as Model Electrolyte Solution.

Electr.	**Temp. KOH** [°C]	**Conc. KOH** [wt.-%]	**Mean Density** [kg/m^3]	**Calc. Density** [kg/m^3]	**Mean Viscosity** [mPas]	**Calc. Viscosity** [mPas]	$\boldsymbol{\Delta}_{\rho,\mathbf{j}}$ [%]	$\boldsymbol{\Delta}_{\rho,\mathbf{min,j}}$/ $\boldsymbol{\Delta}_{\rho,\mathbf{max,j}}$ [%]	$\boldsymbol{\Delta}_{\eta,\mathbf{j}}$ [%]	$\boldsymbol{\Delta}_{\eta,\mathbf{min,j}}$/ $\boldsymbol{\Delta}_{\eta,\mathbf{max,j}}$ [%]
$\mathrm{BaI_2}$	50	32.5	1268.27	1306.61	1.6	1.64	-2.93	-2.95 -2.89	-2.44	-4.13 -0.84
$\mathrm{BaI_2}$	60	32.5	1264.73	1300.33	1.35	1.37	-2.74	-2.77 -2.72	-1.46	-3.35 +0.06
$\mathrm{BaI_2}$	70	32.5	1276.23	1293.24	1.14	1.17	-1.32	-1.33 -1.29	-2.56	-3.66 -0.04
$\mathrm{BaI_2}$	80	32.5	1268.38	1285.39	0.99	1.01	-1.32	-1.33 -1.31	-1.98	-2.84 -1.5
$\mathrm{BaI_2}$	50	30.4	1238.30	1282.59	1.47	1.518	-3.45	-3.47 -3.44	-2.86	-4.74 +0.62
$\mathrm{BaI_2}$	60	31.3	1267.53	1286.83	1.27	1.315	-1.5	-1.51 -1.49	-3.56	-4.56 -2.56
$\mathrm{BaI_2}$	70	32.1	1279.52	1288.74	1.11	1.151	-0.72	-0.72 -0.71	-3.88	-4.6 -3.1
$\mathrm{BaI_2}$	80	32.7	1268.38	1288.71	0.99	1.017	-1.58	-1.58 -1.56	-2.99	-3.8 -2.18
$\mathrm{BaI_2}$	90	34.1	1277.24	1286.68	0.88	0.907	-0.73	-0.75 -0.72	-3.07	-4.48 +0.04

Table 4.9: Density and Viscosity Measurements with KI as Model Electrolyte Solution.

Electr.	**Temp. KOH** [°C]	**Conc. KOH** [wt.-%]	**Mean Density** [kg/m^3]	**Calc. Density** [kg/m^3]	**Mean Viscosity** [mPas]	**Calc. Viscosity** [mPas]	$\boldsymbol{\Delta_{\rho,\mathrm{j}}}$ [%]	$\boldsymbol{\Delta_{\rho,\mathrm{min,j}}}$/ $\boldsymbol{\Delta_{\rho,\mathrm{max,j}}}$ [%]	$\boldsymbol{\Delta_{\eta,\mathrm{j}}}$ [%]	$\boldsymbol{\Delta_{\eta,\mathrm{min,j}}}$/ $\boldsymbol{\Delta_{\eta,\mathrm{max,j}}}$ [%]
KI	100	36	1272.18	1283.21	0.83	0.815	-0.86	-0.87	+1.91	-0.66
								-0.86		+4.58
KI	110	37.2	1284.22	1300.16	0.79	0.784	-1.23	-1.24	+0.3	-0.41
								-1.20		+0.79
KI	120	38.3	1278.05	1299.61	0.73	0.724	-1.66	-1.67	+0.83	-0.37
								-1.65		+3.21
KI	130	39.3	1290.48	1298.0	0.7	0.673	-0.58	-0.59	+4.33	+3.28
								-0.57		+4.96
KI	140	40.3	1285.65	1295.33	0.62	0.628	-0.75	-0.76	-1.04	-3.0
								-0.74		+0.97
KI	150	41.2	1286.09	1291.6	0.61	0.589	-0.43	-0.43	+3.38	+1.89
								-0.42		+4.7
KI	160	42	1276.08	1286.83	0.55	0.554	-0.84	-0.86	-1.01	-3.46
								-0.79		+2.32
KI	170	42.8	1272.17	1281.0	0.5	0.523	-0.69	-0.71	-3.78	-4.96
								-0.67		-2.33
KI	180	43.4	1259.37	1274.26	0.49	0.495	-1.17	-1.17	-0.59	-3.18
								-1.16		+2.86

None of the measured values for viscosity ($\Delta_{\eta,min,j}$,$\Delta_{\eta,max,j}$) and density ($\Delta_{\rho,min,j}$,$\Delta_{\rho,max,j}$) of BaI_2 and KI had a higher relative error than 5 % compared to the calculated density/ viscosity of potassium hydroxide. All measured values seem to have slightly lower values than the calculated values. This applies to lower operation temperatures for density and viscosity in the range where BaI_2 is used as a model electrolyte solution. For KI, used as a model electrolyte at higher operation temperatures, this also applies to the density values. For viscosity values measured for KI the results seem to be slightly higher compared with the calculated values.

4.2.3 UV/Vis Measurements Verifying the Transmission Properties of the Model Electrolyte Solutions

For the model electrolyte solutions used for particle image velocimetry measurements, the transmission properties are checked as the last step after verifying the density, viscosity, and transparency. During the particle image velocimetry measurements, a green LED is used as a light source, and the particles are emitting red light. This is why the transmission properties, especially in the wavelength ranges of visible green and red light, are verified. The measurement method is done as described in Section 3.3.1.

The measurement starts by measuring an empty cuvette as a reference value for 100 %, as a base for the following measurements with the electrolyte solutions. A measurement with distilled water is done for comparison reasons and measurements with BaI_2 and KI. Since both model electrolyte solutions are iodide compounds, they react under the influence of light, for the chemical details, it is referred to Mathews et al. [171]. Therefore, a sample of three weeks old KI solution exposed to light stored in a transparent glass bottle is also tested. The resulting UV/Vis measurements can be seen in Figure 4.16.

The fresh samples of KI and BaI_2 have a similar transmission behavior over the wavelength compared to distilled water. The UV/Vis measurements are carried out for wavelengths between 300 nm up to 800 nm, starting at 800 nm, step-wise descending towards 300 nm, as described in Section 3.3.1. The wavelength of the electrolyte solutions and water are at a high level from 800 nm to approximately 375 nm. Afterwards, the transmission drops to lower transmission values towards the ultraviolet wavelength spectrum. When the transmission is dropping therefrom the absorption increases at lower wavelengths. For the three weeks old sample of KI the drop begins

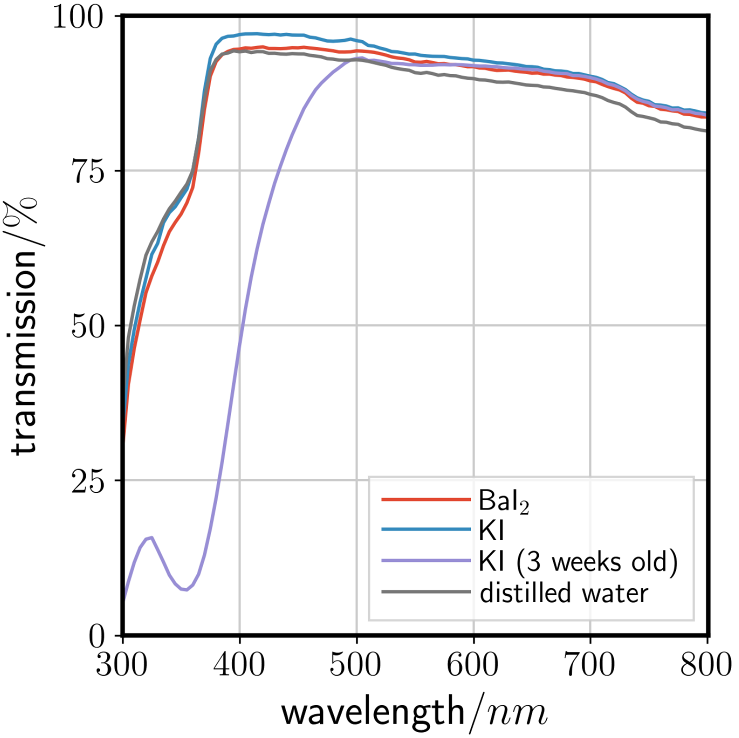

Figure 4.16: UV/Vis Measurements of the Chosen Electrolyte Solutions BaI_2 and KI.

already 100 nm earlier, at approximately 475 nm, compared with the fresh sample. From these measurements, it can be seen that it is important to have the electrolyte solution prepared fresh and stored with as little light exposure as possible. More insight on the color of iodide solutions and their transmissivity behavior is given in [172].

4.2.4 Summary

This sub-section is showing the results of the selection process for electrolyte solutions that are capable of simulating potassium hydroxide at certain temperatures and concentrations with being transparent in color to be able to be used in particle image velocimetry measurements. The chosen electrolyte solutions are an important part in the simulation of the two phase flow of an alkaline electrolysis cell. Empirical equations are used and optimized for the desired viscosity and density values to match the viscosity and density of potassium hydroxide at different temperatures and different concentrations. From the possible choices, the electrolyte solutions have been chosen through a number of criteria e.g. non-toxicity and having a transparent color. Barium iodide has been chosen for the simulation at lower temperatures and potassium iodide for higher temperatures. The calculated properties have been verified by conducting viscosity and density measurements, as well as the determination of the of the measurement error of the devices. Since iodides are known for their decomposition reaction being exposed to light the electrolyte solutions were tested for their transmissivity.

4.3 Two-Phase Flow Behavior Analyzed by Neutron Radiography

In this section, the results of the neutron radiography measurements conducted at ILL in Grenoble, France, are shown. The results discussed in this sub-section are in the process of being published under the title "Operando investigation of the two-phase flow behavior of a zero-gap alkaline electrolysis cell using neutron radiography".
First are the electrochemical results shown and discussed, then the evaluated gas bubble behavior is shown and analyzed separately for anode and cathode. The relation between electrochemical effects on the two-phase flow is evaluated, and the influence of each tested setting, temperature, electrolyte volume flow, and current density is shown.
The two-phase flow behavior is mainly evaluated at the operation conditions listed in Table 4.10. These operation conditions are chosen to have a good variety of operation conditions by choosing the highest and the lowest measured temperature. For the current density and the electrolyte volume flow, the ability to analyze the resulting images also had to be taken into account by choosing the operation points. On images with a low volume flow of 10 ml/min or a high volume flow of 100 ml/min, the flowing gas bubbles are rather difficult to analyze because of either too low or too high transient conditions. The same applies to low respectively high current densities, for low current densities, the amount of gas bubbles is too small, and for high current densities, the flow regime is rather churn flow, which makes especially the gas bubble velocity analysis difficult. The analysis is done for flow behavior with a flow regime of plug or

slug flow. Therefore, 25 ml/min and 50 ml/min are chosen for the volume flow and 0.4 A/cm^2 and 0.6 A/cm^2 for the current density.

Table 4.10: Operation Conditions of the Neutron Radiography Measurements that the Two-Phase Flow is Evaluated for.

Temperature [°C]	**Electrolyte Volume Flow** [ml/min]	**Current Density** [A/cm^2]
80	50	0.4
80	50	0.6
80	25	0.4
80	25	0.6
50	50	0.4
50	50	0.6
50	25	0.4
50	25	0.6

As explained in detail in Section 3.1, the neutron radiography measurements are conducted as through-plane measurements, resulting in 2D images. The evaluated images show the parallel flow channel of the alkaline electrolysis cell. The channel order as they are depicted in the resulting images is shown in Figure 4.17. The channel order starts with a channel of the anode side on the left, then a cathode side channel follows, the order is alternating with 14 anode channels and 14 cathode channels.

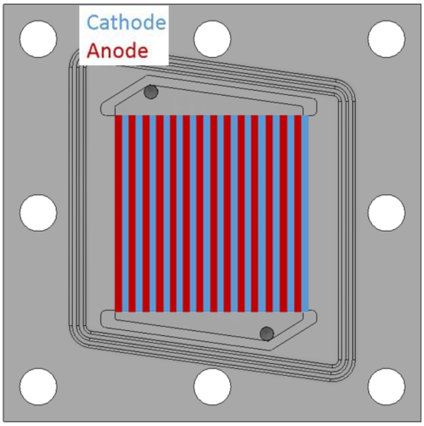

Figure 4.17: Arrangement of Anode and Cathode Flow Channel towards the Neutron Beam.

4.3.1 Electrochemical Behavior

The cell measurements with a zero-gap alkaline electrolysis cell are conducted with the goal of analyzing the two-phase flow behavior inside the flow channel using neutron radiography. Through neutron radiography measurements, it is possible to record the gas bubble movement because the difference in transmission of the neutron beam, the gas, and the metal material of the cell is sufficient to analyze the contrast difference in the resulting images. Different settings for three different properties are tested during the measurements, the electrolyte volume flow, the temperature, and the current density. The different settings are analyzed by measuring polarization curves, conducting neutron radiography, and measuring electrochemical impedance spectroscopy for the different temperature and volume flow combinations as well as for some current densities. The measurements are conducted as described in Section 3.1.2. The electrochemical behavior of the AWE zero-gap cell is influenced by the two-phase flow behavior, which is explained in the following sub-section.

Polarization curves

The polarization curves of the electrolyzer can be divided into three parts. At low current densities, the activation overpotential shapes the course of the polarization curve, at intermediate current densities, the ohmic overpotential shapes the course, and at high current densities, it is shaped by mass transport limitations. The electrodes are mostly blocked by gas bubbles and are not sufficiently supplied with water, therefore, the reaction is hampered and mass transport limitations occur. [173]

Since most alkaline electrolysis cells do not reach current densities where mass transport limitations happen, which also applies to the here used electrolysis cell, this kind of overpotential is not further discussed.

The polarization curves for all temperature/ volume flow combinations measured during neutron radiography measurements are shown in Figure 4.18. The polarization curves of the four adjusted volume flows are compared for each of the measured temperatures.

From all four sub-figures of Figure 4.18, it can be seen that the volume flow presumably does not seem to have an influence on the polarization curves. Also, at a low volume flow of 10 ml/min, no impact can be seen on the cell performance. What can be seen, though, is that especially for 80 °C and 70 °C the polarization curves are not lying entirely on top of one another. As described in Section 3.1.2, the temperature during neutron radiography measurements starts at 80 °C and from there descends over 70 °C, 60 °C to 50 °C. The order in which the electrolyte volume flow was changed can be seen in Appendix A.2.1. Potentially, the cell was not finished with the break-in process. Karacan et al. [174] described the reactions taking place during the break-in in detail. The break-in is done at the highest used current density of 1 A/cm^2, the highest volume flow of 100 ml/min, and the highest temperature of 80 °C. As preparation for the beamtime granted by ILL of 48 hours, the breaking-in was tested during pre-measurements, as can be seen in Figure 4.19 (a). The needed time for the warm-up and the breaking-in was tested. After approximately 10,000 seconds (= ~2 hours and 45 minutes), the cell voltage appeared to have a constant value. Since the breaking-in time is necessary, but does not hold a lot of scientific contribution to the two-phase flow behavior, it was tried to keep the time as short as possible in order to use the time for the main measurements efficiently.

During the beamtime in Grenoble, the break-in was paused for a short period of time in order to measure the electrochemical impedance at various points in time. This might have slowed down the break-in process, as can be seen from Figure 4.19 (b). The end value of the cell voltage, though, is the same as in the continuous break-in period in the pre-measurement.

However, to review the theory that the break-in was not finished during the beamtime, the cell measurements are repeated with a similar measurement procedure, but instead of 5 hours break-in period, the time is extended to 24 hours. The results of the cell voltage can be seen in Figure 4.20.

In the first 10,000 s, the heating of the cell to 80 °C is done. Then, the current density is set to 1 A/cm^2. The cell voltage reaches a constant value at approximately 25,000 s (= ~7 hours) and keeps this value until approximately 50,000 s (= ~14 hours), then the cell voltage is increasing again after reaching a constant value after 70,000 s (= ~ 17 hours of break-in).

The measurements of the polarization curves were repeated after breaking-in the cell for 24 hours. The comparison of the polarization curves measured in Grenoble during beamtime (cf. Figure 4.21 (a)) with the repeated measurement after 24 hours break-in (cf. Figure 4.21 (b)) shows that the repeated measurements of the polarization curves look like typical polarization curves measured with the same cell configuration, also at different temperatures. These polarization curves start at the same point and have a similar course at low current densities where the activation overpotential is dominant. At higher current densities, the polarization curves have a constant gradient (ohmic losses are dominant), and the polarization curves have a steeper gradient the lower the temperature.

For the polarization curves measured during the beamtime, none of the criteria mentioned above fully apply (cf. Figure 4.21). The polarization curves start at various points at low current densities, they do have a slightly curved course instead of a constant gradient, and the polarization curve of 70 °C has approximately the same cell voltage as the 80 °C polarization curve. The polarization curve of 80 °C is supposed to have the lowest voltage (best performance). The cell voltage is supposed to increase with decreasing temperatures. This happens due to decreasing activation overpotential, improved reaction kinetics, and reduced ohmic resistance due to improved electrical conductivity with increasing operation temperature.

Here, the polarization curves of 25 ml/min electrolyte volume flow are compared because this volume flow was the last setting of volume flow for the 80 °C measurements during the beamtime. This shows that the break-in was not finished during the complete measurements for 80 °C. The polarization curves for the other three volume flow values can be found in Appendix A.2.2. Since the electrolysis cell is operated galvanostatic, the not finished break-in process and respectively the cell performance is not relevant to the outcome of the two-phase flow behavior. The current density is the value that is responsible for the gas amount and, together with the electrolyte volume flow, responsible for the two-phase flow behavior. Karacan et al. [174] found out the electrochemical cell behavior is best comparable after the cell is changing current density less than 1 %/ hour (operation in potentiostatic mode) during break-in, which took their AWE cell more than 20 hours to reach. However, the beamtime is too valuable to spend on the break-in process since the two-phase flow is not influenced by it.

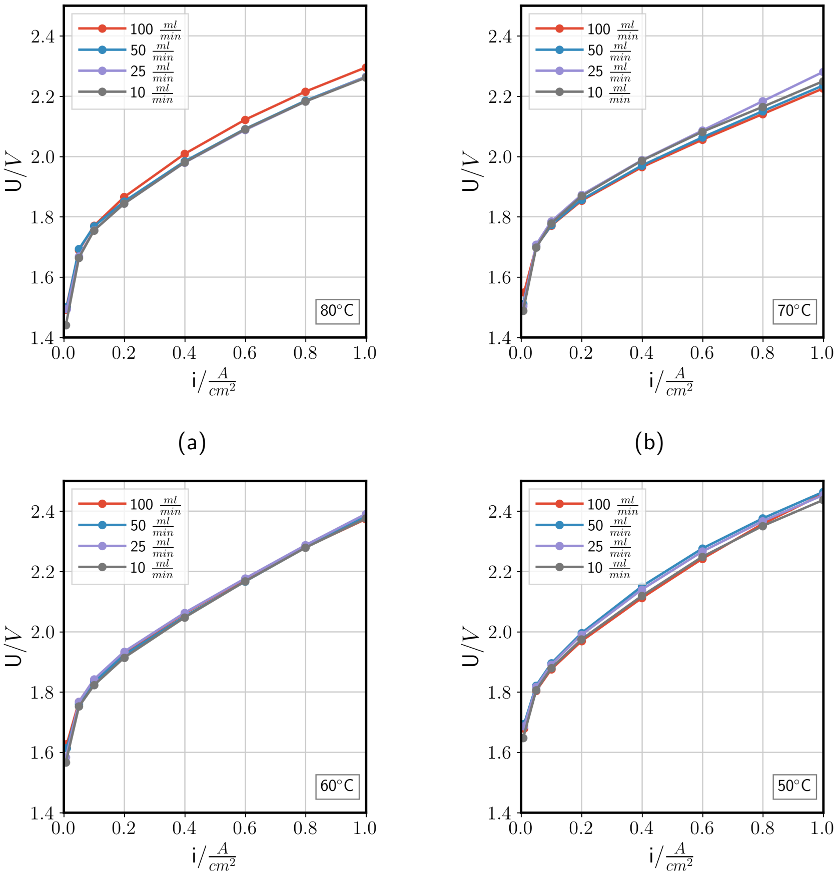

(a) (b)

(c) (d)

Figure 4.18: Polarization Curves measured during Neutron Radiography Measurements at different Electrolyte Volume Flows for 80 °C (a), 70 °C (b), 60 °C (c) and 50 °C (d).

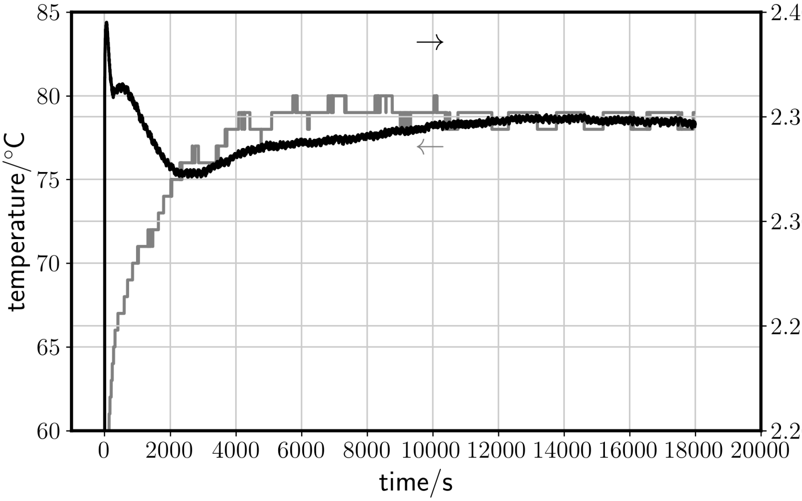

(a)

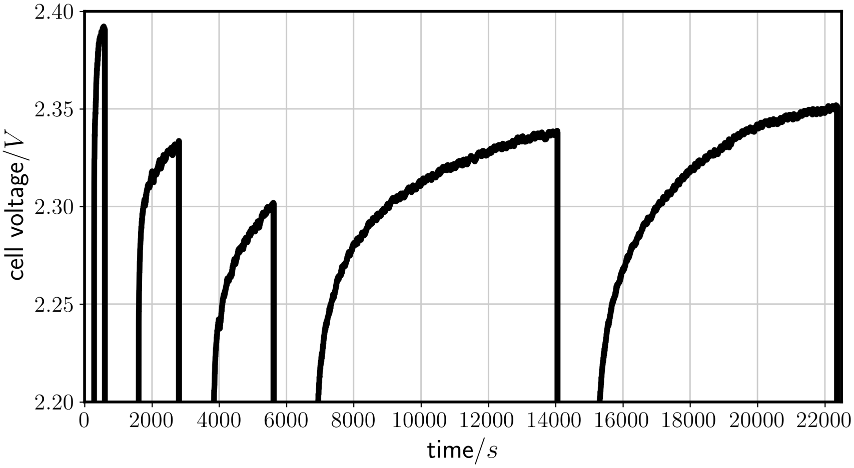

(b)

Figure 4.19: Course of the Cell Temperature and the Cell Voltage during Break-in in Preparatory Measurements for the Beamtime (a) and the Cell Voltage during Break-in in Grenoble with Frequent in between EIS Measurements (b), both with 5 hour Break-in Duration.

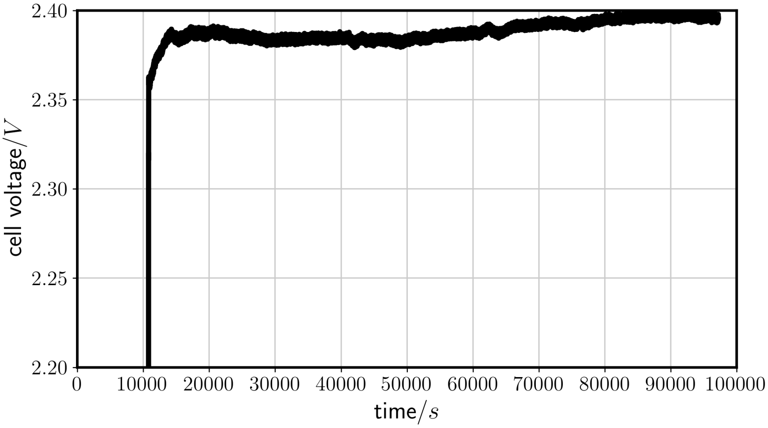

Figure 4.20: Course of the Cell Voltage during Break-in of the Alkaline Electrolysis Cell for 24 hours.

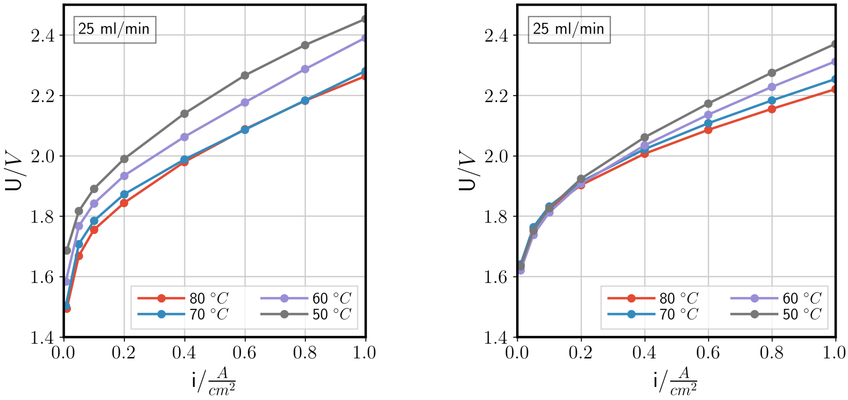

(a)

(b)

Figure 4.21: Polarization Curves at Different Temperatures Measured at 25 ml/min Electrolyte Volume Flow after 5 hours of Break-in (a) compared to 24 hours of Break-in (b).

Electrochemical Impedance Spectroscopy

From electrochemical impedance measurements mainly two different properties are important in this evaluation. Firstly, the high frequency resistance which can be seen from an electrochemical impedance spectrum by the interception with the real part axis (x-axis). Secondly, the radius of the semicircle which relates to the electrochemical reaction at the electrodes of the cell. The impedance spectra are recorded at several time points during the neutron radiography measurements. First, the impedance is measured before, during, and after the break-in of the cell in order to see the change in high frequency resistance and the radius of the semicircle. Afterwards, the high frequency resistance is mainly the interesting property because it gives an indication of the gas bubble's influence (in terms of ohmic resistance) on the cell performance. The different impedance spectra are compared to each other hereafter by comparing the three different settings current density, electrolyte volume flow, and temperature. During the break-in of the cell, the electrochemical impedance is measured before starting the break-in (0 min), after 10 min, 30 min, 1 hour, 3 hours, and at the end of the break-in before starting the first polarization curve (after 5 hours). The spectra can be seen in Figure 4.22.

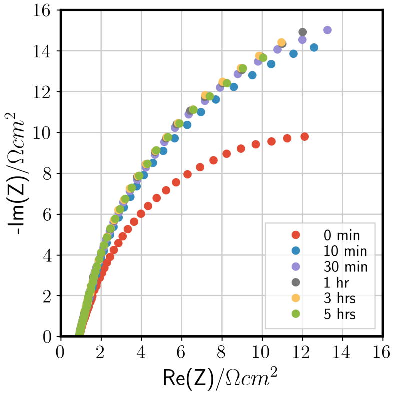

Figure 4.22: Electrochemical Impedance Spectra at different times during Break-in of the Cell measured at 1 mA/cm^2 and 20 mV Amplitude.

For all six measurements, the high frequency resistance seems to be constant. Karacan et al. [174] investigated the break-in behavior of AWE zero-gap cell for benchmarking and named four effects that influence the time of the break-in. The four effects are the formation of gas bubbles, on the cathode side the absorption of atomic hydrogen into the nickel lattice, on the anode side changes of the Ni^{2+} oxide layer, and the mechanical or chemical loss of catalyst material (not relevant here because no catalyst layer is applied). Publications investigating the gas bubble influence of AWE cells with gap found that a bubble curtain is forming on the electrodes. Vogt [175] used natural convection for the electrolyte and showed that switching cathode and electrode during operation takes 45 min to regain a steady state for the electrolysis operation, assuming the bubble curtain to be responsible. Zhang et al. [176] showed that this bubble curtain exists also with flowing electrolyte. For the zero-gap cell used here, the influence of a gas bubble curtain slowly forming and remaining even after stopping the operation cannot be seen in Figure 4.22. The same result was obtained by Rocha et al. [177] for an AWE zero-gap cell. In their investigation for forced convection, the cell voltage did not increase for repeating start and stop of the cell operation, which is assumed to prove that the gas bubble removal is not hindered. In this investigation, if the gas bubbles would form a lasting bubble curtain, the high frequency resistance would increase with increasing time during the break-in. From Figure 4.22, it can be assumed that the break-in process has no influence on the high frequency resistance under the applied operation conditions.

The radius of the semicircle, however, is approximately the same for all measurements except the measurement before the break-in starts (0 min). The reason for that might be the two remaining processes occurring on anode side and cathode side. The effects happening during the break-in of an AWE cell are described in more detail by Hall et al. [178]. They investigated the effects on nickel foil electrodes with cyclic voltammetry and reported similar effects on anode and cathode side as assumed by Karacan et al. [174].

After the break-in, the main measurements start. The electrochemical impedance is measured after each measured polarization curve. Polarization curves are measured for each temperature/ concentration combination. The impedance measurements conducted after measuring the polarization curves are measured with a current density of 1 mA/cm^2 and an amplitude of 20 mV. In Figure 4.23, the electrochemical impedance spectra measured at 1 mA/cm^2 are compared for different electrolyte volume flows for 80 °C (a), 70 °C (b), 60 °C (c) and 50 °C (d).

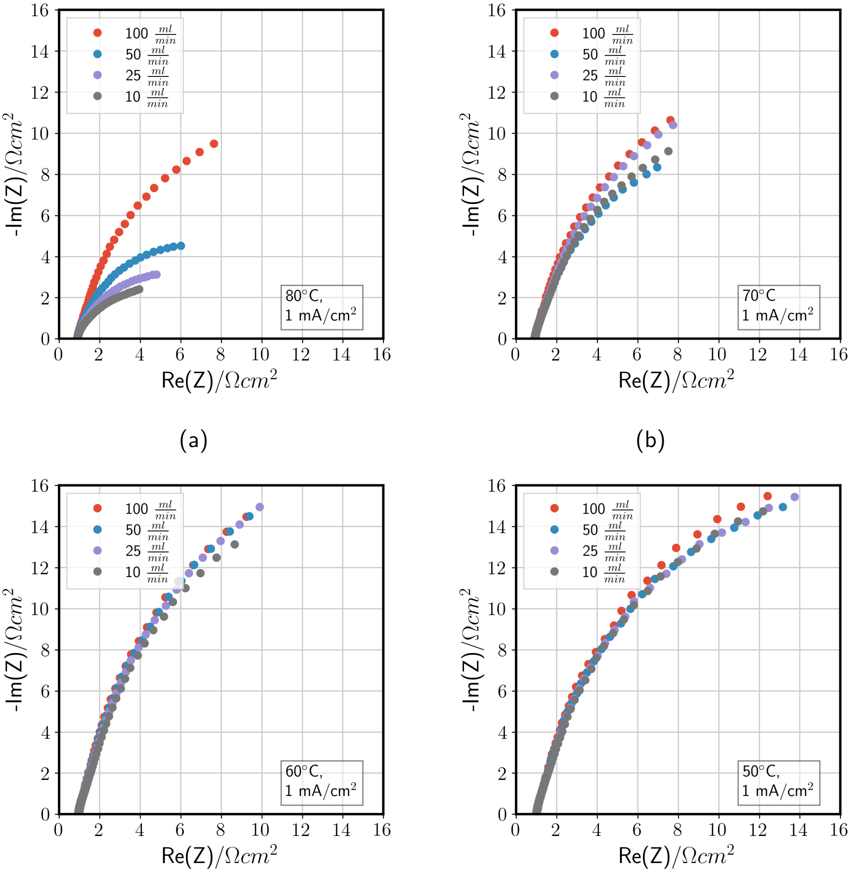

(a) (b)

(c) (d)

Figure 4.23: Electrochemical Impedance Spectra for 80 °C (a), 70 °C (b), 60 °C (c) and 50 °C (d) comparing the Four Electrolyte Volume Flows at 1 mA/cm^2 and an Amplitude of 20 mV.

What can also be seen from the comparison is the not finished break-in process in the 80 °C figure (a) and also in the 70 °C figure (b) in Figure 4.23. For the 60 °C figure (c) and 50 °C figure (d) of Figure 4.23, the radii of the semicircles are approximately the same, which is how it is expected to look like. At 80 °C, the radii for the different volume flows differ a lot, for 70 °C, the radii are closer together but still differ noticeably. From the subfigures, it can be assumed that at the time when the measurements for 60 °C started, the cell was finished with the break-in. The previously mentioned effects taking place at anode and cathode seem to increase the radius of the semicircle for the here used cell design. The radius of an electrochemical impedance spectrum gives information about the cell's charge transfer resistance. At the beginning of the break-in of the cell, the cell voltage, at galvanostatic operation, is higher, and with the progressing break-in process, the cell voltage decreases to a steady point. From the cell voltage, the decreasing charge transfer resistance (decreasing radius of the electrochemical spectrum) can be seen.

In Figure 4.24, the high frequency resistance for different temperatures is compared in each subfigure at a specific electrolyte volume flow measured at 1 mA/cm^2 and an amplitude of 20 mV. The section of the figure is zoomed in to see the high frequency resistance more closely.

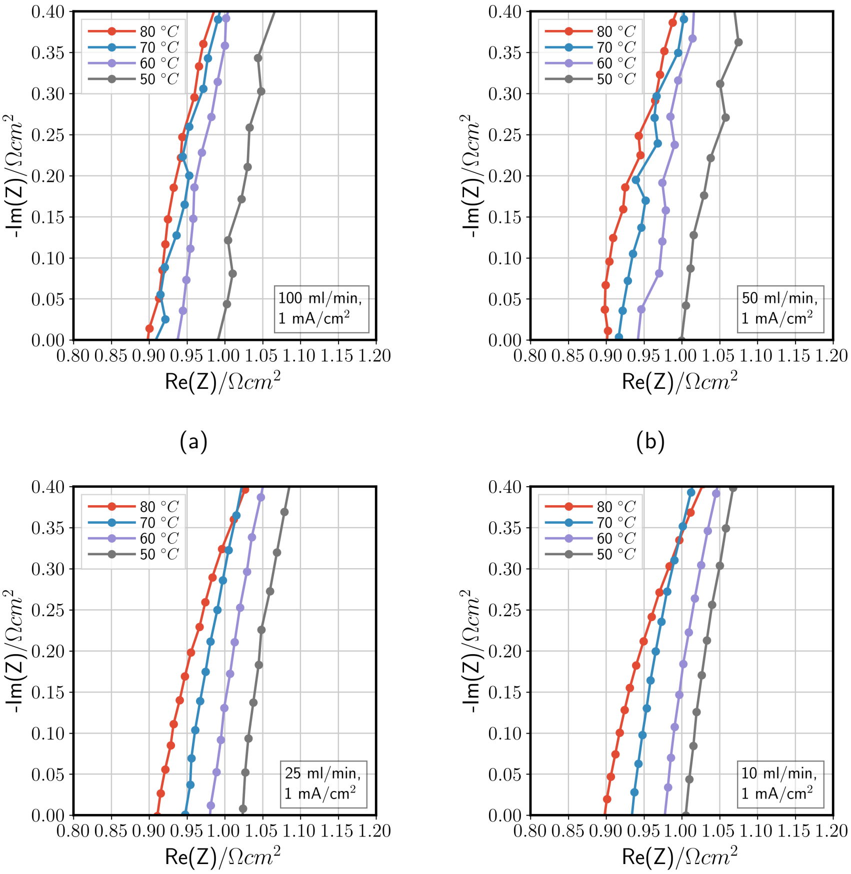

(a) (b)

(c) (d)

Figure 4.24: Comparison of the High Frequency Resistance for 100 ml/min (a), 50 ml/min (b), 25 ml/min (c) and 10 ml/min (d) at different Temperatures Measured at 1 mA/cm^2 and an Amplitude of 20 mV.

In each sub-figure, the increasing high frequency resistance with decreasing temperature can be seen. In addition, comparing every single temperature in the sub-figures with one another, it can again be seen that the electrolyte volume flow does not have an influence on the high frequency resistance at 1 mA/cm^2. Both results are according to the literature. Gilliam et al. [74] showed that the ionic conductivity of potassium hydroxide increases with increasing temperature at constant concentration. Lickert et al. [179] compared the volume flow of water for a PEM electrolysis cell. They found out that up to high current densities (5 A/cm^2), the volume flow does not have an influence on the cell performance.

In addition to the electrochemical impedance measurements measured after measuring a polarization curve, at 80 °C the electrochemical impedance was also measured after measuring 10 mA/cm^2, 50 mA/cm^2 and 100 mA/cm^2 of the polarization curves. The recording of the polarization curve was stopped after the regarding current density, and the potentiostat, used for electrochemical impedance spectroscopy, is turned on to measure the impedance at the same current densities as the polarization curve step was recorded before (stepwise at 10 mA/cm^2, 50 mA/cm^2 and 100 mA/cm^2) with an amplitude of 20 mV each. The comparison of the electrochemical impedance spectra of the different current densities, measured at 80 °C and four different electrolyte volume flows, can be seen in Figure 4.25.

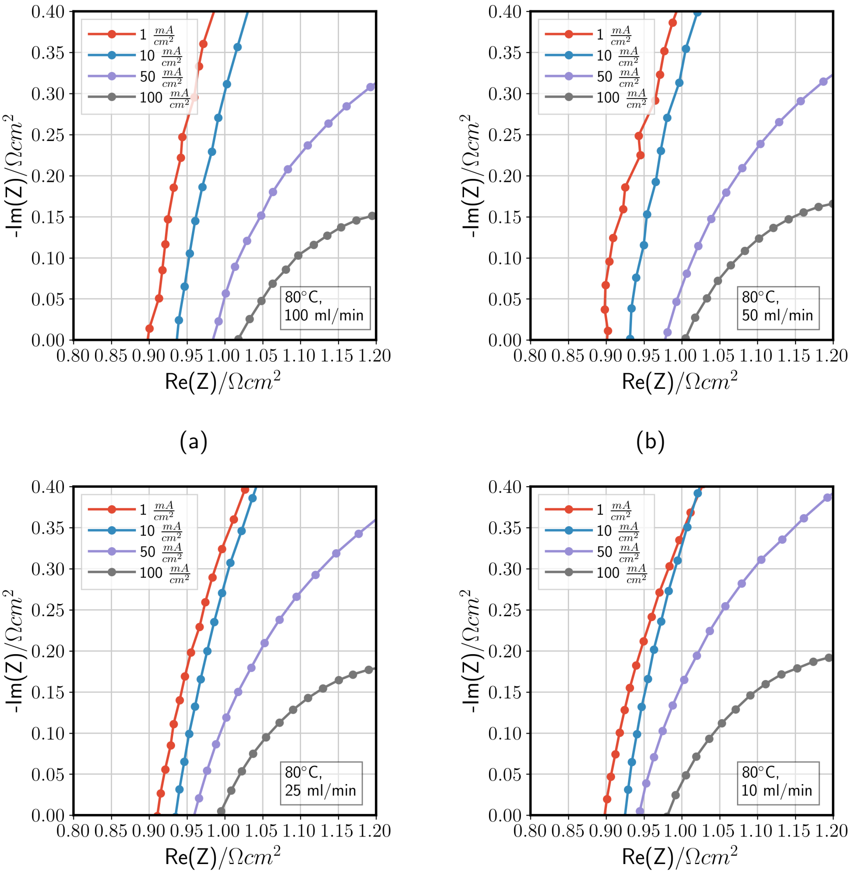

(a) (b)

(c) (d)

Figure 4.25: Comparison of the High Frequency Resistance for 100 ml/min (a), 50 ml/min (b), 25 ml/min (c) and 10 ml/min (d) at Different Current Densities with an Amplitude of 20 mV Measured at 80 °C.

From the different sub-figures of Figure 4.25 the same tendency as reported by Haverkort et al. [5], Phillips et al. [6] and de Groot et al. [7] can be seen. It is known that the high frequency resistance increases with current density. The results shown in this examination once again confirm that the zero-gap design is influenced by gas bubble losses. The sub-figures show the zoomed-in section of the high frequency resistance, where the interception of the curve with the real part axis (x-axis) is visible. Haverkort et al. [5] and de Groot et al. [7] speculated on possible reasons for the increase in ohmic resistance in zero-gap alkaline electrolysis cells, as already discussed in Section 2.2. The influence of gas bubbles on the ohmic resistance is discussed in more detail later on with the evaluation of the neutron radiography images. What can be seen is that the value for the high frequency resistance is about one order of magnitude higher compared to the literature ohmic resistance given for the Zirfon diaphragm (70–1000 $\mathrm{m\Omega\,cm^2}$ at 80 °C, 30 wt.-% KOH) which is supposed to be the biggest part contributing to the high frequency resistance of zero-gap electrolysis cells. The exact reason for the increasing deviation from the ohmic resistance of the Zirfon diaphragm cannot be explained yet.

In Figure 4.26 the same data is shown as in Figure 4.25 but with another arrangement. Here, the focus is laid on the comparison of different electrolyte volume flows measured at 80 °C and shown in each sub-figure for the different current densities the electrochemical impedance was measured for.

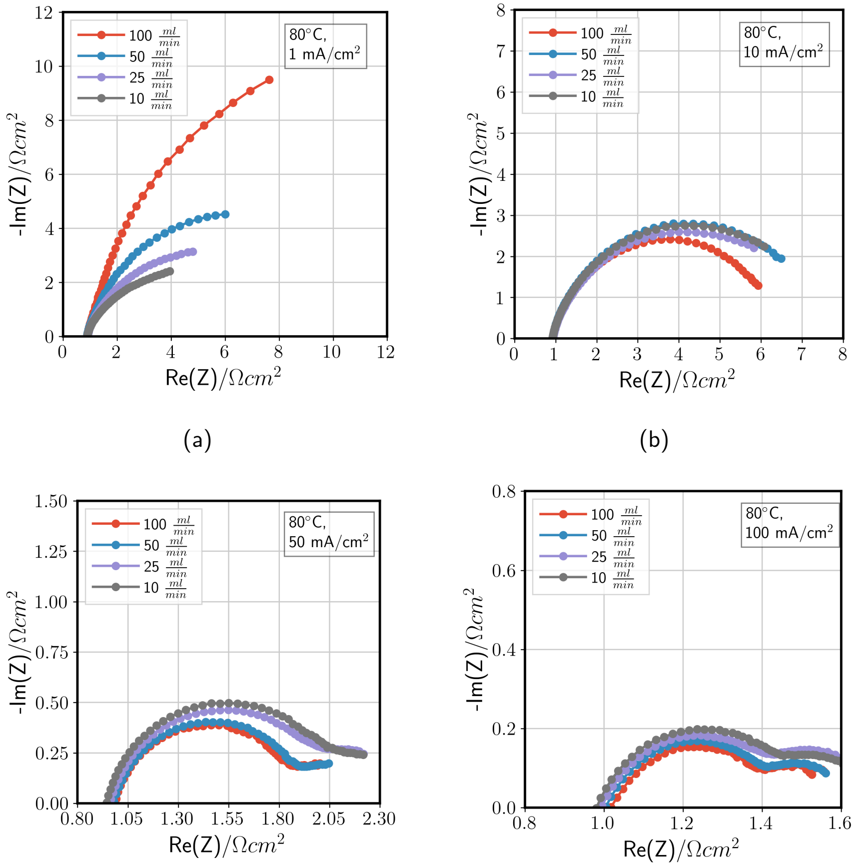

(a) (b)

(c) (d)

Figure 4.26: Comparison of the Electrochemical Impedance Spectra for 1 mA/cm^2 (a), 10 mA/cm^2 (b), 50 mA/cm^2 (c) and 100 mA/cm^2 all with an Amplitude of 20 mV for Different Volume Flows at 80 °C.

For the rather low current densities of 1 mA/cm^2 and 10 mA/cm^2 the high frequency resistance seems to be of similar value for all electrolyte volume flows. For 1 mA/cm^2 the radii of the different electrolyte volume flows decrease with decreasing volume flow. One possible reason might be a better gas bubble removal with higher electrolyte volume flow as reported by Rocha et al. [177]. But since this trend appears to be reversed for the three other shown current densities in Figure 4.26, it is more likely that this phenomenon is caused by the effects of an unfinished break-in process. For

50 mA/cm^2 and 100 mA/cm^2 the high frequency resistance seems to slightly increase with increasing electrolyte volume flow. Yuan et al. [180] summarizes for the two-phase flow of PEM electrolysis that the number of gas bubbles is not directly linked to the mass transport overpotential but the oversaturation. They conclude if the bubble detachment frequency is not high enough, the local oversaturation is increasing, and with that, the mass transport overpotential, or influence of the gas bubbles on the ohmic resistance. By looking closer at the high frequency resistance of the cell at 100 mA/cm^2 in Figure 4.27, it can be seen that the high frequency resistance, which is linked to the ohmic resistance, is increasing with increasing electrolyte volume flow. The polarization curves, however, do not show a sign of the electrolyte volume flow influencing the cell performance (see Figure 4.18). From the conclusions made by Yuan et al. [180] the expectation would be an increasing ohmic resistance with decreasing electrolyte volume flow, since the electrolyte volume flow is most likely linked to the detachment bubbles diameter and therefore to the detachment frequency, as further described in Section 4.3.3. Garcia-Navarro et al. [181] saw a decrease in performance with increasing electrolyte volume flow but linked it to an increasing low frequency resistance and, therefore, a matter of diffusion limitation. The low frequency resistance was not measured in this examination due to the limited available time during neutron radiography measurements. The findings here, as well as the possible explanation from literature, do not lead to a sufficient explanation, if the electrolyte volume flow at higher current densities influences the ohmic resistance, further experimental investigation is needed in this regard.

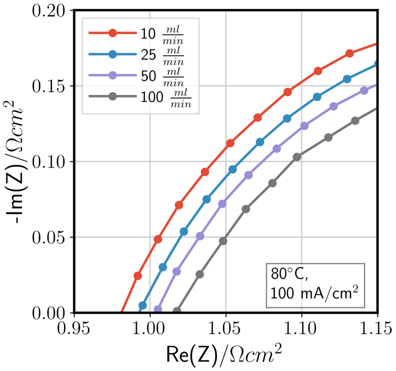

Figure 4.27: Comparison of the Electrochemical Impedance Spectra for 100 mA/cm^2 (a) with an Amplitude of 20 mV for Different Volume Flows at 80 °C.

In the two sub-figures of Figure 4.26 for 50 mA/cm^2 and 100 mA/cm^2, a second semicircle is visible towards lower frequencies. The second semicircle might show a second electrode reaction that is taking place. Hall et al. [178] listed reactions that take place at different electrode potentials for an AWE cell besides water the water splitting reaction.

From the analysis of the polarization curves and electrochemical impedance spectra recorded during neutron radiography measurements, it could be seen that the cell behavior is similar to the reported cell behavior in literature. The cell voltage is decreasing with increasing temperature, the cell performance is not or only slightly affected by electrolyte volume flow. The increase in gas bubble formation increases the ohmic resistance of the cell but is not affected by temperature. With the knowledge that the cell is affected by the two-phase flow behavior, the neutron radiography images are analyzed for potential explanations in the following sub-sections.

4.3.2 Gas Layer Thickness

The gas bubbles inside the alkaline electrolysis cell measured by neutron radiography result in images that can be analyzed by evaluating the gray value of the image. The gray value of these images is a measure for the transmission of the neutron beam and is constant (except for noise deviations) over time for each pixel of the cell when the cell is flooded with electrolyte solution before the current is applied and gas bubbles are formed. When the cell operation starts and gas bubbles begin to form, the neutron beam is attenuated by the gas layer, and the transmitted beam intensity decreases at the location of the gas bubbles. In the resulting gray value images, the gas bubbles have a brighter appearance compared to the images without gas bubbles. From the gray value of the single pixels of the images, the gas layer thickness can be determined. In order to do that, the attenuation coefficient Σ has to be determined before, as explained in Section 3.1 using Beer-Lambert's Law (cf. Equation 4.8). With the attenuation coefficient (Σ), the gas layer thickness (d_{gas}) can be calculated (cf. Equation 4.9). Equation 4.8 and Equation 4.9 use the transmission values obtained from the reference images taken before the measurements of the camera noise (T_{noise}) and the flooded cell without gas bubbles (T_{wet}). Although the camera noise in Equation 4.8 and Equation 4.9 is named like a transmission value, they are actually values for each pixel of the images, which would be misinterpreted as transmission and are caused by the noise of the camera.

$$\frac{T_{image} - T_{noise}}{T_{wet} - T_{noise}} = \frac{\exp\left(-\Sigma \cdot d_{KOH}\right)}{\exp\left(-\Sigma \cdot \left(d_{KOH} - d_{gas}\right)\right)} \tag{4.8}$$

$$d_{gas} = -\frac{1}{\Sigma} \cdot \ln\left(\frac{T_{image} - T_{noise}}{T_{wet} - T_{noise}}\right) \tag{4.9}$$

The resulting attenuation coefficient for the neutron radiography measurement is $\Sigma = 0.331$ mm^{-1}. The value for the attenuation coefficient (Σ) was compared before (at 80 °C, 32.5 wt.-% potassium hydroxide concentration at anode and cathode side) and at the end of the 48 hours measurement period (at 50 °C). This comparison is done in order to check whether the concentration difference of potassium hydroxide, which is occurring and increasing during electrolysis operation, can be detected in the attenuation coefficient in the period of measurement. For this short measurement time, the attenuation coefficient does not show a significant change. Assuming an operation of 48 hours at 1 A/cm^2 straight, the concentration would change from 32.5 wt.-% to 36.6 wt.-% on the cathode side and to 29.2 wt.-% on the anode side. The current density is much lower most of the time during the measurement, which is why the change of concentration is also much lower in reality. This value is given to have an idea in which range the maximum concentration change lies.
The used alkaline electrolysis cell for the measurements has parallel flow channels and a triangular inflow area, as shown in Figure 4.28.

The inlet of the flow is positioned at the tip of the triangle, which is approximately at one third of the active cell area of the x-coordinate of the active cell area. The anode and cathode flowfield plates are structurally identical, but from the image perspective, the cathode flow inlet is at one third from the left side, and the anode flow inlet at one third from the right side. The coordinate system used for neutron radiography is shown in Figure 4.28
In Figure 4.29 to 4.32, the mean gas layer thickness is shown. Mean gas layer thickness means that the gas layer thickness is calculated for each pixel of each image and is averaged, in this case, over 2500 images for each pixel. The 2500 images are taken from the end of the 5 minutes measurement period to avoid having transient two-phase flow conditions. To have a better overview, the flow channel for anode and cathode are shown in different figures for every of the eight evaluated operation points (cf. Table 4.10). The figures of the same operation point are always positioned next to each other, and the anode side is shown on the left side and the cathode side on the

right side.
From the images in Figure 4.29 to Figure 4.32, it can be observed that the average gas layer thickness is greatest in the upper corners opposite the respective outlet. The buoyancy and coalescence of forming gas bubbles leads to more gas in the upper part of the flow-field. At higher current densities, the gas layer is thicker because more gas is produced. Moreover, the gas layer of the cathode flow channels is thicker because twice as much gas is being produced compared to the anode side. For the same current density, the gas layer thickness is increasing with the temperature because the gas solubility is decreasing with it [182]. To understand the gas layer thickness or gas distribution in relation to electrolyte volume flow, current density and temperature, it is important to take the effects inside the cell into account. As the literature investigating the two-phase flow of alkaline electrolysis cells is scarce, the flow effects are compared to flow investigations conducted for PEM electrolysis. The difference between the two electrolysis types is that of using water instead of potassium hydroxide as the electrolyte solution, which results in a difference in surface tension and contact angle at the three-phase boundary of the channel material, liquid electrolyte, and gas bubble, respectively. The porous transport layer (PTL) in alkaline electrolysis cells is usually nickel-based, whereas the PTL material in PEM cells is typically titanium-based. The second relevant difference is the necessity of a functioning hydroxide ion transportation capacity through the electrolyte solution for alkaline electrolysis cells, which can be mitigated by gas bubbles. Nonetheless, the flow effects occurring in an alkaline electrolysis cell are comparable to those occurring in a PEM cell (the flow effects are compared to the anode side of PEM electrolysis cells, given that mostly no electrolyte is supplied to the cathode side) [180]. According to Leonard et al. [183], the electrolyte volume flow has little or no influence on the gas bubble diameter but on the gas bubble's detachment rate. This leads to a shift in transitioning from one flow regime to the other. A higher electrolyte volume flow therefore decreases the ohmic resistance according to Yuan et al. [180] because the local oversaturation is decreasing due to more gas bubbles forming. The investigation of Majasan et al. [184] shows that flow channels with a higher electrolyte flow rate have the tendency to contain smaller gas bubbles, whereas the flow channels with a lower electrolyte flow rate tend to contain gas bubbles with a bigger diameter or gas slugs. The flow field geometry utilized by Majasan et al. [184] is similar to the flow field geometry employed in this investigation. Their flow field used parallel flow channels and the electrolyte was distributed in a similar way. Due to the flow field design using parallel flow channels, the electrolyte flow rate was not equally distributed inside the flow channels. Wang [185] describes the behavior of the

electrolyte flow at a T-junction. At low Reynolds numbers (low flow velocities), the flow is equally divided into two separate streams. At increasing Reynolds numbers (increasing flow velocities), the arm without change (in this case, less change) in directions is supplied with a higher volume flow because of inertia. For the flowfield geometry used here, this means that by increasing the electrolyte volume flow, more of the electrolyte solution is transported along the arms of the flow distribution triangle because of inertia, creating a higher electrolyte supply to the flow channels close to the inlet, respectively, right at the end of the longer arm opposite the side of the electrolyte inlet, with less distributed to the other flow channels. Majasan et al. [184] observed that with increasing current density, a more unique electrolyte velocity over the flow channels became apparent, which they explain with a decreasing pressure loss with increasing gas content of the two-phase flow. Their observation leads to an almost equally distributed electrolyte flow within the flow channel for current densities greater than 1 A/cm^2; for lower current densities, the non-uniform electrolyte flow distribution persists. The gas layer thickness in the flow field used here is thickest for the upper corner located on the side where the flow inlet is located. Maier et al. [186] used the same PEM cell as Majasan et al. [184] and investigated the water thickness of the GDL on the anode side for different GDL materials. In their investigation, the GDL had the thinnest water layer (thickest gas layer) in the upper right-hand corner, which Majasan et al. [184] identified as the channel with the highest flow velocity. According to Wang [185], for the geometry of the inlet area used here, the electrolyte volume flow should result in a higher volume flow in the outer flow channels, which then, according to Majasan et al. [184], should result in a lower gas layer thickness in these channels. As this does not apply to the observations in Figure 4.29 to Figure 4.32 a closer examination was made of the similarities and differences of the cell used by Majasan et al. [184] and Maier et al. [186] and the cell used here. As the gas layer thickness was mainly in one corner of the cell, which is opposite the two-phase flow outlet of the flow field, it seems likely that the gas distribution is not only dependent on the geometrical factors of the inlet and the channel's geometry but also on the outlet. In this cell, the longer arm appeared to create a bottleneck for the gas bubbles to leave the flow outlet area. The water layer investigations of Maier et al. [186] seem to show the same effect for their channel closest to the outlet. In their findings, the outlet channel into which all flow field channels drained their gas–electrolyte mixture was supposedly filled up with gas from left to right, which made it harder for the last channels to push the gas out. A higher electrolyte volume flow inside the channels decreases the local oversaturation and therefore increases the ionic conductivity, such that the local gas amount produced is increasing and the gas layer is getting thicker. With a thicker gas layer, the conductivity is decreased. The buoyancy and coalescence of forming gas bubbles leads to more gas in the upper part of the flow field. At higher current densities, the gas layer is thicker because more gas is being produced. The gas layer of the cathode flow channels is also thicker because twice as much gas is produced compared to the anode side. For the same current density, the gas layer thickness is increasing with temperature because the gas solubility is decreasing with it [183]. Comparing the same operation point with different electrolyte volume flows (see Figure 4.29 to Figure 4.32), there are contradictory tendencies with respect to the influence on gas layer thickness. The potential reason for this is that at higher electrolyte volume flows, the gas bubbles detach at a smaller gas bubble size. As small gas bubbles could not be identified in the neutron radiography images because they could not be distinguished from measurement noise, the gas layer might appear to have been thinner. However, even if that was the case, from the impedance it can be seen that the ohmic resistance was slightly increasing with increasing electrolyte volume flow. The visual results and impedance measurements seem to show both an opposite effect to what is described by Yuan et al. [180]. If the rate of gas transported out of the flow field and forming gas is changed to more gas being present in the flow channels, it would result in a higher ohmic resistance, which is supported by gas being present at lower positions in the flow channels (see Figures 4.29 to Figure 4.32).

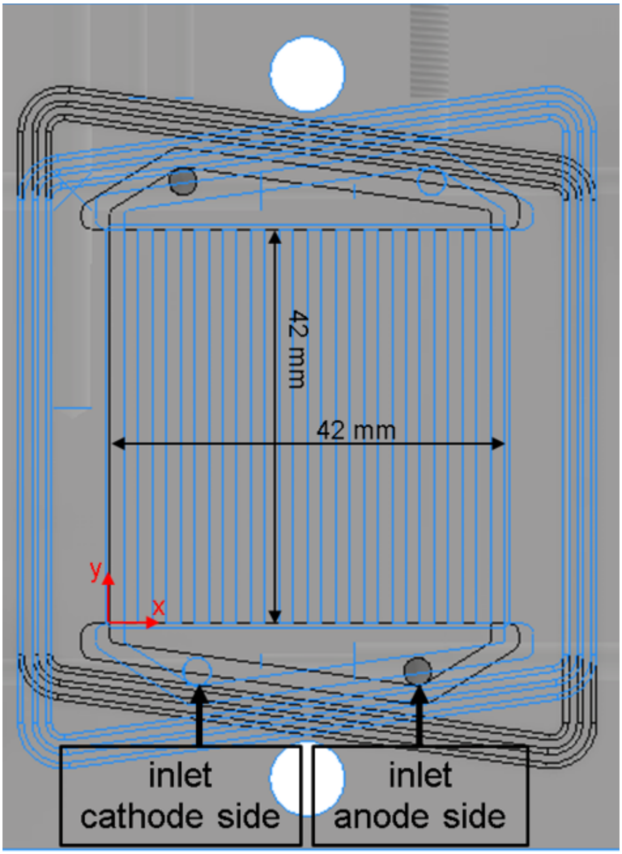

Figure 4.28: Detailed Cutout of the Used Electrolysis Cell with Depicting the Cathode (Blue Structure) and the Anode (Black Structure) Inlets and how they are Mapped on the Neutron Radiography Images.

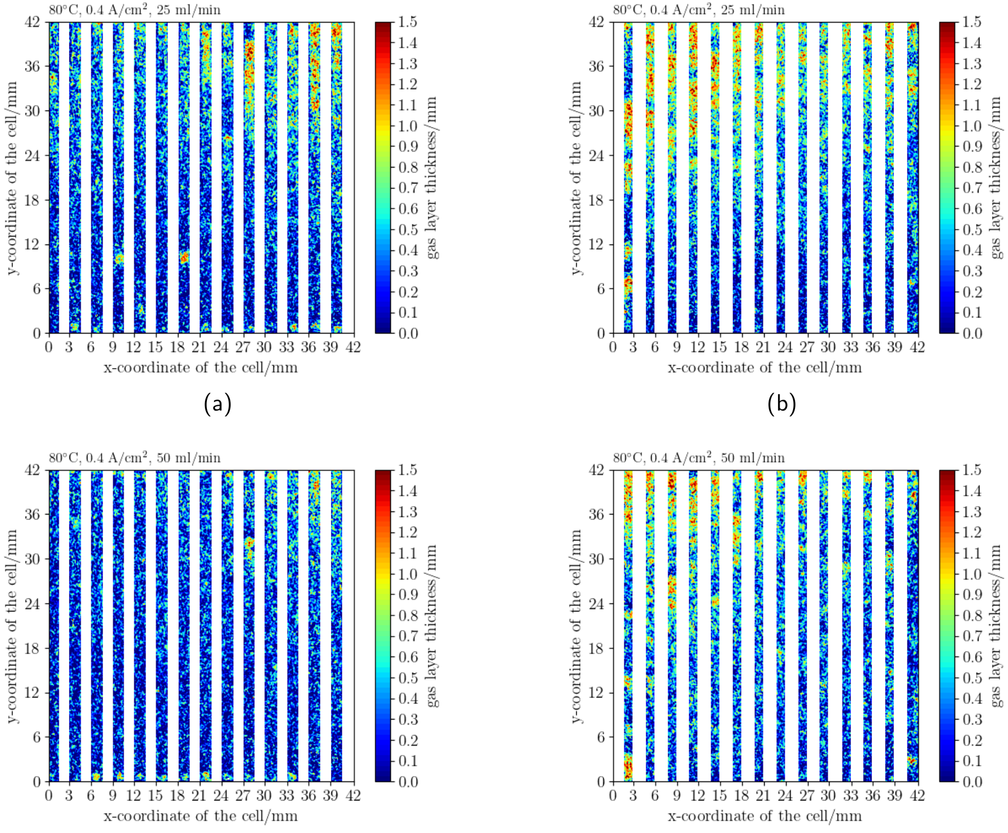

(a) (b)

(c) (d)

Figure 4.29: Mean Gas Layer Thickness at 80°C and 0.4 A/cm^2 for 25ml/min Anode (a), 25 ml/min Cathode (b), 50 ml/min Anode (c) and 50 ml/min Cathode (d).

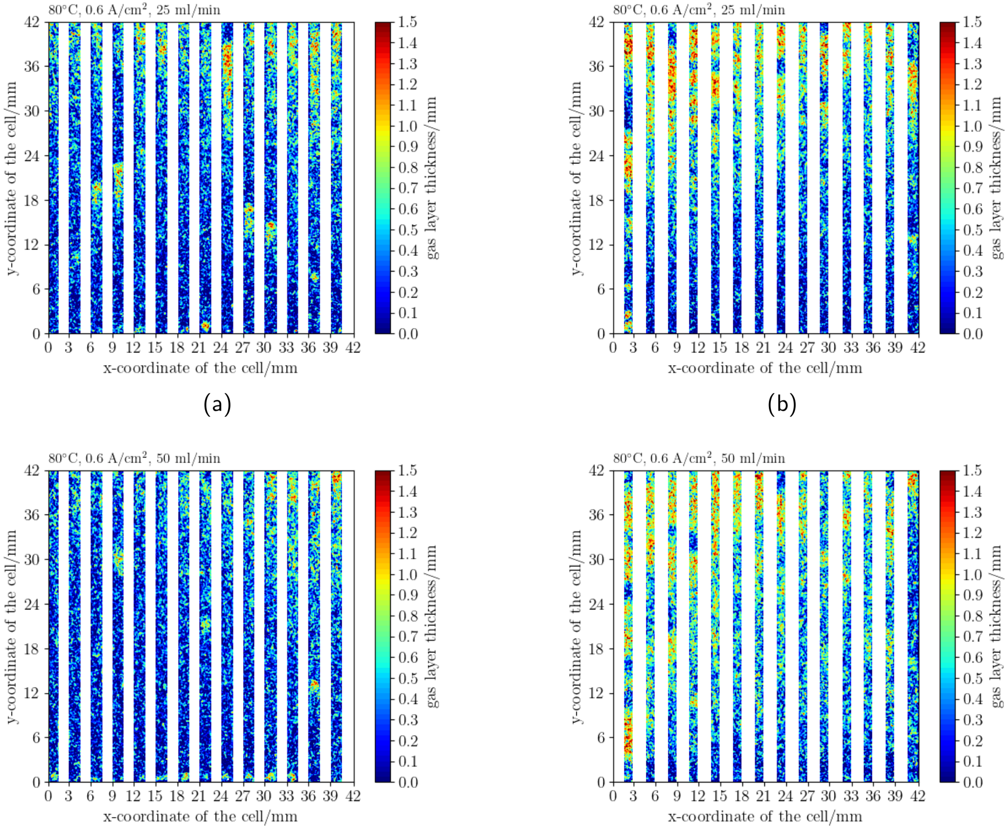

(a) (b)

(c) (d)

Figure 4.30: Mean Gas Layer Thickness at 80 °C and 0.6 A/cm^2 for 25 ml/min Anode (a), 25 ml/min Cathode (b), 50 ml/min Anode (c) and 50 ml/min Cathode (d).

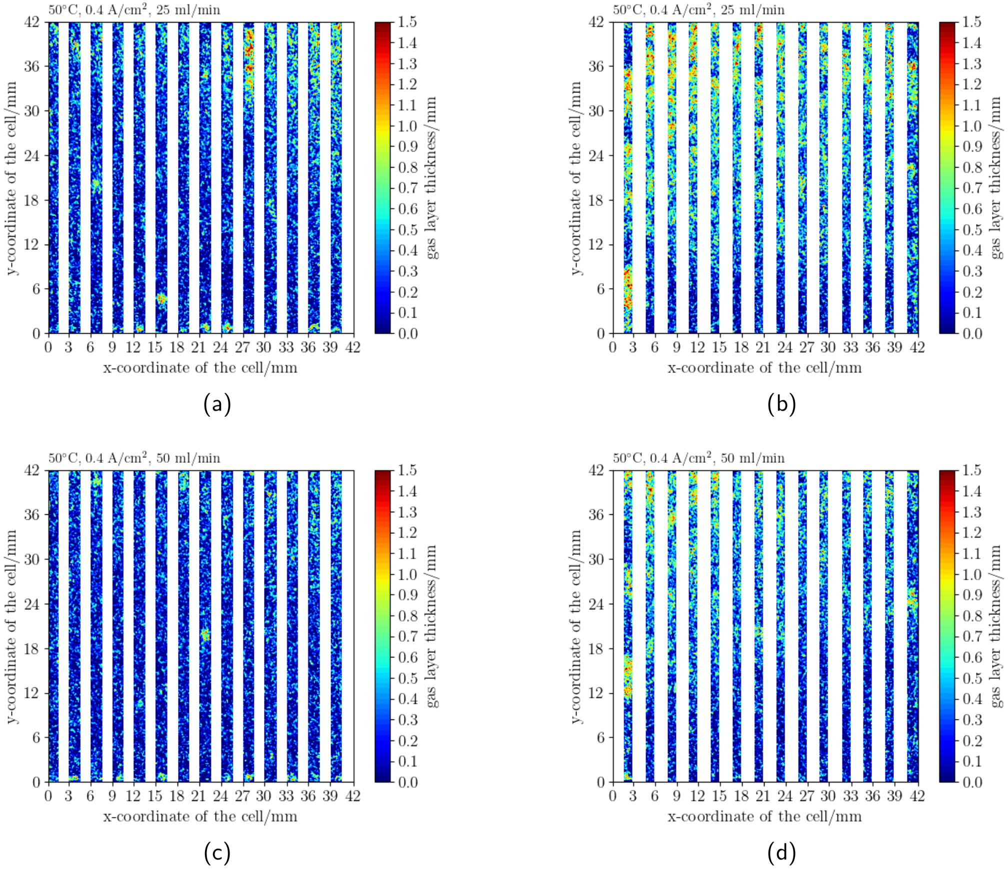

Figure 4.31: Mean Gas Layer Thickness at 50 °C and 0.4 A/cm^2 for 25 ml/min Anode (a), 25 ml/min Cathode (b), 50 ml/min Anode (c) and 50 ml/min Cathode (d).

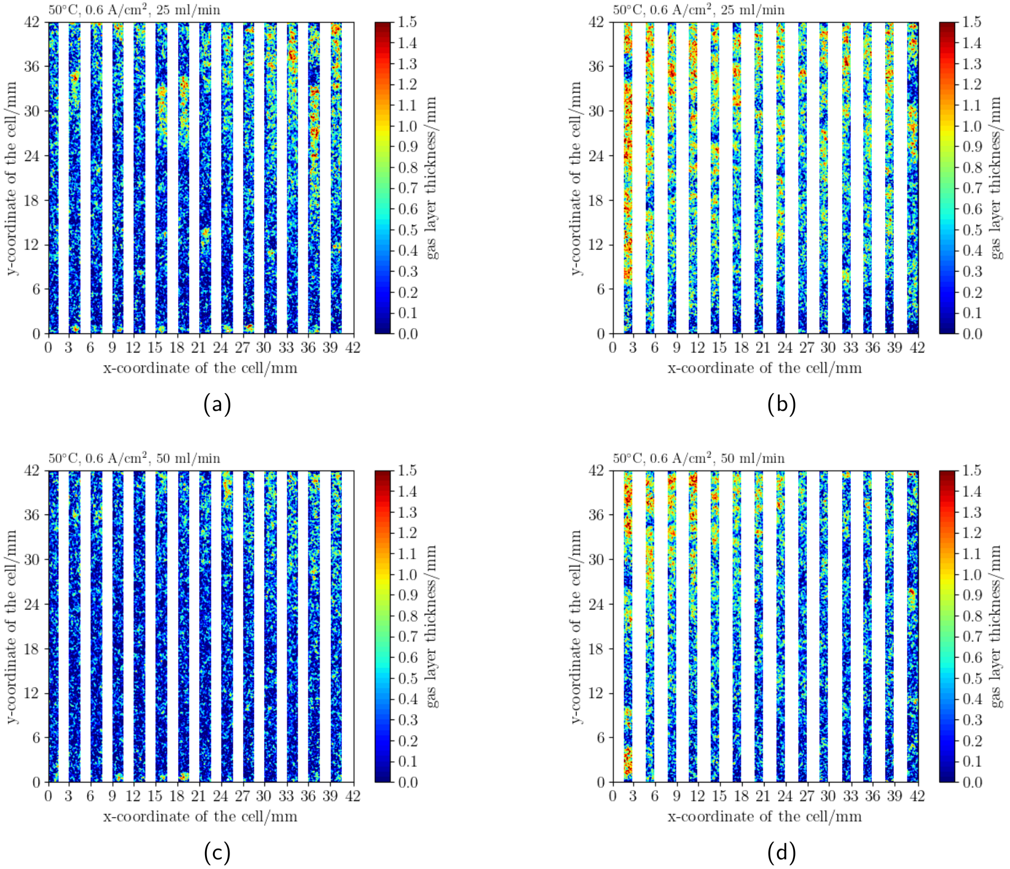

Figure 4.32: Mean Gas Layer Thickness at 50 °C and 0.6 A/cm^2 for 25 ml/min Anode (a), 25 ml/min Cathode (b), 50 ml/min Anode (c) and 50 ml/min Cathode (d).

The gas layer thickness, which is determined in this examination using neutron radiography, can be compared to the gas layer thickness calculated through Faraday's Law. For the comparison of the measured and the calculated gas layer thicknesses, a mean value of the averaged gas layer thickness over 2,500 images taken by neutron radiography is calculated by calculating the mean value over all pixels, which is the mean value of the whole cell, anode, and cathode side combined. The gas layer thickness calculated by Faraday's law is determined using Equation 4.10 as already explained in Section 3.1.4.

$$d_{gas}(y) = \frac{\left(\frac{1}{z_{H_2}} + \frac{1}{z_{O_2}}\right) \cdot \frac{jA(y)}{F} \cdot V_m \cdot \eta_F}{\left(\frac{1}{z_{H_2}} + \frac{1}{z_{O_2}}\right) \cdot \frac{jA(y)}{F} \cdot V_m \cdot \eta_F + \dot{V}_{KOH}} \cdot \frac{V_{tot}(y)}{A(y)} \tag{4.10}$$

The relation of total gas volume flow (oxygen and hydrogen) ($\dot{V}_{gas}(y) = \left(\frac{1}{z_{H_2}} + \frac{1}{z_{O_2}}\right) \cdot \frac{jA(y)}{F} \cdot V_m$) to the total volume flow (gas volume flow and the electrolyte volume flow of potassium hydroxide on anode and cathode side) ($\dot{V}_{gas}(y) + \dot{V}_{KOH}$) is compared to the relation of total gas volume inside the cell ($d_{gas} \cdot A(y)$) and the total volume of the flow channel ($V_{tot}(y)$). For the gas volume flow, the Faraday efficiency η_F is taken into account. For the calculation of the Faraday efficiency of alkaline stacks, the empirical equation developed by Mónica Sánchez et al. [130] (see Equation 3.5) can be used considering parasitic currents. In this case, a Faraday efficiency of 100 % is assumed since, here, a single cell is used. The gas layer thickness is dependent on the y-coordinate of the flow channel (see Figure 4.28), with increasing y-coordinate, the gas layer thickness is increasing. To determine a mean gas layer thickness to compare it to the neutron radiography measurement results for the mean gas layer thickness, Equation 4.11 and Equation 4.12 are used. With Equation 4.11, the mean gas volume flow ($\overline{\dot{V}_{gas}}$) is calculated with b being the width of the flowfield of 42 mm and L is equivalent to the full flow channel length of 42 mm. With Equation 4.12, the mean gas layer thickness ($\overline{d_{gas}}$) is calculated with $t_{channel}$ being the depth of the flow channel of 1.5 mm.

$$\overline{\dot{V}_{gas}} = \frac{1}{L} \int_0^{y=L} \left[\left(\frac{1}{z_{H_2}} + \frac{1}{z_{O_2}}\right) \cdot \frac{jb}{F} \cdot V_m \right] dy \tag{4.11}$$

$$\overline{d_{gas}} = \frac{\overline{\dot{V}_{gas}} \cdot \eta_F}{\overline{\dot{V}_{gas}} \cdot \eta_F + \dot{V}_{KOH}} \cdot t_{channel} \tag{4.12}$$

The resulting gas layer thicknesses are shown for 80 °C and all four measured electrolyte volume flows as shown in Figure 4.33 for the measured gas layer thickness (Figure 4.33 (a)) and for the calculated gas layer thickness (Figure 4.33 (b)).

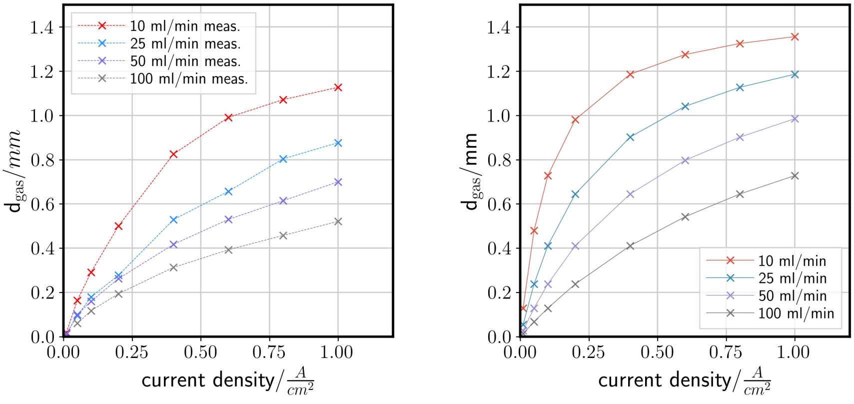

(a) (b)

Figure 4.33: Comparison of the Measured Gas Layer Thickness through Neutron Radiography (a) and the Calculated Gas Layer Thickness by Equation 4.12 (b) for 80 °C for all Measured Current Densities and for all Measured Volume Flows.

Comparing both figures, it can be seen that the mean gas layer thickness measured by neutron radiography is a little less for every operation point. The difference between measured and calculated mean gas layer thickness is greater for small current densities. The same applies by looking at the comparison of the gas layer thicknesses for the eight operation points (see Table 4.10) analyzed in more detail in this examination. The comparison is shown in Figure 4.34.

The figure shows the measured values in darker green, respectively, gray and the calculated values in lighter colors. For all in Figure 4.34 depicted operation points, the calculated gas layer thicknesses are higher compared to the measured gas layer thicknesses. The gas layer thickness is thicker the higher the current density and is decreasing with increasing electrolyte volume flow. By calculating the mean gas layer thickness using Equation 4.12, the calculated gas layer thickness considers the changing gas volume flow with increasing y-coordinate of the flow channel. However, the equation does not consider any increased residence time of the gas bubbles through wall friction, coalescence or changing buoyancy. Figure 4.29 to Figure 4.32 show that the gas layer thickness is not equal throughout the channel length, which is not accounted

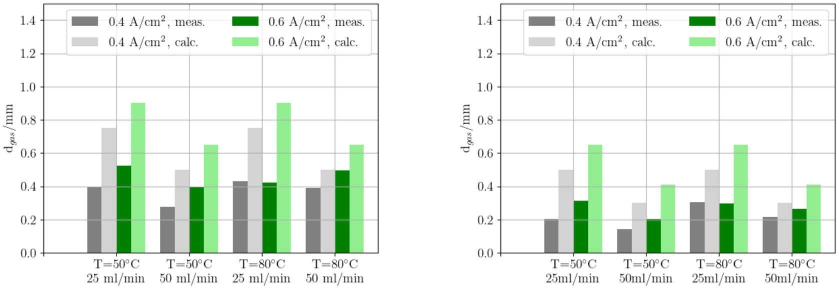

(a) (b)

Figure 4.34: Comparison of the Measured Gas Layer Thickness through Neutron Radiography (Dark Gray (0.4 A/cm^2) and Dark Green (0.6 A/cm^2)) and the Calculated Gas Layer Thickness by Equation 2.20 (Light Gray (0.4 A/cm^2) and Light Green (0.6 A/cm^2)) for Cathode (a) and Anode (b) for Combinations of 50 °C, 80 °C and 25 ml/min and 50 ml/min.

for in Equation 4.12 either. Deviations could also be a result of the measurement method itself and the way in which the images are created during neutron radiography measurements and the accuracy of the baseline images, as well as filter, subsequent image processing influences, and the image blurring due to finite spatial resolution.

A possible reason for a smaller mean gas layer thickness for the measured gas layer thickness in general and especially for lower current densities might be that small gas bubbles are not detected during the neutron radiography measurements because they cannot be distinguished from the measurement noise. From Figure 4.33 it can be seen that the difference in calculated mean gas layer thickness and measured gas layer thickness decreases with increasing current density. With increasing current density, the forming gas volume flow is increasing, and the formed gas bubbles, especially after coalescence, are bigger. This observation would support the assumption that smaller gas bubbles are not detected.

The decreasing gas saturation of the electrolyte solution with increasing temperature is also not considered in the calculation of the gas layer thickness. The crossover is also not considered in the calculated values. The amount of crossover, however, is in a range of 10^{-4} % of the total gas production [170]. In contrast to the influence of the current density, the gas saturation influence with temperature cannot be seen as clearly from the measurement data. The gas layer thicknesses measured with an electrolyte volume flow of 50 ml/min would maintain the theory of a lower gas solubility at higher temperatures and, therefore, a higher gas layer thickness at higher temperatures. But looking at 25 ml/min the trend can not be seen anymore, for 80 °C and 50 °C it is mixed, where the thicker gas layer thickness is measured.

From all observed and described effects, it can be concluded that all these effects play a role in the two-phase flow and that they are mitigated or intensified with current density, temperature, and electrolyte volume flow. A predominant influence factor can not be identified by analyzing the gas layer thickness.

Maier et al. [186] investigated the influence of different gas diffusion layer materials in a PEM electrolysis cell with a parallel flow channel at the anode side using imaging techniques. They found out that even at low current densities with only small gas amounts being present, the water saturation inside the porous layer is not fully saturated. They concluded that this is due to not connected pores to the overall pore network but also because pores, which are connected to the pore network and are not or are insufficiently supplied with water. Haverkort et al. [5] found similar results for an alkaline zero-gap electrolysis cell. They covered the frontal area of the electrode with epoxy and got similar results for the polarization curves compared with an electrode without epoxy. They assumed that the frontal area in an alkaline electrolysis cell is not active due to gas bubbles blocking the pores of the separator or electrode material blocking the separator pores.

From the neutron radiography investigation, a reduced active cell area due to blockage of gas bubbles cannot be proven but has to be taken into account as a possible reason for the difference between measured and calculated values for the gas layer thickness. This might be an explanation that not an overall trend of the influence factors temperature, electrolyte volume flow, and current density can be seen. The comparison between theoretical and measured gas layer thickness shows the urgency of improved measurement methods to investigate the two-phase flow. Even at higher current densities, the difference between measured and calculated gas layer thickness is between 20 - 25 %. If almost a quarter of the gas layer is not detectable with the established, powerful measurement methods like neutron radiography, it is difficult to find general conclusions about the two-phase flow behavior.

4.3.3 Gas Bubble Velocity

The gas bubble velocity of the gas bubbles inside the alkaline electrolysis cell, measured by neutron radiography are detected and tracked by *Trackmate*, a plug-in of the image processing open-source software *ImageJ* [127]. The procedure of detection and tracking with *Trackmate* is described in Section 3.1.3. An example of the output generated by *Trackmate* can be seen in Figure 4.35. A sequence of images is uploaded to *ImageJ* [127] and processed.

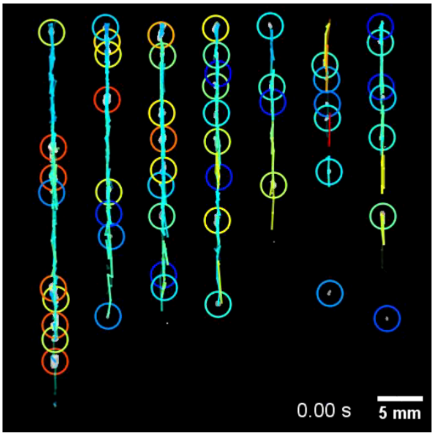

Figure 4.35: Output Generated by *Trackmate* in Form of Gas Bubble Velocity and Gas Bubble Detection Recognition Rate.

The output generated by *Trackmate* gives the trajectory of single gas bubbles over the different frames. In Figure 4.35, it can be seen, that the detected bubbles are marked by a circle. The trajectories of the single gas bubbles are marked by colored lines. The color of the line is a measure of the gas bubble velocity. Since *Trackmate* was developed in order to track microorganisms, it is able to track moving objects in all possible directions and is also able to identify the merging/ splitting of moving objects. In this case, the gas bubbles are moving upwards but have basically no movement in x-direction (for axis definition, see Figure 4.28). To avoid the algorithm misinterpreting anode and cathode gas bubbles to merge, split, or identify movement in x-direction, although there are two gas bubbles in neighbouring anode and cathode channel present, only every second flow channel of anode side and every second channel on cathode side is evaluated. The chosen anode and cathode images of the flow channel are masked and processed separately in *Trackmate*. The comparison of the velocity distribution over the flow channels of the flow field, with the set of the excluded channels lead to a similar velocity distribution, which is why the analysis with every second channel of the flowfield was assumed to be representative enough for all channels.

For the gas bubble velocity analysis, all recorded 15,000 images of the single operation points are used. The gas bubble velocity is analyzed in two different ways in the following. On the one hand side, the gas bubble velocity is averaged for every single gas bubble and plotted at the location of the cell, where the bubble was first recognized by *Trackmate*. For a better overview, the flow channels are sliced in increments of 2 mm along their y-coordinate. The mean gas bubble velocities for each gas bubble are averaged in this increment. For each increment, the resulting mean gas bubble velocity is shown as a colormap. The results can be seen in Figure 4.37 for 80 °C and in Figure 4.36 for 50 °C. The second way to display the gas bubble velocity is by showing the gas bubble velocity of each gas bubble at the specific location along the flow channel. For a better overview, the channels are again divided into segments of 2 mm length, and the velocity is averaged in this segment. The regarding figures are shown in Figure 4.38 and Figure 4.39. As a remark, the anode and cathode channel are plotted together in one figure, for both ways to analyze the velocity of gas bubbles, although the results were evaluated separately for anode and cathode in *Trackmate*. The color map is depicted in colors from blue (0 m/s) to red (50 m/s), if regions in the channel are depicted in gray, then the average velocity for this channel region has a negative value. Negative velocity values occur, especially in the upper region in the last segments of the channel. By looking at the single pictures of the operation points, it can be seen that often gas bubbles are stuck for some time at the end of the channel and oscillate with the pulsation of the membrane pump, which results in a negative velocity. The oscillation most likely causes these gas bubbles to be recognized and detected more than once. For visual differentiation of anode and cathode flow channels in Figure 4.36 to Figure 4.39, the anode channel background color is shown in light red, and the cathode channel in white color.

Before showing the detailed velocity values distributed over the flowfield analyzed with both evaluation methods described, an overview of the mean gas bubble velocity for every analyzed operation point is given in Table 4.11, as well as the number of detected gas bubbles detected by *Trackmate*. The interpretation is done together with the interpretation of Figure 4.37 to Figure 4.38.

Description of the Gas Bubble Velocities Analyzed by the Position where they are First Detected

The description of Figure 4.36 and Figure 4.37 is structured as follows; First, the effects of current density, electrolyte volume flow, and temperature on the gas bubble velocity at the coordinate of the first detection in the flow channels are described, then the differences between anode and cathode, and last, the effects caused by the cell

Table 4.11: Mean Velocity and Number of Detected Gas Bubbles Evaluated by *Trackmate*.

Temp. [°C]	**Electrolyte Volume Flow** [ml/min]	**Current Density** [A/cm^2]	**Mean Velocity** [mm/s]	**Number of Detected Gas Bubbles** [-]	**Mean Velocity** [mm/s]	**Number of Detected Gas Bubbles** [-]
			Anode		Cathode	
80	50	0.4	26.14	1527	26.37	18513
80	50	0.6	24.05	4309	23.49	32081
80	25	0.4	10.32	13972	18.5	39983
80	25	0.6	10.91	7543	11.56	19599
50	50	0.4	12.02	3281	21.48	57626
50	50	0.6	12.08	2271	22.21	42272
50	25	0.4	11.12	7232	24.96	31429
50	25	0.6	14.21	14129	23.69	42112

geometry and other general effects.

Figure 4.36 and Figure 4.37 show the number of gas bubbles that are detected by *Trackmate*, the exact number can be seen in Table 4.11. The number of detected gas bubbles is increasing with current density for the operation points 80 °C and a higher electrolyte volume flow of 50 ml/min and for 50 °C and a lower electrolyte volume flow of 25 ml/min. For the rest of the operation points, the number of gas bubbles is decreasing with current density. Even with small gas bubbles not being detected on the neutron radiography images, from Figure 4.33 it can be seen that the gas layer thickness and, with that, the detectable gas amount is increasing with increasing current density and the gas layer thickness is thicker for lower electrolyte volume flow. This means that the number of gas bubbles is not directly linked to the amount of gas, which might be mainly because of the ability to detect the gas bubbles on the images, coalescence, and gas solubility. For 80 °C and 50 ml/min, the results seen from Figure 4.33, Figure 4.37, Figure 4.36 and Table 4.11 are in good accordance for the following properties. The gas layer thickness is increasing with current density, the number of gas bubbles is increasing with current density, and with a decreasing electrolyte volume flow, the gas layer thickness is increasing, as well as the number of gas bubbles. For 80 °C and 25 ml/min, the number of gas bubbles detected is increasing compared to 25 ml/min at the same current density, but the number of gas bubbles at a lower current density of 0.4 A/cm^2 is higher compared to the number of higher current density (0.6 A/cm^2). At a smaller electrolyte volume flow, the gas bubbles grow bigger, because the detachment is later in time, and therefore the gas bubble diameter is bigger. The detector is able to detect bigger gas bubbles and is limited to a certain size, if the gas bubbles are too small, they cannot be distinguished from measurement noise. With increasing current density at 80 °C and 25 ml/min with a lower gas solubility at the higher temperatures and a greater gas bubble diameter because of the lower electrolyte volume flow, the gas bubbles seem to coalesce more and form longer gas bubble slugs. For 50 °C this seems not to be the case for lower electrolyte volume flows, which might be because the gas solubility is higher. Therefore, at higher electrolyte volume flow, it can be seen for increasing current density that the number of gas bubbles is decreasing, which could also only be explained by a higher degree of coalescence. From the number of detected gas bubbles, it can be seen that a lot fewer gas bubbles are detected on the anode side compared to the cathode one. For 25 ml/min, the difference is 2.5–4 times less. The difference is even greater between both sides at a higher volume flow, at 50 ml/min (between 7–19 times lower). The lower number of detected gas bubbles, especially at higher electrolyte volume flows, can be explained by an earlier detachment at higher electrolyte volume flows. To some extent, the difference might also be caused by the limitation of being able to identify small gas bubbles in the neutron radiography images.

Comparing the differences in gas bubble velocities caused by different current densities for different operating points, it appears that the gas bubbles at higher current densities start slower at a lower y-coordinate. The slower gas bubble velocity might be caused by the greater gas amount produced at higher current densities. The greater gas amount is likely to cause more coalescence, especially with increasing y-coordinate of the flow channels. To some extent, the transportation of gas out of the flow channels might even be hindered, which might be the reason why the velocity drops before the flow exits the channel. With higher current density, more gas bubbles are detected at a lower y-coordinates in the flow channels. On the neutron radiography images, gas bubbles must attain a certain size to be distinguished from measurement noise, and therefore, more gas bubbles can be detected at higher current densities. The gas bubbles are already bigger at lower y-coordinates at higher current densities. Other than that, the current density does not appear to have a significant influence on the gas bubble velocity or the mean gas bubble velocity on the anode and cathode sides. In contrast to the observation made here, Majasan et al. [184] observed a linear increase in the gas bubble velocity at a current density range comparable to the range of this evaluation. They explained the increasing gas bubble velocity with increasing current density with a lower pressure drop on the basis of increasing amounts of gas in the electrolyte solution.

The electrolyte volume flow has a direct influence on the gas bubble velocity for two reasons. Firstly, the electrolyte solution drags the gas bubbles with them or pushes them through the channel, depending on the gas bubble size. Secondly, the electrolyte volume flow has an influence on the detachment diameter and, therefore, on the size of the gas bubbles. If the gas bubbles are small, they are dragged by the electrolyte solution, which does not necessarily mean they have a similar velocity, at a bigger diameter of the size of the channel width, they are being pushed probably at the same velocity as the electrolyte solution. Small gas bubbles should be less objective to wall friction and, therefore, could have higher velocities than bigger ones. This would be supported by the gas bubbles having higher velocities the lower they are detected in the channel at a point where they have not coalesced yet. The gas bubble size, however, cannot be evaluated here. From Figure 4.37 and Figure 4.36 it can be seen that the gas bubbles for higher electrolyte volume flow of 50 ml/min are first detected at higher y-coordinate in the channel compared to the ones measured at 25 ml/min, which probably shows the smaller gas bubble diameter cannot be detected and the gas bubbles are first detected after coalescing with other gas bubbles on their way up the channel. Majasan et al. [184] did find an increasing performance with increasing electrolyte volume flow. They suggested a better heat supply, shorter slug length, and better reactant availability to be the reason. A dependency between electrolyte volume flow and electrolysis performance cannot be seen in this examination. Whereas it must be mentioned that Majasan et al. [184] found this dependency for higher current densities compared to the ones used here.

The gas bubble velocity seems to be slightly higher at lower temperatures by looking at the gas bubble velocity distribution (see Figure 4.37 and Figure 4.36) and the mean gas bubble velocities (see Table 2) mostly show the same result. At lower temperatures, the gas solubility is higher, and less gas in form of gas bubbles is present, which might be the reason for a higher gas bubble velocity since the gas bubbles might be smaller and are less objective to wall friction and coalescence. By looking at the plain numbers of gas bubbles in Table 4.11, no influence of the temperature on the gas bubble number can be seen.

Comparing the gas bubble velocity of anode and cathode it can be seen that the highest gas bubble velocities occur in the cathode channel. Oxygen has a higher density compared to hydrogen, which might lead to a higher gas bubble velocity due to buoyancy, but they are more objective to coalescence and wall friction, whereas the smaller hydrogen gas bubbles can reach higher velocities.

Due to the geometry of the cell and the parallel flow channels, the following effects can be observed; More gas bubbles are detected on the side where the electrolyte inlet is located on anode and cathode side (see Figure 4.28). The gas bubbles are first detected lower in the flow channel on the inlet side, whereas the gas bubbles are faster in the flow channel opposite to the inlet.

As a general observation, it can be seen that the gas bubble velocity of gas bubbles, which form at a low point in the channel, is higher and decreases with increasing y-coordinate of detection. The reason might be that the lower the gas bubbles form, the lower the degree of coalescence in the beginning of their formation, and the smaller they are in the beginning and the faster they can be on average on their path through the channel. Additionally, they have less wall friction

Similar findings were published by Majasan et al. [184]. They investigated the two-phase flow behavior of a PEM electrolysis flow cell by taking temperature, current density, and electrolyte volume flow into account as influence factors on the cell performance and the gas bubble velocity. They also used a flow field with a parallel flow channel and observed an uneven distribution in electrolyte flow and gas bubble distribution. The liquid flow rate was higher on the side opposite to the inlet in their cell, and the gas amount was lower, but the gas bubble velocity was higher. These findings are in good accordance with the observations made in this examination regarding the difference in the geometry of the flow distribution area on the inlet and outlet. Majasan et al. [184] used a straight channel, from which the parallel channels are located with a 90 ° angle. In this case, the electrolyte flow distribution area has a triangle shape with the inlet located more to one side with a shorter arm of the triangle and the opposite side of the inlet with a longer arm. As Wang [185] describes the electrolyte flows because of inertia with geometries like this along the arms of the flow distribution triangle, which results in higher electrolyte volume flows in the outer channel and the highest electrolyte volume flow at the end of the longer arm of the triangle.

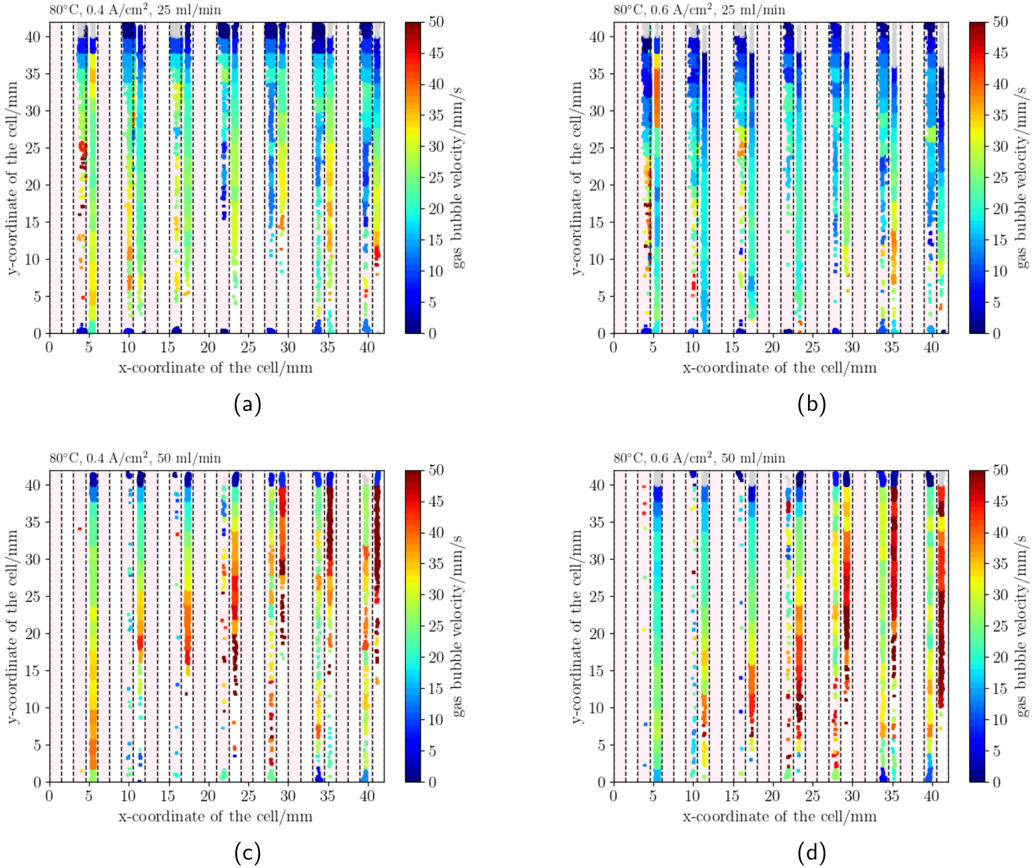

(a) (b) (c) (d)

Figure 4.36: Single Gas Bubbles Detected by *Trackmate* at the Position Where they First are Detected Depicted by their Mean Velocity for 80 °C, 0.4 A/cm^2 and 25 ml/min (a), 80 °C, 0.6 A/cm^2 and 25 ml/min (b), 80 °C, 0.4 A/cm^2 and 50 ml/min (c) and 80 °C, 0.6 A/cm^2 and 50 ml/min (d).

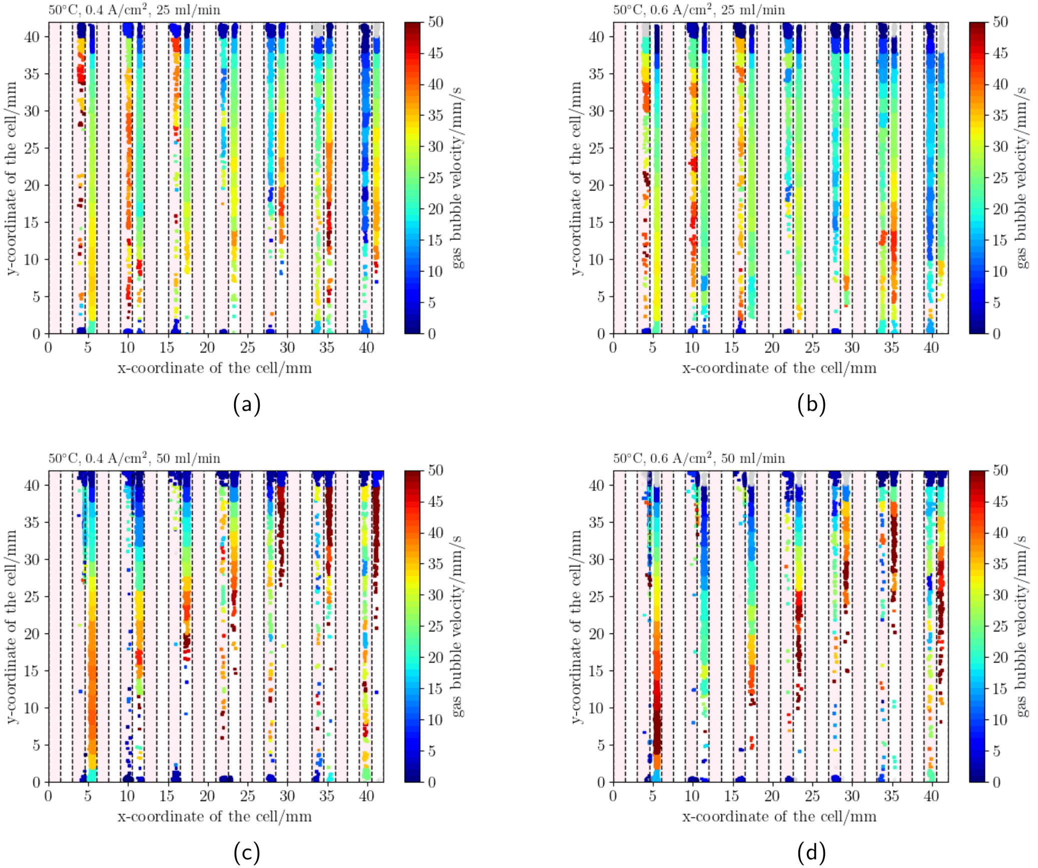

(a) (b)

(c) (d)

Figure 4.37: Single Gas Bubbles Detected by *Trackmate* at the Position Where they First are Detected Depicted by their Mean Velocity for 50 °C, 0.4 A/cm^2 and 25 ml/min (a), 50 °C, 0.6 A/cm^2 and 25 ml/min (b), 50 °C, 0.4 A/cm^2 and 50 ml/min (c) and 50 °C, 0.6 A/cm^2 and 50 ml/min (d).

Description of the Gas Bubble Velocity Analyzed at the Position where they are Detected

In Figure 4.38 and Figure 4.39 the detected gas bubbles are plotted at each location, where they are detected with the velocity that the regarding gas bubble has at the particular location. The number of the data points does not show the number of detected gas bubbles. If a gas bubble is detected on e.g. 30 frames, the plot has 29 data points of the same gas bubble at different locations with different velocities in Figure 4.38 and Figure 4.39.

From the figures, the areas in the channels can be seen where no gas bubbles are detected at all. At lower temperature (50 °C) and faster electrolyte volume flow (50 ml/min) for both analyzed current densities (Figure 4.39 (c) and (d)) in the anode channels opposite from the electrolyte inlet (left side) at the lower half of the channels, there are almost no detected gas bubbles. The closer the channel is located to the electrolyte inlet, the lower in the channel gas bubbles are starting to be detected. The same can be seen for the cathode flow channels. For anode and cathode flow channels, the same effect can be seen at 80 °C and 50 ml/min for both analyzed current densities (Figure 4.38 (c) and (d)). For both temperatures at a volume flow of 25 ml/min at both current densities (Figure 4.38 (a) and (b) and Figure 4.39 (a) and (b)) the detection of gas bubbles is distributed basically over every coordinate of the flow channel on anode and cathode side. The aforementioned effects might be explained by the better gas solubility at lower temperatures and the smaller detachment diameter of the gas bubbles at higher electrolyte volume flows, which leads to small gas bubbles that are not recognized in the neutron radiography images due to the indistinguishability to measurement noise. The effects that can be seen in the gas bubble velocity distribution figures are mostly very similar to the effects already explained for Figure 4.36 and Figure 4.37. The interesting observation in Figure 4.38 and Figure 4.39 are the gas bubble velocity patterns throughout the channel. For all analyzed operation conditions, the gas bubble velocity shows a fluctuation of velocity throughout the channels. In general, the velocity is increasing from low velocities to higher velocities throughout the channel and at the end of the channel to lower velocities again. The course of velocities, however, is section-wise fluctuating between higher velocities and lower velocities. Since the used pump is a membrane pump, which is oscillating, it is necessary to consider that the fluctuation is caused by the pump. However, since the images are averaged for gas bubbles from 15000 images (5 minutes), the effects should not be visible here. The more likely explanation is that the forming and coalescent gas bubbles are accelerated by buoyancy and the electrolyte volume flow and decelerated again when meeting a slower gas bubble slug in front and accelerating again after coalescing. A comparable investigation has not been found in the literature.

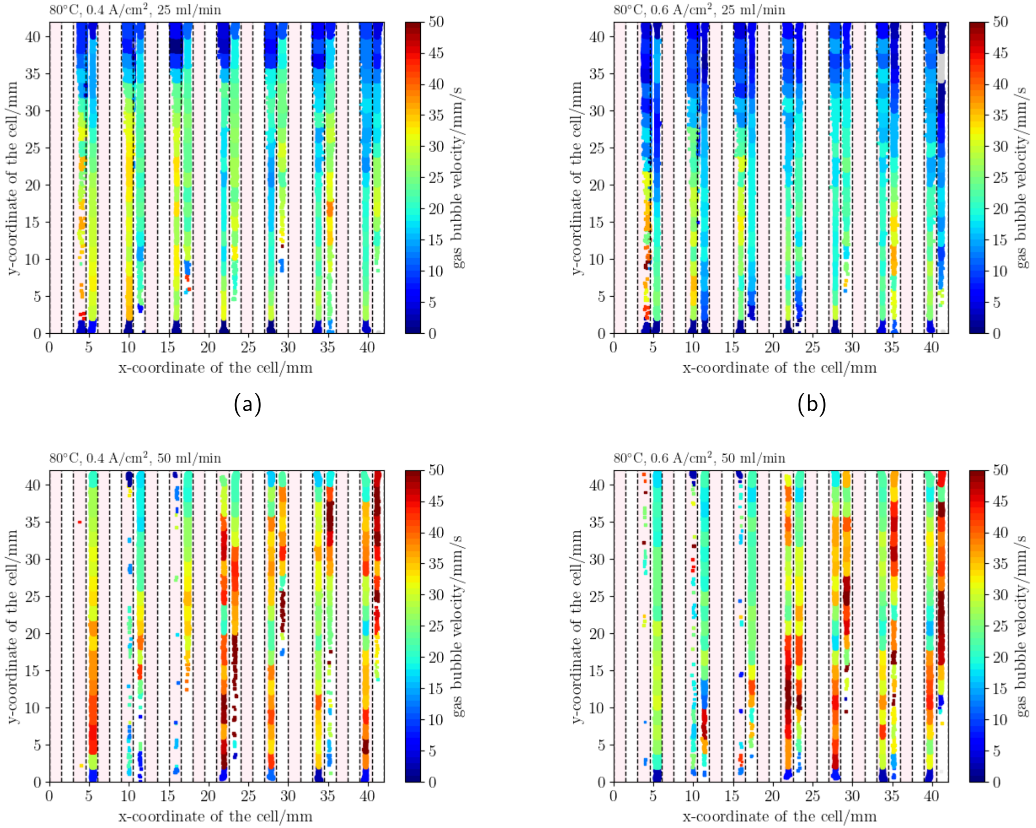

(a) (b) (c) (d)

Figure 4.38: Tracked Gas Bubble Velocity Distribution in the Flow Channel for 80 °C, 0.4 A/cm^2 and 25 ml/min (a), 80 °C, 0.6 A/cm^2 and 25 ml/min (b), 80 °C, 0.4 A/cm^2 and 50 ml/min (c) and 80 °C, 0.6 A/cm^2 and 50 ml/min (d).

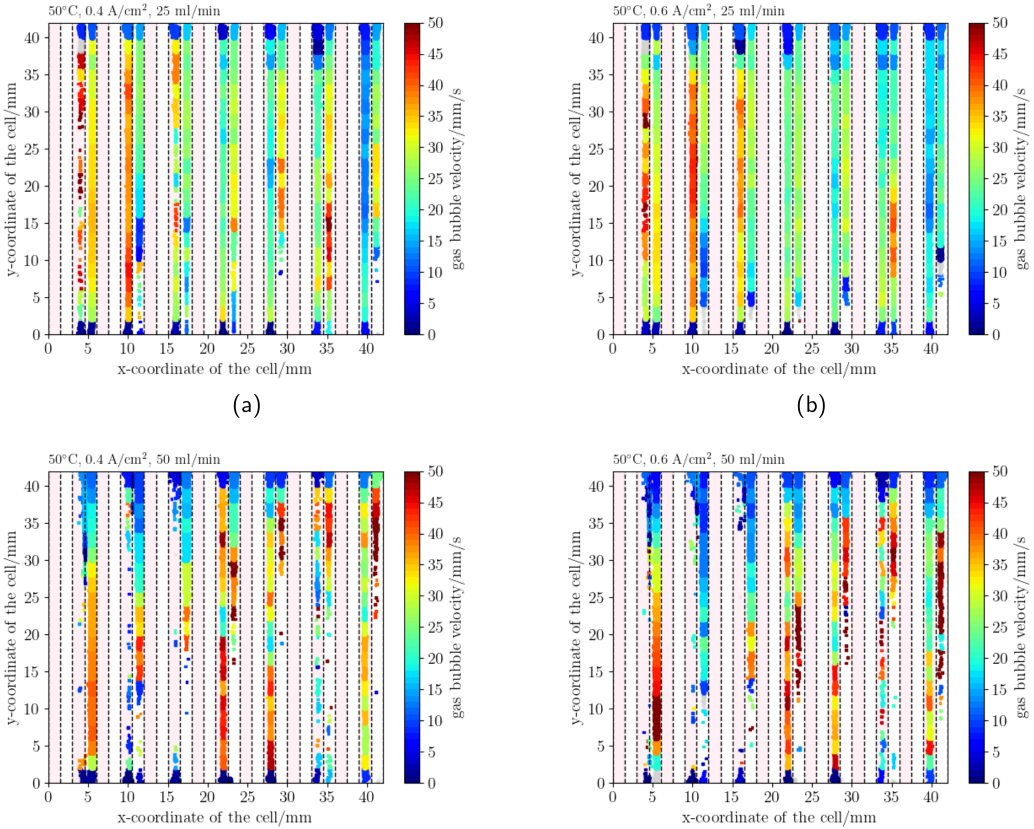

(a) (b) (c) (d)

Figure 4.39: Tracked Gas Bubble Velocity Distribution in the Flow Channel for 50 °C, 0.4 A/cm^2 and 25 ml/min (a), 50 °C, 0.6 A/cm^2 and 25 ml/min (b), 50 °C, 0.4 A/cm^2 and 50 ml/min (c) and 50 °C, 0.6 A/cm^2 and 50 ml/min (d).

4.3.4 Contact Angle

The contact angle measurements with the method described in Section 3.3.4 determines the contact angle at the three-phase boundary oxygen (anode side) or hydrogen (cathode side) in potassium hydroxide with the nickel surface of the flow channel. The contact angle to the nickel foam surface is not visible in the images, because of the through-plane direction of the measurements.

In Figure 4.40 the resulting contact angles are shown for the different operation points. In each subfigure, the contact angles are shown for the anode (A) and cathode (C) side. For each side the mean contact angle of the gas bubbles is shown, divided into the mean contact angle of the left side of the gas bubble in the channel and the mean contact angle on the right side of the gas bubbles in the channel. Since the results for 80 °C look very similar to the results of 50 °C, 80 °C is shown in Appendix A.2.3. In Figure 4.40, for all sub-figures ((a) to (d)), the contact angle increases for the left side contact angle of anode and cathode with x coordinate of the cell and decreases for anode and cathode for the right side contact angle. The expectation for the contact angle was that the right side and left side angle of bubbles in the same channel at the same operation point is very similar. The possible reasons why the resulting angles differ so much from right to left side angles could originate from the evaluation algorithm and the cell assembly. As explained by Yu et al. [152], the difficulty in determining the contact angle is to identify the channel boundary. In the neutron radiography images, the boundary of the channel is not clearly visible because of the measurement noise. Additionally, the channels have a width of 1.5 mm, and the images have a pixel size of 91 µm, which results in a pixel size of approximately 16.5 pixel per channel and means that there is no clear channel boundary. Nonetheless, by shifting the channel boundaries pixel-wise to one side or the other the results for the contact angle of the right and left side do not change significantly. The figures with the results are shown in Appendix A.2.3. Therefore, the more likely cause for the significant difference in right side and left side contact angle is the cell assembly combined with manufacturing tolerances. The cell is supposed to have the channel of the anode side exactly where the land on the cathode side is located. If the flowfield geometry from anode to cathode side differs slightly or the two flowfield plates are slightly shifted during cell assembly, this could cause the resulting contact angle differences. The effect that the contact angle is getting smaller respectively bigger with the x-coordinate of the cell might actually show that the flowfield plates are slightly shifted.

Another possible explanation for the deviation between the right and left side contact angles of the gas bubbles could be, that the gas bubbles are influenced by the flow distribution area. In previous sections, it was already discussed that the electrolyte flow is not uniform over the different channels, which might also influence the electrolyte flow from left side to right side within the single channel. Therefore, the gas bubbles could be directed more towards one side of the channel. But if so, it would be expected that the gas bubbles of the anode and cathode side for the right side, respectively, the left side, are directed in different directions because their flow inlet is located on opposite sides. From Figure 4.40 it can be seen that this is not the case.

A quantitative result for the contact angle cannot be achieved for every channel, but it is assumed that the average overall contact angle is an approximate value for the comparison of the contact angles measured during particle image velocimetry measurements. It is assumed that the contact angles, which are determined too small on one side of the cell and too big on the other side for the gas bubbles balance each other. The averaged contact angles for the different operation conditions can be seen in Table 4.12. The averaged values do look as expected and explained earlier in this sub-section; The contact angles of the right side of the gas bubbles and the left side of the gas bubbles are expected to have approximately the same values. The average contact angles for all the operation points show similar values. In literature, no comparable results of contact angles of three-phase boundaries of this combination could be found for value validation. Lafmejani et al. [187] used 50 ° to simulate oxygen gas bubbles of a PEM electrolysis cell. Unfortunately, they did not state for which operation conditions this value is valid and where it comes from. Song et al. [188] measured the contact angle of water droplets in nitrogen atmosphere under different pressure values. The lowest pressure shown is 50 bar, and the contact angle on stainless steel is approximately 80 °. The here obtained values have a similar range as the two mentioned above for similar systems.

Table 4.12: Averaged Contact Angle overall Gas Bubbles of a Single Operation Point.

Temperature [°C]	**Electrolyte Volume Flow** [ml/min]	**Current Density** [A/cm^2]	**Left Contact Angle** [°]	**Right Contact Angle** [°]
80	50	0.4	54.5	53.2
80	50	0.6	57.8	56.3
80	25	0.4	57.2	56.8
80	25	0.6	57.7	56.5
50	50	0.4	52.5	54.4
50	50	0.6	54.5	56.6
50	25	0.4	57.4	55.9
50	25	0.6	56.6	56.6

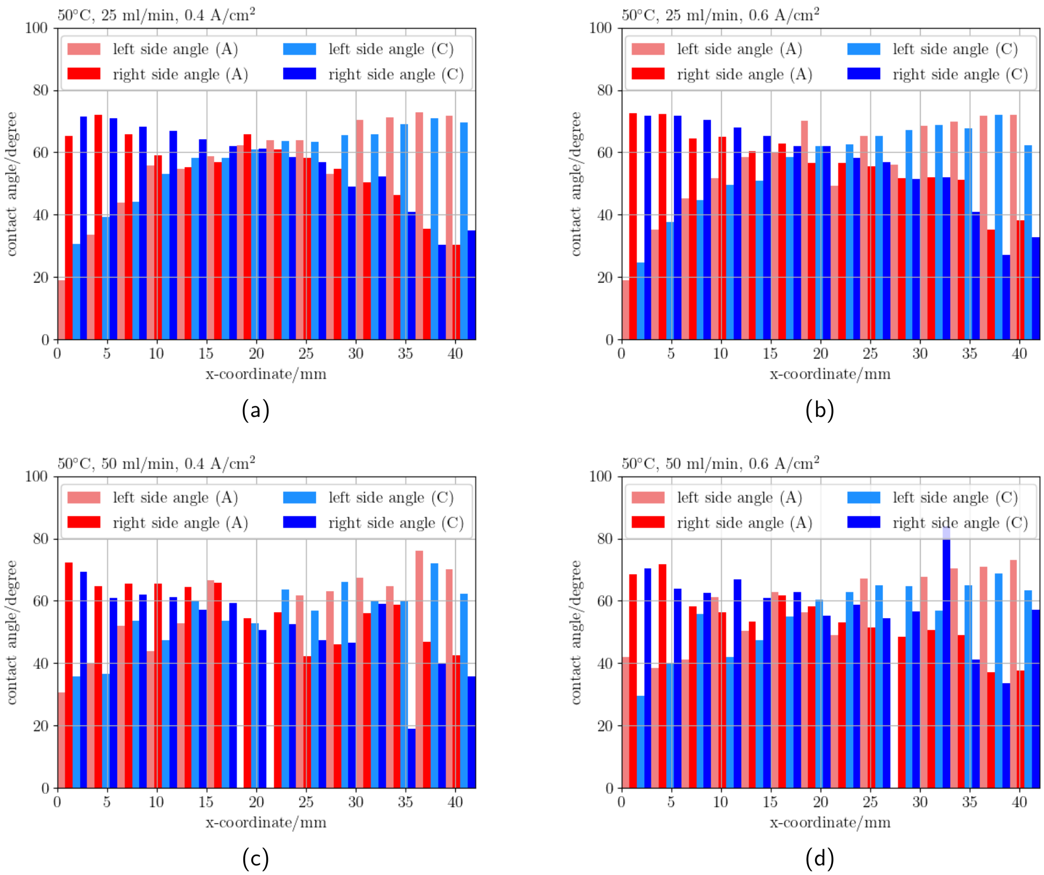

(a) (b) (c) (d)

Figure 4.40: Contact Angle Distribution in the Flow Channel for 50 °C, 0.4 A/cm^2 and 25 ml/min (a), 50 °C, 0.6 A/cm^2 and 25 ml/min (b), 50 °C, 0.4 A/cm^2 and 50 ml/min (c) and 50 °C, 0.6 A/cm^2 and 50 ml/min (d).

4.3.5 Summary

The neutron radiography measurements are conducted using the to date world's most powerful neutron source and achieving the lowest ever recorded frame rate of the two-phase flow of an alkaline electrolysis cell. The in this section described measurement results are used as baseline data to compare them to the multiphase particle image velocimetry measurements, which can be used as a simpler alternative to visualize the two-phase flows of electrochemical flow cells. The electrochemical investigations of the alkaline electrolysis cell at different operation conditions showed that the polarisation curves were not affected by electrolyte volume flow, but the cell increased efficiency with increasing temperature. Additionally, the importance of investigating the breaking-in behavior of the cell was discussed. The EIS spectra have shown an increase of the high frequency resistance with decreasing temperature. The electrolyte volume flow did not seem to influence the high frequency resistance at low current density, but there seemed to be an influence that the high frequency resistance slightly increased with increasing volume flow, visible from 50 mA/cm^2 on. The gas layer thickness seems to be influenced by the temperature and the current density, with increasing current density and increasing temperature the gas layer thickness seemed to be increasing. The electrolyte volume flow is showing contradictory tendencies on the gas layer thickness. The geometry and especially the inlet and outlet location seemed to have a substantial influence on the gas bubble distribution of the flowfield and the gas bubble velocity. The temperature and the electrolyte volume flow have shown some tendencies that do not have a clear indication of their relation towards the gas bubble distribution and velocity. For the current density, however, no influence could be identified. The gas bubble velocities seem to be rather fluctuating instead of being linear, decelerating or accelerating. The calculated contact angle values have shown different contact angles for the left and the right side of the gas bubble in the flow channel, which is discussed in this section and more likely to be caused by the computation method or the cell design or the cell design rather than a real physical occurrence.

4.4 Two-phase Flow Behavior using Particle Image Velocimetry

In this section, the results of the two-phase flow modeling of an alkaline electrolysis zero-gap flow cell using a transparent half-cell and its investigation using multiphase particle image velocimetry are shown. The methodology is described in detail in Section 3.2. The velocity of the liquid phase was measured by dividing the cell into nine segments (cf. Figure 3.9). The gas bubble velocity is recorded for all 14 channels at once. In addition to the gas bubble and liquid phase velocity, the gas amount is determined in percentages. The gas bubble velocity range and the gas amount are compared to the results of the neutron radiography measurements, and the comparability of the measurement methods is assessed.

During the particle image velocimetry measurements, the cell is operated with an orientation towards the camera, as depicted in Figure 4.41. The inlet of the electrolyte solution is on the lower left side of the cell, which is equal to the cathode electrolyte inlet position on the neutron radiography images (see Figure 4.28). For the anode side the results in this section are shown according to the orientation in Figure 4.41 with the shown coordinate system. The only exception is Figure 4.49 and Figure 4.48; The two figures have the cell orientation used in neutron radiography (see Figure 4.28) in order to compare the correct flow channel from neutron radiography and transparent cell measured with particle image velocimetry measurements.

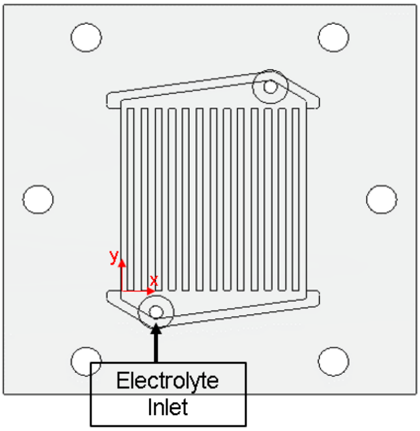

Figure 4.41: Quartz Glass Cell Orientation and Location of the Electrolyte Inlet.

4.4.1 Velocity of the Liquid Phase

The particle image velocimetry measurements are conducted separately for each of the nine segments (cf. Figure 3.9). The recording is done with a frame rate of 2000 frames per second for the duration of 1 second. The flow channels are divided into segments in order to achieve reliable results for the particle velocity with a sufficient number of pixels per particle, as explained in Section 3.2.1. Recording the whole flowfield at once would result in particle sizes of one pixel or even smaller. With nine segments, the particle size is about four to nine pixels, which is sufficient for the tracking with the *openpiv* [142] Python open-source package. For the evaluation, a window size of 32 pixels is used with an overlap of 16 pixels. An example of a resulting vector field for the particle image velocimetry measurements can be seen in Figure 4.42.

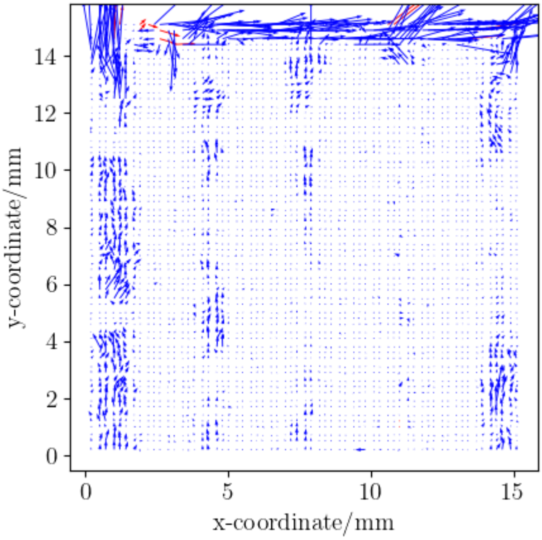

Figure 4.42: Exemplary Resulting Vector Field with Blue Vectors for the Velocity of the Particles and Red Vectors excluded as Outliers.

The vector field shows field 1 (cf. Figure 3.9) as an example of how the velocity vectors of the particle image velocimetry particles look like. The five flow channels can be seen, and on the upper edge, particles flow out of the channel inside the flow distribution area. A local threshold is set in order to filter spurious velocity vectors. The threshold, in this case, is set to 4 times the frame rate (4 x 2000 fps). If the absolute difference of the velocity vector with the local median is greater than the threshold, the vectors are excluded and marked as red vectors in Figure 4.42.

The results of the particle velocity distribution throughout the flow channel are shown in Figure 4.43 to Figure 4.46. From the electrolyte velocities measured by particle image velocimetry, a few points can be seen, which are already discussed in Section 4.3.3. According to Wang [185], the electrolyte flow flows along the triangular arms first before flowing into the flow channel because of inertia instead of branching into the flow channel, which results in a greater electrolyte volume flow in the outer channel in the cell. For an electrolyte volume flow of 25 ml/min, the effect is stronger visible for the longer triangle arm of the flow distribution area. The highest flow velocities are on the opposite side of the flow inlet at the side of the longer arm of the triangular flow distribution area. For a higher electrolyte volume flow of 50 ml/min, the electrolyte velocity in the flow channel is generally higher, compared to 25 ml/min electrolyte volume flow because a higher volume flow of electrolyte flows through the same flow channel geometry. Additionally, the flow velocity at 50 ml/min appears to be higher in the channel located at the shorter and the longer arm (left and right side) of the flow distribution triangle compared to 25 ml/min, which indicates that the electrolyte flow is distributed more uniform compared to 25 ml/min. No significant influence of the current density and the temperature can be identified.

It would be expected that the electrolyte velocity is increasing towards increasing y-coordinate within the channel because the cross-section available for the liquid flow is getting thinner the more gas is forming inside the channels. From Figure 4.43 to Figure 4.46, it can be seen that the electrolyte velocity is rather decreasing compared to parts at lower y-coordinate of the flow channel. This observation suggests that at locations with a large amount of gas, particle tracking is more difficult because the particles flow around the gas bubbles at the channel walls and might be decelerated by wall friction and agglomeration or are not being detected because they are not visible because of reflections on the channel wall. The particle image velocimetry measurements for each segment are measured for one second, and when a gas bubble is blocking the channel during that time (e.g. Figure 4.47), the particle velocity is really low. Other problems are caused by the pulsation of the membrane pump. If the pulsation of the pump is at the same time as the measurement, the velocity can even be directed backwards in downwards movement through the flow channel (gray areas).

However, the measurement results show that the principle of multiphase flow particle image velocimetry works for operation points with moderate gas amounts. From Figure 4.42, it can be seen that the particle tracking works fine with gas bubbles in the flow channel with respect to reflection or excessive amount of obviously misplaced velocity vectors. At the locations where gas bubbles are positioned in the flow channel, simply no or only very few particles are tracked, and in the liquid phase, the velocity vectors seem reasonable. Additionally, the flow behavior is laminar with a maximum Reynolds number of $\mathrm{Re}_{max} = 125$. For reliable, quantitative results, however, the measurement duration needs to be extended.

Possible sources of error are the model electrolyte density and viscosity values. Errors could occur because of temperature deviations or because of concentration deviations during the mixing of the solution. Additionally, the gas volume could deviate from the specified value. The nickel foam of the cell used for multiphase particle image velocimetry was cleaned in regular intervals because particles got stuck in the pores. All error values are sufficiently small (way below 1 %). The exact values for the relevant measurement errors for the multiphase particle image velocimetry measurements can be found in Appendix A.3.

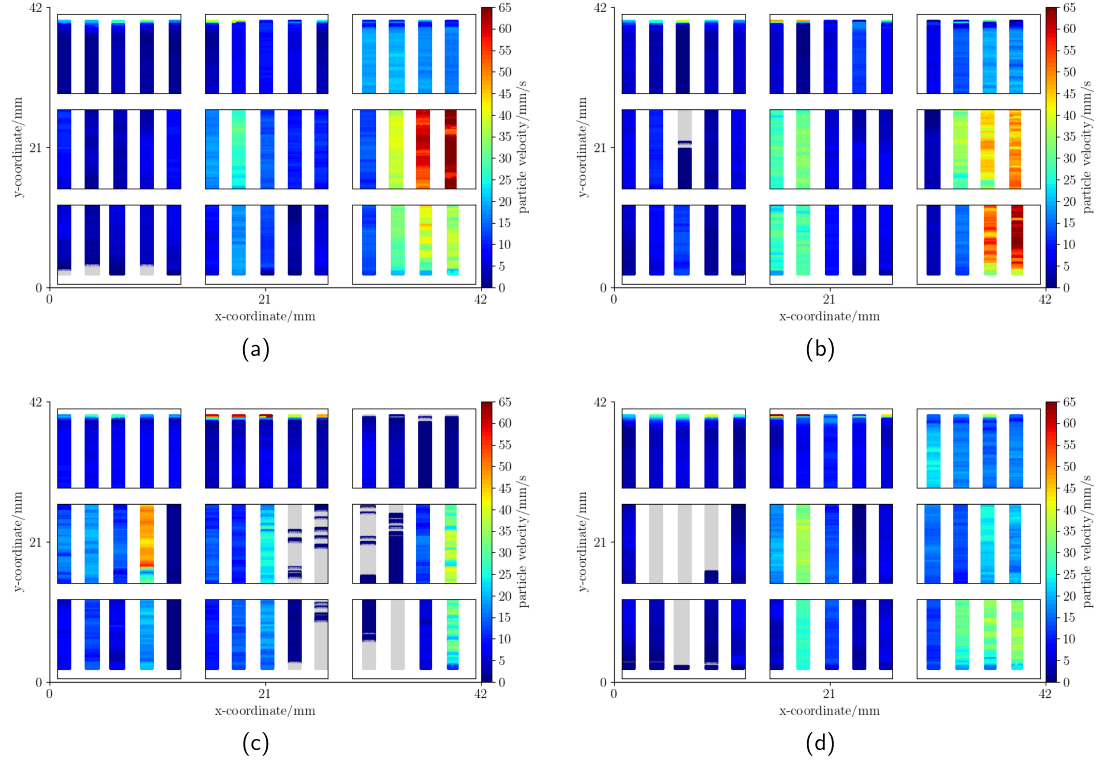

(a) (b) (c) (d)

Figure 4.43: Velocity Distribution of the Seeded Particles in the Electrolyte Solution in the Flow Channel during Particle Image Velocimetry Measurements Simulated for 50 °C, 25 ml/min, 0.4 A/cm^2 Cathode Side (a), 0.4 A/cm^2 Anode Side (b), 0.6 A/cm^2 Cathode Side (c) and 0.6 A/cm^2 Anode Side (d).

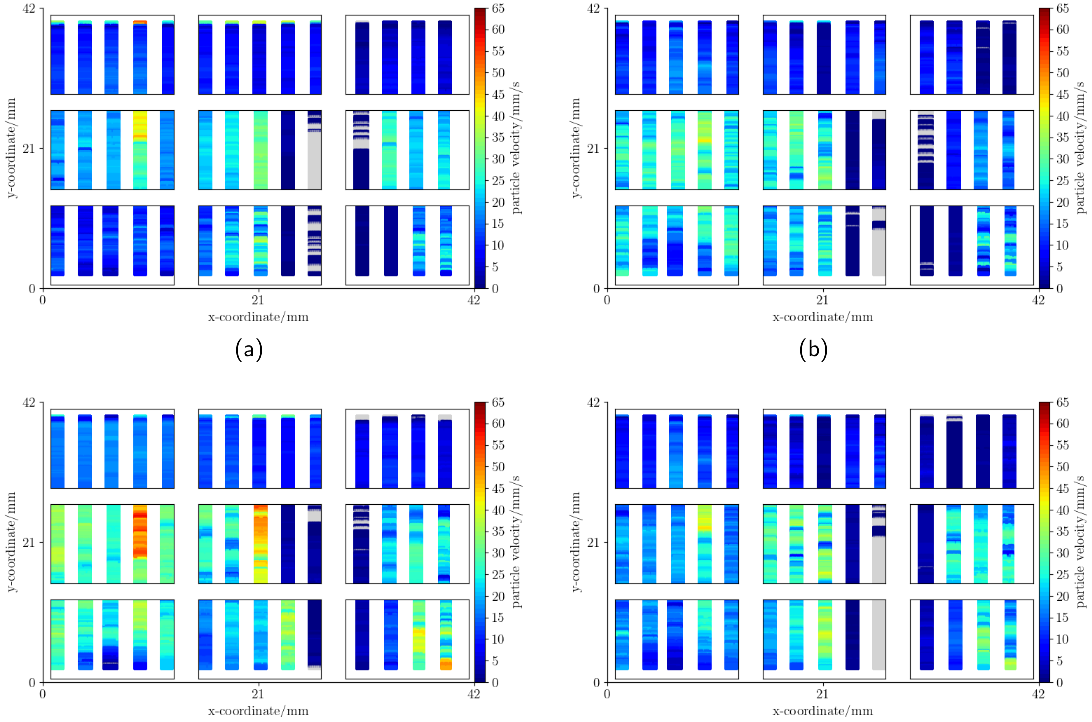

(a) (b)

(c) (d)

Figure 4.44: Velocity Distribution of the Seeded Particles in the Electrolyte Solution in the Flow Channel during Particle Image Velocimetry Measurements Simulated for 50 °C, 50 ml/min, 0.4 A/cm^2 Cathode Side (a), 0.4 A/cm^2 Anode Side (b), 0.6 A/cm^2 Cathode Side (c) and 0.6 A/cm^2 Anode Side (d).

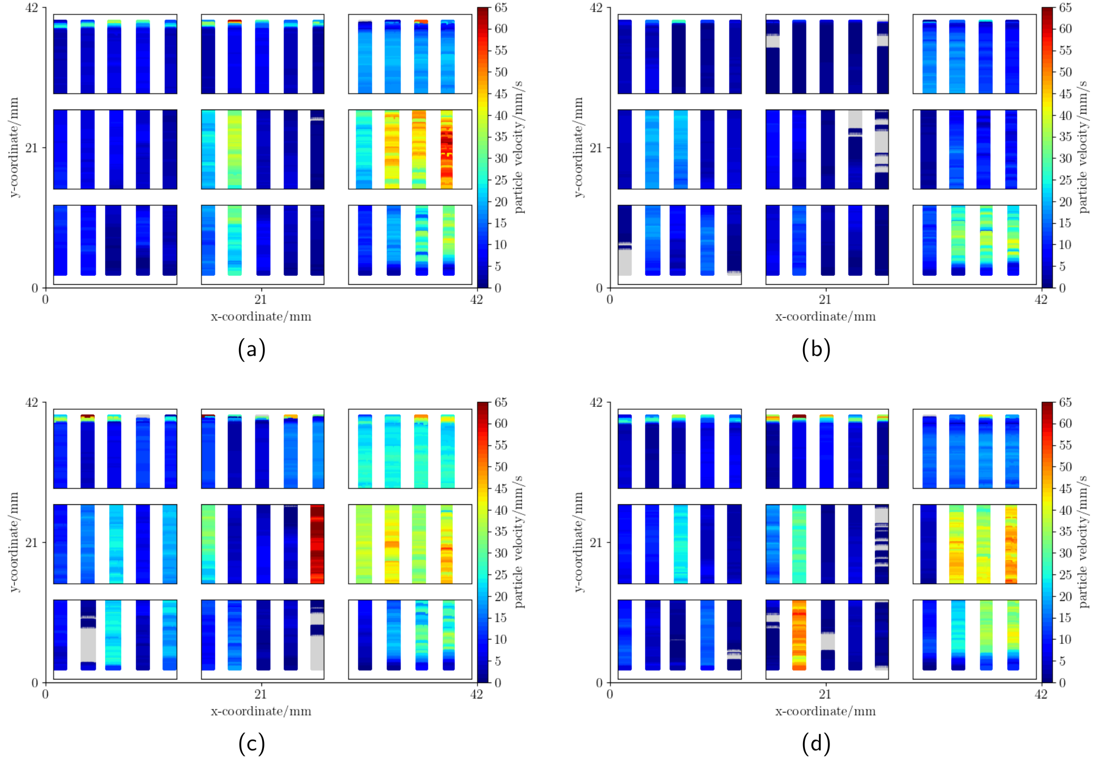

Figure 4.45: Velocity Distribution of the Seeded Particles in the Electrolyte Solution in the Flow Channel during Particle Image Velocimetry Measurements Simulated for 80 °C, 25 ml/min, 0.4 A/cm^2 Cathode Side (a), 0.4 A/cm^2 Anode Side (b), 0.6 A/cm^2 Cathode Side (c) and 0.6 A/cm^2 Anode Side (d).

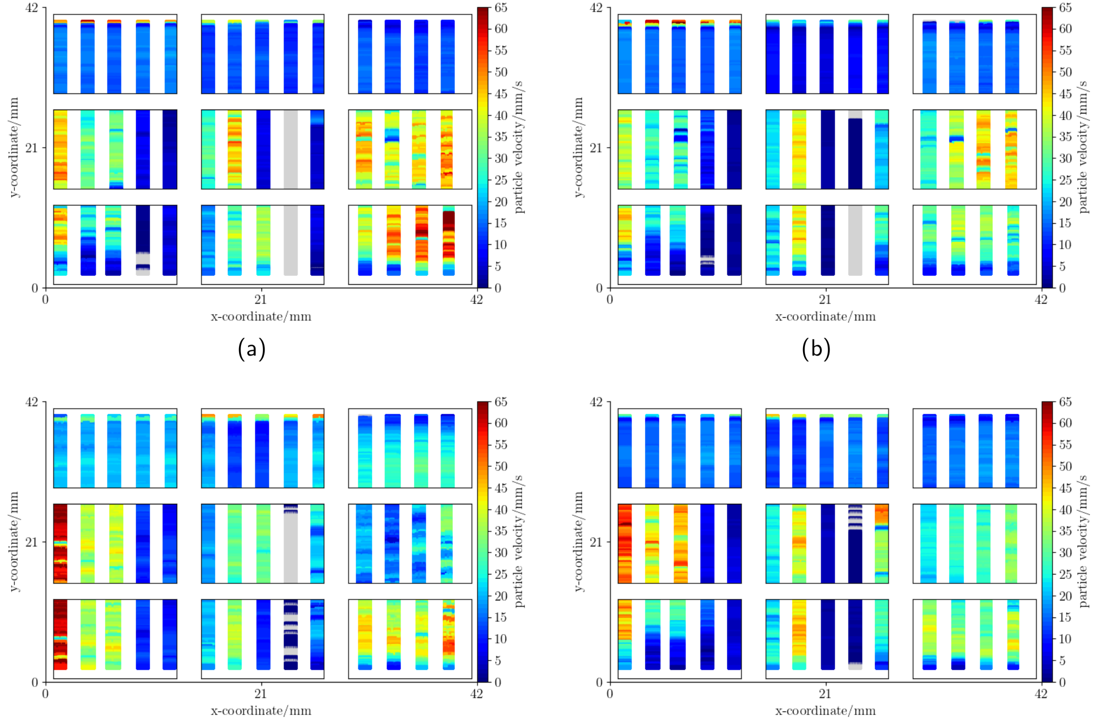

(a)

(b)

(c)

(d)

Figure 4.46: Velocity Distribution of the Seeded Particles in the Electrolyte Solution in the Flow Channel during Particle Image Velocimetry Measurements Simulated for 80 °C, 50 ml/min, 0.4 A/cm^2 Cathode Side (a), 0.4 A/cm^2 Anode Side (b), 0.6 A/cm^2 Cathode Side (c) and 0.6 A/cm^2 Anode Side (d).

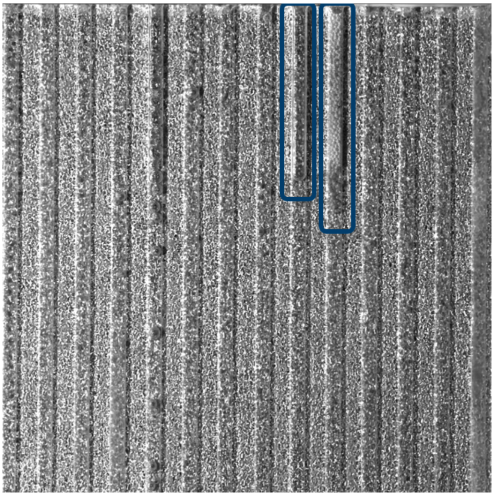

Figure 4.47: Example of Gas Bubbles Blocking Flow Channel during Particle Image Velocimetry Measurement (Marked in Blue).

4.4.2 Comparison of Multiphase Particle Image Velocimetry Measurements with Neutron Radiography Measurements

Multiphase particle image velocimetry is used in the literature only a few times and has never been used to evaluate the flow behavior of electrolysis cells. In this subchapter, the results of multiphase particle image velocimetry are compared to the ones of the neutron radiography measurements. In order to evaluate the accuracy of the model electrolysis cell to experimentally simulate the two-phase flow behavior inside an electrochemical cell, four different properties are compared with the neutron radiography measurement results. The four properties are the percentage gas amount inside the flow channel, the contact angles, the gas velocity, and the comparison of electrolyte velocity determined by particle image velocimetry and gas bubble velocity determined by neutron radiography.

Comparison of Gas Amount

The gas amount of both measurement methods is compared in percentage. From the neutron radiography measurements, three-dimensional information on the gas thickness is available, which can be determined by analyzing the resulting gray value and comparing it to a default value, as explained in Section 3.1. For the particle image velocimetry measurements, only two-dimensional images are available because the gas amount is evaluated optically. The assumption is made that the gas amount of both measurement methods is similar when the same amount of gas is introduced to the modeled cell out of glass, as is produced inside the alkaline electrolysis cell. Additionally, the gas bubbles are assumed to have the same gas bubble diameter because, in both cases, they form at, or are being introduced through the same nickel foam electrode material. Therefore, the gas amount in percentage is calculated using the cross-section of the gas bubbles obtained from the 2D images. The percentage gas amount is assumed to be a suitable measure for the comparison of both measurement methods.

The difference between the neutron radiography images and the images obtained through particle image velocimetry measurements is that the neutron radiography images contain a higher degree of measurement noise. The consequence is that small gas bubbles cannot be detected, because they lie in the same pixel size range as the measurement noise. The particle image velocimetry images are far less sensitive to measurement noise, which is why also smaller gas bubbles can be detected. Since the gas amount is evaluated in percentage, the small gas bubbles, which are not detected in neutron radiography images, result only in a deviation from the gas amount of the particle image velocimetry images if they are not uniformly distributed over the flow channel. The images of both measurement methods are pre-processed. For both kinds of images, different filters and methods are used to binarize the images and detect the gas bubbles as described in Section 3.2.5 and Section 3.1.4. Both kinds of images have different signal-to-noise ratios. All the mentioned factors play a role in the quality of the comparison. Therefore, it is assumed that the measurement values of the gas amounts are in good accordance if they are within an error range of ± 10 %.

Figure 4.48 and Figure 4.49 show the results of the comparison as a bar plot with the gas amount in percentage as the height of the bar. The x-axis represents the x-coordinate of the cell, and the flow channels are marked by black solid lines. One flow channel contains two different bars, one with the gas amount evaluated by particle image velocimetry measurements (lighter bars) and one with the gas amount evaluated through neutron radiography (darker bars). Blue bars depict the cathode channel, and red bars the anode channel.

The gas distribution over the flow channel, as described in Section 4.3.2, caused by the triangular flow distribution area, is also visible here. Most gas is located in the flow channel on the side of the electrolyte solution inlet. The channels at the electrolyte inlet have the highest gas amount, and then it decreases towards the opposite side in x-direction of the electrolyte inlet and is at two-thirds increasing again. The same pattern can be seen for the gas amount measured through particle image velocimetry measurements. The deviation of the percentage gas amount values for the gas amount obtained through both measurement methods is summarized in Table 4.13. The columns in Table 4.13 that are numbered from 1 to 14 refer to the 14 channels on anode, respectively, on cathode side.

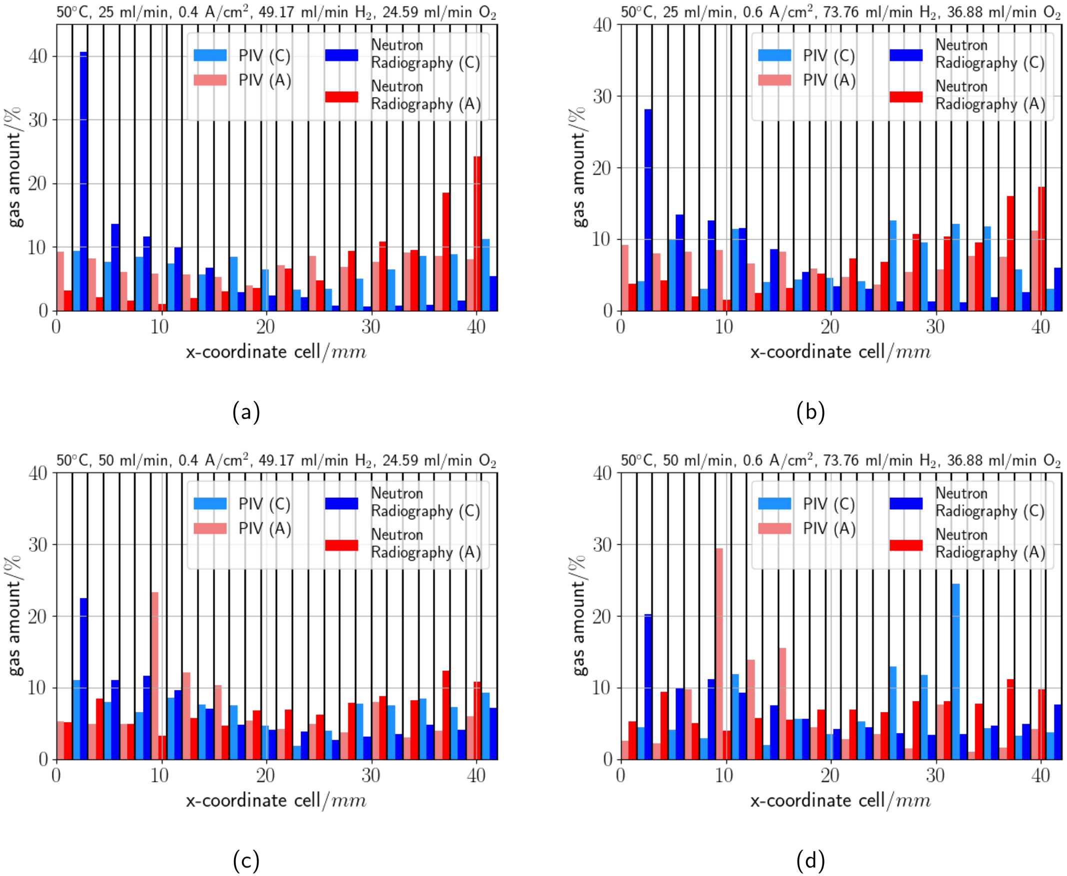

(a)

(b)

(c)

(d)

Figure 4.48: Comparison of the Gas Amount Measured by Neutron Radiography Measurements and Particle Image Velocimetry Measurements in the Flow Channel for 50 °C, 0.4 A/cm^2 and 25 ml/min (a), 50 °C, 0.6 A/cm^2 and 25 ml/min (b), 50 °C, 0.4 A/cm^2 and 50 ml/min (c) and 50 °C, 0.6 A/cm^2 and 50 ml/min (d).

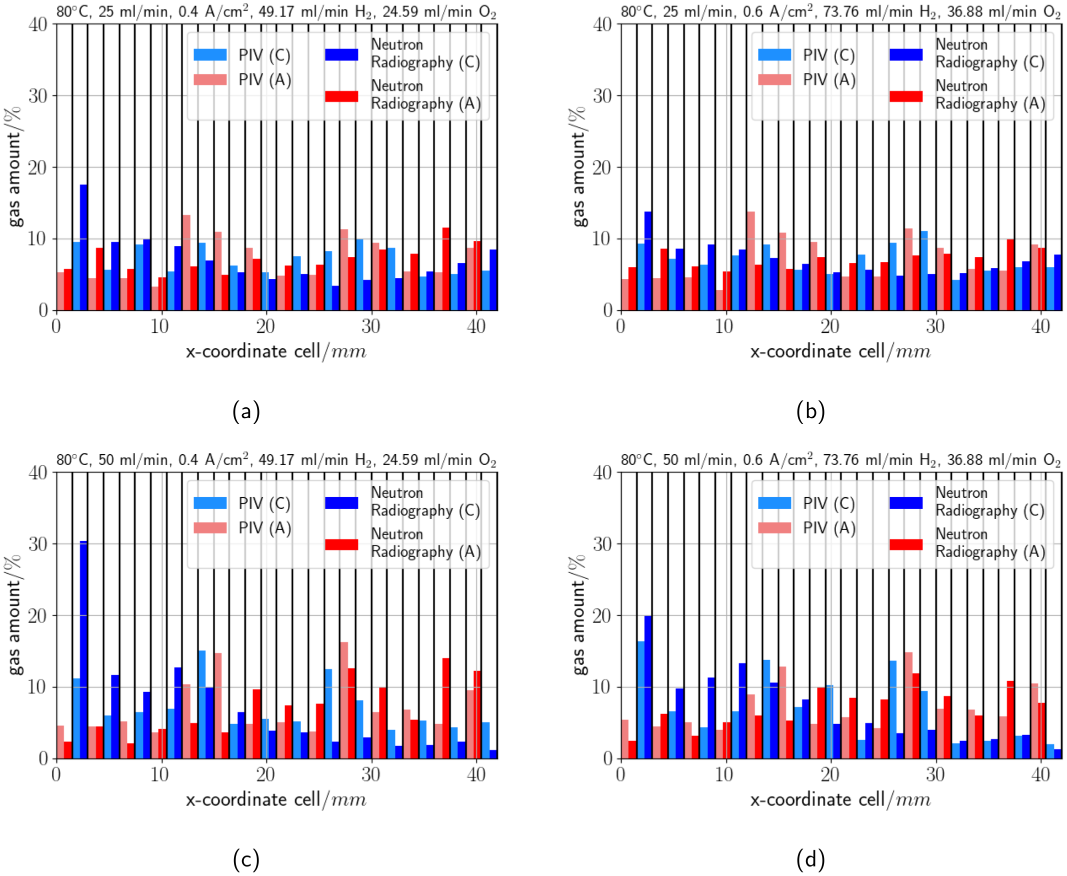

Figure 4.49: Comparison of the Gas Amount Measured by Neutron Radiography Measurements and Particle Image Velocimetry Measurements in the Flow Channel for 80 °C, 0.4 A/cm^2 and 25 ml/min (a), 80 °C, 0.6 A/cm^2 and 25 ml/min (b), 80 °C, 0.4 A/cm^2 and 50 ml/min (c) and 80 °C, 0.6 A/cm^2 and 50 ml/min (d).

The deviation is determined through $\Delta = x_{neutron}/\% - x_{PIV}/\%$. If the values for the gas amount obtained by neutron radiography ($x_{neutron}$) have higher values, Δ has positive values. In the table, the values with a higher deviation than 10 % are marked. As can be seen, most of the values are within the set limitation of 10 %. The only channel that has a lot of deviating gas amount values is the first channel. All of the high deviating values in the first channel are for the cathode side and most of the overall values with a higher deviation than 10 %. The reason for that could be that the gas for the simulation of the two-phase flow behavior during the particle image velocimetry measurements is nitrogen. From the gas properties and molecule size, nitrogen is very close to oxygen, but not close to hydrogen, this might result the deviations. But nonetheless, only 9 % of the total gas amount values for hydrogen deviate more than 10 % from each other. For the oxygen side, only 4 % deviate more than 10 %. The deviation, whether the gas amount in the channel of the alkaline electrolysis cell is higher or in the flow channel of the glass cell, is equally distributed. This shows that there is no systematic error between the gas amounts obtained by both measurement methods.

Table 4.13: Deviation of Gas Amount inside the Flow Channel during Neutron Radiography Measurements and Particle Image Velocimetry Measurements.

ϑ_{cell} [°C]	$\dot{V}$ $[\frac{ml}{min}]$	**i** $[\frac{A}{cm^2}]$	**Gas**	**1** [%]	**2** [%]	**3** [%]	**4** [%]	**5** [%]	**6** [%]	**7** [%]	**8** [%]	**9** [%]	**10** [%]	**11** [%]	**12** [%]	**13** [%]	**14** [%]
80	50	0.4	H_2	$\boxed{19.15}$	5.65	2.85	5.79	-5.09	1.61	-1.67	-1.55	$\boxed{-10.22}$	-5.19	-2.18	-3.33	-1.95	-3.88
80	50	0.4	O_2	-2.16	-0.05	-3.11	0.47	-5.48	$\boxed{-11.00}$	4.89	2.31	3.87	-3.57	3.33	-1.46	9.21	2.74
80	50	0.6	H_2	3.64	3.28	6.89	6.73	-3.08	1.10	-5.44	2.35	$\boxed{-10.16}$	-5.38	0.37	0.18	0.17	-0.65
80	50	0.6	O_2	-2.86	1.87	-1.82	0.97	-2.98	-7.62	5.21	2.80	3.97	-2.90	1.76	-0.73	5.01	-2.69
80	25	0.4	H_2	8.02	3.91	0.84	3.55	-2.49	-0.92	-0.96	-2.45	-4.85	-5.75	-4.15	0.77	1.59	2.90
80	25	0.4	O_2	0.46	4.17	1.27	1.27	-7.23	-6.06	-1.63	1.37	1.38	-3.79	-0.95	2.53	6.23	0.96
80	25	0.6	H_2	4.46	1.51	2.87	0.76	-1.83	0.72	0.24	-2.14	-4.49	-5.91	0.93	0.25	0.83	1.79
80	25	0.6	O_2	1.65	4.16	1.44	2.50	-7.49	-4.99	-2.11	1.94	2.02	-3.74	-0.82	1.61	4.38	-0.55
50	50	0.4	H_2	$\boxed{11.35}$	3.03	5.11	1.09	-0.57	-2.72	-0.59	1.97	-1.27	-4.58	-4.01	-3.54	-3.10	-2.17
50	50	0.4	O_2	-0.13	3.56	-0.03	$\boxed{-20.01}$	-6.38	-5.71	1.45	2.62	1.24	4.17	0.82	5.18	8.38	4.82
50	50	0.6	H_2	$\boxed{15.78}$	5.98	8.20	-2.50	5.53	0.03	0.75	-0.93	-9.37	-8.40	$\boxed{-20.96}$	0.37	1.64	3.87
50	50	0.6	O_2	2.71	7.11	-4.76	$\boxed{-25.50}$	-8.10	-10.00	2.54	4.08	3.12	6.67	0.39	6.63	9.53	5.59
50	25	0.4	H_2	$\boxed{31.19}$	6.01	3.23	2.72	1.05	-5.51	-4.08	-1.15	-2.60	-4.40	-5.63	-7.70	-7.29	-5.83
50	25	0.4	O_2	-6.12	-6.07	-4.57	-4.81	-3.67	-2.16	-0.30	-0.51	-3.88	2.50	3.24	0.31	9.89	$\boxed{16.15}$
50	25	0.6	H_2	$\boxed{23.99}$	3.55	9.61	0.18	4.52	1.02	-1.21	-1.08	$\boxed{-11.26}$	-8.31	$\boxed{-10.85}$	-9.92	-3.10	2.88
50	25	0.6	O_2	-5.39	-3.76	-6.14	-6.95	-4.18	-5.07	-0.73	2.60	3.16	5.33	4.54	1.94	8.52	6.13

Comparison of Contact Angle

In Figure 4.50 exemplary for the operation point 80 °C, 50 ml/min and 0.4 A/cm^2 the results for the contact angle evaluation of the gas bubbles measured by neutron radiography (Figure 4.50 (a)) and the ones measured by multiphase particle image velocimetry (Figure 4.50 (b)) are compared. For the contact angles measured by multiphase particle image velocimetry, it can be seen that not for all channels contact angles could be detected, and for some channels, only for one side of the gas bubble, a contact angle was found. The contact angle algorithm had difficulty analyzing the gas bubbles coming from multiphase particle image velocimetry. The remaining operation points are shown in Appendix A.3.2. Comparing the raw data of both measurement methods, it can be seen that the gas bubbles that appear to be one gas bubble on the neutron radiography images consist actually of many smaller gas bubbles of different sizes (see Figure 4.51). Additionally, the algorithms to binarize the images are different. For neutron radiography images, algorithms from Helmholtz Zentrum Berlin[7] are used, whereas the images of multiphase particle image velocimetry are binarized by the algorithm described in Section 3.3.4, which might make a difference on the ability to evaluate the contact angles. Therefore, the requirements on the algorithm to determine the contact angle changes from determining a contact angle on gas bubbles approximately the size of the channel cross-section to determining the contact angle, which is only a fraction of the channel cross-section, are different. This is probably the reason why the algorithm has difficulties in reliably calculating the contact angles from the multiphase particle image velocimetry images. From the analyzed results, it can be seen that the contact angle values of both measurement methods are in the same range. Surprisingly, the results of the contact angles measured by multiphase particle image velocimetry also show signs of a curved shape with different contact angles for the right and left side contact angle. Since the used cell for multiphase particle image velocimetry measurements is a half-cell, the explanation cannot be shifted flowfield plates as assumed for the contact angles of the neutron radiography measurements but must be explained by another reason not shown in literature yet.

---

[7] https://www.helmholtz-berlin.de/forschung/oe/ce/materialforschung/index_en.html

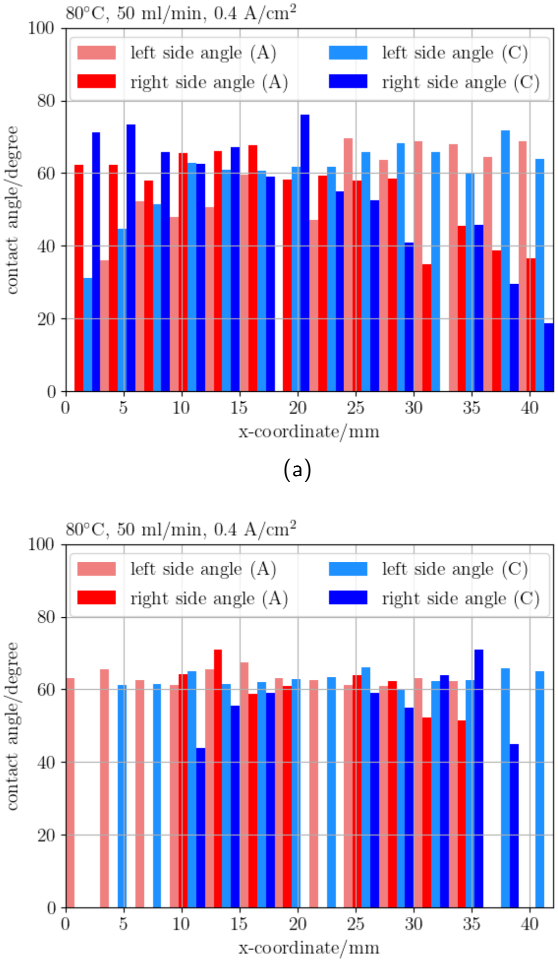

(a)

(b)

Figure 4.50: Contact Angle for the Operation Point 80 °C, 50 ml/min and 0.4 A/cm^2 Measured by Neutron Radiography (a) and with Multiphase Particle Image Velocimetry (b).

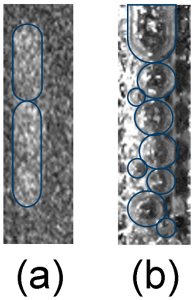

Figure 4.51: Comparison of the Gas Bubble Visibility and Sizes of the Gas Bubbles Recorded by Neutron Radiography (a) and Gas Bubble Size Recorded by Particle Image Velocimetry (b) in a Segment of One Flow Channel, Gas Bubbles Marked in Blue.

Comparison of the Gas Bubble Velocity

The velocities of the gas bubbles inside the flow channel of neutron radiography measurements are compared with the gas bubble velocity measured inside the modeled alkaline electrolysis cell in this subsection. The operation point of 50 °C, 50 ml/min, and 0.6 A/cm^2 is analyzed for anode and cathode side. For the gas bubbles measured by neutron radiography, the gas bubbles velocities are averaged over five minutes (equivalent to 15,000 images) for every flow channel, and within the flow channel, segments of 2 mm (in y-direction) are averaged locally. The analysis is done using *Trackmate* as explained in detail in Section 3.1.3. The gas bubbles of both measurement methods shown in this sub-chapter are shown at the location where the velocity is measured.
For the gas bubbles analyzed inside the model cell using multiphase particle image velocimetry, 2,000 images (equivalent to 1 second) are analyzed by *Trackmate* for the mentioned operation point. For other operation points, the results can be found in Appendix A.3 for 100 images (equivalent to 0.05 seconds) each.
In Figure 4.52 and Figure 4.53 it can be seen that the velocity distribution inside the electrochemical cell is not similar to the velocity distribution inside the flow channel of the model cell. The analysis is also done using *Trackmate* as explained in detail in Section 3.2.5.

The gas bubbles recorded by multiphase flow image velocimetry are more highly resolved, the exact boundaries of the gas bubbles are visible, and small gas bubbles can be seen. In Figure 4.51, gas bubbles recorded by both measurement methods are shown for comparison. Since more details of the gas bubbles and especially smaller gas bubbles, are visible, the gas bubble velocity, in general, is faster for the gas bubbles measured by particle image velocimetry measurements compared to the gas bubble velocity values recorded by neutron radiography. The reason for small gas bubbles to be faster is that they have less wall friction and are more likely to slip through the void in the channel instead of coalescing or being decelerated by big gas bubbles in front. An additional reason for higher gas bubble velocity was already mentioned in Section 2.2. Small gas bubbles might slide on the electrode before they detach [46]. It would be possible to detect the gas bubble velocity of slipping gas bubbles to identify the phenomena, however due to the images being two-dimensional it is to identify these gas bubbles specifically. Additionally, from the distribution of the gas bubbles in Figure 4.52 and Figure 4.53, it can be seen that in the particle image velocimetry measured gas bubble velocity analysis, gas bubbles are detected almost on every place in the channel in contrast to the gas bubbles measured by neutron radiography. The number in detected gas bubbles shown in Figure 4.52 (a) is 58 % of the number detected in Figure 4.52 (b). The number would be logical considering that Figure 4.52 (a) analyzes only half of the channel of Figure 4.52 (b), but comparing the gas bubbles per channel and time, neutron radiography with 20 gas bubbles per channel and second, compared to 5240 gas bubbles per channel and second detected on the multiphase particle image velocimetry images, shows that neutron radiography images miss a lot of information which is covered in measurement noise.

It would be interesting to compare gas bubble velocities from both measurement methods with a similar gas bubble size and remove smaller gas bubbles, which are not visible in neutron radiography images. Filtering for the gas bubble radius is, in principle, possible within *Trackmate*, but due to the calculation method of *Trackmate*, it would lead to falsified results here. *Trackmate* is calculating the mean diameter of moving objects by optimizing the radius of 20 concentric, tangent circles around the moving object with the centre at the centre of the moving object. For more information regarding the diameter of the moving object, it is referred to [126].

The diameter of the gas bubbles is averaged. This means for gas bubbles of an elongated shape typical for slug flow, the diameter is greater than the channel width and is dependent on the length of the slug. Therefore, the *Trackmate* filtering option is not used in this examination.

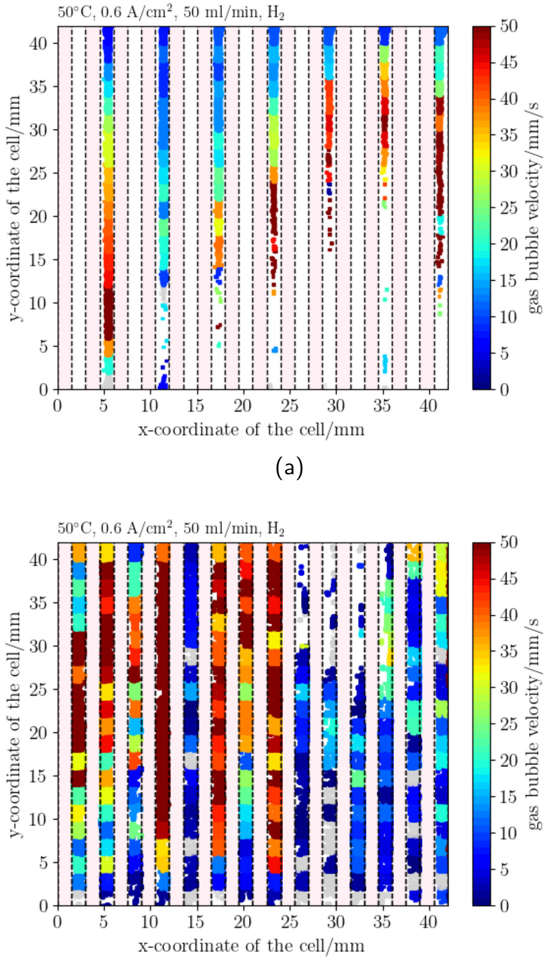

(a)

(b)

Figure 4.52: Comparison of the Gas Bubble Velocity Distribution for H_2 of Gas Bubbles Recorded by Neutron Radiography (a) and Gas Bubbles Recorded by Particle Image Velocimetry (b).

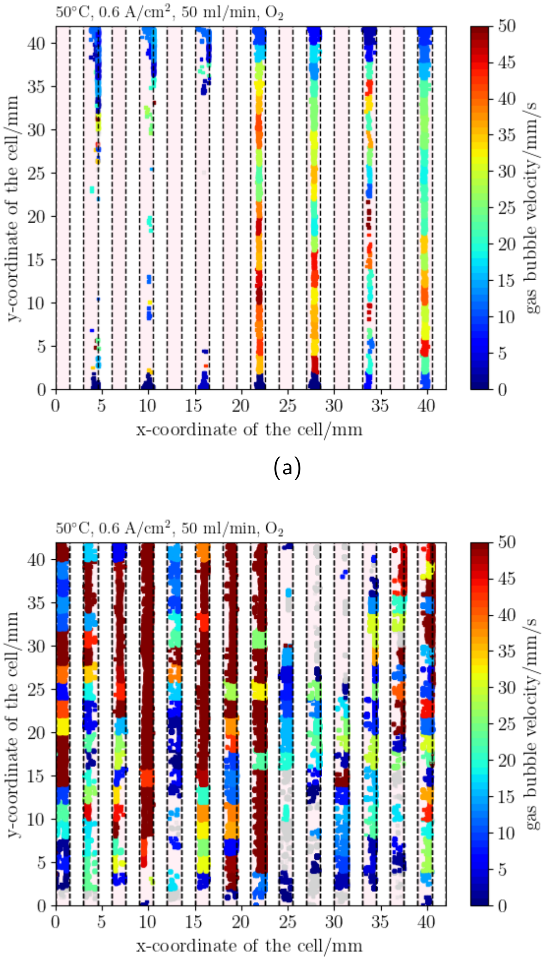

(a)

(b)

Figure 4.53: Comparison of the Gas Bubble Velocity Distribution for O_2 of Gas Bubbles Recorded by Neutron Radiography (a) and Gas Bubbles Recorded by Particle Image Velocimetry (b).

Gas Bubble Velocity Evaluation and its Dependency on the Electrolyte Solution Velocity

Comparing the gas bubble velocity and the velocity of the electrolyte solution, it can be seen that the velocities are in the same velocity range. The gas bubbles measured by neutron radiography show a gas bubble velocity distribution which differs from the gas bubble velocity distribution measured by multiphase particle image velocimetry. The observation of the gas bubble velocities shows that especially the greater gas bubbles or greater agglomerates of gas bubbles, according to Figure 4.51, are pushed out of the cell. From the multiphase particle image velocimetry images, where smaller gas bubbles can be seen, the distribution of the gas bubbles can be seen. In the upper part of the cell, the flow regime seems to be more plug or slug flow (cf. Figure 2.6) in the lower part of the channel, the flow regime is bubbly flow. The change in flow regime depends on the current density, the electrolyte volume flow, and the operation temperature. Gas bubbles or gas bubbles agglomerates, which are the size of the flow channel width, seem to have a similar velocity to the electrolyte solution that surrounds them because they show the same oscillating movement caused by the membrane pump. The smaller gas bubbles, however, seem to move faster than the electrolyte solution.

Chinnov et al. [189] investigated the flow regime of short rectangular flow channels. They defined an additional flow regime, the stratified regime, where gas bubbles occupy the upper channel. In their investigation, they found similar velocities for the liquid phase and the gas bubbles. The flow regime described sounds like the flow regime, which evolved during the measurements of this examination, and the similar velocities for gas bubbles and liquid phase are in good accordance with the findings of this investigation.

4.4.3 Summary

This section contains the results of the multiphase particle image velocimetry measurements. These measurements were proposed as an alternative method to visualize the two-phase flow of alkaline electrolysis cells more easily. The investigation showed the electrolyte flow velocity is influenced by the geometry of the cell, the electrolyte velocity is higher opposite to the electrolyte inlet. The velocity increased with increasing volume flow, as expected, but also got more evenly distributed over the flowfield.

The temperature or the current density does not seem to influence the velocity of the electrolyte. From the measurement results, it was obvious that the gas bubbles can disturb the particle flow in terms of creating a smaller pathway around them, where they are being a subject to wall friction. Comparing the gas percentage inside the channels, the same pattern of distribution could be found and by setting a 10 % deviation threshold, only 9 % of the hydrogen data exceeded the threshold and 4 % of the oxygen channel. The higher deviation was caused probably by using nitrogen, which is a gas that is similar to oxygen, but not so similar to hydrogen. Comparing the contact angle results with the results of the neutron radiography measurements, it can be seen that the results have very similar values and also show the difference in left and right contact angle. The results of both visualization methods, comparing the gas bubble velocity, results in quiet different velocity distributions. However, looking at the identified number of gas bubbles for the multiphase particle image velocimetry, it can be seen that the number of identified gas bubbles is much higher. Which shows that a lot of small gas bubbles are simply below the detection threshold of neutron radiography. Looking at the gas bubble velocity compared to the electrolyte, it can be seen that the gas bubble velocity is in the same range as the electrolyte for bigger gas bubbles, smaller gas bubbles tend to be faster.

5 Summary and Conclusion

In this dissertation, a new methodology is presented to investigate the two-phase flow behavior of an alkaline electrolysis cell. Through-plane measurements of electrochemical cells for visualization of the gas bubbles inside an electrochemical flow cell are either done by using imaging methods, like neutron radiography or x-ray measurements, or the two-phase flow is investigated by using a transparent electrochemical cell. Imaging techniques need a lot of preparatory effort, the measurement time is limited, and the availability is restricted, the measurements are expensive and, therefore, come with high costs or are only granted at scientific necessity financed by public funding. Furthermore, transportable test rigs and equipment are needed.

Transparent cells are a good alternative to visualize the two-phase flow of electrochemical cells, but difficult to realize for highly concentrated electrolyte solutions and pressurized operation at elevated temperatures of alkaline electrolyzer. Because of these difficulties, a simpler and easier accessible way to investigate the two-phase flow behavior inside an alkaline electrolysis cell has been developed by introducing a method to investigate the flow behavior using multiphase particle image velocimetry.

A transparent flowfield plate is used to simulate one half-cell of an alkaline electrolysis cell. The gas inside the channels is introduced through the simulated electrode and is exchanged for nitrogen instead of oxygen and hydrogen. The electrolyte solution is exchanged for an electrolyte with an identical density and viscosity as potassium hydroxide at the regarding operation condition. The criteria for the model electrolyte solution is that the desired density and viscosity are at lower temperatures than they are for potassium hydroxide.

The developed method has the potential to simplify the evaluation of the two-phase flow for validation of Computational Fluid Dynamics (CFD) simulations or flowfield optimization for more efficient cell designs for alkaline electrolysis cells. Additionally, with respect to difficult operation conditions, for example, at intermediate temperature alkaline electrolysis, the presented method offers the possibility to simulate these operation conditions in terms of temperature and pressurized operation without actually measuring under these conditions, but at much easier conditions to realize. Multiphase flow particle image velocimetry can be used for the investigation of the multiphase flow behavior of electrochemical flow cells. To prove the suitability of multiphase flow particle image velocimetry, the gas bubble behavior inside the flow channel of an alkaline water electrolysis zero-gap cell is investigated by neutron radiography measurements for various temperatures, electrolyte flow velocities, and current densities. The cell behavior is characterized by electrochemical measurements, such as polarization curves and electrochemical impedance spectroscopy. Regarding the two-phase flow behavior, the gas layer thickness, gas bubble velocity, and the contact angle of gas bubbles inside the flow channel on the three-phase boundary of oxygen/ hydrogen with potassium hydroxide solution and the nickel channel are analyzed. The properties characterizing the two-phase flow are determined at several different operation conditions, varying temperature, electrolyte volume flow, and current density. With the knowledge of how the two-phase flow of an actual alkaline electrolysis cell behaves, it is possible to evaluate the two-phase flow behavior of a model electrolysis cell investigated by multiphase flow particle image velocimetry.

Physical Properties of Potassium Hydroxide

In preparation for the multiphase flow particle image velocimetry, a thorough analysis of the three different properties, mass density, dynamic viscosity, and ionic conductivity, of potassium hydroxide has been done. For each property, a literature review of available measurement data has been carried out for operation conditions relevant to alkaline electrolysis at low and, for the first time, also for intermediate temperatures. With the available data, empirical equations have been developed through coefficient optimization. The developed equations were compared to the published measurement sets, as well as the data against each other. For ionic conductivity, an equation has been developed to determine the optimal concentration for potassium hydroxide dependent on the temperature to achieve the highest ionic conductivity of the electrolyte solution.

Replacement of Potassium Hydroxide by a Model Electrolyte Solution

The electrolyte solution and the gases of the model electrolysis cell were replaced by fluids able to model potassium hydroxide at different operation conditions and hydrogen and oxygen. For the replacement of potassium hydroxide by model electrolyte solutions, a thorough literature review and analysis of the mass density, dynamic viscosity, and ionic conductivity of potassium hydroxide was done. Empirical equations were developed for the named properties of potassium hydroxide. With the aim of being able to investigate the two-phase flow behavior of an alkaline electrolysis cell at temperatures between 50°C and 180°C, model electrolyte solutions have been found that are able to reach the desired conditions of density and viscosity at temperatures below 60°C without the need of pressurized operation. Barium iodide (BaI_2) is found to be able to simulate potassium hydroxide at temperatures between 50°C and 80°C and concentrations at optimal ionic conductivity at being actually operated between 11°C and 26°C. For intermediate temperatures, potassium iodide (KI) is found suitable to simulate potassium hydroxide at temperatures between 90°C and 180°C for concentrations at optimal ionic conductivity with simulation temperatures between 35°C and 60°C. The calculated properties of the selected electrolyte solutions have been validated through measurements, and their suitability for particle image velocimetry measurements has been verified. Hydrogen and oxygen gases were both replaced by nitrogen for safety reasons.

Gas Layer Thickness

For the neutron radiography measurement, through-plane measurements with an alkaline electrolysis cell have been conducted. The used cell has alternating cathode and anode parallel flow channels to measure anode and cathode side at the same time. For the first time, a frame rate of 50 frames per second could be realized in operando neutron radiography measurements.

For the used cell geometry, it is possible to see that the gas layer thickness is thicker in the upper part of the cell due to the fact that gas bubbles need to have a certain size in order to distinguish them from measurement noise. Additionally, the gas layer is thicker on the side where the electrolyte inlet is located, which indicates that the electrolyte supply is better on this side, and therefore, these channels are being prevented from local depletion (anode) or oversaturation (cathode), which both affects the ionic conductivity negatively. With increasing temperature, a higher gas layer thickness could be observed, likely due to gas solubility. An increasing current density results in a thicker gas layer thickness because the gas production is directly linked to the current density. Whereas a lower electrolyte volume flow resulted in an increasing gas layer thickness. Possible explanations are a later detachment of gas bubbles and, therefore, a greater gas bubble size, which is detectable with neutron radiography measurements, and a slower transport out of the flow channel. For the multiphase particle image velocimetry measurements, a glass cell is used with the same parallel flow channel geometry as used for neutron radiography measurements, in this case, it is able to model either cathode side or anode side separately at the same time.

The comparability of the two measurement methods has been assessed using three different properties, the gas amount inside the flow channel, the contact angle at the three-phase boundary at the flow channel wall, and the gas bubble velocity. The gas amount inside the flow channel has been determined from binarized images and is compared proportionally in percent.

The percentage distribution of gas inside the flow channel of anode and cathode side are for 96 % within the set 10 % deviation boundary between the two measurement methods for oxygen and 91 % for hydrogen. The higher deviation for hydrogen gas amount is assumed to be caused by using nitrogen inside the modeled cell as gas, which is similar to oxygen but chemically more different from hydrogen.

The evaluation of the percentage gas amount is done with the assumption that small gas bubbles are equally distributed over the channel. A comparison of the absolute gas amount resulting from neutron radiography measurements and multiphase flow particle image velocimetry measurements seems not to be useful since small gas bubbles are not detectable from neutron radiography images.

Additionally, the gas layer thickness inside an alkaline electrolysis cell has been analyzed using neutron radiography measurements and compared to theoretical, calculated gas layer thickness values. The results show that the calculated gas layer thickness for all current densities is slightly thicker. With decreasing current density, the difference between calculated and measured gas layer thicknesses increases. The electrolyte volume flow also seems to have an influence on the gas layer thickness, the higher the electrolyte volume flow, the thinner the gas layer. The most probable explanation for the deviation between calculated and measured gas layer thickness is that small gas bubbles are not visible in the neutron radiography images. This proposes that not the whole gas amount is visible when conducting neutron radiography measurements with the here used temporal resolution and settings.

Contact Angle

The contact angle is determined by a published method from literature. The contact angle results are compared in absolute values. The averaged values of the contact angle over all channels of neutron radiography measurements and multiphase particle image velocimetry are in the same range. The absolute values comparing the contact angle channel by channel do not. The reason is most likely a slight shift during assembly of the alkaline electrolysis cell used during neutron radiography. A change in contact angle depending on the operation conditions could not be observed.

Gas Bubble and Electrolyte Velocity

The gas bubble velocities of both neutron radiography images and multiphase flow particle image velocimetry are analyzed by *Trackmate*. From neutron radiography measurements, it can be seen that the temperature does not seem to have an influence on the gas bubble velocity. Whereas, for the electrolyte volume flow, it could be seen that the gas bubble velocity is decreasing with decreasing electrolyte volume flow, which is likely due to a larger diameter because of a later detachment, more wall friction during their movement through the flow channel and the bigger gas bubbles being more objective to the higher convective force that pushes the bubbles through the channel. At lower current densities, the gas bubble velocity is slightly lower, which might result from a lower buoyancy compared to bigger gas bubbles.

Multiphase flow particle image velocimetry has a better temporal and spatial resolution, which results in less measurement noise and the ability to detect the outlines of the gas bubbles even at small sizes. The different conditions of both measurement methods result, therefore, in the qualitative observation that the gas bubble velocity for two-phase flow particle image velocimetry measurements have a similar gas bubble velocity range compared to gas bubble velocity inside an alkaline electrolysis cell with slightly higher velocities. The higher velocities result presumably from being able to track small gas bubbles to the velocity analysis of the two-phase flow particle image velocimetry measurements.

From the electrolyte velocity distribution measured with multiphase particle image velocimetry, it can be seen that there is no influence visible from current density and temperature. The particle detection in the direct vicinity of large gas bubbles or large agglomerates of gas bubbles turns out to be difficult. The particles flow with the electrolyte around the gas bubbles and might be affected by effects like wall friction, agglomeration, and reflections of the channel walls. The electrolyte volume flow is influencing the flow velocity. Especially greater gas bubbles are affected by the convective forces of the electrolyte flow.

Conclusion

In this dissertation, operando neutron radiography measurements have been successfully conducted with a never-achieved temporal resolution. During the measurements, electrochemical properties have been determined from polarization curves and electrochemical impedance spectroscopy at a variety of temperatures, current densities, and electrolyte volume flow. The measurement resulted in gas layer thicknesses, gas bubble velocities, and contact angles for the different operation conditions. The for alkaline electrolysis important properties of potassium hydroxide, density, dynamic viscosity, and ionic conductivity have been reviewed. From published measurement data, empirical equations have been developed, and for the first time, the temperature range of empirical equations for potassium hydroxide is extended up to temperatures well above 100 °C. With the knowledge of density and dynamic viscosity, model electrolyte solutions to replace potassium hydroxide have been found to be able to conduct two-phase flow investigations at lower temperatures as necessary when using potassium hydroxide as electrolyte solution. With one of these model electrolyte solutions, multiphase particle image velocimetry measurements have been conducted using a transparent half cell with the same geometrical properties as the alkaline electrolysis cell to conduct neutron radiography measurements to simulate the electrolysis process. Inside the used half-cell, the two-phase flow behavior is simulated using nitrogen as a gas. With multiphase particle image velocimetry, the gas amount distribution inside the channel, gas bubble, and electrolyte solution velocity, as well as the contact angles at the three-phase boundary of gas, liquid and cell material, have been determined. The results obtained by neutron radiography and multiphase particle image velocimetry have been compared and validated. It could be shown that the percentage distribution of gas inside the channel behaves very similarly, comparing the electrochemical alkaline electrolysis cell and the simulated glass cell. The mean contact angles have very similar values in both cells. It is shown that the multiphase particle image velocimetry measurements are able to identify even small gas bubbles, and therefore, the number of detected gas bubbles is a lot higher compared to the results of neutron radiography measurements.

Additionally, it could be seen that the velocity distribution inside the cells changes if small gas bubbles are detected.

In the following, the advantages of using multiphase particle image velocimetry over using neutron radiography are summarized; With multiphase particle image velocimetry, the needed operation temperatures are lower, and therefore, there is no need for pressurized operation. The temporal resolution is, to some extent, higher, which leads to being able to detect even small gas bubbles. The measurement equipment is easier available since it is comparably simple and, generally, the measurement method is less cost-intensive.

6 Outlook

Experimental investigations of the two-phase flow in electrolysis cells are rare and most available studies are on PEM electrolysis. Since the two-phase flow behavior is influencing the cell efficiency significantly, reliable and easily accessible measurement methods are needed. Here, the gas bubble movement inside the flowfield was analyzed, which gave a lot of insight and resulted in important, missing knowledge about the two-phase flow behavior of alkaline electrolysis cells. For future measurements using neutron radiography, the temporal resolution can now be optimized using the gained results of the gas bubble velocity dependent on certain properties. With this knowledge, the imaging frequency can be adapted, and the measurement noise can be reduced. Another research question, which is frequently discussed for alkaline electrolysis cells, is the ohmic resistance and the gas bubbles influence on the ohmic resistance. Imaging techniques like neutron radiography have the ability, together with a suitable cell, to record the gas bubble formation and movement inside the porous layer as well as the detachment into the flow channel. Here, it was shown that the temporal resolution is high enough to show operando effects inside the cell. Additionally, imaging techniques have the opportunity to measure the cell and record tomographic images. Three-dimensional data measured over time are a great possibility to validate flow simulations accurately. Another interesting effect of alkaline electrolysis is the influence of different potassium hydroxide concentrations on the two-phase flow behavior as well as the identification of concentration differences through neutron radiography, for example, during long electrolysis operation with connected and non-connected electrolyte tanks on the attenuation coefficient. In this examination, it was already shown that over a short measurement duration, the attenuation coefficient does not noticeably change, to extending the measurement time would be the next step.

The results of multiphase particle image velocimetry have shown that the method is a great opportunity to investigate the two-phase flow inside the flow channel, which can be done at different operation conditions. In a next step, the investigation should be extended to higher operation temperatures to simulate pressurized operation.

To establish the measurement method as a standard and help make it available to the scientific community it is necessary to develop robust, reliable, and accessible image processing algorithms, which can be adapted to the individual needs of different measurement set-ups.

With the help of multiphase particle image velocimetry, potentially all electrochemical devices with two-phase flows can be investigated. Therefore, the method has the opportunity to help improve the efficiency of electrolysis cells and with that to help with the transition towards using climate-friendly energy production and usage.

Bibliography

[1] S. Shiva Kumar et al. “An overview of water electrolysis technologies for green hydrogen production”. In: *Energy Reports* 8 (2022), pages 13793–13813. DOI: 10.1016/j.egyr.2022.10.127.

[2] H. Wendt et al. “Die Bedeutung der Wasserelektrolyse in Zeiten der Energiewende”. In: *Chemie Ingenieur Technik* 86.1-2 (2014), pages 144–148. DOI: 10.1002/cite.201300005.

[3] F. P. Lohmann-Richters et al. “Review—Challenges and Opportunities for Increased Current Density in Alkaline Electrolysis by Increasing the Operating Temperature”. In: *Journal of The Electrochemical Society* 168.11 (2021), page 114501. DOI: 10.1149/1945-7111/ac34cc.

[4] A. Hodges et al. “A high-performance capillary-fed electrolysis cell promises more cost-competitive renewable hydrogen”. In: *Nature Communications* 13.1 (2022), page 1304. DOI: 10.1038/s41467-022-28953-x.

[5] J. W. Haverkort et al. “Voltage losses in zero-gap alkaline water electrolysis”. In: *Journal of Power Sources* 497 (2021), page 229864. DOI: 10.1016/j.jpowsour.2021.229864.

[6] R. Phillips et al. “Minimising the ohmic resistance of an alkaline electrolysis cell through effective cell design”. In: *International Journal of Hydrogen Energy* 42.38 (2017), pages 23986–23994. DOI: 10.1016/j.ijhydene.2017.07.184.

[7] M. T. de Groot et al. “Ohmic resistance in zero gap alkaline electrolysis with a Zirfon diaphragm”. In: *Electrochimica Acta* 369 (2021), page 137684. DOI: 10.1016/j.electacta.2020.137684.

[8] D. M. F. Santos et al. “Hydrogen production by alkaline water electrolysis”. In: *Química Nova* 36.8 (2013), pages 1176–1193. DOI: 10.1590/S0100-40422013000800017.

[9] D. E. Hall. "Alkaline Water Electrolysis Anode Materials". In: *Journal of The Electrochemical Society* 132.2 (1985), pages 41C–48C. DOI: 10.1149/1.2113856.

[10] M. T. de Groot et al. "Optimal operating parameters for advanced alkaline water electrolysis". In: *International Journal of Hydrogen Energy* 47.82 (2022), pages 34773–34783. DOI: 10.1016/j.ijhydene.2022.08.075.

[11] S. A. Grigoriev et al. "Alkaline Electrolysers". In: *Comprehensive Renewable Energy*. Elsevier, 2022, pages 459–472. DOI: 10.1016/B978-0-12-819727-1.00024-8.

[12] J.-H. Kim et al. "Low-cost and energy-efficient asymmetric nickel electrode for alkaline water electrolysis". In: *International Journal of Hydrogen Energy* 40.34 (2015), pages 10720–10725. DOI: 10.1016/j.ijhydene.2015.07.025.

[13] C. Chatzichristodoulou et al. "High Temperature Alkaline Electrolysis Cells with Metal Foam Based Gas Diffusion Electrodes". In: *Journal of The Electrochemical Society* 163.11 (2016), F3036–F3040. DOI: 10.1149/2.0051611jes.

[14] R. L. LeRoy. "Hydrogen Production by the Electrolysis of Water: The Kinetic and Thermodynamic Framework". In: *Journal of The Electrochemical Society* 130.11 (1983), pages 2158–2163. DOI: 10.1149/1.2119544.

[15] J. Brauns et al. "Alkaline Water Electrolysis Powered by Renewable Energy: A Review". In: *Processes* 8.2 (2020), page 248. DOI: 10.3390/pr8020248.

[16] R. L. Costa et al. "Electrolysis as a Source of Hydrogen and Oxygen". In: *Allis-Chalmers Mfg. Co., Milwaukee* (1967).

[17] F. Allebrod et al. "Electrical conductivity measurements of aqueous and immobilized potassium hydroxide". In: *International Journal of Hydrogen Energy* 37.21 (2012), pages 16505–16514. DOI: 10.1016/j.ijhydene.2012.02.088.

[18] N. Nagai. "Existence of optimum space between electrodes on hydrogen production by water electrolysis". In: *International Journal of Hydrogen Energy* 28.1 (2003), pages 35–41. DOI: 10.1016/S0360-3199(02)00027-7.

[19] R. Phillips et al. "Zero gap alkaline electrolysis cell design for renewable energy storage as hydrogen gas". In: *RSC Advances* 6.102 (2016), pages 100643–100651. DOI: 10.1039/C6RA22242K.

[20] J. Gras et al. "Corrosion of stainless steels and nickel-based alloys for alkaline water electrolysis". In: *International Journal of Hydrogen Energy* 18.7 (1993), pages 561–566. DOI: 10.1016/0360-3199(93)90175-A.

[21] I. Abe et al. “Hydrogen Production by High Temperature, High Pressure Water Electrolysis I, Plant Development”. In: *Hydrogen Energy Progress. 3,1: Proceedings of the 3rd World Hydrogen Energy Conference, 23.6. – 26.6.80* 29 (1980).

[22] P. Combrade. *Behaviour of nickel and some nickel base alloys in contact with caustic anolyte at 160 and 200 C*. 1982.

[23] R. B. Rebak. “Stress corrosion cracking (SCC) of nickel-based alloys”. In: *Stress corrosion cracking*. Edited by V. S. Raja et al. Philadelphia, PA: Woodhead Pub, 2011, pages 273–306. DOI: 10.1533/9780857093769.3.273.

[24] K. M. Pruett. *Chemical resistance guide for metals and alloys II: A guide to chemical resistance of metals and alloys*. La Jolla, California: Compass Publications, 2012.

[25] G. Kreysa, editor. *Potassium hydroxide, ammonium and ammonium hydroxide: Corrosive agents and their interaction with materials*. 2., compl. rev. and ext. ed. Volume vol. 9. Corrosion handbook. Frankfurt: Wiley-VCH, 2007.

[26] N. V. Agfa-Gevaert. *Technical Data Sheet ZIRFON PERL UTP 500*. 2020.

[27] J. Divisek et al. “Improvements of water electrolysis in alkaline media at intermediate temperatures”. In: *International Journal of Hydrogen Energy* 7.9 (1982), pages 695–701. DOI: 10.1016/0360-3199(82)90017-9.

[28] J. Divisek et al. “A bipolar cell for advanced alkaline water electrolysis”. In: *International Journal of Hydrogen Energy* 7.9 (1982), pages 703–710. DOI: 10.1016/0360-3199(82)90018-0.

[29] J. Divisek et al. “Improved components for advanced alkaline water electrolysis”. In: *International Journal of Hydrogen Energy* 13.3 (1988), pages 141–150. DOI: 10.1016/0360-3199(88)90014-6.

[30] J. Divisek et al. “Improved construction of an electrolytic cell for advanced alkaline water electrolysis”. In: *International Journal of Hydrogen Energy* 10.6 (1985), pages 383–388. DOI: 10.1016/0360-3199(85)90064-3.

[31] H. Wendt et al. “Ceramic diaphragms for advanced alkaline water electrolysis”. In: *Journal of Applied Electrochemistry* 19.4 (1989), pages 605–610. DOI: 10.1007/BF01022121.

[32] H. Wendt et al. “Nine years of research and development on advanced water electrolysis. A review of the research programme of the Commission of the European Communities”. In: *Journal of Applied Electrochemistry* 18.1 (1988), pages 1–14. DOI: 10.1007/BF01016198.

[33] H. Wendt et al. “Cermet diaphragms and integrated electrode-diaphragm units for advanced alkaline water electrolysis”. In: *International Journal of Hydrogen Energy* 10.6 (1985), pages 375–381. DOI: 10.1016/0360-3199(85)90063-1.

[34] F. Allebrod et al. “Cobalt and molybdenum activated electrodes in foam based alkaline electrolysis cells at 150–250 °C and 40 bar”. In: *Journal of Power Sources* 255 (2014), pages 394–403. DOI: 10.1016/j.jpowsour.2014.01.024.

[35] F. Allebrod et al. “Alkaline electrolysis cell at high temperature and pressure of 250 °C and 42 bar”. In: *Journal of Power Sources* 229 (2013), pages 22–31. DOI: 10.1016/j.jpowsour.2012.11.105.

[36] H. Wendt et al. “Anode and cathode-activation, diaphragm-construction and electrolyzer configuration in advanced alkaline water electrolysis”. In: *International Journal of Hydrogen Energy* 9.4 (1984), pages 297–302. DOI: 10.1016/0360-3199(84)90080-6.

[37] M. Schalenbach et al. “A Perspective on Low-Temperature Water Electrolysis – Challenges in Alkaline and Acidic Technology”. In: *International Journal of Electrochemical Science* (2018), pages 1173–1226. DOI: 10.20964/2018.02.26.

[38] J. Fischer et al. “Fundamental investigations and electrochemical engineering aspects concerning an advanced concept for alkaline water electrolysis”. In: *AIChE Journal* 26.5 (1980), pages 794–802. DOI: 10.1002/aic.690260513.

[39] J. Newman et al. *Electrochemical Systems*. 3rd ed. Somerset: Wiley, 2012.

[40] F. Hine et al. “Hydrodynamic Studies on a Vertical Electrolyzer with Gas Evolution under Forced Circulation”. In: *Journal of The Electrochemical Society* 131.1 (1984), pages 83–89. DOI: 10.1149/1.2115551.

[41] H. Vogt et al. “The bubble coverage of gas-evolving electrodes in stagnant electrolytes”. In: *Electrochimica Acta* 50.10 (2005), pages 2073–2079. DOI: 10.1016/j.electacta.2004.09.025.

[42] S. Shibata. “Supersolubility of Hydyogen in Acidic Solution in the Vicinity of Hydrogen-Evolving Platinum Cathodes in Different Surface States”. In: *Denki Kagaku oyobi Kogyo Butsuri Kagaku* 44.11 (1976), pages 709–712. DOI: 10.5796/kogyobutsurikagaku.44.709.

[43] H. Vogt. "The rate of gas evolution at electrodes—II. An estimate of the efficiency of gas evolution on the basis of bubble growth data". In: *Electrochimica Acta* 29.2 (1984), pages 175–180. DOI: 10.1016/0013-4686(84)87044-9.

[44] H. Vogt. "The rate of gas evolution of electrodes—I. An estimate of the efficiency of gas evolution from the supersaturation of electrolyte adjacent to a gas-evolving electrode". In: *Electrochimica Acta* 29.2 (1984), pages 167–173. DOI: 10.1016/0013-4686(84)87043-7.

[45] P. Boissonneau et al. "An experimental investigation of bubble-induced free convection in a small electrochemical cell". In: *Journal of Applied Electrochemistry* 30.7 (2000), pages 767–775. DOI: 10.1023/A:1004034807331.

[46] J. Manthey et al. "A sensitivity analysis on the bubble departure diameter for bubble growth due to oxygen super-saturation in highly purified water". In: *International Journal of Thermofluids* 18 (2023), page 100327. DOI: 10.1016/j.ijft.2023.100327.

[47] R. R. Lessard et al. "Bubble Coalescence and Gas Transfer in Aqueous Electrolytic Solutions". In: *Industrial & Engineering Chemistry Fundamentals* 10.2 (1971), pages 260–269. DOI: 10.1021/i160038a012.

[48] G. Marrucci et al. "Coalescence of gas bubbles in aqueous solutions of inorganic electrolytes". In: *Chemical Engineering Science* 22.9 (1967), pages 1257–1265. DOI: 10.1016/0009-2509(67)80190-8.

[49] M. J. Prince et al. "Bubble coalescence and break-up in air-sparged bubble columns". In: *AIChE Journal* 36.10 (1990), pages 1485–1499. DOI: 10.1002/aic.690361004.

[50] L. Janssen. "Behaviour of and mass transfer at gas-evolving electrodes". In: *Electrochimica Acta* 34.2 (1989), pages 161–169. DOI: 10.1016/0013-4686(89)87081-1.

[51] H. Ito et al. "Experimental study on porous current collectors of PEM electrolyzers". In: *International Journal of Hydrogen Energy* 37.9 (2012), pages 7418–7428. DOI: 10.1016/j.ijhydene.2012.01.095.

[52] K. Mishima et al. "Some characteristics of air-water two-phase flow in small diameter vertical tubes". In: *International Journal of Multiphase Flow* 22.4 (1996), pages 703–712. DOI: 10.1016/0301-9322(96)00010-9.

[53] M. Ishii et al. “Two-fluid model and hydrodynamic constitutive relations”. In: *Nuclear Engineering and Design* 82.2-3 (1984), pages 107–126. DOI: 10.1016/0029-5493(84)90207-3.

[54] V. Talanquer et al. “Nucleation of bubbles in binary fluids”. In: *The Journal of chemical physics* 102.5 (1995), pages 2156–2164. DOI: 10.1063/1.468737.

[55] K. J. Vachaparambil et al. “Explanation of Bubble Nucleation Mechanisms: A Gradient Theory Approach”. In: *Journal of The Electrochemical Society* 165.10 (2018), E504–E512. DOI: 10.1149/2.1031810jes.

[56] S. R. German et al. “Electrochemistry of single nanobubbles. Estimating the critical size of bubble-forming nuclei for gas-evolving electrode reactions”. In: *Faraday discussions* 193 (2016), pages 223–240. DOI: 10.1039/c6fd00099a.

[57] O. F. Selamet et al. “Visualization of Gas Bubble Behavior of a Regenerative Fuel Cell in Electrolysis Mode by Soft X-ray Radiography”. In: *ECS Transactions* 58.1 (2013), pages 353–360. DOI: 10.1149/05801.0353ecst.

[58] V. Kienzlen et al. “Location of hydrogen gas evolution on perforated plate electrodes in zero gap cells”. In: *International Journal of Hydrogen Energy* 19.9 (1994), pages 729–732. DOI: 10.1016/0360-3199(94)90235-6.

[59] G. F. Swiegers et al. “The prospects of developing a highly energy-efficient water electrolyser by eliminating or mitigating bubble effects”. In: *Sustainable Energy & Fuels* 5.5 (2021), pages 1280–1310. DOI: 10.1039/D0SE01886D.

[60] M. Maier et al. “Mass transport in PEM water electrolysers: A review”. In: *International Journal of Hydrogen Energy* 47.1 (2022), pages 30–56. DOI: 10.1016/j.ijhydene.2021.10.013.

[61] I. Dedigama et al. “Current density mapping and optical flow visualisation of a polymer electrolyte membrane water electrolyser”. In: *Journal of Power Sources* 265 (2014), pages 97–103. DOI: 10.1016/j.jpowsour.2014.04.120.

[62] P. Chandran et al. “Study on the characteristics of hydrogen bubble formation and its transport during electrolysis of water”. In: *Chemical Engineering Science* 138 (2015), pages 99–109. DOI: 10.1016/j.ces.2015.07.041.

[63] O. Panchenko et al. “Influence of Stoichiometry on the Two-Phase Flow Behavior of Proton Exchange Membrane Electrolyzers”. In: *Energies* 12.3 (2019), page 350. DOI: 10.3390/en12030350.

[64] O. Panchenko et al. "In-situ two-phase flow investigation of different porous transport layer for a polymer electrolyte membrane (PEM) electrolyzer with neutron spectroscopy". In: *Journal of Power Sources* 390 (2018), pages 108–115. DOI: 10.1016/j.jpowsour.2018.04.044.

[65] O. Panchenko. *Massentransportphänomene in Schichtsystemen eines Elektrolyseurs*. Zentralbibliothek, 2019.

[66] M. A. Hoeh et al. "In operando synchrotron X-ray radiography studies of polymer electrolyte membrane water electrolyzers". In: *Electrochemistry Communications* 55 (2015), pages 55–59. DOI: 10.1016/j.elecom.2015.03.009.

[67] M. A. Hoeh. *Poröse Transportschichten für die Polymerelektrolytmembran-Wasserelektrolyse*. Schriften des Forschungszentrums Jülich. Reihe Energie & Umwelt/Energy & environment. Jülich: Forschungszentrum Jülich GmbH, Zentralbibliothek, Verlag, 2017.

[68] M. A. Hoeh et al. "In-Operando Neutron Radiography Studies of Polymer Electrolyte Membrane Water Electrolyzers". In: *ECS Transactions* 69.17 (2015), pages 1135–1140. DOI: 10.1149/06917.1135ecst.

[69] B. Kögl et al. "Ähnlichkeitstheorie". In: *Grundlagen der Verfahrenstechnik*. Edited by B. Kögl et al. Vienna: Springer Vienna, 1981, pages 120–178. DOI: 10.1007/978-3-7091-2270-9{\textunderscore}5.

[70] J. Räty et al. *UV-Visible Reflection Spectroscopy of Liquids*. Volume 92. Springer Series in Optical Sciences. Berlin, Heidelberg: Springer Berlin Heidelberg, 2004.

[71] L. L. Lee. *Molecular thermodynamics of electrolyte solutions*. Singapore: World Scientific, 2008.

[72] I. M. Abdulagatov et al. "Densities, apparent and partial molar volumes of aqueous KBr solutions at high temperatures and high pressures". In: *Fluid Phase Equilibria* 246.1-2 (2006), pages 96–110. DOI: 10.1016/j.fluid.2006.05.015.

[73] H. Harms. *Die dichte flussiger und fester stoffe*. [Place of publication not identified]: Springer, 1941. DOI: 10.1007/978-3-663-02163-6.

[74] R. Gilliam et al. "A review of specific conductivities of potassium hydroxide solutions for various concentrations and temperatures". In: *International Journal of Hydrogen Energy* 32.3 (2007), pages 359–364. DOI: 10.1016/j.ijhydene.2006.10.062.

[75] D. Le Bideau et al. “Review of necessary thermophysical properties and their sensivities with temperature and electrolyte mass fractions for alkaline water electrolysis multiphysics modelling”. In: *International Journal of Hydrogen Energy* 44.10 (2019), pages 4553–4569. DOI: 10.1016/j.ijhydene.2018.12.222.

[76] I. D. Zaytsev et al. *Properties of aqueous solutions of electrolytes*. Boca Raton: CRC Press, 1992.

[77] P. Ripoche et al. “Determination des Characteristiques Physicochimiques des Solutions Aqueuses Concentrees D'Hydroxyde de Potassium Jusqu'a 180OC. I: Les Densites et les Viscosites”. In: 1980.

[78] L. B. Hitchcock et al. “Viscosity and Density of Pure Alkaline Solutions and Their Mixtures”. In: *Industrial & Engineering Chemistry* 27.4 (1935), pages 461–466. DOI: 10.1021/ie50304a027.

[79] L. F. Sedano et al. “Maximum in density of electrolyte solutions: Learning about ion-water interactions and testing the Madrid-2019 force field”. In: *The Journal of chemical physics* 156.15 (2022), page 154502. DOI: 10.1063/5.0087679.

[80] M. D. Lechner. *Einführung in die Kinetik*. Berlin, Heidelberg: Springer Berlin Heidelberg, 2018. DOI: 10.1007/978-3-662-57455-3.

[81] G. W. Ehrenstein. *Viskosität*. 1. Auflage. Erlanger Kunststoff-Schadensanalyse. München: Hanser, Carl, 2022.

[82] G. M. Pancenkov. *Druckabhängigkeit der Viskosität von Flüssigkeiten*. 1986. DOI: 10.18419/opus-6291.

[83] A. S. Qureshi et al. “Generalized Correponding States Correlations for the Viscosity and Thermal Conductivity of Aqueous Electrolyte Solutions”. In: *Chemical Engineering Communications* 136.1 (1995), pages 27–44. DOI: 10.1080/00986449508936352.

[84] W. M. Vogel. “Some Physicochemical Properties of KOH-H2O System-Range-55 to 85 Weight Percent and 120 Degrees to 250 Degrees C”. In: *Journal of Chemical & Engineering Data* Vol. 12, No. 4 (1967), pages 465–472.

[85] M. A. Klochko et al. “Electrical conductivity and viscosity of aqueous solutions of NaOH and KOH”. In: *Russian Journal of Inorganic Chemistry* 4.9 (1959), pages 964–968.

[86] H. Semat et al. *Physics*. New York: Rinehart & Company, 1958.

[87] P. C. Ho et al. "Conductivity of Dilute Aqueous Electrolyte Solutions at High Temperatures and Pressures Using a Flow Cell". In: *Journal of Solution Chemistry* 29.3 (2000), pages 217–235. DOI: 10.1023/A:1005146332605.

[88] G. Tammann et al. "Der Druckeinfluß auf das elektrische Leitvermögen von Salzlösungen". In: *Zeitschrift für anorganische und allgemeine Chemie* 183.1 (1929), pages 1–29. DOI: 10.1002/zaac.19291830102.

[89] K.-Y. a. Law. *Surface wetting : characterization, contact angle, and fundamentals*. Springer, 2016.

[90] P. Wang et al. "Modeling Surface Tension of Concentrated and Mixed-Solvent Electrolyte Systems". In: *Industrial & Engineering Chemistry Research* 50.7 (2011), pages 4086–4098. DOI: 10.1021/ie101915n.

[91] P. Ripoche et al. "Determination des Characteristiques Physicochimiques des Solutions Aqueuses Concentrees D'Hydroxyde de Potassium Jusqu'a 180OC. III: Les Tensions Superficielles et la Solubilite de L'Hydrogene et de L'Oxygene". In: 1980.

[92] N. Kardjilov et al. "Neutron imaging in materials science". In: *Materials Today* 14.6 (2011), pages 248–256. DOI: 10.1016/S1369-7021(11)70139-0.

[93] E. H. Lehmann et al. "Hydrogen distribution measurements by neutrons". In: *Applied radiation and isotopes : including data, instrumentation and methods for use in agriculture, industry and medicine* 61.4 (2004), pages 503–509. DOI: 10.1016/j.apradiso.2004.03.075.

[94] J. Banhart. *Advanced tomographic methods in materials research and engineering*. Volume v.66. Monographs on the physics and chemistry of materials. Oxford and New York: Oxford University Press, 2008.

[95] W. Demtröder. *Experimentalphysik 2: Elektrizität und Optik*. 7., korr. und erw, Auflage 2017. Springer-Lehrbuch. Berlin, Heidelberg: Springer Berlin Heidelberg, 2017.

[96] O. F. Selamet et al. "Two-phase flow in a proton exchange membrane electrolyzer visualized in situ by simultaneous neutron radiography and optical imaging". In: *International Journal of Hydrogen Energy* 38.14 (2013), pages 5823–5835. DOI: 10.1016/j.ijhydene.2013.02.087.

[97] J. Seweryn et al. "Communication\textemdashNeutron Radiography of the Water/Gas Distribution in the Porous Layers of an Operating Electrolyser". In: *Journal of The Electrochemical Society* 163.11 (2016), F3009–F3011. DOI: 10.1149/2.0641607jes.

[98] F. de Beer et al. "PEM Water Electrolysis: Preliminary Investigations Using Neutron Radiography". In: *Physics Procedia* 88 (2017), pages 19–26. DOI: 10.1016/j.phpro.2017.06.002.

[99] M. Gebhard et al. "Design of an In-Operando Cell for X-Ray and Neutron Imaging of Oxygen-Depolarized Cathodes in Chlor-Alkali Electrolysis". In: *Materials* 12.8 (2019), page 1275. DOI: 10.3390/ma12081275.

[100] C. Minnaar et al. "Current Density Distribution of Electrolyzer Flow Fields: In Situ Current Mapping and Neutron Radiography". In: *Energy & Fuels* 34.1 (2020), pages 1014–1023. DOI: 10.1021/acs.energyfuels.9b03814.

[101] D. B. Barker et al. "Measuring fluid velocities with speckle patterns". In: *Optics letters* 1.4 (1977), pages 135–137. DOI: 10.1364/OL.1.000135.

[102] P. G. Simpkins et al. "Laser speckle measurements of transient Bénard convection". In: *Journal of Fluid Mechanics* 89.4 (1978), pages 665–671. DOI: 10.1017/S0022112078002797.

[103] H. Meng et al. "Holographic particle velocimetry: a 3D measurement technique for vortex interactions, coherent structures and turbulence". In: *Fluid Dynamics Research* 8.1-4 (1991), pages 33–52. DOI: 10.1016/0169-5983(91)90029-I.

[104] R. J. Adrian. "Particle-Imaging Techniques for Experimental Fluid Mechanics". In: *Annual Review of Fluid Mechanics* 23.1 (1991), pages 261–304. DOI: 10.1146/annurev.fl.23.010191.001401.

[105] R. J. Adrian. "Scattering particle characteristics and their effect on pulsed laser measurements of fluid flow: speckle velocimetry vs particle image velocimetry". In: *Applied optics* 23.11 (1984), pages 1690–1691. DOI: 10.1364/AO.23.001690.

[106] M. Raffel et al. *Particle Image Velocimetry*. Cham: Springer International Publishing, 2018. DOI: 10.1007/978-3-319-68852-7.

[107] H. T. Huang et al. "Limitation and improvement of PIV". In: *Experiments in Fluids* 15.3 (1993), pages 168–174. DOI: 10.1007/BF00189883.

[108] R. D. Keane et al. "Optimization of particle image velocimeters. I. Double pulsed systems". In: *Measurement Science and Technology* 1.11 (1990), pages 1202–1215. DOI: 10.1088/0957-0233/1/11/013.

[109] R. D. Keane et al. "Theory of cross-correlation analysis of PIV images". In: *Applied Scientific Research* 49 (1992), pages 191–251.

[110] C. Brücker. *PIV in multiphase flows*. 2000.

[111] R. C. Chen et al. "Particle image velocimetry for characterizing the flow structure in three-dimensional gas-liquid-solid fluidized beds". In: *Chemical Engineering Science* 47.13-14 (1992), pages 3615–3622. DOI: 10.1016/0009-2509(92)85077-O.

[112] N. G. Deen et al. "Two-Phase PIV in Bubbly Flows: Status and Trends". In: *Chemical Engineering & Technology* 25.1 (2002), page 97. DOI: 10.1002/1521-4125(200201)25:1{\textless}97::AID-CEAT97{\textgreater}3.0.CO;2-7.

[113] Z. C. Liu et al. "Simultaneous imaging of the velocity fields of two phases". In: *Particulate two-phase flow* (1993).

[114] X. Song et al. "Separation of particle-bubble images in multiphase flow". In: *International Workshop on PIV'99- Santa Barbara, 3 rd, Santa Barbara, CA*, pages 15–20.

[115] Y. A. Hassan et al. "Simultaneous velocity measurements of both components of a two-phase flow using particle image velocimetry". In: *International Journal of Multiphase Flow* 18.3 (1992), pages 371–395.

[116] S. Hilgers et al. "PIV measurements in multiphase flow using CCD-and photo-camera". In: *ASME-PUBLICATIONS-FED* 209 (1995), pages 151–154.

[117] M. L. Jakobsen et al. "Particle image velocimetry: simultaneous two-phase flow measurements". In: *Measurement Science and Technology* 7.9 (1996), page 1270.

[118] K. T. Kiger et al. "Two-phase piv for dilute solid/liquid flow". In: *International Workshop on PIV'99- Santa Barbara, 3 rd, Santa Barbara, CA*, pages 157–162.

[119] L. Gui et al. "Phase-separated PIV measurements of the flow around systems of bubbles rising in water". In: *ASME FEDSM*, pages 22–26.

[120] N. G. Deen et al., editors. *Upper limit of the gas fraction in PIV measurements in dispersed gas–liquid flows*. 2001.

[121] K. T. Kiger et al. “PIV technique for the simultaneous measurement of dilute two-phase flows”. In: *J. Fluids Eng.* 122.4 (2000), pages 811–818.

[122] N. G. Deen et al. “Comparison of PIV and LDA measurement methods applied to the gas-liquid flow in a bubble column”. In: *10th international symposium on applications (2000)*, pages 1–12.

[123] A. Tengattini et al. “NeXT-Grenoble, the Neutron and X-ray tomograph in Grenoble”. In: *Nuclear Instruments and Methods in Physics Research Section A: Accelerators, Spectrometers, Detectors and Associated Equipment* 968 (2020), page 163939. DOI: 10.1016/j.nima.2020.163939.

[124] S. H. Williams et al. “Detection system for microimaging with neutrons”. In: *Journal of instrumentation* 7.02 (2012), P02014.

[125] Rayleigh. “XV. On the theory of optical images, with special reference to the microscope”. In: *The London, Edinburgh, and Dublin Philosophical Magazine and Journal of Science* 42.255 (1896), pages 167–195. DOI: 10.1080/14786449608620902.

[126] D. Ershov et al. “TrackMate 7: integrating state-of-the-art segmentation algorithms into tracking pipelines”. In: *Nature Methods* 19.7 (2022), pages 829–832. DOI: 10.1038/s41592-022-01507-1.

[127] W. S. Rasband. *ImageJ*. Bethesda, Maryland, USA, 1997.

[128] D. Marr et al. “Theory of edge detection”. In: *Proceedings of the Royal Society of London. Series B, Biological sciences* 207.1167 (1980), pages 187–217. DOI: 10.1098/rspb.1980.0020.

[129] K. Jaqaman et al. “Robust single-particle tracking in live-cell time-lapse sequences”. In: *Nature Methods* 5.8 (2008), pages 695–702. DOI: 10.1038/nmeth.1237.

[130] Mónica Sánchez et al. “Aspen Plus model of an alkaline electrolysis system for hydrogen production”. In: *International Journal of Hydrogen Energy* 45.7 (2020), pages 3916–3929. DOI: 10.1016/j.ijhydene.2019.12.027.

[131] C. R. Harris et al. “Array programming with NumPy”. In: *Nature* 585.7825 (2020), pages 357–362. DOI: 10.1038/s41586-020-2649-2.

[132] G. Bradski. “The OpenCV Library”. In: *Dr. Dobb’s Journal of Software Tools* (2000).

[133] V. Weitbrecht et al. *Geschwindigekitsmessungen mit Particle-Image-Velocimetry: Labor- und Feldmessungen*. Mitteilungsblatt der Bundesanstalt für Wasserbau 90. Karlsruhe: Bundesanstalt für Wasserbau (BAW), 2007.

[134] E. R. Likhachev. "Dependence of water viscosity on temperature and pressure". In: *Technical Physics* 48.4 (2003), pages 514–515. DOI: 10.1134/1.1568496.

[135] P. Virtanen et al. "SciPy 1.0: fundamental algorithms for scientific computing in Python". In: *Nature Methods* 17.3 (2020), pages 261–272. DOI: 10.1038/s41592-019-0686-2.

[136] J. Nocedal et al. *Numerical Optimization*. 2nd Edition. Springer Science+Business Media, LLC., 2006.

[137] The SciPy community. *scipy.optimize.least_squares*. 2022.

[138] O. Ulleberg. "Modeling of advanced alkaline electrolyzers: a system simulation approach". In: *International Journal of Hydrogen Energy* 28.1 (2003), pages 21–33. DOI: 10.1016/S0360-3199(02)00033-2.

[139] P. Hanafizadeh et al. "The Effect of Gas Properties on Bubble Formation, Growth, and Detachment". In: *Particulate Science and Technology* 33.6 (2015), pages 645–651. DOI: 10.1080/02726351.2015.1017033.

[140] N. R. Pallas et al. "The surface tension of water". In: *Colloids and Surfaces* 6.3 (1983), pages 221–227. DOI: 10.1016/0166-6622(83)80014-6.

[141] M. Samimy et al. "Motion of particles with inertia in a compressible free shear layer". In: *Physics of Fluids A: Fluid Dynamics* 3.8 (1991), pages 1915–1923. DOI: 10.1063/1.857921.

[142] Alex Liberzon et al. *OpenPIV/openpiv-python: OpenPIV-Python v0.23.4*. 2021. DOI: 10.5281/ZENODO.4409178.

[143] D. A. Skoog et al. *Instrumentelle Analytik: Grundlagen - Geräte - Anwendungen*. Springer-Lehrbuch. Berlin, Heidelberg: Springer Berlin Heidelberg, Imprint, and Springer, 1996. DOI: 10.1007/978-3-662-07916-4.

[144] PerkinElmer Inc. *Inside the PerkinElmer LAMBDA 950/850/650 Series*. 2004.

[145] Anton Paar GmbH. *Instruction Manual and Safety Information: Portable Density Meter*. 2022.

[146] Anton Paar GmbH. *Density and Density measurement*. 2022.

[147] Beuth Verlag GmbH. *Kunststoffe_- Polymere/Harze in flüssigem, emulgiertem oder dispergiertem Zustand_- Bestimmung der Viskosität mit einem Rotationsviskosimeter bei definiertem Geschwindigkeitsgefälle*. Berlin. DOI: 10.31030/2725724.

[148] Beuth Verlag GmbH. *Dichtemessgeräte nach dem Schwingerprinzip_- Teil_1: Laborgeräte*. Berlin. DOI: 10.31030/8130836.

[149] T. Mezger. *The rheology handbook: For users of rotational and oscillatory rheimeters*. 3rd, rev. ed. European Coatings Tech Files. Hannover: Vincentz Network, 2013.

[150] Zentrum für Messen und Kalibriere & Analytik GmbH. *Newtonsche Normalprobender Viskosität*. 2018.

[151] R. H. Ewoldt et al. "Experimental Challenges of Shear Rheology: How to Avoid Bad Data". In: *Complex Fluids in Biological Systems*. Edited by S. E. Spagnolie. Biological and Medical Physics, Biomedical Engineering. New York, NY: Springer New York, 2015, pages 207–241. DOI: 10.1007/978-1-4939-2065-5{\textunderscore}6.

[152] J. Yu et al. "Apparent contact angles of liquid water droplet breaking through a gas diffusion layer of polymer electrolyte membrane fuel cell". In: *International Journal of Hydrogen Energy* 43.12 (2018), pages 6318–6330. DOI: 10.1016/j.ijhydene.2018.01.168.

[153] S. F. Chini et al. "A method for measuring contact angle of asymmetric and symmetric drops". In: *Colloids and Surfaces A: Physicochemical and Engineering Aspects* 388.1-3 (2011), pages 29–37. DOI: 10.1016/j.colsurfa.2011.08.001.

[154] The SciPy community. *scipy.ndimage.gaussian_filter*.

[155] Y. V. Yushkevich et al. "Electric Conductivity of KOH Solutions at High Temperatures". In: *Elektrokhimiya* 3.12 (1967), pages 1491–1493.

[156] D. A. Lown et al. "Proton transfer conductance in aqueous solution. Part 1.—Conductance of concentrated aqueous alkali metal hydroxide solutions at elevated temperatures and pressures". In: *Trans. Faraday Soc.* 67.0 (1971), pages 132–148. DOI: 10.1039/TF9716700132.

[157] L. S. Darken et al. "Conductances of Aqueous Solutions of the Hydroxides of Lithium, Sodium and Potassium at 25°". In: *Journal of the American Chemical Society* 64.3 (1942), pages 621–623. DOI: 10.1021/ja01255a046.

[158] D. M. See et al. "Temperature and Concentration Dependence of the Specific Conductivity of Concentrated Solutions of Potassium Hydroxide". In: *Journal of Chemical & Engineering Data* 42.6 (1997), pages 1266–1268. DOI: 10.1021/je970140x.

[159] Occidental Chemical Corporation. *The Caustic Potash Handbook*. 2018.

[160] G. Akerlof et al. "The Density of Aqueous Solutions of Potassium Hydroxide". In: *Journal of the American Chemical Society* 63.4 (1941), pages 1085–1088. DOI: 10.1021/ja01849a054.

[161] V. P. Mashovets et al. "Density of aqueous KOH solutions at high temperatures over a wide range of concentrations". In: *Zhurnal Prikladnoi Khimii* 38.10 (1965), pages 2344–2347.

[162] M. J. Tham et al. "Densities of potassium hydroxide solutions". In: *Journal of Chemical & Engineering Data* 12.4 (1967), pages 525–526. DOI: 10.1021/je60035a017.

[163] I. N. Maksimova et al. "EQUATIONS FOR CALCULATING DENSITY, VISCOSITY, AND ELECTRICAL-CONDUCTIVITY OF POTASSIUM HYDROXIDE SOLUTIONS AT . . .". In: *Zhurnal Prikladnoi Khimii* 47.7 (1974), pages 1666–1668.

[164] O. Söhnel et al. *Densities of aqueous solutions of inorganic substances*. Amsterdam - Oxford - New York - Tokyo: Elsevier, 1985.

[165] Y.-J. Guo et al. "Density and viscosity of aqueous solution of K2CrO4/KOH mixed electrolytes". In: *Transactions of Nonferrous Metals Society of China* 20 (2010), s32–s36. DOI: 10.1016/S1003-6326(10)60007-6.

[166] K. I. Kuznetsov et al. "Measurements of the Dynamic Viscosity and Density of KOH Solutions at Atmospheric Pressure". In: *High Temperature* 58.6 (2020), pages 806–811. DOI: 10.1134/S0018151X20060127.

[167] O. Faust. "Oberflächenspannung und Viscosität von wäßriger Kalium-, Natrium-, Thalium-, Barytlauge ud Natriumcarbonatlösung". In: *Zetschrift für Anorganische und Allgemeine Chemie* 160 (1927), pages 373–376.

[168] The SciPy community. *scipy.optimize.minimize*. 2022.

[169] F. Gao et al. "Implementing the Nelder-Mead simplex algorithm with adaptive parameters". In: *Computational Optimization and Applications* 51.1 (2012), pages 259–277. DOI: 10.1007/s10589-010-9329-3.

[170] A. Hodges et al. “Critical Analysis of Published Physical Property Data for Aqueous Potassium Hydroxide. Collation into Detailed Models for Alkaline Electrolysis”. In: *Journal of Chemical & Engineering Data* (2023). DOI: 10.1021/acs.jced.3c00040.

[171] J. H. Mathews et al. “The Photolysis of Potassium Iodate”. In: *The Journal of Physical Chemistry* 18.8 (1914), pages 641–652. DOI: 10.1021/j150152a002.

[172] F. H. Getman. “The Color of Iodine Solutions 1”. In: *Journal of the American Chemical Society* 50.11 (1928), pages 2883–2890. DOI: 10.1021/ja01398a005.

[173] E. Amores et al. “Development of an operation strategy for hydrogen production using solar PV energy based on fluid dynamic aspects”. In: *Open Engineering* 7.1 (2017), pages 141–152. DOI: 10.1515/eng-2017-0020.

[174] C. Karacan et al. “Challenges and important considerations when benchmarking single-cell alkaline electrolyzers”. In: *International Journal of Hydrogen Energy* 47.7 (2022), pages 4294–4303. DOI: 10.1016/j.ijhydene.2021.11.068.

[175] H. Vogt. “The actual current density of gas-evolving electrodes—Notes on the bubble coverage”. In: *Electrochimica Acta* 78 (2012), pages 183–187. DOI: 10.1016/j.electacta.2012.05.124.

[176] D. Zhang et al. “Evaluating the Behavior of Electrolytic Gas Bubbles and Their Effect on the Cell Voltage in Alkaline Water Electrolysis”. In: *Industrial & Engineering Chemistry Research* 51.42 (2012), pages 13825–13832. DOI: 10.1021/ie301029e.

[177] F. Rocha et al. “Effect of pore size and electrolyte flow rate on the bubble removal efficiency of 3D pure Ni foam electrodes during alkaline water electrolysis”. In: *Journal of Environmental Chemical Engineering* 10.3 (2022), page 107648. DOI: 10.1016/j.jece.2022.107648.

[178] D. S. Hall et al. “The Electrochemistry of Metallic Nickel: Oxides, Hydroxides, Hydrides and Alkaline Hydrogen Evolution”. In: *Journal of The Electrochemical Society* 160.3 (2013), F235–F243. DOI: 10.1149/2.026303jes.

[179] T. Lickert et al. “On the influence of the anodic porous transport layer on PEM electrolysis performance at high current densities”. In: *International Journal of Hydrogen Energy* 45.11 (2020), pages 6047–6058. DOI: 10.1016/j.ijhydene.2019.12.204.

[180] S. Yuan et al. “Bubble evolution and transport in PEM water electrolysis: Mechanism, impact, and management”. In: *Progress in Energy and Combustion Science* 96 (2023), page 101075. DOI: 10.1016/j.pecs.2023.101075.

[181] J. C. Garcia-Navarro et al. “Measuring and modeling mass transport losses in proton exchange membrane water electrolyzers using electrochemical impedance spectroscopy”. In: *Journal of Power Sources* 431 (2019), pages 189–204. DOI: 10.1016/j.jpowsour.2019.05.027.

[182] P. Haug et al. “Influence of process conditions on gas purity in alkaline water electrolysis”. In: *International Journal of Hydrogen Energy* 42.15 (2017), pages 9406–9418. DOI: 10.1016/j.ijhydene.2016.12.111.

[183] E. Leonard et al. “Operando X-ray tomography and sub-second radiography for characterizing transport in polymer electrolyte membrane electrolyzer”. In: *Electrochimica Acta* 276 (2018), pages 424–433. DOI: 10.1016/j.electacta.2018.04.144.

[184] J. O. Majasan et al. “Two-phase flow behaviour and performance of polymer electrolyte membrane electrolysers: Electrochemical and optical characterisation”. In: *International Journal of Hydrogen Energy* 43.33 (2018), pages 15659–15672. DOI: 10.1016/j.ijhydene.2018.07.003.

[185] J. Wang. “Theory and practice of flow field designs for fuel cell scaling-up: A critical review”. In: *Applied Energy* 157 (2015), pages 640–663. DOI: 10.1016/j.apenergy.2015.01.032.

[186] M. Maier et al. “Mass transport in polymer electrolyte membrane water electrolyser liquid-gas diffusion layers: A combined neutron imaging and X-ray computed tomography study”. In: *Journal of Power Sources* 455 (2020), page 227968. DOI: 10.1016/j.jpowsour.2020.227968.

[187] S. S. Lafmejani et al. “VOF modelling of gas–liquid flow in PEM water electrolysis cell micro-channels”. In: *International Journal of Hydrogen Energy* 42.26 (2017), pages 16333–16344. DOI: 10.1016/j.ijhydene.2017.05.079.

[188] J.-W. Song et al. “Temperature dependence of contact angles of water on a stainless steel surface at elevated temperatures and pressures: In situ characterization and thermodynamic analysis”. In: *Journal of colloid and interface science* 561 (2020), pages 870–880. DOI: 10.1016/j.jcis.2019.11.070.

[189] E. A. Chinnov et al. "Regimes of Two-Phase Flow in Short Rectangular Channel". In: *Microgravity Science and Technology* 21.S1 (2009), pages 199–205. DOI: 10.1007/s12217-009-9152-6.

List of Figures

List of Tables

A Appendix

A.1 Characterisation of the Model Electrolyte Solutions

A.1.1 Viscosity Measurements

Calibration Oil

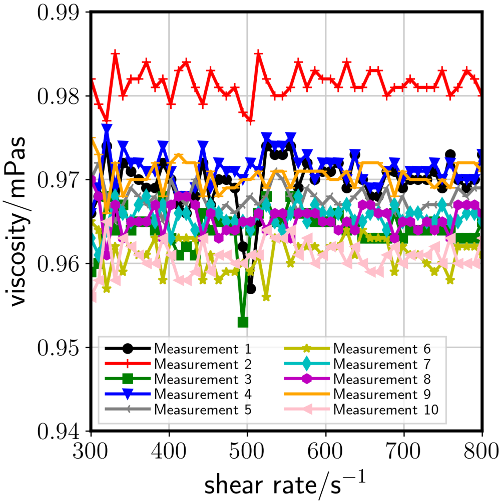

Figure A.1: Ten Viscosity Measurements with the Calibration Oil 1BW at 20 °C.

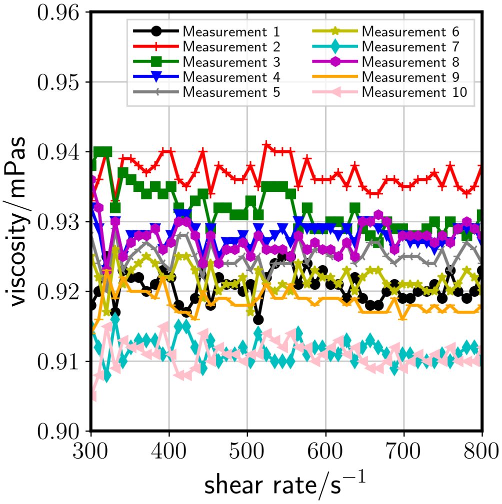

Figure A.2: Ten Viscosity Measurements with the Calibration Oil 1BW at 23 °C.

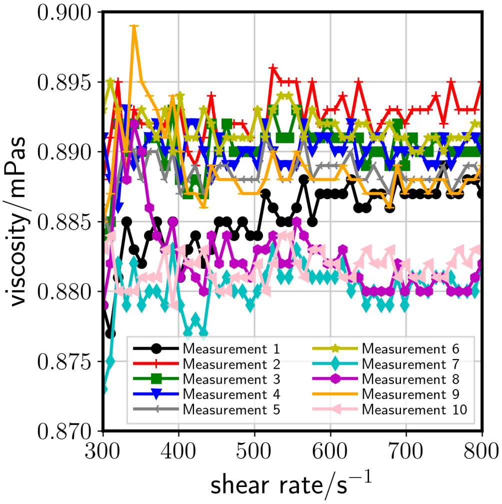

Figure A.3: Ten Viscosity Measurements with the Calibration Oil 1BW at 25 °C.

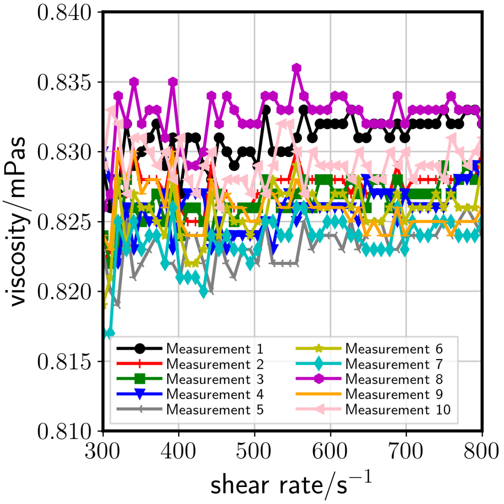

Figure A.4: Ten Viscosity Measurements with the Calibration Oil 1BW at 30 °C.

Barium Iodide and Potassium Iodide

Table A.1: Dynamic Viscosity of Barium Iodide and Potassium Iodide.

Electrol.	**Temp.** [°C]	**Conc.** [wt.-%]	**1** [mPas]	**2** [mPas]	**3** [mPas]	**4** [mPas]	**5** [mPas]	**6** [mPas]	**7** [mPas]	**8** [mPas]	**9** [mPas]	**10** [mPas]
BaI_2	8.63	26.27	1.58775	1.6239	1.5722	1.60885	1.59375	1.6018	1.5957	1.59235	1.62625	1.5969
BaI_2	15.36	25.94	1.3351	1.35415	1.32415	1.3446	1.3513	1.32945	1.36615	1.3719	1.3776	1.3327
BaI_2	22.06	25.62	1.14175	1.1517	1.16475	1.1362	1.14245	1.13655	1.12715	1.12725	1.1454	1.13125
BaI_2	11.15	24.24	1.47665	1.4706	1.52735	1.4883	1.48475	1.45765	1.48195	1.4629	1.45015	1.44605
BaI_2	17.03	24.73	1.2627	1.27915	1.26	1.28135	1.25505	1.26575	1.27725	1.25935	1.272	1.26875
BaI_2	22.89	25.06	1.10075	1.10065	1.11165	1.1043	1.1053	1.10855	1.0981	1.1149	1.11535	1.10365
BaI_2	28.73	25.26	0.99155	0.9948	0.98365	0.98485	0.9784	0.98635	0.9905	0.9836	0.9913	0.98125
BaI_2	34.59	25.35	0.87945	0.90735	0.8881	0.87715	0.87965	0.87835	0.8677	0.87105	0.8766	0.8664
KI	25.09	30.45	0.841	0.85174	0.82675	0.8383	0.8193	0.81655	0.8174	0.8096	0.85235	.83265
KI	26.97	32.12	0.78765	0.78845	0.78835	0.7822	0.78485	0.7902	0.78075	0.78725	0.78715	0.7864
KI	32.28	31.53	0.74725	0.7296	0.72605	0.7255	0.73335	0.725	0.72845	0.73185	0.7321	0.7213
KI	32.36	36.08	0.69955	0.69505	0.6991	0.70635	0.7056	0.70155	0.70375	0.7043	0.70255	0.7019
KI	32.35	40.65	0.61685	0.6235	0.6255	0.61655	0.60915	0.6299	0.61795	0.62365	0.61765	0.6341
KI	32.26	45.24	0.6079	0.604	0.60015	0.6072	0.60825	0.6075	0.61145	0.6107	0.61515	0.6167
KI	32.09	49.87	0.5473	0.54565	0.54245	0.5475	0.5554	0.5437	0.5567	0.54355	0.56685	0.53485
KI	31.83	54.53	0.50805	0.5027	0.5016	0.49705	0.5022	0.50395	0.5108	0.50025	0.5072	0.4984
KI	31.49	59.25	0.49095	0.49635	0.5021	0.4931	0.49245	0.50915	0.4899	0.47925	0.484	0.48335

A.1.2 Density Measurements

Table A.2: Mass Density of Barium Iodide and Potassium Iodide.

Electrolyte	**Conc.** [wt.-%]	**Temp.** [°C]	**1** [g/cm^3]	**2** [g/cm^3]	**3** [g/cm^3]	**4** [g/cm^3]	**5** [g/cm^3]	**6** [g/cm^3]	**7** [g/cm^3]	**8** [g/cm^3]	**9** [g/cm^3]	**10** [g/cm^3]
BaI_2	26.27	8.63	1.2688	1.268	1.2681	1.2682	1.2682	1.2681	1.2683	1.2681	1.2684	1.2685
BaI_2	25.94	15.36	1.265	1.2647	1.2648	1.2648	1.2649	1.2648	1.2643	1.2645	1.2647	1.2648
BaI_2	25.62	22.06	1.2762	1.2765	1.2763	1.2762	1.2762	1.2761	1.2762	1.2763	1.2761	1.2762
BaI_2	24.24	11.15	1.2381	1.2385	1.2383	1.2383	1.2384	1.2382	1.2383	1.2384	1.2384	1.2381
BaI_2	24.73	17.03	1.2675	1.2677	1.2675	1.2674	1.2674	1.2675	1.2676	1.2675	1.2675	1.2677
BaI_2	25.06	22.89	1.2796	1.2795	1.2796	1.2794	1.2796	1.2795	1.2795	1.2794	1.2796	1.2795
BaI_2	25.26	28.73	1.2683	1.2684	1.2683	1.2686	1.2684	1.2683	1.2685	1.2683	1.2683	1.2684
BaI_2	25.35	34.59	1.2772	1.2774	1.2772	1.2772	1.277	1.2773	1.2772	1.2774	1.2772	1.2773
KI	30.45	25.09	1.2722	1.2722	1.2721	1.2722	1.2722	1.2722	1.2722	1.2722	1.2721	1.2722
KI	32.12	26.97	1.2845	1.2842	1.2842	1.2841	1.2842	1.2842	1.2842	1.2842	1.2842	1.2842
KI	32.28	31.53	1.2782	1.2779	1.2779	1.2779	1.2781	1.2781	1.2781	1.2781	1.2781	1.2781
KI	32.36	36.08	1.2904	1.2904	1.2903	1.2905	1.2905	1.2905	1.2906	1.2906	1.2904	1.2906
KI	32.35	40.65	1.2857	1.2857	1.2855	1.2855	1.2857	1.2857	1.2857	1.2856	1.2857	1.2857
KI	32.26	45.24	1.2861	1.2861	1.286	1.2861	1.2861	1.2862	1.2861	1.2861	1.2861	1.286
KI	32.09	49.87	1.2758	1.2758	1.2758	1.2761	1.2761	1.2766	1.2761	1.2762	1.2762	1.2761
KI	31.83	54.53	1.2720	1.2720	1.2720	1.2720	1.2723	1.2723	1.2721	1.2724	1.2723	1.2723
KI	31.49	59.25	1.2594	1.2595	1.2593	1.2593	1.2593	1.2594	1.2593	1.2593	1.2594	1.2595

A.2 Neutron Radiography Measurements

A.2.1 Measurement Procedure

Table A.3: Measurement Procedure of Neutron Radiography Measurements .

Step	Duration	Temperature Anode	Temperature Cathode	Current Density	Volume Flow	Temperature Preheater Anode	Temperature Preheater Cathode	EIS Measurement	
								Current	Amplitude
	[s]	[°C]	[° C]	[A/cm^2]	[ml/min]	[° C]	[° C]	[A]	[mV]
1	10800	80	80	0	100	85	85	0.02	20
2	600	80	80	1	100	85	85		
3	1800	80	80	0	100	85	85	0.02	20
4	1200	80	80	1	100	85	85		
5	1800	80	80	0	100	85	85	0.02	20
6	1800	80	80	1	100	85	85		
7	1800	80	80	0	100	85	85	0.02	20
8	7200	80	80	1	100	85	85		
9	1800	80	80	0	100	85	85	0.02	20
10	7200	80	80	1	100	85	85		
11	1800	80	80	0	100	85	85	0.02	20
12	300	80	80	0.010	100	85	85		

Table A.3: Measurement Procedure of Neutron Radiography Measurements (continued).

Step	Duration	Temperature Anode	Temperature Cathode	Current Density	Volume Flow	Temperature Preheater Anode	Temperature Preheater Cathode	EIS Measurement Current	Amplitude
	[s]	[°C]	[° C]	[A/cm^2]	[ml/min]	[° C]	[° C]	[A]	[mV]
13	1800	80	80	0.000	100	85	85	0.1764	20
14	300	80	80	0.050	100	85	85		
15	1800	80	80	0	100	85	85	0.882	20
16	300	80	80	0.1	100	85	85		
17	1800	80	80	0	100	85	85	1.764	20
18	300	80	80	0.2	100	85	85		
19	300	80	80	0.4	100	85	85		
20	300	80	80	0.6	100	85	85		
21	0	80	80	0.7	100	85	85		
22	300	80	80	0.8	100	85	85		
23	0	80	80	0.9	100	85	85		
24	300	80	80	1	100	85	85		
25	1800	80	80	0	100	85	85	0.02	20
26	2700	80	80	0.010	50	85	85		
27	300	80	80	0.010	50	85	85		
28	1800	80	80	0.000	50	85	85	0.1764	20
29	300	80	80	0.050	50	85	85		

Table A.3: Measurement Procedure of Neutron Radiography Measurements (continued).

Step	**Duration**	**Temperature Anode**	**Temperature Cathode**	**Current Density**	**Volume Flow**	**Temperature Preheater Anode**	**Temperature Preheater Cathode**	**EIS Measurement**	
								Current	**Amplitude**
	[s]	[°C]	[° C]	[A/cm^2]	[ml/min]	[° C]	[° C]	[A]	[mV]
30	1800	80	80	0.000	50	85	85	0.882	20
31	300	80	80	0.1	50	85	85		
32	1800	80	80	0	50	85	85	1.764	20
33	300	80	80	0.2	50	85	85		
34	300	80	80	0.4	50	85	85		
35	300	80	80	0.6	50	85	85		
36	0	80	80	0.7	50	85	85		
37	300	80	80	0.8	50	85	85		
38	0	80	80	0.9	50	85	85		
39	300	80	80	1	50	85	85		
40	1800	80	80	0	10	85	85	0.02	20
41	2700	80	80	0.010	10	85	85		
42	300	80	80	0.010	10	85	85		
43	1800	80	80	0.000	10	85	85	0.1764	20
44	300	80	80	0.050	10	85	85		
45	1800	80	80	0.000	10	85	85	0.882	20
46	300	80	80	0.1	10	85	85		

Table A.3: Measurement Procedure of Neutron Radiography Measurements (continued).

Step	**Duration**	**Temperature Anode**	**Temperature Cathode**	**Current Density**	**Volume Flow**	**Temperature Preheater Anode**	**Temperature Preheater Cathode**	**EIS Measurement**	
								Current	**Amplitude**
	[s]	[°C]	[° C]	[A/cm^2]	[ml/min]	[° C]	[° C]	[A]	[mV]
47	1800	80	80	0	10	85	85	1.764	20
48	300	80	80	0.2	10	85	85		
49	300	80	80	0.4	10	85	85		
50	300	80	80	0.6	10	85	85		
51	0	80	80	0.7	10	85	85		
52	300	80	80	0.8	10	85	85		
53	0	80	80	0.9	10	85	85		
54	300	80	80	1	10	85	85		
55	1800	80	80	0	10	85	85	0.02	20
56	2700	80	80	0.010	25	85	85		
57	300	80	80	0.010	25	85	85		
58	1800	80	80	0.000	25	85	85	0.1764	20
59	300	80	80	0.050	25	85	85		
60	1800	80	80	0.000	25	85	85	0.882	20
61	300	80	80	0.1	25	85	85		
62	1800	80	80	0	25	85	85	1.764	20
63	300	80	80	0.2	25	85	85		

Table A.3: Measurement Procedure of Neutron Radiography Measurements (continued).

Step	Duration	Temperature Anode	Temperature Cathode	Current Density	Volume Flow	Temperature Preheater Anode	Temperature Preheater Cathode	EIS Measurement	
								Current	Amplitude
	[s]	[°C]	[° C]	[A/cm^2]	[ml/min]	[° C]	[° C]	[A]	[mV]
64	300	80	80	0.4	25	85	85		
65	300	80	80	0.6	25	85	85		
66	0	80	80	0.7	25	85	85		
67	300	80	80	0.8	25	85	85		
68	0	80	80	0.9	25	85	85		
69	300	80	80	1	25	85	85		
70	1800	80	80	0	25	85	85	0.02	20
71	2700	70	70	0.010	50	75	75		
72	300	70	70	0.010	50	75	75		
73	300	70	70	0.050	50	75	75		
74	300	70	70	0.1	50	75	75		
75	300	70	70	0.2	50	75	75		
76	300	70	70	0.4	50	75	75		
77	300	70	70	0.6	50	75	75		
78	0	70	70	0.7	50	75	75		
79	300	70	70	0.8	50	75	75		
80	0	70	70	0.9	50	75	75		

Table A.3: Measurement Procedure of Neutron Radiography Measurements (continued).

Step	**Duration** [s]	**Temperature Anode** [°C]	**Temperature Cathode** [° C]	**Current Density** [A/cm^2]	**Volume Flow** [ml/min]	**Temperature Preheater Anode** [° C]	**Temperature Preheater Cathode** [° C]	**EIS Measurement** **Current** [A]	**EIS Measurement** **Amplitude** [mV]
81	300	70	70	1	50	75	75		
82	1800	70	70	0	50	75	75	0.02	20
83	2700	70	70	0.010	100	75	75		
84	300	70	70	0.010	100	75	75		
85	300	70	70	0.050	100	75	75		
86	300	70	70	0.1	100	75	75		
87	300	70	70	0.2	100	75	75		
88	300	70	70	0.4	100	75	75		
89	300	70	70	0.6	100	75	75		
90	0	70	70	0.7	100	75	75		
91	300	70	70	0.8	100	75	75		
92	0	70	70	0.9	100	75	75		
93	300	70	70	1	100	75	75		
94	1800	70	70	0	100	75	75	0.02	20
95	2700	70	70	0.010	10	75	75		
96	300	70	70	0.010	10	75	75		
97	300	70	70	0.050	10	75	75		

Table A.3: Measurement Procedure of Neutron Radiography Measurements (continued).

Step	**Duration**	**Temperature Anode**	**Temperature Cathode**	**Current Density**	**Volume Flow**	**Temperature Preheater Anode**	**Temperature Preheater Cathode**	**EIS Measurement Current**	**EIS Measurement Amplitude**
	[s]	[°C]	[° C]	[A/cm^2]	[ml/min]	[° C]	[° C]	[A]	[mV]
98	300	70	70	0.1	10	75	75		
99	300	70	70	0.2	10	75	75		
100	300	70	70	0.4	10	75	75		
101	300	70	70	0.6	10	75	75		
102	0	70	70	0.7	10	75	75		
103	300	70	70	0.8	10	75	75		
104	0	70	70	0.9	10	75	75		
105	300	70	70	1	10	75	75		
106	1800	70	70	0	10	75	75	0.02	20
107	2700	70	70	0.010	25	75	75		
108	300	70	70	0.010	25	75	75		
109	300	70	70	0.050	25	75	75		
110	300	70	70	0.1	25	75	75		
111	300	70	70	0.2	25	75	75		
112	300	70	70	0.4	25	75	75		
113	300	70	70	0.6	25	75	75		
114	0	70	70	0.7	25	75	75		

Table A.3: Measurement Procedure of Neutron Radiography Measurements (continued).

Step	**Duration**	**Temperature Anode**	**Temperature Cathode**	**Current Density**	**Volume Flow**	**Temperature Preheater Anode**	**Temperature Preheater Cathode**	**EIS Measurement**	
								Current	**Amplitude**
	[s]	[°C]	[° C]	[A/cm^2]	[ml/min]	[° C]	[° C]	[A]	[mV]
115	300	70	70	0.8	25	75	75		
116	0	70	70	0.9	25	75	75		
117	300	70	70	1	25	75	75		
118	1800	70	70	0	25	75	75	0.02	20
119	2700	60	60	0.010	50	65	65		
120	300	60	60	0.010	50	65	65		
121	300	60	60	0.050	50	65	65		
122	300	60	60	0.1	50	65	65		
123	300	60	60	0.2	50	65	65		
124	300	60	60	0.4	50	65	65		
125	300	60	60	0.6	50	65	65		
126	0	60	60	0.7	50	65	65		
127	300	60	60	0.8	50	65	65		
128	0	60	60	0.9	50	65	65		
129	300	60	60	1	50	65	65		
130	1800	60	60	0	50	65	65	0.02	20
131	2700	60	60	0.010	10	65	65		

Table A.3: Measurement Procedure of Neutron Radiography Measurements (continued).

Step	**Duration** [s]	**Temperature Anode** [°C]	**Temperature Cathode** [° C]	**Current Density** [A/cm^2]	**Volume Flow** [ml/min]	**Temperature Preheater Anode** [° C]	**Temperature Preheater Cathode** [° C]	**EIS Measurement Current** [A]	**EIS Measurement Amplitude** [mV]
132	300	60	60	0.010	10	65	65		
133	300	60	60	0.050	10	65	65		
134	300	60	60	0.1	10	65	65		
135	300	60	60	0.2	10	65	65		
136	300	60	60	0.4	10	65	65		
137	300	60	60	0.6	10	65	65		
138	0	60	60	0.7	10	65	65		
139	300	60	60	0.8	10	65	65		
140	0	60	60	0.9	10	65	65		
141	300	60	60	1	10	65	65		
142	1800	60	60	0	10	65	65	0.02	20
143	2700	60	60	0.010	25	65	65		
144	300	60	60	0.010	25	65	65		
145	300	60	60	0.050	25	65	65		
146	300	60	60	0.1	25	65	65		
147	300	60	60	0.2	25	65	65		
148	300	60	60	0.4	25	65	65		

Table A.3: Measurement Procedure of Neutron Radiography Measurements (continued).

Step	**Duration** [s]	**Temperature Anode** [°C]	**Temperature Cathode** [° C]	**Current Density** [A/cm^2]	**Volume Flow** [ml/min]	**Temperature Preheater Anode** [° C]	**Temperature Preheater Cathode** [° C]	**EIS Measurement Current** [A]	**EIS Measurement Amplitude** [mV]
149	300	60	60	0.6	25	65	65		
150	0	60	60	0.7	25	65	65		
151	300	60	60	0.8	25	65	65		
152	0	60	60	0.9	25	65	65		
153	300	60	60	1	25	65	65		
154	1800	60	60	0	25	65	65	0.02	20
155	2700	60	60	0.010	100	65	65		
156	300	60	60	0.010	100	65	65		
157	300	60	60	0.050	100	65	65		
158	300	60	60	0.1	100	65	65		
159	300	60	60	0.2	100	65	65		
160	300	60	60	0.4	100	65	65		
161	300	60	60	0.6	100	65	65		
162	0	60	60	0.7	100	65	65		
163	300	60	60	0.8	100	65	65		
164	0	60	60	0.9	100	65	65		
165	300	60	60	1	100	65	65		

Table A.3: Measurement Procedure of Neutron Radiography Measurements (continued).

Step	**Duration** [s]	**Temperature Anode** [°C]	**Temperature Cathode** [° C]	**Current Density** [A/cm^2]	**Volume Flow** [ml/min]	**Temperature Preheater Anode** [° C]	**Temperature Preheater Cathode** [° C]	**EIS Measurement Current** [A]	**EIS Measurement Amplitude** [mV]
166	1800	60	60	0	100	65	65	0.02	20
167	2700	50	50	0.010	25	55	55		
168	300	50	50	0.010	25	55	55		
169	300	50	50	0.050	25	55	55		
170	300	50	50	0.1	25	55	55		
171	300	50	50	0.2	25	55	55		
172	300	50	50	0.4	25	55	55		
173	300	50	50	0.6	25	55	55		
174	0	50	50	0.7	25	55	55		
175	300	50	50	0.8	25	55	55		
176	0	50	50	0.9	25	55	55		
177	300	50	50	1	25	55	55		
178	1800	50	50	0	25	55	55	0.02	20
179	2700	50	50	0.010	100	55	55		
180	300	50	50	0.010	100	55	55		
181	300	50	50	0.050	100	55	55		
182	300	50	50	0.1	100	55	55		

Table A.3: Measurement Procedure of Neutron Radiography Measurements (continued).

Step	**Duration**	**Temperature Anode**	**Temperature Cathode**	**Current Density**	**Volume Flow**	**Temperature Preheater Anode**	**Temperature Preheater Cathode**	**EIS Measurement**	
								Current	**Amplitude**
	[s]	[°C]	[° C]	[A/cm^2]	[ml/min]	[° C]	[° C]	[A]	[mV]
183	300	50	50	0.2	100	55	55		
184	300	50	50	0.4	100	55	55		
185	300	50	50	0.6	100	55	55		
186	0	50	50	0.7	100	55	55		
187	300	50	50	0.8	100	55	55		
188	0	50	50	0.9	100	55	55		
189	300	50	50	1	100	55	55		
190	1800	50	50	0	100	55	55	0.02	20
191	2700	50	50	0.010	10	55	55		
192	300	50	50	0.010	10	55	55		
193	300	50	50	0.050	10	55	55		
194	300	50	50	0.1	10	55	55		
195	300	50	50	0.2	10	55	55		
196	300	50	50	0.4	10	55	55		
197	300	50	50	0.6	10	55	55		
198	0	50	50	0.7	10	55	55		
199	300	50	50	0.8	10	55	55		

Table A.3: Measurement Procedure of Neutron Radiography Measurements (continued).

Step	**Duration**	**Temperature Anode**	**Temperature Cathode**	**Current Density**	**Volume Flow**	**Temperature Preheater Anode**	**Temperature Preheater Cathode**	**EIS Measurement Current**	**EIS Measurement Amplitude**
	[s]	[°C]	[° C]	[A/cm^2]	[ml/min]	[° C]	[° C]	[A]	[mV]
200	0	50	50	0.9	10	55	55		
201	300	50	50	1	10	55	55		
202	1800	50	50	0	10	55	55	0.02	20
203	2700	50	50	0.010	50	55	55		
204	300	50	50	0.010	50	55	55		
205	300	50	50	0.050	50	55	55		
206	300	50	50	0.1	50	55	55		
207	300	50	50	0.2	50	55	55		
208	300	50	50	0.4	50	55	55		
209	300	50	50	0.6	50	55	55		
210	0	50	50	0.7	50	55	55		
211	300	50	50	0.8	50	55	55		
212	0	50	50	0.9	50	55	55		
213	300	50	50	1	50	55	55		

A.2.2 Polarization Curves

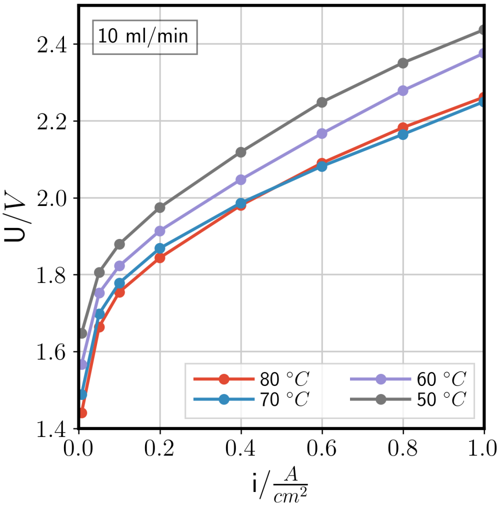

Figure A.5: Polarization Curves at different Temperatures measured at 10 ml/min electrolyte volume flow after 5 hours of break-in.

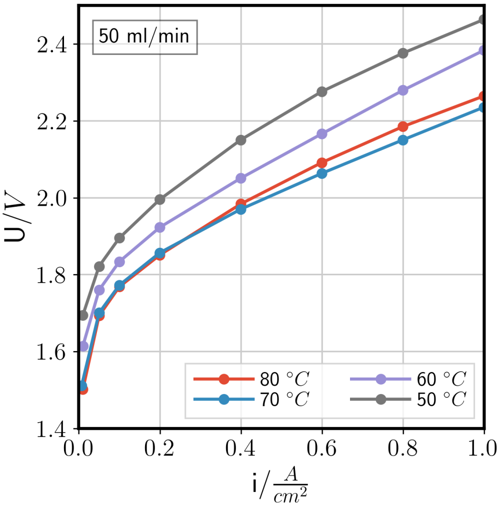

Figure A.6: Polarization Curves at different Temperatures measured at 50 ml/min electrolyte volume flow after 5 hours of break-in.

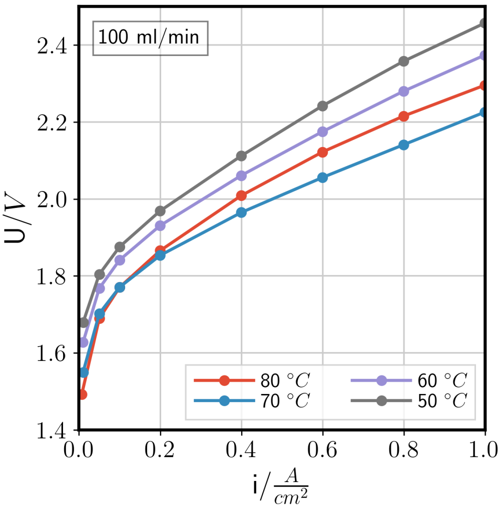

Figure A.7: Polarization Curves at different Temperatures measured at 100 ml/min electrolyte volume flow after 5 hours of break-in.

A.2.3 Contact Angle

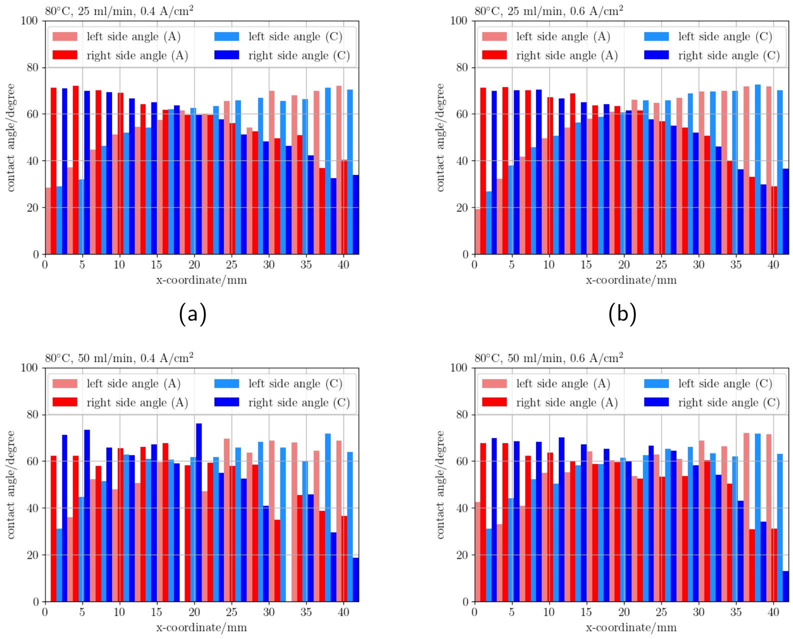

(a) (b) (c) (d)

Figure A.8: Contact Angle Distribution in the Flow Channel for 80 °C, 0.4 A/cm^2 and 25 ml/min (a), 80 °C, 0.6 A/cm^2 and 25 ml/min (b), 80 °C, 0.4 A/cm^2 and 50 ml/min (c) and 80 °C, 0.6 A/cm^2 and 50 ml/min (d).

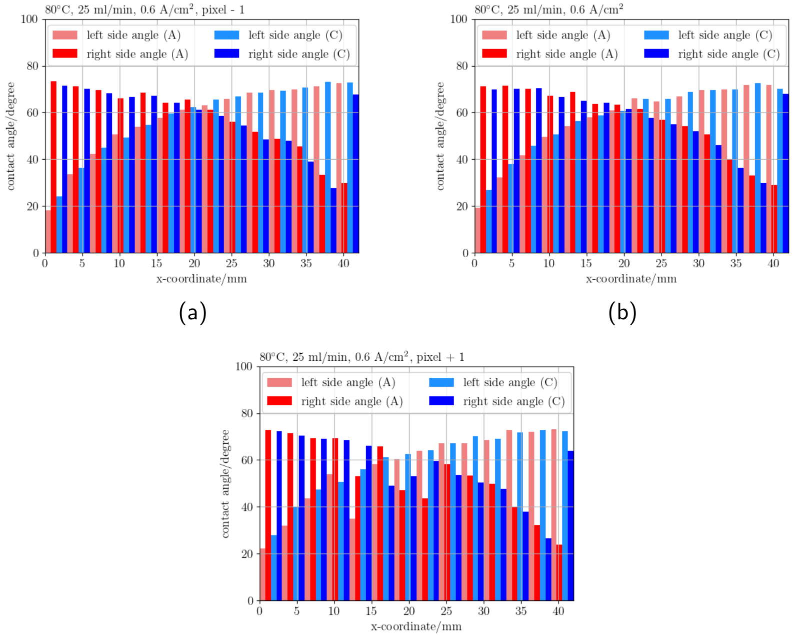

(a)

(b)

(c)

Figure A.9: Contact Angle Distribution in the Flow Channel for 80 °C, 0.6 A/cm^2 and 25 ml/min with pixel boundary changed one pixel to the left side (a), with pixel boundary unchanged (b), with pixel boundary changed one pixel to the right side (c).

A.3 Particle Image Velocimetry

A.3.1 Gas Bubble Velocity

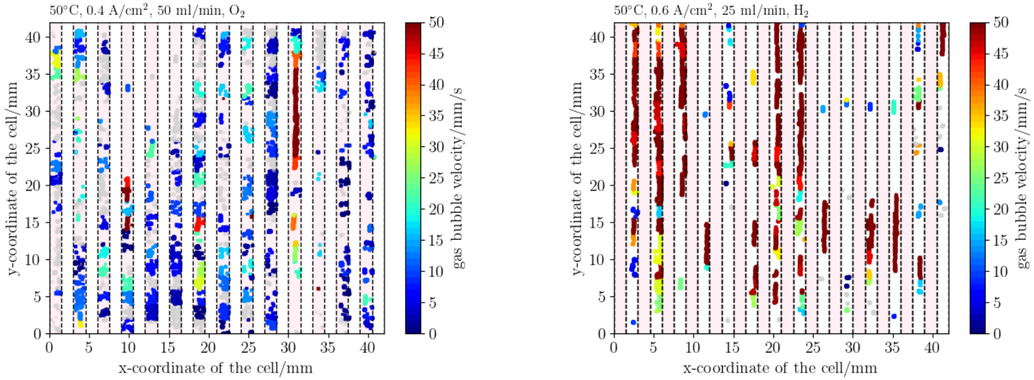

(a) (b)

Figure A.10: Gas Bubble Velocity for 50 °C, 0.4 A/cm^2 and 50 ml/min on the anode side (a) and for 50 °C, 0.6 A/cm^2 and 25 ml/min on the cathode side (b).

A.3.2 Contact Angle

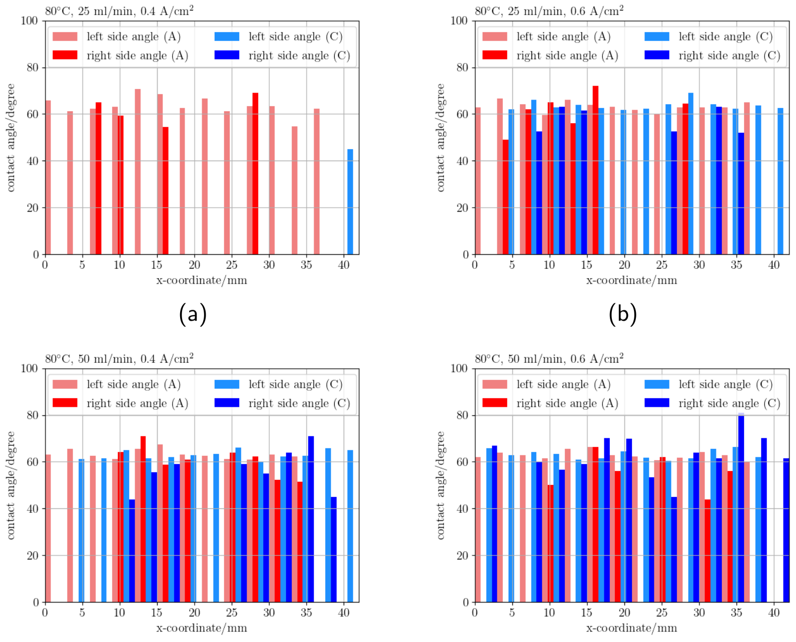

80°C, 25 ml/min, 0.4 A/cm²

80°C, 25 ml/min, 0.6 A/cm²

80°C, 50 ml/min, 0.4 A/cm²

80°C, 50 ml/min, 0.6 A/cm²

(a) (b)

(c) (d)

Figure A.11: Contact Angle Distribution in the Flow Channel for 80 °C, 0.4 A/cm^2 and 25 ml/min (a), 80 °C, 0.6 A/cm^2 and 25 ml/min (b), 80 °C, 0.4 A/cm^2 and 50 ml/min (c) and 80 °C, 0.6 A/cm^2 and 50 ml/min (d) Measured by Multiphase Particle Image Velocimetry.

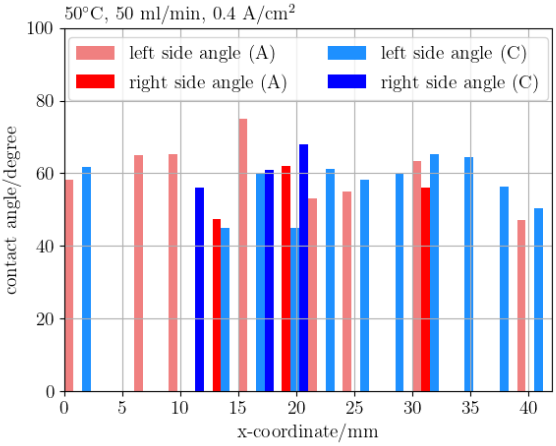

(a)

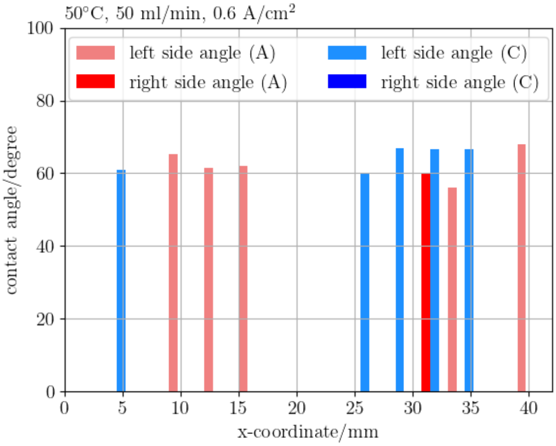

(b)

Figure A.12: Contact Angle Distribution in the Flow Channel for 50 °C, 0.4 A/cm^2 and 50 ml/min (a), 80 °C, 0.6 A/cm^2 and 50 ml/min (b) Measured by Multiphase Particle Image Velocimetry.

A.3.3 Measurement Error

Table A.4: Measurement Error of the Multiphase Particle Image Velocimetry Measurements.

Temperature KOH [°C]	Density Error [kg/m^3]	Viscosity Error [$mPas$]
50	-0.02 +0.06	-2.1e-3 +2.5e-3
80	-0.05 +0.06	-7.1e-3 +3.6e-3

The maximum density error from mixing BaI_2 solution is ± 1 kg/m^3. The maximum deviation of gas volume flow is ± 0.05 ml/min.

Band / Volume 648
Multi-scenario, high-resolution Lagrangian transport modeling for the analysis of the Asian tropopause aerosol layer
J. H. Clemens (2024), 143 pp
ISBN: 978-3-95806-792-9

Band / Volume 649
Prospektive Lebenszyklusanalysen von Power-to-Gas-Optionen
J. C. Koj (2024), XVIII, 197 pp
ISBN: 978-3-95806-794-3

Band / Volume 650
Assimilation of groundwater level and cosmic-ray neutron sensor soil moisture measurements into integrated terrestrial system models for better predictions
F. Li (2024), xvii, 172 pp
ISBN: 978-3-95806-796-7

Band / Volume 651
Integration of a rib-channel design to improve air-side contacting in solid oxide cell (SOC) stacks
Y. S. Ayhan (2024), 82 pp
ISBN: 978-3-95806-797-4

Band / Volume 652
Modelling Secondary Circulation in Convective Boundary Layer Using Large Eddy Simulation
L. Zhang (2024), 84 pp
ISBN: 978-3-95806-799-8

Band / Volume 653
Optionen zur Umsetzung der Klimaschutzziele im Verkehrssektor
S. Kraus (2025), XI, 317 pp
ISBN: 978-3-95806-802-5

Band / Volume 654
Modellierung der flächendifferenzierten Grundwasserneubildung für Schleswig-Holstein im Beobachtungszeitraum 1961 – 2021 und für Klimaszenarien bis 2100
I. McNamara, B. Tetzlaff, F. Wendland, T. Wolters (2025), 191 pp
ISBN: 978-3-95806-803-2

Band / Volume 655
Entwicklung alternativer Brenngaselektroden für die Hochtemperatur-Elektrolyse
F. E. Winterhalder (2025), vii, 161 pp
ISBN: 978-3-95806-805-6

Band / Volume 656
Oxide-based All-Solid-State Batteries for and from Recycling Processes
V. M. Kiyek (2025), viii, 128 pp, xix
ISBN: 978-3-95806-806-3

Band / Volume 657
Investigation of current and future anthropogenic chemical regimes in simulation chamber experiments
M. Färber (2025), 213 pp
ISBN: 978-3-95806-809-4

Band / Volume 658
Dynamischer Betrieb von Polymer-Elektrolyt-Membran Wasserelektrolyseuren
E. Rauls (2025), XIV, 239 pp
ISBN: 978-3-95806-811-7

Band / Volume 659
Pore-scale reactive transport modeling in cementitious materials: Development and application of a high-performance computing code based on the Lattice-Boltzmann method
S. Rohmen (2025), X, 295 pp
ISBN: 978-3-95806-812-4

Band / Volume 660
Recyclingmöglichkeiten für die Keramikkomponenten einer Festoxidzelle
S. Sarner (2025), VIII, 122 pp
ISBN: 978-3-95806-816-2

Band / Volume 661
Methodological Approach Enabling the Two-phase Flow Investigation in Alkaline Electrolysis under Demanding Conditions
S. Renz (2025), IX, 252 pp
ISBN: 978-3-95806-821-6

Weitere ***Schriften des Verlags im Forschungszentrum Jülich*** unter
http://wwwzb1.fz-juelich.de/verlagextern1/index.asp

Energie & Umwelt / Energy & Environment
Band / Volume 661
ISBN 978-3-95806-821-6

Mitglied der Helmholtz-Gemeinschaft

JÜLICH
Forschungszentrum